MECHANICAL ACTIVTION OF ULTRAMAFIC MINE WASTE MATERIALS FOR ENHANCED MINERAL CARBONATION

by

Jiajie Li

B.A.Sc., University of Science and Technology Beijing, 2006

M.A.Sc., University of Science and Technology Beijing, 2009

A THESIS SUBMITTED IN PARTIAL FULFILLMENT OF

THE REQUIREMENTS FOR THE DEGREE OF

DOCTOR OF PHILOSOPHY

in

THE FACULTY OF GRADUATE AND POSTDOCTORAL STUDIES

(Mining Engineering)

THE UNIVERSITY OF BRITISH COLUMBIA

(Vancouver)

May 2017

Abstract

The potential success of integrating mineral carbonation, as a pathway to CO_2 sequestration, in mining projects, is dependent on the mineralogical composition and characteristics of its waste rock and tailings. Ultramafic rocks have proven the best potential substrate for mineral carbonation and their ability to alter and to convert CO_2 into its carbonate mineral form is dependent on the original mineralogy and particle surface area. CO_2 conversion kinetics is complex and with the application of appropriate comminution technologies, its efficiency can be enhanced. The objective of this research is to evaluate mechanical activation to enhance the carbonation storage capacity of mine waste material. Three approaches were taken in this research. The first approach was to characterize the microstructure of the mechanically-activated mineral olivine, a predominant mineral constituent of ultramafic rocks, using X-ray diffraction patterns and line profile analysis methods with full pattern fitting method. The second approach was to compare the structural and chemical changes of mine waste with pure olivine, both of which were activated by various mechanical forces under both wet or dry conditions and subsequently carbonated in a direct aqueous carbonation process. Regardless of milling conditions, forsterite (Mg_2SiO_4), the olivine mineral variety in the mine waste, was found to be the main mineral being mechanically-activated and carbonated. It was determined that lizardite ($Mg_3(Si_2O_5)(OH)_4$), a hydrated magnesium silicate also common in ultramafic hosted mineral deposits, acted as catalyzer assisting forsterite reaching high levels of activation. This condition generated a greater CO_2 conversion to carbonate than that of pure olivine with the equal specific milling energy input. The stirred mill proved to be the most efficient form of mechanical activation vis-a-vis the direct aqueous carbonation process, followed by the planetary mill and the vibratory mill. The third approach analyzes the feasibility of mechanical activation in an integrated mineral carbonation process in a nickel mine considering

the life cycle of the process. The minimum operating cost for 60% CO_2 sequestration efficiency was 105-107 \$/t CO_2 avoided. At this point, the Turnagain project can potentially sequester 238 Mt/y CO_2 using its waste during the 28-year life of mine.

Preface

This thesis is composed of a series of papers that have either been published in peer-reviewed scholarly journals or have been submitted for review and subsequent publication. The following is a statement of contributions made to the jointly authored paper contained in this thesis:

1. Li, J and Hitch, M., 2017. A review of mechanical activation of magnesium silicates for mineral carbonation. Submitted to a journal for publication, Li wrote the entire paper. Hitch provided proofreading. This paper forms chapter 2 of this thesis.
2. Li, J and Hitch, M., 2016. Characterization of the microstructure of mechanically-activated olivine using X-ray diffraction pattern analysis. Minerals Engineering. 86: 24-33. Li is responsible conducting all experiments and data analysis, and writing the manuscript. Hitch provided proofreading. This paper forms chapter 3 of this thesis.
3. Li, J and Hitch, M., 2015. Ultra-fine grinding and mechanical activation of mine waste using high speed stirred mill for mineral carbonation. International Journal of Minerals, Metallurgy, and Material. 22(10): 1005-1016. Li conducted all the testing and wrote the manuscript. Hitch provided proofreading. This paper forms chapter 4 of this thesis.
4. Li, J and Hitch, M., 2017. Ultra-fine grinding and mechanical activation of mine waste using high speed stirred mill for mineral carbonation, International Journal of Mineral Processing. 158: 18-26. Li is responsible conducting all experiments and data analysis, and writing the manuscript. Hitch provided proofreading. This paper forms chapter 5 of this thesis.
5. Li, J and Hitch, M., 2017. Structural and chemical changes in mine waste mechanically activated in various milling environments, Powder Technology. 308: 13-19. Li performed

all experiments and data analysis, and wrote the manuscript. Hitch provided proofreading. This paper forms chapter 6 of this thesis.

6. Li, J and Hitch, M., 2017. Economic analysis on the application of mechanical activation in an integrated mineral carbonation processes. International Biodeterioration & Biodegradation. In press. DOI: 10.1016/j.ibiod.2016.08.026. Li performed all experiments and data analysis, and wrote the manuscript. Hitch and Pawlik provided proofreading. This paper forms chapter 7 of this thesis.

Three additional papers have been published in peer-reviewed scholarly journals, and six papers or posters have been presented in international conferences, which are outcomes work during PhD study. However, the following publication are not listed in this thesis.

1. Li, J and Hitch, M., 2016. Carbon dioxide adsorption isotherm study on mine waste for integrated CO_2 capture and sequestration processes. Powder Technology. 291: 408-413. Li performed all the experiments, data analysis and wrote the paper. Hitch and Pawlik facilitated with the research concept and design. Hitch provided proofreading.
2. Li, J and Hitch, M., 2016. Mechanical activation of ultramafic mine waste rock in dry condition for enhanced mineral carbonation, Minerals Engineering. 95: 1-4. Li is performed all experiments and data analysis, and wrote the manuscript. Hitch provided proofreading.
3. Li, J and Hitch, M., 2015. Carbon dioxide sorption isotherm study on pristine and acid-treated olivine and its application in the vacuum swing adsorption process, Minerals, 5(2): 259-275. Li is performed all experiments and data analysis, and wrote the manuscript. Hitch and Pawlik facilitated with the research concept and design. Hitch provided proofreading.

4. Li, J and Hitch, M., 2015. Mechanical activation of ultramafic mine waste for mineral carbonation using planetary milling, Presentation, In the 1st International Symposium and 4th Sino-Hungarian Workshop on Remediation and Restoration of Polluted Mining Areas, Wuhan, Hubei, China. Li performed all experiments and data analysis, and wrote the manuscript and present in the conference. Hitch provided proofreading.
5. Li, J and Hitch, M., 2014. Mechanical activation strategies for integrated mineral carbonation. Poster, in Carbon Management Canada 4th annual conference, Banff, AB, Canada. Li performed all experiments and data analysis, and wrote the poster and present in the conference. Hitch provided proofreading.
6. Hitch, M. and Li, J, 2013. Fine milling and mechanochemical activation of mine wastes for enhanced CO_2 mineral carbonation. Presentation, in International Conference on Mine Planning and Equipment Selection, Dresden, Germany. Li performed all experiments and data analysis, and wrote the manuscript and present in the conference. Hitch provided proofreading.
7. Hitch, M, Li, J., Dipple, G., 2013. Fine milling and mechanochemical activation of mine wastes for enhanced CO_2 mineral carbonation. Presentation, in American Geophysical Union, Fall Meeting, San Francisco, CA, United State. Li performed all experiments and data analysis, and wrote the presentation. Hitch provided proofreading. Dipple present in the conference.
8. Power, I., Dipple, G., Hitch, M., Mayer, U., Southam, G., Wen, J., Thomson, M., Wilson, S., Su, D., Harrison, A., Li, J., McCutcheon, J., Atashin, S., and Ahmed, A. 2014. Accelerating carbon mineralization in mine waste. Poster, in Carbon Management Canada

4th annual Conference, Banff, AB, Power wrote the poster and present in the conference. Li contributed a part of the poster.

9. Ballantyne, S., Hindle, S., Jacobs, A., Li, J., Hitch, M. 2010. Integrating CO_2 management in BC's mining industry: Research at the Norman B. Keevil Institute of Mining Engineering. Poster, in CIM Conference, Vancouver, BC, Canada. Ballantyne wrote the poster and present in the conference. Li contributed a part of the poster.

Table of Contents

List of Tables

List of Figures

List of Symbols

A – the degree of amorphization

A_0 – the total surface area (m^2)

A_{Fo} – the average amorphization degree of fosterite

A_L – the cosine Fourier coefficients of the peak profile

A_L^S – A_L relates to the crystal size

$A_{Li(100)}$ – the amorphization degree of lizardite (100) phase

A_{XRD} – the area of selected XRD peak (a.u.)

a, b, c – the lattice parameters (nm)

a', b' – coefficients in Equation 2.1

B – a parameter in the Williamson-Hall plots, where $B = \frac{\beta_f \cos\theta}{\lambda}$,

B_0 – the background of the diffraction peak for a non-activated mineral (a.u.)

B_X – the background of the diffraction peak for the mechanically activated mineral (a.u.)

b_v – the Burgers vector of dislocation

C – the contrast factor of the dislocations

C_s – the solid content by weight (%)

C_{XRD} – the degree of the crystalline phase after mechanical activation

$CO_{2,\ avoided}$ – the amount of CO_2 avoided (t)

$CO_{2,\ sequestrated}$ – the amount of CO_2 sequestrated (t)

$CO_{2,\ emitted}$ – the amount of CO_2 emitted (t)

$\overline{C}$ – the average dislocation contrast factor

Cum. W_N – the cumulative net specific energy consumption which can be used as specific energy input during IsaMill milling (kWh/t)

D – the crystallite size (nm)

D_V – the volume weighted crystallite size (nm)

d – the lattice spacing of an unstrained sample (nm)

Δd – the change in d at a strained status

d_{10} – 10% passing size (μm)

d_{50} – 50% passing size (μm)

d_{90} – 90% passing size (μm)

d_{BET} – the BET size (μm)

d_{hkl} – the interplanar spacing (nm)

d^* – a parameter in the Williamson-Hall plots, where $d^* = \frac{2\sin\theta}{\lambda}$.

E_C – energy consumption for mineral carbonation (kWh)

E_M – energy consumption from mechanical activation (kWh)

E_{power} – the amount of power used in the carbonation process (kWh)

E_{heat} – the amount of heat used in the carbonation process (kWh),

e – Euler's number (2.718)

f – the strain function in MWP method

f_m – the exponent in the shrinking core model

f_r – the ratio between the initially-observed rate constant of the sample

g – the diffraction vector

ΔH_T – macro energy state of activated solid (kJ/mol)

ΔH_d – the relative lattice distortion as a measure of dislocation density (kJ/mol)

ΔH_S – the specific surface area as a measure of the grain boundary with the surrounding medium (kJ/mol)

ΔH_A – the formation of amorphous material (kJ/mol)

ΔH_P – the formation of new phases such as polymorphic transformation (kJ/mol)

h, k, l – Miller indices of diffraction planes

I_{M} – the mill intensity

I_B – the intensity of background (a.u.)

I_{max} – the maximum height of a XRD peak (a.u.)

I_0 – the integral intensity of a diffraction peak for a non-activated mineral (a.u.)

I_X – the integral intensity of a diffraction peak for the mechanically activated mineral (a.u.)

IAP_i – the ion activity product for forsterite at the modeling step i

K – a unit cell geometry-dependent constant in Scherrer equation

K_{f_0} – the equilibrium constant for forsterite

k_0 – the initial rate constant (mol/(m^{2}s))

L – the Fourier length

L_0 – the edge length diameter of a crystallite

M – the mass of sample milled per hour (t/h)

M^* – the arrangement of dislocations

m – the median of the log normal crystallite size distribution calculated by the MWP method

N_0 – the initial moles of olivine

N_i – the amount of olivine still not dissolved during i^{th} interval

n – the order of reflection (n=1, 2, 3…)

P_0 – the operational power (kW)

P_{50} – the mean particle size

P_{80} – 80% passing size

P_{CO_2} – the CO_2 partial pressure (bar),

P_N – the specific power (kW)

P_{NL} – the power draw (kW) when running the mill empty with no material or media

Q – the flow rate of sample feed in the mill chamber (m^3/h)

R_e^* – the effective outer cut-off radius of dislocation.

R_{fom} – the residual value of the figure-of-merit function in Rietveld method

R_{wp} – the weighted profile residue in line profile fitting method

R_X – the CO_2 sequestration reaction efficiency

r – the reaction rate dependent of pH

S_G – granulometric surface area (m^2/g)

S_{BET} – the BET surface area (m^2/g)

T – the absolute temperature (K)

t_C – carbonation time (hour)

t_M – the time of mechanical activation, or milling residence time (hour)

V – the volume of a lattice (nm^3)

V_M – the net mill volume (L)

w_i – the coefficient in R_{fom}, which is $1/y_i(obs)$

W_N – the specific milling energy input (kWh/t)

$W_{O(L)}$ – an estimation for the total scale energy consumption if these mills were used in an industrial process (kWh/t)

x_{CO_2} – the weight percent of CO_2 in solid products (%)

$y_i(calc)$ – the calculated intensity at i^{th} step (a.u.)

$y_i(obs)$ – the measured intensity at i^{th} step (a.u.)

β – the integral breadth of a XRD peak

β' – corrects the surface area for the presence of contamination

β_C – the Cauchy components of β

β_D – the total-strain-integral breadth

β_{DC} – the Cauchy component of strain-integral breadth

β_{DG} – the Gaussian component of strain-integral breadth

β_f – the integral width of the sample

β_G – the Gaussian components of β

β_S – the total-size-integral breadth

β_{SG} – the Cauchy component of size-integral breadth

β_{SG} – the Gaussian component of size-integral breadth

ε – the strain, which is defined as $\varepsilon = \Delta d / d$

ε_A – the percent weight added if all the available cations convert to carbonates (%)

ε_{power} – the amount of CO_2 produced when generating the necessary amount of power (kg CO_2/kWh)

ε_{heat} – the amount of CO_2 produced when generating the necessary amount of heat (kg CO_2/kWh)

$< \varepsilon_L^2 >$ – the mean square strain

$< \varepsilon_L^2 >^{1/2}$ – the root mean square strain (RMSS)

σ – the variance of the log normal crystallite size distribution calculated by the MWP method

θ – the diffraction angle (°), and 2θ is the peak position of XRD profile

λ – the wavelength (nm)

ρ – the average dislocation density (m^{-2})

ρ_s – the slurry density (t/m^3)

ρ' – the density of material (g/cm^3)

τ – the shear stress (Pa)

τ_y – the Bingham yield stress (Pa)

η – the Bingham viscosity (Pa·s)

η_{CO_2} – the CO_2 avoidance ratio (%)

γ – the shear rate (s^{-1})

List of Abbreviations

AA – atomic absorption spectrometry

AEM – analytical electron microscopy

AFM – atomic force microscope

ARC – Albany Research Center

ÅAU – Åbo Akademi University

BET – Brunauer-Emett-Teller adsorption theory

CA – chemical activation

CCS – CO_2 capture and sequestration

CF_4 – Perfluoromethan.

CH_4 – Methane

CO_2 – carbon dioxide

DC – direct carbonation

DRIFT – diffuse reflectance Fourier transform infrared

ECBM – enhance coal bed methane

EGR – enhance gas recovery

EMPA – electron microprobe analyses

EPR – electron paramagnetic resonance

EOR – enhance oil recovery

FWHM – the full-width at half of the maximum height of a XRD peak

FTIR – fourier transform infrared

Fo – forsterite

GOF – goodness of fit, where GOF=R_{wp}/R_{exp}

FOLU – CO_2 from forestry and other land use

F-gases – fluorinated gases

GMD – Global Monitoring Division

GHG – greenhouse gases

GTP – global temperature change potential

GWP – global warming potential

GWP100 – CO_2-equivalent emissions calculated based on 100-year Global Warming Potential

HA – thermal activation

HFCs-152a – Hydrofluorocarbon-152a, Difluoroethan.

ICP – inductively coupled plasma

ICP-ES – inductively coupled plasma- emission spectrometry

IGCC – coal-based integrated gasification combined cycle system

ICSD – the Inorganic Crystal Structure Database

IDC – indirect carbonation

IEA – International Energy Agency

IPCC – the Intergovernmental Panel on Climate Change

IR – infrared spectroscopy

IUPAC – International Union of Pure and Applied Chemistry

LOI – loss on ignition

LPA – line profile analysis

Li – lizardite

MA – mechanical activation

MC – mineral carbonation

MEA – monoethanolamine

MWP – Multiple Whole Profile fitting method

MS – magnetic separation

NA – not applied

NETL – National Energy Technology Laboratory

NGCC – natural gas combined cycle plant

NIST – National Institute of Standards and Technology

N_2O – nitrous oxide

PM – Planetary mill

PGE – platinum group element

ppm – part per million

RCPs – Representative Concentration Pathways

SCPC – supercritical pulverized coal burning plant

SEM – scanning electron microscope

SM – Stirred mill

STM – scanning tunneling microscope

TEM – transmission electron microscopy

TGA – thermal gravimetric analyses

TOT/C – total carbon

tpd – tonne per day

UNFCCC – Nations Framework Convention on Climate Change

VM – Vibratory mill

WGIII – Work Group III

XPS – X-ray photoelectron spectroscopy

XRD – X-ray diffraction

XRF – X-ray fluoresces

XRPD – X-ray powder diffraction

Acknowledgements

I would like to convey my sincere gratitude and appreciation to following people who have provided their enormous support during my studies at the University of British Columbia.

This work would not have been possible without the assistance of them.

First of all, I would like to express my heartfelt gratitude to my supervisor Dr. Michael Hitch for his encouragement, continued support and invaluable mentoring throughout my thesis. Your patience and indulgence provided me freedom and confidence to grow up as a researcher. You offered not only massive research opportunities about integrated mineral carbonation, but also an abundant interpersonal interaction, and I will carry the pride in my heart as a member of the research group forever. Thank you for giving me the occasion to be who I really want to be.

I would like to extend my thankfulness to my committee members: Dr. Marek Pawlik, for leading me to research area of surface chemistry and answering my endless questions; Dr. Bern Klein, who contributed his knowledge in the field of comminution and suggestions about carbon cycle analysis; Dr. Gregory Dipple for his valuable comments on energy comsuption and mineral carbonation; and Dr. Ulirich Mayer for his advice and guidance in my comprehensive exam.

I am thankful to Dr. Janusz Laskowski for his priceless guidance on the thesis proposal.

I appreciate Ms. Sally Finora, Mr. Pius Lo, Mr. Aaron Hope, Ms. Jenny Lai, Dr. Mati Raudsepp and Mr. Gethin Owen for administrative and technical assistance.

The thoughtful discussion, support, and cooperation from other members in our research group are greatly appreciated. Particularly, I would like to thank Dr. Anthony Jacobs, Ms. Sheila Ballantyne, and Ms. Sarah Hindle from the Norman B. Keevil Institute of Mining Engineering, UBC; Dr. Ian Powder, and Ms. Anna Harrison in the Department of Earth and Ocean Science, UBC; Dr. John Wen, and Ms. Sanam Atashin in the Department of Mechanical and Mechatronics

Engineering, University of Waterloo. I also want to express my gratitude to Dr. Libin Tong, Mr. Chengtie Wang, Mr. Amit Kumar, Ms. Yan Tong, Dr. Jophat Engwayu, Dr. Leopoldo Gutierrez, Dr. Wenying Liu, and Dr. Haitham Ahmed for their assistance and friendship. In addition, I would like to thank my undergraduate research assistant, José Lourenço Neto for his hard work and friendship.

I would like to thank the main office of the Norman B. Keevil Institute of Mining Engineering at UBC, in particular Leslie Nichols, Maria Lui, for giving me the flexibility to both work and pursue this academic adventure simultaneously. Moreover, I also appreciate all the faculty and stuff of the Norman B. Keevil Institute of Mining Engineering at UBC.

This research would not be possible without the generous funding from China Scholarship Council and Carbon Management Canada National Centre of Excellence for financial support. I am also thankful for the financial assistance in the form of a Faculty of Applied Science Graduate Award and International Partial Tuition Scholarship.

Finally, my deepest gratitude goes to my family for their everlasting love, as well as enormous tangible and emotional support during all my years of education. To my parents, Mr. Bingnan Li and Mrs. Runlan Zheng, thanks for instilling in me the value of hard work and having a firm faith in me. To my son, Zixuan Yu, the strength of my everyday triumph. Thank you for coming to my life during this study and making me smile. Most of all, Dr. Zhengxing Yu, my beloved husband, I am extremely grateful for your encouragement and inspiration, and all the sacrifices you have made for me. The completion of this work would not have been possible without you.

The thesis is dedicated to the continued support of

my husband, son, and parents.

Chapter 1: Introduction

Climate change poses a significant threat to human life on Earth. The main cause of climate change is human activity that disturbs the balance of the carbon cycle and increases the concentration of atmospheric carbon dioxide (CO_2). Carbon capture and storage (CCS) is one of the most effective ways of mitigating global warming, and it can potentially be integrated via ultramafic mining deposit for commercial application. This chapter provides an introduction to the relationship between CO_2 and climate change; the carbon cycle; a review of literatures related to carbon capture and storage, as well as the present state of integrated mineral carbonation in mining industry; and outline's this dissertation's research objective, research questions and hypotheses, and chapter organization.

1.1 Climate change and carbon dioxide

Over the past 30 years, the global climate has been warming at a faster pace than in any other period since 1850 (IPCC, 2014: pg. 40). Scientists have gathered undeniable evidence of global warming, including: increased atmospheric and ocean temperatures, significant glacial melting, and rising sea levels (IPCC, 2013). All of these changes increase the risk of climatic hazards, such as severe storms, flooding, frost, and multi-decade droughts (IPCC, 2013). At present, climate change has already had an adverse impact on human and natural systems. Since climate change is irreversible, humans must take measures both to adapt to it and to mitigate its effects (IPCC, 2014).

The first scientific account of global warming was published in 1824, when Jean-Baptiste Joseph Fourier proposed his theory of the Greenhouse Effect (Cowie, 2013: pg.5). Fourier argued that the infrared radiation (long-wave, > 4 μm) from the sun and the resulting radiation reflected from the Earth's surface are all absorbed by the atmosphere, and that this infrared energy is re-

emitted in all directions, thus warming the lower atmosphere and the Earth's surface (Cowie, 2013). In 1861, John Tyndall quantified the heating–absorbing properties of gases (Cowie, 2013: pg.7), some of which are now labeled as greenhouse gases (GHGs). Examples of greenhouse gases include methane (CH_4), nitrous oxide (N_2O), and carbon dioxide (CO_2), fluorinated gases (F-gases) (such as hydrofluoriocarbures HFCs, perfluorocarbons PFCs, and sulphurhexafluoride SF_6). Table 1.1 lists the lifetime, global warming potential (GWP), and global temperature change potential (GTP) of selected GHGs.

Table 1.1 Emission metric value of selected GHG (Source: IPCC 2014: Box 3.2. Table 1, pg. 87).

		GWP[a]		GTP[b]	
	Lifetime (yr)	Cumulative forcing over 20 years	Cumulative forcing over 100 years	Temperature change after 20 years	Temperature change after 100 years
CO_2	-	1	1	1	1
CH_4	12.4	84	28	67	4
N_2O	121	264	265	277	234
CF_4[c]	50,000	4880	6630	5270	8040
HFCs-152a[d]	1.5	506	138	174	19

Note: a) GWP is an index compares a greenhouse gas to CO_2 based on radiative forcing, accumulated over a chosen time horizon. b) GTP is an index based on the temperature response of the greenhouse gas compared to the effect of CO_2. c) CF_4 is Perfluoromethan. d) HFCs-152a is Hydrofluorocarbon-152a, Difluoroethan.

In 1896, Svante Arrhenius first postulated that the emission of anthropogenic CO_2 could result in global warming (Cowie, 2013: pg.8). After many years of investigation and development, scientists are more than 95% certain about this causal connection (IPCC, 2014: pg. v). There are two strong lines of evidence supporting the theory of anthropogenic climate change. First of all, CO_2 is the primary anthropogenic GHG that has contributed to global warming since the industrial revolution, and, as Figure 1.1 illustrates, the emission of anthropogenic GHG has increased

dramatically since that time. The annual emission of anthropogenic GHG increased about 80% between 1970 and 2010, rising from 27 to 49 Gt. of all GHGs, CO_2 is responsible for 73% to 76% of annual GHG emissions (IPCC, 2014: pg.5). Finally, annual CO_2 emissions are increasing at a much higher rate than that of other GHGs. Given that it forms the vast majority of global GHG emissions and is increasing at a more rapid rate than any other GHG, it is clear that CO_2 is the most important GHG when it comes to understanding climate change.

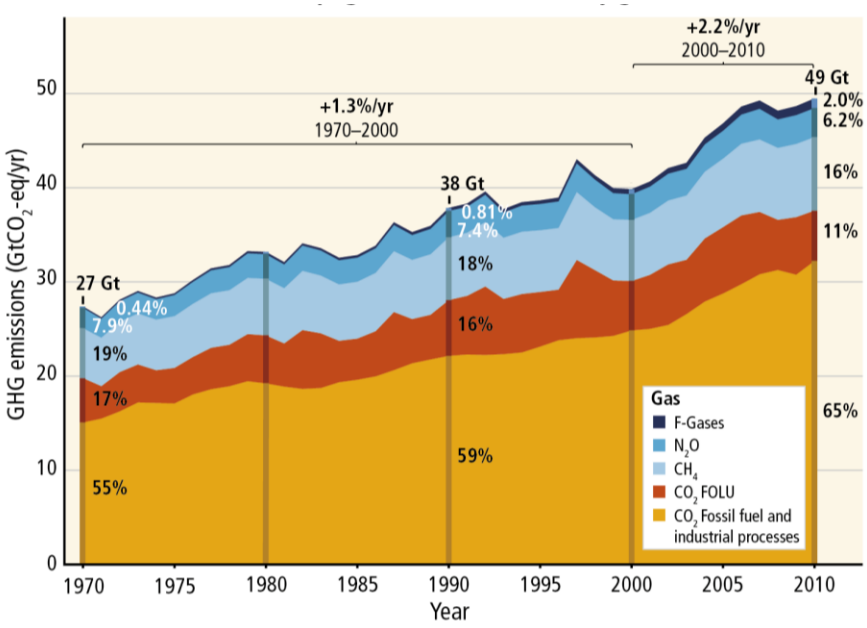

Figure 1.1 Total annual anthropogenic greenhouse gas (GHG) emissions (gigatonne of CO_2-equivalent per year, $GtCO_2$-eq/yr) for the period 1970 to 2010 by gases: CO_2 from fossil fuel combustion and industrial processes; CO_2 from Forestry and Other Land Use (FOLU); methane (CH_4); nitrous oxide (N_2O); fluorinated gases covered under the Kyoto Protocol (F-gases). CO_2-equivalent emissions calculated based on 100-year Global Warming Potential (GWP100) values. (Source: IPCC 2014: Figure 1.6, pg. 46)

Secondly, the atmospheric CO_2 concentration and average surface temperature on Earth tend to fluctuate in tandem over an 800,000 year cycle (Fig. 1.2) (Romão, 2015). Before the industrial era, the Earth was able to naturally regulate atmospheric CO_2 concentrations, keeping them below 280 part per million (ppm). The atmospheric CO_2 concentration, as measured at the

Mauna Loa Observatory in Hawaii, has increased nearly 2 ppm per year since 2000, reaching 402 ppm in August 2016—43.6% above pre-industrial levels (GMD, 2016). At the same time, the average global temperature—which is determined by combining land and ocean surface temperatures—shows a warming of 0.8 °C above pre-industrial levels (Ray, 2015: pg. 3). If no additional efforts are made to constrain or manage anthropogenic GHG emissions, the CO_2 equivalent concentration is expected to exceed 1,000 ppm by 2100, which would result in a global mean surface temperature increase of 2.6 to 4.8 °C (Fig. 1.3) (IPCC, 2014: pg. 60).

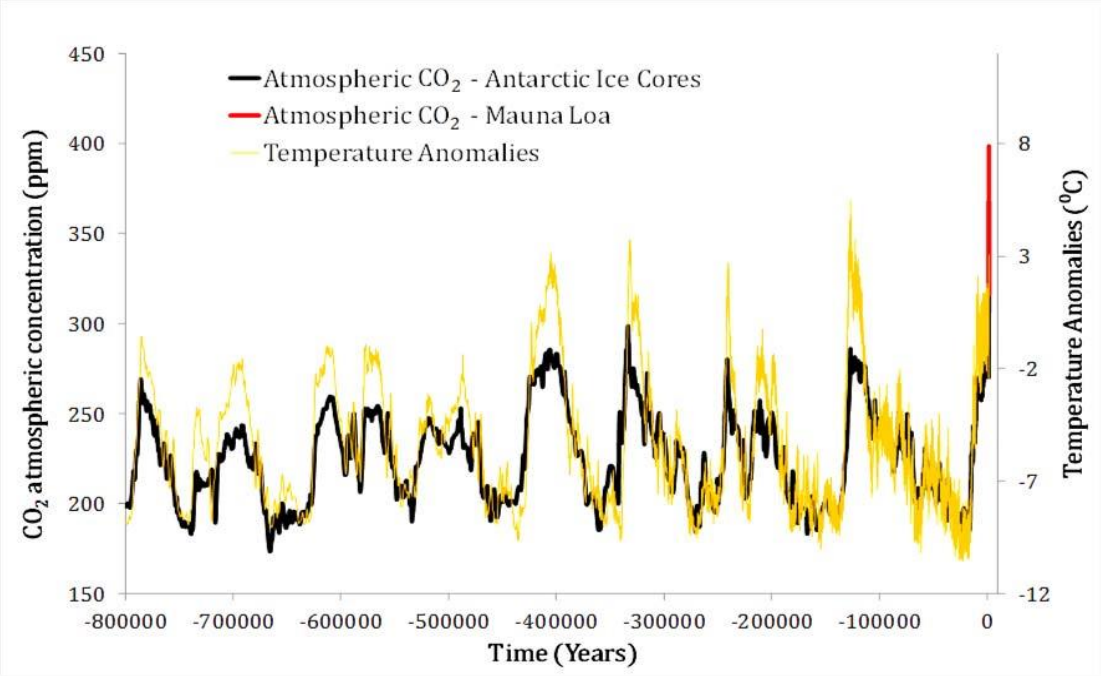

Figure 1.2 Relation between CO_2 emissions and temperature anomalies over time (Source: Romão, (2015: Figure 2, pg.3)).

International efforts to mitigate climate change began in earnest in 1992 when the United Nations Framework Convention on Climate Change (UNFCCC) was introduced and adopted. UNFCCC aimed at "stabilized greenhouse gas concentrations in the atmosphere at a level that

would prevent dangerous anthropogenic interference with the climate system" (United Nations, 1992). Afterwards, the CO_2 emission targets of UNFCCC-involved countries were outlined in Kyoto Protocol for the period of 2008 to 2012 (UNFCCC, 1998), the Doha Amendment to the protocol for the period of 2013 to 2020 (UNFCCC, 2012), and Paris Agreement for the period of 2020 to 2030 (UNFCCC, 2015). The Paris Agreement was negotiated with the awareness that global warming is a serious threat, and its ultimate goal was to limit global warming to less than 2 °C and to pursue efforts to limit the rise to 1.5 °C relative to pre-industrial levels (UNFCCC, 2015). However, in order to reach these goals, the involved countries must find affordable and practical solutions for managing carbon.

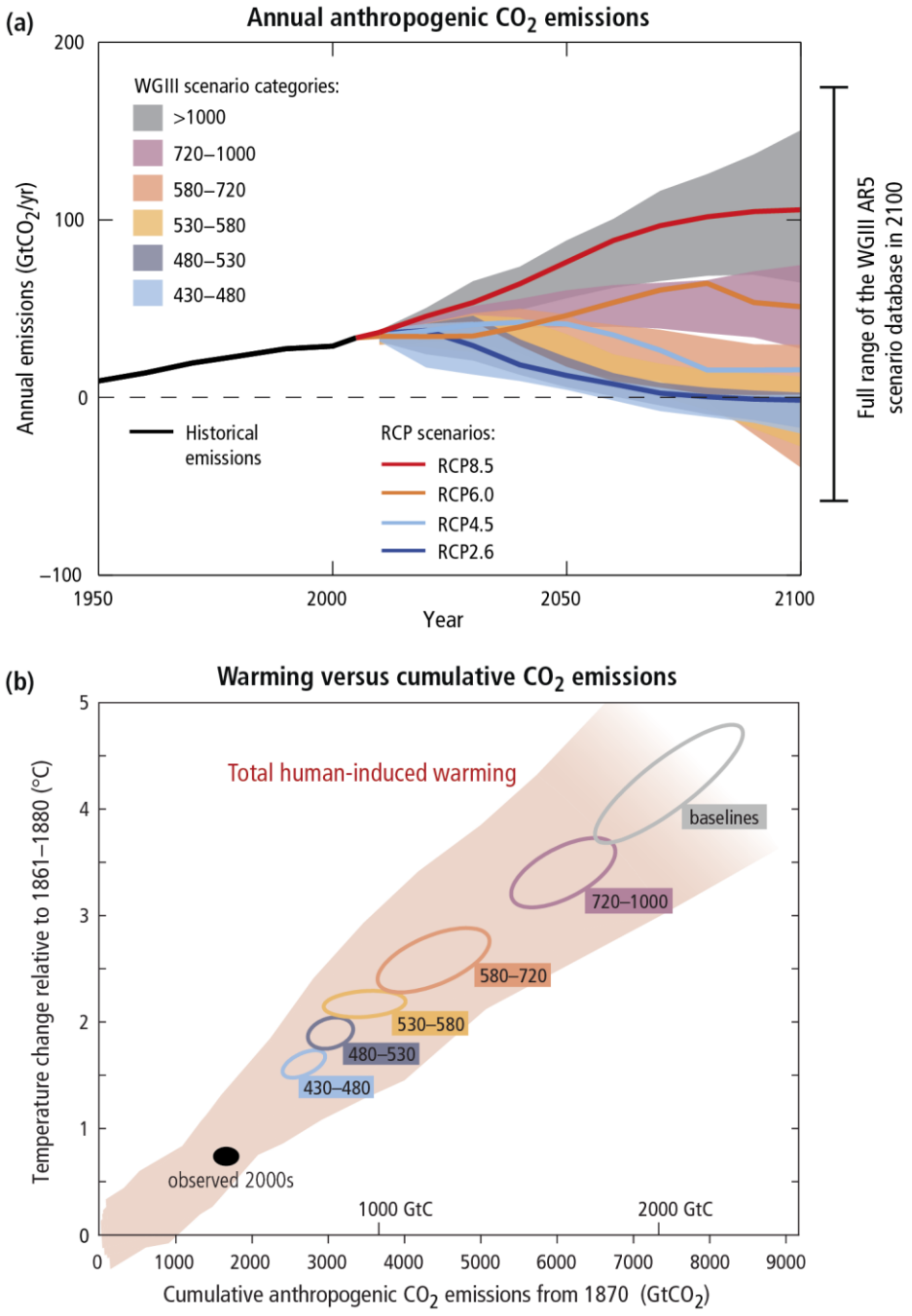

Figure 1.3 Projection of future changes. (a) Emissions of CO_2 alone in the Representative Concentration Pathways (RCPs) (lines) and the associated scenario categories used in Work Group III (WGIII) (colored areas show 5 to 95% range). (b) Global mean surface temperature increase as a function of cumulative total global CO_2 emissions from various lines of evidence. The colored plume illustrates the multi-model spread over the four RCP scenarios and fades with the decreasing number of available models in RCP8.5. Ellipses show total anthropogenic warming in 2100 versus cumulative CO_2 emissions from 1870 to 2100 from a simple climate model (median climate response) under the scenario categories used in WGIII. The filled black ellipse shows observed emissions to 2005 and observed temperatures in the decade 2000–2009 with associated uncertainties. (Source: IPCC 2014: Figure SPM5, pg. 9).

1.2 Carbon cycle

Carbon reserves in the Earth's crust act as 'dead or non-reactive' carbon in the lithosphere, and 'live' carbon in the atmosphere, hydrosphere, and biosphere (Table 1.1) (Hänchen, 2007). Typically, there are two natural carbon cycles: a geochemical cycle comprising of the exchange between live carbon and dead carbon in the lithosphere (e.g. volcanism, weathering); and a biochemical cycle involving the live carbon circulating through atmosphere, water bodies, soil, and biosphere (e.g. bio-recycling of organic matter). The geochemical cycle has remained in balance for millions of years and has guaranteed an almost constant carbon preserve in the live reservoir of the biochemical cycle (Killops and Killops, 2005).

Table 1.2 The distribution of carbon on earth's crust (Hänchen, 2007: pg. 5)

Carbon type	Location	Carbon reservoir	Carbon variety
Dead carbon (99.4%)	lithosphere	Carbonate minerals (80%)	Limestone, dolomite
		Sedimentary rocks (20%)	Kerogen, graphite
Live carbon (0.06%)	Atmosphere	Atmosphere (2%)	Atmospheric CO_2
	Hydrosphere	Oceans (90%)	Oceanic HCO_3^- and CO_3^{2-}
	Biosphere	Dead surface organic matters (7%)	Humus
		Living organism (1%)	Plants, animals

The concentration of atmospheric CO_2 has increased since the industrial revolution due to two major anthropogenic causes: forestry and other land use, and fossil fuel use and industrial production. Although CO_2 emissions from forestry and other land uses has grown at a rather slow rate, the increase in CO_2 emissions from fossil fuel usage and industrial production has been much more rapid and much greater in volume (Fig. 1.1) (IPCC, 2014). Fossil fuels—such as liquid fuels, natural gas, and coal—are a cheap and convenient energy source; as such, they have become the de facto energy source that have been adopted to meet the energy demands created by global

economic and population growth. U.S. Energy Information Administration (2016: pg 9) estimates that fossil fuels will continue to be the dominant global source of energy, and that they will still account for 78% of the world's total energy consumption in 2040.

Fossil fuel is a type of dead carbon, and only 0.0053% of dead carbon can be recovered as fossil fuel (Huijgen and Comans, 2003: pg. 5). The burning of fossil fuels causes a carbon flux from the lithosphere to the atmosphere (as CO_2), which is estimated to be 10 to 15 times that of the natural process (Hänchen, 2007: pg. 5). However, strategies and solutions that reverse this process by creating a carbon flux from the atmosphere back to the lithosphere—namely, CO_2 mineralization (or mineral carbonation)—can permanently solve the current anthropogenic CO_2 problem.

1.3 Carbon storage

Currently, various strategies and solutions have been adopted by various countries for the purpose of eliminating anthropogenic CO_2 emissions. These approaches include: improving energy efficiency; using energy sources that are less carbon-intensive (i.e. natural gas, hydrogen, and nuclear power) or renewable (i.e. solar, wind, hydropower, geothermal and bio-energy); enhancing biological sinks (i.e. afforestation and reforestation); and CO_2 capture and storage (CCS) (Leung et al., 2014). Of these approaches, CCS is the only option that can meet the enormous demand for CO_2 reduction. It is estimated that CCS could reduce 85-90% of CO_2 from large-emission sources and energy-intensive emitters (Leung et al., 2014: pg. 427).

In the CCS process, CO_2 is concentrated from diluted sources and conveyed to storage. Research on and demonstration of CCS technology has grown significantly in recent years with the hope that it can one day become economically feasible (Boot-Handford et al., 2014; IPCC, 2005; Leung et al., 2014; MacDowell et al., 2010). The CCS value chain contains four components:

the source of CO_2 emissions, CO_2 capture and separation, CO_2 compression and transportation, and CO_2 storage or utilization.

1.3.1 Source of CO_2 emission

The sources of CO_2 for CCS are usually point source emissions that result from the combustion or gasification of fossil fuel and biomass to generate heat and power. The largest proportion of global CO_2 emissions comes from thermal power plants. Currently, research on CCS has mainly focused on modern power plants, such as supercritical pulverized coal (SCPC) thermal plants, natural gas combined cycle (NGCC) plants, and coal-based integrated gasification combined cycle (IGCC) systems (IPCC, 2005; Rubin et al., 2015). The second largest source of CO_2 emissions comes from industrial processes, such as cement manufacturing, iron and steel smelting, chemical production, biofuels, natural gas treatment, and oil refining (Boot-Handford et al., 2014). In 2013, the level of global CO_2 emissions from large industrial plants were roughly half of that produced by power plants since the industrial revolution (IEA, 2013). The application of CCS at industrial plants is of increasing interest due to the continuous growth in CO_2 emissions from industrial processes and the need to curb the growing impacts of climate change. It should be noted that dispersed sources, including emissions from automobiles and airplanes, are the research focus for air capture. Air capture is also a complementary approach to CCS, as it deals with CO_2 leakage from storage facilities (Lackner et al., 2012).

1.3.2 CO_2 capture and separation

There are three approaches to CO_2 capture at power plants: post-combustion (CO_2/H_2 separation), pre-combustion (CO_2/N_2 separation), and oxy-fuel combustion (CO_2/H_2O separation). The selection of a CO_2 capture method depends on the type of power plant. For example, the

preferred CO_2 capture options for coal-fired plants and gas fired plants are pre-combustion and post-combustion capture, respectively (Leung et al., 2014).

The separation of CO_2 can be achieved through the use of absorption, adsorption, cryogenic distillation, membranes, gas hydrates, and chemical looping (Kenarsari et al., 2013). Currently, the most mature capture technology, which is widely used in modern power plants, is post-combustion capture via chemical absorption using monoethanolamine (MEA) (Azapagic and Cue, 2015). However, the regeneration of CO_2 from MEA is energy-intensive, and searching for cost-effective solvents, sorbents, and membranes is challenging for large scale CO_2 capture (Kenarsari et al., 2013).

1.3.3 CO_2 compression and transportation

Captured CO_2 is usually compressed above 10 MPa and transported to the storage site. CO_2 can be transported by pipeline, ship, rail, or road (IPCC, 2005). CO_2 transportation via pipeline is the most viable option for continuously delivering large volumes of gas over many years, and has the added benefit of potential cost savings from reusing the existing pipeline for gas or oil transportation (Leung et al., 2014). Alternatively, the use of cargo ships may be an economical option for transporting relatively small volumes (i.e. less than million tonnes of CO_2 per year) of CO_2 over large distances (> 1000 km) (IPCC, 2005: pg. 31).

1.3.4 CO_2 storage and utilization

The CO_2 storage and utilization technology works by isolating the gas physically, chemically, and biologically via geological storage and mineral carbonation (Huijgen and Comans, 2003). Geological storage is predominantly achieved by depositing supercritical CO_2 into underground voids, such as depleted oil and gas reservoirs, un-mineable coal seams, deep saline aquifers, and the deep ocean (Leung et al., 2014). CO_2 is used in the petroleum and gas industry

to displace hydrocarbons and to promote greater commercial value through methods such as enhanced oil recovery (EOR), enhanced gas recovery (EGR), and enhanced coal bed methane recovery (CBM). Geological storage is the most established practice in EOR (Doucet, 2011), and is the most feasible option to fix large CO_2 quantities. In 2015, there were 15 large scale CCS projects in operation worldwide, with an additional 7 large scale CCS projects scheduled to be operational by 2017 (Herzog, 2016: pg. 6). All of these 22 CCS projects operate by storing CO_2 underground, with 16 of them using EOR technology (Global CCS Institution, 2016). The dominant concern related to these physical storage options are that the potential for CO_2 leakage, which must be monitored long-term (Jones et al., 2015).

Mineral carbonation is the only option that can permanently store CO_2 without long-term monitering (Bobicki, 2014). Mineral carbonation chemically binds CO_2 in calcium-, magnesium- and iron-rich silicate minerals to fix CO_2 as carbonate minerals (Lackner, 2003). This reaction is a naturally-occurring process that slowly binds CO_2 to carbonates over several hundreds to thousands of years. Numerous researchers have attempted to accelerate the reaction between CO_2 and alkaline minerals both in-situ and ex-situ (Azdarpour et al., 2015; Geerlings and Zevenhoven, 2013; Huijgen and Comans, 2005, 2003; IPCC, 2005; Olajire, 2013; Power et al., 2013b; Romanov et al., 2015; Sanna et al., 2014; Sipilä et al., 2008; Yuen et al., 2016).

The chemical reaction that takes place during carbonation occurs in two broad environmental conditions. In-situ mineral carbonation injects CO_2 into mantle peridotite and basalts deposits, and the reaction occurs in an underground, hydrothermal environment. Conversely, ex-situ mineral carbonation is achieved in a separate reactor or an industrial process where the operational conditions are easy to control (Geerlings and Zevenhoven, 2013). Ex-situ mineral carbonation can also apply CO_2 as a carbon source for chemical production (i.e.

carbonates), which can be used as building materials, aggregations, and cementitious phases (Markewitz et al., 2012). At present, mineral carbonation has only reached the demonstration and pilot scales (Sanna et al., 2014). Although no economically and financially viable mineral carbonation process has been developed so far, some attractive concepts and experimental results suggest the possibility for scaling up and commercializing the carbonation process over the next decade (Doucet, 2011). For example, the Carbfix pilot project in Iceland can carbonate 95% of injected CO_2 in less than 2 years (Matter et al., 2016: pg. 1312). The direct aqueous carbonation route proposed at National Energy Technology Laboratory (NETL), formerly Albany Research Council (ARC) in the U.S., (O'Connor et al., 2005) has been evaluating the most promising ex-situ process for industrial application, and this process is commonly used as a base line against which other methods of carbonation are compared. The indirect two step pH-swing carbonation method developed at Finland's Åbo Akademi University (ÅAU) has produced results that are able to compete with the NETL process when using serpentine as CO_2 feedstock (Nduagu et al., 2012). In cases where geological storage is not applicable, mineral carbonation processes could be an alternative option for the storage of small to medium CO_2 emissions (< 2.5 Mt CO_2) (Sanna et al., 2014: pg. 8051). Figure 1.4 shows an example of the CCS process via ex-situ mineral carbonation.

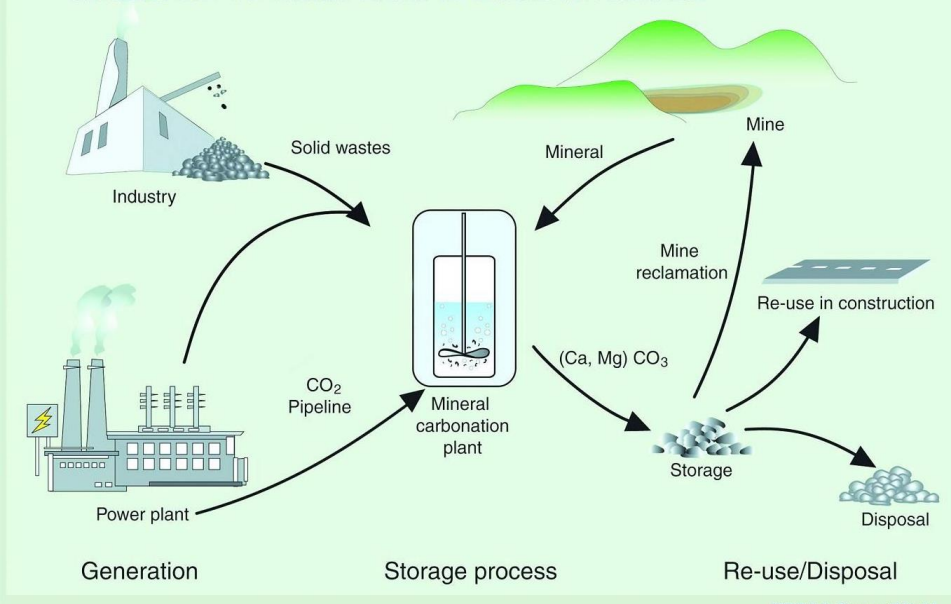

Figure 1.4 Material fluxes and process steps associated with the mineral carbonation of silicate rocks or industrial residues (Source: IPCC, 2005, technical report: Fig. TS.10, pg. 40)

1.3.5 CCS cost estimation

One of the major challenges for CCS is to reduce its cost for large scale application. Table 1.3 lists the cost of the CCS technology as of 2014; it should be noted, however, that the cost is expected to decrease as technology improves. At present, the most cost efficient form of ex-situ mineral carbonation is still approximately 6.25 times of that of geological storage (Table 3.1). In order to gain acceptance among public and private stakeholders, ex-situ mineral carbonation has to become financially self-sufficient. However, the cost of ex-situ mineral carbonation can be reduced through improvements, such as: eliminating the CO_2 capture process by using flue gases directly for carbonation (Vitillo, 2015; Wang et al., 2014); generating commercial value by reusing the carbonated products as building materials and aggregates (Gadikota et al., 2015; Pan et al., 2016); and using industrial waste residue, which is cheap and readily available adjacent to the

source of CO_2, as CO_2 feedstock (Bobicki et al., 2012; Bodor et al., 2013; Kirchofer et al., 2013; Kruse and Strosnider, 2015; Pan et al., 2015).

Table 1.3 The current cost of each CCS component

CCS component	Technology	Cost ($/t CO_2)	References
CO_2 capture[a]	Post-combustion (coal-fired)	34	(Leung et al., 2014: pg. 430)
	Pre-combustion (coal-fired)	23	(Leung et al., 2014: pg. 430)
	Oxy-fuel (coal-fired)	36	(Leung et al., 2014: pg. 430)
	Post-combustion (gas-fired)	58	(Leung et al., 2014: pg. 430)
	Pre-combustion (gas-fired)	112	(Leung et al., 2014: pg. 430)
	Oxy-fuel (gas-fired)	102	(Leung et al., 2014: pg. 430)
CO_2 transportation	Railway	12.64	(Leung et al., 2014: pg. 432)
	Ship	7.48	(Leung et al., 2014: pg. 432)
	Pipeline	7.05	(Leung et al., 2014: pg. 432)
CO_2 storage & utilization	Geological storage [b, c]	8	(Sanna et al., 2014: pg. 8049)
	In-situ mineral carbonation [c]	17	(Sanna et al., 2014: pg. 8049)
	Ex-situ mineral carbonation	50-300	(Sanna et al., 2014: pg. 8049)

Note: a) include CO_2 compression to 100 bar, b) not containing monitoring cost, c) contains CO_2 transportation cost.

Life cycle assessment on the cost of the full chain of CCS process is commonly adopted to evaluate the feasibility of a CCS project (Azapagic and Cue, 2015; Bodénan et al., 2014; Giannoulakis et al., 2014; Nduagu et al., 2012). Table 1.4 lists the cost of some projects using updated technology. From an economic perspective, the integrated mineral carbonation processes (Hitch and Dipple, 2012) have the potential to compete with the geological storage method within the mining industry (Rubin et al., 2015).

Table 1.4 The cost of selected CCS projects

CO_2 source	CO_2 capture	CO_2 transportation	CO_2 storage	Cost ($/t CO_2 avoided)	References
NGCC[a]	Post-combustion	Pipeline	Geological storage	59-143	(Rubin et al., 2015: pg. 389)
SCPC[b]	Post-combustion	Pipeline	Geological storage	46-99	(Rubin et al., 2015: pg. 389)
IGCC[c]	Pre-combustion	Pipeline	Geological storage	38-84	(Rubin et al., 2015: pg. 390)
NGCC	Post-combustion	Pipeline	EOR[d]	10-112	(Rubin et al., 2015: pg. 389)
SCPC	Post-combustion	Pipeline	EOR	(5)-58	(Rubin et al., 2015: pg. 389)
IGCC	Pre-combustion	Pipeline	EOR	(16)-46	(Rubin et al., 2015: pg. 390)
Oil and gas exploration and development	Not given	Pipeline	Mineral carbonation	28-238	(Hitch and Dipple, 2012: pg. 272)
NGCC	Not applied	Pipeline	Mineral carbonation	120-159	(Khoo et al., 2011: pg. 11356)

Note: a) NGCC is the natural gas combined cycle plant; b) SCPC is the supercritical pulverized coal burning plant; c) IGCC is the coal-based integrated gasification combined cycle system; d) EOR is the geological storage with enhanced oil recovery credits.

1.4 Integrated mineral carbonation in the mining industry

As a carbon-intensive industry, mining is facing ever-increasing pressure to reduce CO_2 emissions as a result of emerging carbon dioxide management policies such as cap and trade, and carbon taxation (Ballantyne, 2010). The use of the integrated mineral carbonation processes in the mining industry, using ultramafic mine waste materials (waste rock, tailings, slag, waste water) as CO_2 feedstock (Kruse and Strosnider, 2015), is advantageous for its ability to manage CO_2 emissions and remediate potentially hazardous materials (i.e. chrysotile) in mine waste (McCutcheon et al., 2015). By using mine waste materials, especially tailings, many of the costs associated with the comminution required for mineral carbonation are absorbed as part of the

traditional process of metallic mineral extraction. This has a large impact on the costs associated with altering tailings to a carbonate form. With a mineral carbonation process added in, some marginal projects, such as low-grade nickel deposits, may potentially lower their cut-off grades in order to become economically feasible (Hitch et al., 2010; Hindle, 2011).

The ultramafic-hosted ore deposits that are favored in the integrated mineral carbonation process include chrysotile mines (Larachi et al., 2010), nickel mines (Bobicki et al., 2015; Jacobs and Hitch, 2011; Sarvaramini et al., 2014), chromium mines (Pasquier et al., 2014a; Veetil et al., 2015a), and platinum group element (PGE) mines (Meyer et al., 2014; Vogeli et al., 2011). Ultramafic rock-hosted deposits are abundant worldwide and their CO_2 storage potential is large (Hitch et al., 2010). Fig. 1.5 shows the potential large and super-large ultramafic mine sites that are suitable for the integrated mineral carbonation process (Picot et al., 2011). Notably, the annual amount of mining tailings produced globally could potentially offset approximately 1.5% of annual global CO_2 emissions (Power et al., 2013b: pg. 339).

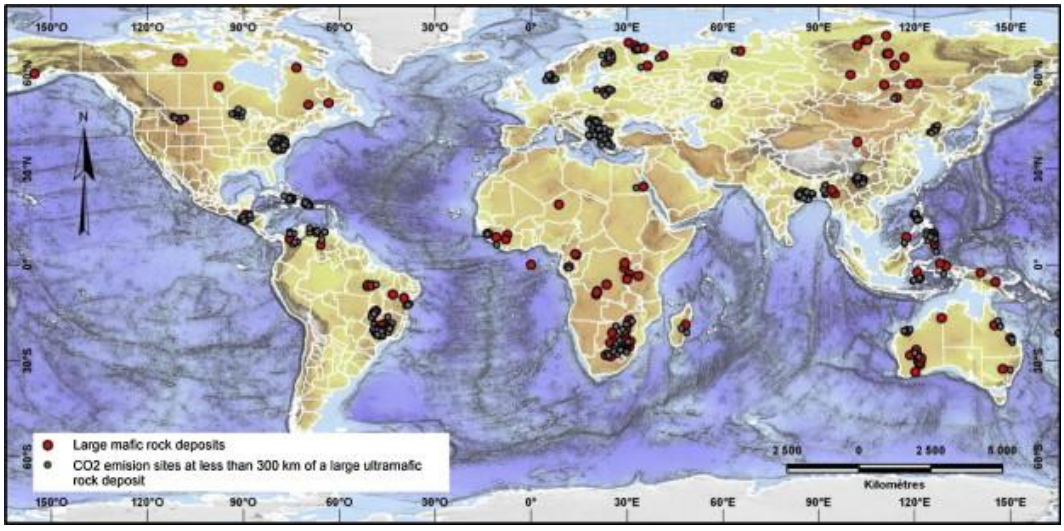

Figure 1.5 Ultramfic rock-hosted ore deposits lying less than 300km from a CO_2-emission site (Bodénan et al., 2014: pg. 54)

The carbonation of ultramafic mine waste initially uses a passive technique at tailing dams from both closed and active mines (Wilson, 2005). Instead of human input, passive carbonation exposes tailings to the Earth's atmosphere, hydrosphere, and biosphere, allowing for natural weathering and gradual carbonation. The passive carbonation rate of tailings can be enhanced through simple modification, such as optimizing the surface area of tailings (Wilson, 2005) and/or adding carbonic anhydase to catalyze the hydration of aqueous CO_2 and to promote carbonate precipitation (Power et al., 2016, 2013a). Furthermore, seeding acid-generating materials with *Acidithiobacillus spp*. enhances magnesium ion leaching from silicate minerals (Power et al., 2010); applying a cyanobacteria accelerates the precipitation of platy hydromagnesite (McCutcheon et al., 2014; Power et al., 2011); pre-seeding carbonates promotes the carbonation nucleation (Zarandi et al., 2016); pumping CO_2 into tailing water increases CO_2 gas content (Harrison et al., 2013); and periodically adding small amounts of water keeps partial pore saturation at optimum levels (Assima et al., 2013) which promotes the conversion of CO_2 gas into a carbonate form. Moreover, the by-products of carbonation, such as photoautotroph biomass, can be harvested as biofuel (Power et al., 2011). Since the carbonation is under ambient temperature and pressure conditions, the energy consumption of modified passive carbonation is low. In addition, not all tailings are suitable for this method; for example, tailings that are extremely carbonated (Power et al., 2010), and massive, serpentine-enriched mine residues (Assima et al., 2014).

In an active mining operation, it is possible to apply the ex-situ carbonation to fresh tailings. Fresh tailings are more active for carbonation than weathered ones due to minimal authigenic carbonate content (Power et al., 2010). Accelerated mineral carbonation technology includes feedstock pretreatment (i.e. thermal, chemical and/or mechanical activation), followed by a direct

or indirect carbonation process in gas-solid phases or aqueous phases at high temperature and high pressure. These advanced technologies have been adopted to estimate the suitability of mine waste materials as CO_2 feedstock (Table 1.5). Current investigations into integrated mineral carbonation processes mostly focus on mine waste that contains serpentine and brucite (Bobicki, 2014; Harrison, 2014). The most common methods for mine waste pre-treatment are thermal activation using calcination (Pasquier et al., 2014a; Veetil et al., 2015a), microwave heating (Bobicki, 2014), steam mediation (Larachi et al., 2012), and chemical activation using organic or inorganic acid (Bobicki, 2014; Teir et al., 2009). These pre-treatment methods dehydrate serpentine and/or disorder its crystal structure, which greatly acelerates serpentine carbonation. However, pre-treatment methods, such as thermal activation and chemical activation by organic ligands, may not appreciably accelerate the reaction rate of olivine (Declercq et al., 2013). Partially-weathered olivine is the most abundant form of ultramafic rock in nature (Styles et al., 2012). Studies of mine waste materials consisting of partially-weathered olivine are of great significance and provide the potential for ex-situ mineral carbonation to become widely employed in the mining industry.

Table 1.5 Summary of current studies on ex-situ mineral carbonation of mine waste materials.

Mining deposit	Majority minerals	CO_2 source	Rock pre-treatment	Carbonation method	References
American chromite mine, Quebec	Serpentine	Flue gas	TA	DC gas-solid	(Veetil et al., 2015b)
Old ilmenite mine, Quebec	Anorthosite	Flue gas	NA	DC gas-solid DC aqueous	(Ben Ghacham et al., 2015)
Okanogan nickel deposit, Washington State; Thompson nickel bell, Manitoba	Serpentine	Pure CO_2	TA, CA	DC aqueous	(Bobicki et al., 2015)
American chromite mine, Quebec	Serpentine	Flue gas	TA	DC aqueous	(Pasquier et al., 2014a, 2014b)
Black Lake mine, Quebec	Serpentine	Flue gas	TA, MS	DC gas-solid	(Veetil et al., 2014)
Lonmin Platnum mine, South Africa	Enstatite, plagioclase feldspar	Pure CO_2	CA	IDC aqueous	(Meyer et al., 2014)
Nickel Slag, New Caledonia	Olivine, serpentine	Pure CO_2	TA, CA, MA	DC aqueous, IDC aqueous	(Bodénan et al., 2014)
Turnagain deposit, British Columbia	Olivine, serpentine	Pure CO_2	NA	DC aqueous	(Jacobs, 2014)
Black Lake mine, Quebec; Dumont nickel project pilot	Chrysotile, lizardite,	Flue gas	NA	DC gas-solid	(Sarvaramini et al., 2014)
Thetford mines, Quebec	Chrysotile	CO_2 mix	TA	DC gas-solid	(Larachi et al., 2010)
Hitura nickel mine, Central Finland.	Serpentine	Pure CO_2	CA	IDC aqueous	(Teir et al., 2009)

Note: HA is thermal activation, CA is chemical activation, MA is mechanical activation; MS is magnetic separation, NA is not applied, DC is direct carbonation, IDC is indirect carbonation.

This research evaluates how the cost of ex-situ mineral carbonation can be reduced by implementing the process at a low-grade nickel deposit with waste materials containing both olivine and serpentine. At the same time, this study uses mechanical activation as a pretreatment method to enhance the carbonation rate of mine waste materials. Mechanical activation is simple and environmentally friendly, and can acheive in one intensive milling instrument without any

additional chemicals (Baláž, 2008). Historically, mechanical activation has been suggested to be a way of pre-treating olivine for enhance its leaching rate (O'Connor et al., 2005). Furthermore, the mechanical activation of serpentine via dry grinding can dehydrate the hydroxyl group, which results in a calcining effect that is similar to thermal activation in that it has relatively low energy consumption (Gualtieri et al., 2012).

1.5 Dissertation structure

This section outlines this dissertation's research objective, research questions, and chapter organization.

1.5.1 Research objective

The primary objective of this research is to elucidate the reaction mechanisms that occur during the mechanical activation of mine waste (i.e. partially weathered olivine). The purpose in elucidating these mechanisms is to help design an integrated mineral carbonation strategy that employs mechanical activation and can be retrofitted for current mineral processing plants and incorporated into future ones. In order to realize this goal, a combination of experimental and analytical technology will be used to investigate the mechanical activation of mine waste for enhanced carbonation. This study focuses on the following aspects of the carbonation process: (1) pre-treating mine waste materials using mechanical activation in both wet and dry conditions; (2) characterizing the changes in particle size, surface area, surface morphology, crystal structure, and the composition of minerals in the mine waste materials during mechanical activation; (3) evaluating the effectiveness of mechanical activation and direct aqueous carbonation; and (4) identifying approaches for economically enhancing the rate of carbonation. The hypothesis of this study is that the mechanical activation of ultramafic mine waste materials (containing forsterite

and lizardite) will promote their ability to convert CO_2, thus demonstrating its viability as an integrated mineral carbonation process for use in the mining industry.

1.5.2 Research questions

There are three questions that address the outcome of this dissertation. Each question is accompanied by a discussion of the associated problems, solutions, hypotheses, and challenges.

Question 1: Can the microstructure of olivine be characterized so that it will allow researchers to accurately analyze how mechanical energy activates the individual microstructure characteristic of olivine, or mine waste materials that contain olivine, for enhanced mineral carbonation?

Discussion: Accurately characterizing the crystal structure of minerals plays an important role in analyzing the mechanism of mechanical activation. Previous studies of mechanical activation on olivine and serpentine mostly focus on the degree of amorphization but neglect other characteristics, such as crystallite size, micro-strain, lattice parameter, and dislocation density. Many studies on the fundamental application of mechanical activation have provided the basis for determining the microstructure of various minerals using line profile analysis (LPA) on the X-ray diffraction pattern. It has been hypothesized that the microstructure of olivine can easily be characterized using LPA. However, the challenge posed by this research question requires a comparative analysis of the existing LPA technologies to determine the most applicable method for implementation in olivine-containing mine waste materials.

Question 2: Can mechanical energy activate the mine waste materials in such a way that will result in higher rates of downstream carbonation?

Discussion: The successful enhancement of carbonation of magnesium silicates using mechanical activation as a pre-treatment method is well-documented in the literature. However,

the findings presented in this growing body of research tend only to focus on pure minerals, which is problematic because there is no abundance of pure mineral deposits in mine waste materials; the use of mechanical activation on partially-weathered minerals should be evaluated singularly. In addition, the use of mechanical activation on olivine and serpentine has been investigated and well-documented. The variation in the extent to which they can be mechanically activated has been shown to be largely controlled by their mineralogy and the grinding environment. It has been postulated that mine waste material can be mechanically activated for carbonation. The support for this hypothesis can be observed in the changes to the physical, structural, and chemical characteristics of samples that occur due to mechanical activation, as well as the stoichiometric silicate-to-carbonate conversion in a direct aqueous carbonation process. The challenge of research question 2 is to analyze the difference between mechanically activating mine wastes and pure olivine in various grinding conditions.

Question 3: Can mechanical activation be economically applied in an integrated mineral carbonation process in the mining industry?

Discussion: The application of mechanical activation would normally be limited due to its high energy requirements. However, Haug (2010) has suggested that 'capturing' mechanical activation as an integrated part of the milling process makes it possible to implement it economically. Indeed, as the body of literature focusing on the economic analysis of mineral carbonation has matured, there have been studies that have shown that integration of mineral carbonation in the mining industry possesses promising net present value (Hitch and Dipple 2012). The hypothesis of this dissertation is that the application potential of mineral carbonation using mechanical activation as pre-treatment method is enhanced when it is integrated into the mining industry. The challenge of this research question is how to optimize the mechanical activation and

carbonation process, and to identify the best way to integrate this process into the mineral processing plant.

1.5.3 Chapter organization

The body of this thesis is comprised of six chapters that detail the investigation described in this introduction. Chapters 2 through 7 have previously been published in or submitted to peer-reviewed journals in the form of a review paper (Chapter 2) and five research papers (Chapters 3 to 7).

Chapter 1: This chapter provides a general overview and the background information relevant to this study. In addition, the first chapter describes the study's objectives, relevant research questions, and approaches that will be employed.

Chapter 2: This chapter provides a comprehensive literature review on mechanical activation—with a focus on olivine and serpentine—and analyzes the influence of mechanical activation on downstream carbonation. This chapter also provides a discussion of the background of mechanical activation, the influence of milling conditions on mechanical activation, and the behaviors of mechanically-activated magnesium silicates in the downstream carbonation process. Chapter 2 concludes by considering possibilities for future studies. A version of this chapter has been submitted to for publication.

Li, J and Hitch, M., 2017. "A review of mechanical activation of magnesium silicates for mineral carbonation."

Chapter 3: This chapter presents an analytical method that uses line profile analysis (LPA) on XRD patterns to resolve the microstructure parameters of mechanically-activated olivine. The LPA methods allow for the examination of individual microstructure information, such as lattice parameters, crystallite size and its distribution, micro-strain, and dislocation density. This chapter

presents a ‘proof-of-concept’ study that demonstrate the potential to resolve the microstructure of olivine in mechanically-activated mine waste by applying the Rietveld method on XRD patterns. A version of this chapter has been published in:

Li, J and Hitch, M., 2015. “Characterization of the microstructure of mechanically-activated olivine using X-ray diffraction pattern analysis”, *Minerals Engineering*, 86: 24-33.

Chapter 4: This chapter discusses the experimental results of mechanical activation on mine waste materials under wet conditions. The focus of this experiment was to examine material characterization and direct aqueous carbonation. The mechanism of co-grinding olivine and serpentine in wet conditions was obtained by comparing mine waste material and pure olivine that had been exposed to similar experimental conditions. In addition, the correlations between each mechanical activation effect (changes in particle size, specific surface area, crystallinity) and carbonation conversion were studied to describe how mechanical energy activates mine waste for carbonation. A version of this chapter has been published in:

Li, J and Hitch, M., 2015. “Ultra-fine grinding and mechanical activation of mine waste using high speed stirred mill for mineral carbonation.” *International Journal of Minerals, Metallurgy, and Material*. 22(10): 1005-1016.

Chapter 5: This chapter describes the physical, structural, and chemical changes of mine waste materials and pure olivine with specific milling energy input under intensive dry grinding. This study uses the same material characterization and direct aqueous carbonation process as in Chapter 4, and it evaluates the role of forsterite and lizardite during the mechanical activation and carbonation of mine waste. A version of this chapter has been published in:

Li, J and Hitch, M., 2017. “Ultra-fine grinding and mechanical activation of mine waste using a planetary mill for mineral carbonation.” *International Journal of Mineral Processing*. 158: 18-26.

Chapter 6: This chapter evaluates the mechanical activation of mine waste (i.e. partially serpentinized olivine) using different milling machines (planetary mill, vibratory mill, and stirred mill), with a special focus on changes in microstructure and chemical transformation. To identify mechanically-induced changes in the mine waste, laser diffraction, nitrogen adsorption, X-ray diffraction, and infrared spectroscopy are used. Direct aqueous carbonation is also used to identify the best type of mechanical activation for carbon storage in the mine waste. A version of this chapter has been published in:

Li, J and Hitch, M., 2017. “Structural and chemical changes in mine waste mechanically activated in various milling environments.” *Powder Technology*. 308: 13-19.

Chapter 7: This chapter uses experimental data to identify the optimal condition for the mechanical activation and direct aqueous carbonation of mine waste materials. In addition, this study develops an economic analysis of the integrated mineral carbonation process in a low-grade nickel mine that uses mechanical activation as pre-treatment method. The economic analysis of this mine considers factors such as energy requirements, cost modeling, and carbon balance. A version of this chapter has been published in:

Li, J and Hitch, M., 2017. “Economic analysis on the application of mechanical activation in an integrated mineral carbonation processes.” *International Biodeterioration & Biodegradation*. In press. DOI: 10.1016/j.ibiod.2016.08.026.

Chapter 8: This chapter summarizes the main findings and conclusions, major contributions, and provides suggestions for future work.

Chapter 2: A review of mechanical activation of magnesium silicates for mineral carbonation [1]

2.1 Introduction

As reported by the Global Monitoring Division (Keeling, 2015; Tans, 2015), due to human activity, atmospheric concentration of CO_2 has increased at a rate of 2 ppm (parts per million) per year since 2000, and had reached 399 ppm by July 2014. This 2014 value is 50 ppm above the upper safety limit. It is thus a matter of urgency to adopt efficient measures to reduce atmospheric CO_2 and/or ease the release of the gas in order to prevent hazardous consequences, including global warming, climate change, and ocean acidification. Mineral carbonation technology is one method which has been employed to permanently and safely decrease concentrations of CO_2 in the atmosphere by accelerating a nature weathering process in which CO_2 is chemically bound to calcium and/or magnesium silicates (reaction 2.1) (Huijgen and Comans, 2005).

$$(Ca, Mg)SiO_3 + CO_2 \rightarrow (Ca, Mg)CO_3 + SiO_2 \quad (2.1)$$

To overcome the slow reaction kinetics of the natural weathering process that occurs over thousands or even millions of years, researchers have focused their efforts on carefully selecting process routes, process conditions, as well as pre-treatment options (Huijgen and Comans, 2005, 2003; Olajire, 2013; Power et al., 2013b; Sanna et al., 2014; Sipilä et al., 2008; Zevenhoven et al., 2011).

Mechanical activation, together with thermal activation and chemical activation are three classic pre-treatment options in mineral carbonation (Huijgen and Comans, 2005). Since it can

[1] A version of this chapter has been submitted for publication. Li, J and Hitch, M., 2015. A review of mechanical activation of magnesium silicates for mineral carbonation.

only be conducted in a high intensity mill, mechanical activation has the distinct advantages of simplicity and effectiveness. Mechanical activation is ecologically cleaner than chemical activation since no chemicals are used in the process. Mechanical activation offers a high activation level that is similar to that of calcinations conducted with lower levels of energy consumption, thus rendering it preferable to thermal activation (Zhang et al., 1997). The high level of operation energy consumed is the only drawback of mechanical activation. However, when integrated as part of the complete milling process, energy consumption can be reduced, thus making mechanical activation a practical option (Haug et al., 2010). Literature related to chemical activation (pH-swing process) (Azdarpour et al., 2015) and thermal activation on serpentine (Dlugogorski and Balucan, 2014) has been reviewed in detail. However, mechanical activation of ultramafic rocks has received only simple mention in relation to mineral carbonation.

The objective of this section is to review of the literature summarizes current research on the mechanical activation of Mg-silicate for mineral carbonation. The basic theory of mechanochemistry is introduced in the section 2.2. Then mechanical activation on Mg-Silicate with focus on olivine and serpentine is analyzed (section 2.3), followed by the evaluation of the carbonation technologies based on mechanically-activated Mg-Silicate (section 2.4). Finally, the potential application in integrated mineral carbonation and limitation of the research up to now is presented in section 2.5.

2.2 Mechanical activation background

Mechanochemistry involves the application of mechanical energy to induce reactions. It has the same significance as thermochemistry, electrochemistry, and photochemistry in the area of physical chemistry (Baláz, 2003; Baláž, 2008). Mechanochemistry has become one of the primary material-pressing methods that is widely used in mineral processing, extractive metallurgy,

pharmaceutics, and preparative chemistry, including both organic and inorganic synthesis (Boldyrev, 2006). As a sub-branch of mechanochemistry, mechanical activation (MA) also uses mechanical energy to create changes. However, instead of inducing a chemical reaction, the main purpose of mechanical activation is to enhance the reaction rate for subsequent processing by adding an input of energy into the system (Pourghahramani, 2007).

Mill grinding, which typically involves a combination of the mechanical action of pressure and shear, is the most common operation used in both conventional comminution and mechanochemistry (Boldyrev, 2006). Conventional comminution and mechanical activation are divided by grinding limit, over which the particle deformation mechanism changes from brittle to plastic (Boldyrev et al., 1996). Mills used for mechanical activation also have several times higher energy density than do conventional tumbling mills. A level of mechanical activated status can be achieved in high intensity mills such as the planetary ball mill, the vibratory ball mill, the stirred ball mill, the motor mill, and the jet mill (Baláž, 2008). The electron energy at the contact spot of colliding particles can reach more than 10 eV, which is much higher than the thermal reaction at temperatures higher than 1000 ºC (4 eV) and ultraviolet photochemical (6 eV) (Wei et al., 2009).This explains why some reactions, rarely achieved through traditional methods, can occur in a mechanically-activated state.

The phenomenon of energy relaxation during mechanical activation contributes to the activation status. With regard to relaxation time, Ljachov defined two types of disorder and instability in activated material: short-lived defects (relaxation time 10^{-7}-10^{-3} s) and long-lived defects (relaxation time 10^{-3}-10^{6} s) (Avvakumov et al., 2001). Short-lived defects decay immediately as they are generated. When they reach their highest level of activation, a solid can be destroyed by fracturing over a short decay time. In contrast, some long-lived defects, which are

very hot and unstable, are generated as a result of deep imperfections in an activated solid. Although activation energy decreases considerably during a long-lived period of time, it never returns back to its initial state, so a residual activity (residual disorder) remains (Avvakumov et al., 2001). The influence of long-lived defects is the main reason for the modification of the results in the downstream process after mechanical activation. However, the reactions during mechanical activation take advantage of both types of defects, especially the short lived defects.

The solid state properties of materials can be modified through mechanical activation. In addition to reducing particle size and increasing surface area, mechanical activation changes the characteristics of the crystal lattice. The correlation of these changes to the rate of downstream reaction can be roughly described by Equation 2.1 (Tkáčová and Baláž, 1988).

$$k_0 = a' + b'(S_{\mathrm{BET}} / C_{\mathrm{XRD}}) \tag{2.1}$$

where, k_0 is the initial rate constant, S_{BET} is the specific surface area and C_{XRD} is the degree of the crystalline phase after mechanical activation. a' and b' are coefficients.

From the view of energy transfer, excess energy is stored in non-equilibrium and disordered crystal lattice during mechanical activation, and the activation energy of any subsequent reaction of the material is lowered (Tkáčová et al., 1993). The most suitable description for characterizing the macro energy state of activated solid (ΔH_T) equals to the sum of the energy of microstates (Equation 2.2) (Pourghahramani, 2007).

$$\Delta H_T = \Delta H_d + \Delta H_S + \Delta H_A + \Delta H_P \tag{2.2}$$

Where, ΔH_d is the relative lattice distortion as a measure of dislocation density (Tromans and Meech, 2001). ΔH_S is the specific surface area as a measure of the grain boundary with the

surrounding medium (Heegn, 1979). ΔH_A is the formation of amorphous material (Heegn, 1979). ΔH_P is the formation of new phases such as polymorphic transformation. Other defects, especially in short-term activated states, are essential too. However, they can only be quantified theoretically and cannot be determined experimentally. The existing approximation does not consider these defects.

The techniques used to characterize the mechanically-activated materials include infrared spectroscopy (IR), X-ray photoelectron spectroscopy (XPS), scanning electron microscope (SEM), scanning tunneling microscope (STM), atomic force microscope (AFM), transmission electron microscopy (TEM), X-Ray Diffraction (XRD), Mossbauer spectroscopy, and electron paramagnetic resonance (EPR), thermal gravimetric analyses (TGA), analytical electron microscopy (AEM), electron microprobe analyses (EMPA) (Baláž, 2008).

2.3 Mechanical activation on magnesium silicate

Due to their abundance in nature, relative high purity and low mass requirements for binding one unit CO_2, olivine $(Mg, Fe)_2SiO_4$ and serpentine $Mg_3Si_2O_5(OH)_4$ are the most suitable Ca/Mg silicate mineral feedstock for CO_2 mineral carbonation (Goff et al., 2000). This paper focuses mainly on the mechanical activation of olivine and serpentine. As a result of differences in the crystal structures of olivine and serpentine, the effects of their mechanical activations differ from each other. Other Ca/Mg silicates such as wollastonite $CaSiO_3$, enstatite $MgSiO_3$, diopside $CaMgSi_2O_6$, and talc $Mg_3Si_4O_{10}(OH)_2$ also provide suitable mineral feedstock. However, the mechanical activation on these minerals lies outside of the scope of this paper.

2.3.1 Mechanical activation on olivine

Since olivine is recognized as the most vulnerable to weathering using CO_2 (Goldich, 1938), little exploration has been conducted on the Mechanical approach until the proposal of mineral carbonation as a permanent solution for storing CO_2 was made (Seifritz, 1990). The proof-of-concept of the mechanical activation of olivine and serpentine for mineral carbonation has been studied by O'Connor et al. at the Albany Research Center (ARC), where many parameters for increasing the reaction rate under laboratory conditions have been investigated (O'Connor et al., 2005). The reaction extent of olivine carbonation has been found to be dramatically reduced through only 1 hour of dry grinding in an attrition mill (O'Connor et al., 2001). Following these findings, the mechanical activation of olivine was studied in detail with an eye towards its industrial implications by the research group at ARC, the Norwegian University of Science and Technology, and the Slovak Academy of Sciences. Various mechanical activation conditions such as a wet/dry grinding mode, and various high intensity mills were tested.

2.3.1.1 The mechanism of mechanical activation on olivine

The olivine group $(Mg,Fe)_2SiO_4$, is a group of igneous minerals which is commonly abundant, and quickly weathered, on the Earth's subsurface. Olivine is a mixture of magnesium-rich forsterite (Mg_2SiO_4) and iron-rich fayalite (Fe_2SiO_4). Forsterite is more common than fayalite (Klein et al., 1993). It is yellow to yellow-green in color, dense (density 3.27-3.37 g/cm^3) and hard (Mohs hardness 6.5-7) (Barthelmy, 2014; Halder and Tisljar, 2013: pg. 59). Normally, high concentrations of the elements Mn and Ni are also present. The structure of olivine has an independent SiO_4 tetrahedra linked by divalent ions (such as Mg^{2+}, Fe^{2+}) in octahedral coordination (Kerisit et al., 2013). Fig. 2.1 shows the structure of olivine, which is (010) surface looking along [001].

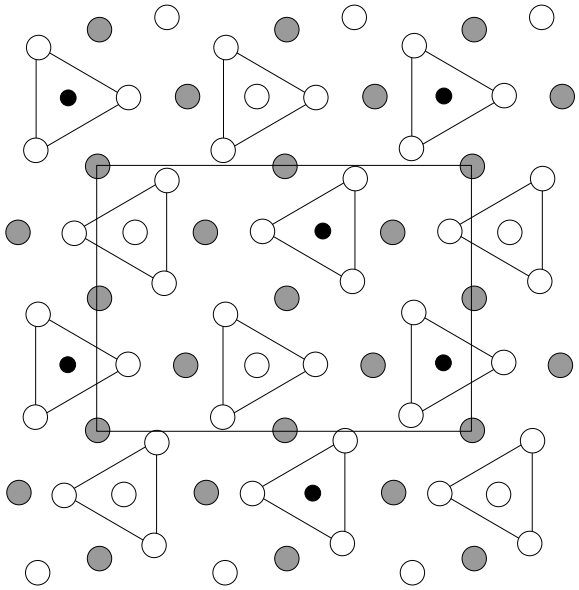

Figure 2.1 The atomic scale structure of olivine. A white circle represents an oxygen atom, a black circle represents a silicon atom, a grey circle represents a magnesium atom, a black rectangle indicates a projection of the unit cell. Modified from ref. (Bruno et al., 2014: pg. 2500).

Turianicová et al. has laid out the mechanism of mechanical activation on olivine with a subsequent direct aqueous carbonation process (Turianicová et al., 2013). First, an activated state of olivine with a partially disordered (*) structure is formed during mechanical activation (reaction 2.2). Amorphous MgO and SiO_2 are assumed to be the main components of the disordered olivine, where the structure of MgO is easier to destroy than that of SiO_2 (Fabian et al., 2010). Within an aqueous solution(pH=8), brucite $Mg(OH)_2$ is produced from amorphous MgO (reaction 2.3) (Turianicová et al., 2013: pg. 76). $Mg(OH)_2$ bears a quick reaction kinetics benefit for mineral carbonation (Fagerlund et al., 2012: pg. 10391). It is preferable for industrial application (Zevenhoven et al., 2011: pg. 51).

$$Mg_2SiO_4(s) \xrightarrow{\text{milling}} Mg_2SiO_4^*(s) \tag{2.2}$$

$$Mg_2SiO_4^*(s) + H_2O \rightarrow 2Mg(OH)_2 + SiO_2 \quad pH=8 \tag{2.3}$$

2.3.1.2 The effects of energy input on the mechanical activation on olivine

(1) Changes in surface properties

The main changes associated to olivine after a specific time of mechanical activation include its surface property and crystal structure. According to all observations, as the grinding time or the mechanical energy input increases, the surface area initially grows progressively. Some time later, even though the surface area continues to change as a result of various different grinding conditions, the main trend of the changes is that the surface area increases more slowly, ceases to change, or sometimes even decreases. Fig. 2.2 shows the specific surface area of dry mechanically-activated olivine as a function of specific milling energy input. Regardless of the mill type, the optimum amount of energy to achieve the maximum specific surface area is around 4,000 kWh/t (Atashin et al., 2015). The non-linear increase of surface area can be explained by an overlapping of the dispersion process and the formation of secondary particles which are aggregates or agglomerates of ultrafine particles as the grinding proceeds (Baláž, 2008).

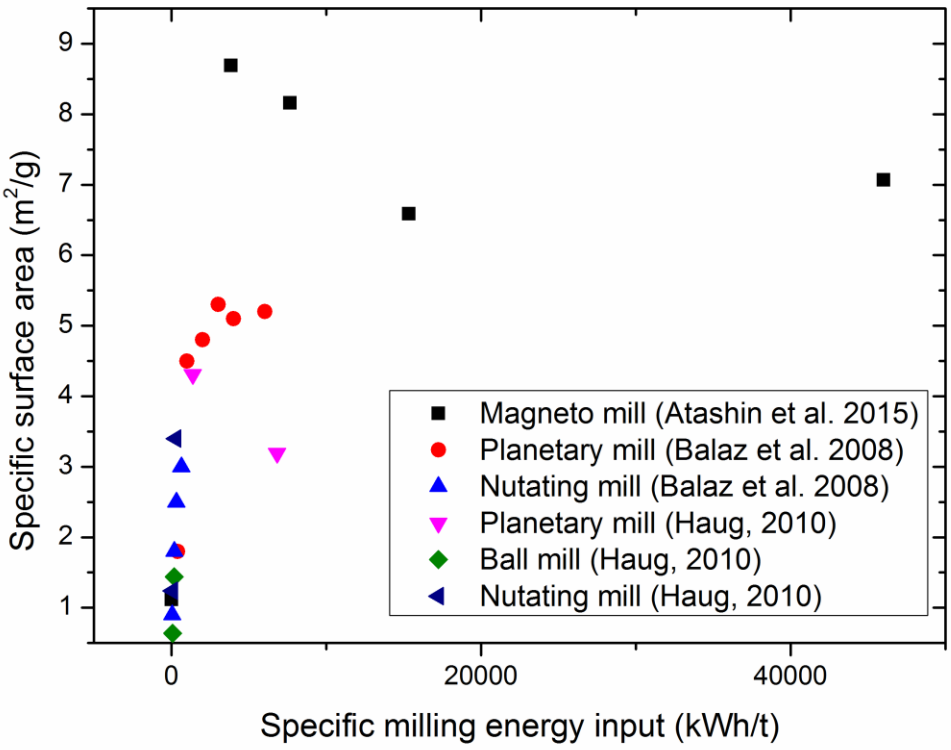

Figure 2.2 The changes of specific surface area with specific milling energy input. Modified from ref. (Atashin et al., 2015: pg. 559). Reprinted with permission from (Atashin et al., 2015). Copyright 2015 Elsevier Limited.

Under the SEM micrograph, the morphology of secondary particles created by mechanical activation can be visually observed. The finest olivine particles are wear-resistant. Even after 30 min of mechanical activation, larger agglomerate composites of acute angle on 2–3 μm particles can be found (Kleiv and Thornhill, 2006). After prolonged dry grinding (24 hours), a cold welding phenomenon can be observed. At this time, the morphology tends to change from irregular to round shapes, particle size distribution becomes narrower, and aggregates become well-bonded with much finer grains with the increase of mechanical energy (Summers et al., 2005).

(2) Changes in crystal structure

Changes in the crystal structure of mechanically-activated olivine are mostly obtained from the large widened and reduced intensity of the X-ray diffraction (XRD) peaks. Usually the crystallinity (C_{XRD}) (Equation 2.3) and the degree of amorphization (A) (Equation 2.4) are calculated to present the structure changes (Ohlberg and Strickler, 1962: pg. 170).

$$C_{XRD} = \frac{B_0 I_x}{B_x I_0} \times 100\% \tag{2.3}$$

$$A = 1 - C_{XRD} \tag{2.4}$$

Where, I_0 is the integral intensity of a diffraction peak for a non-activated mineral, B_0 is the background of the diffraction peak for a non-activated mineral and I_x and B_x are the same values for the mechanically activated mineral. The non-activated sample is assumed to be 100% crystallized. C_{XRD} and A are bulk property that includes the effects of fine particle size, crystallite size, strain and deformation of the crystal lattice. Both C_{XRD} and A correlate crudely with the specific energy input, but different correlations among milling mode (wet/dry) and high intensity mills (Sandvik et al., 2011; Summers et al., 2005). Fig. 2.3 shows the correlation between the crystallinity percentage of dry mechanically activated olivine and specific milling energy input. Diffraction peak of forsterite (020) was used to analyze. In the initial phase of mechanical activation, the crystallinity percentage of ground olivine decreases with increasing milling energy input. Beyond energy 8,000 kWh/t, the crystallinity percentage does not change considerably.

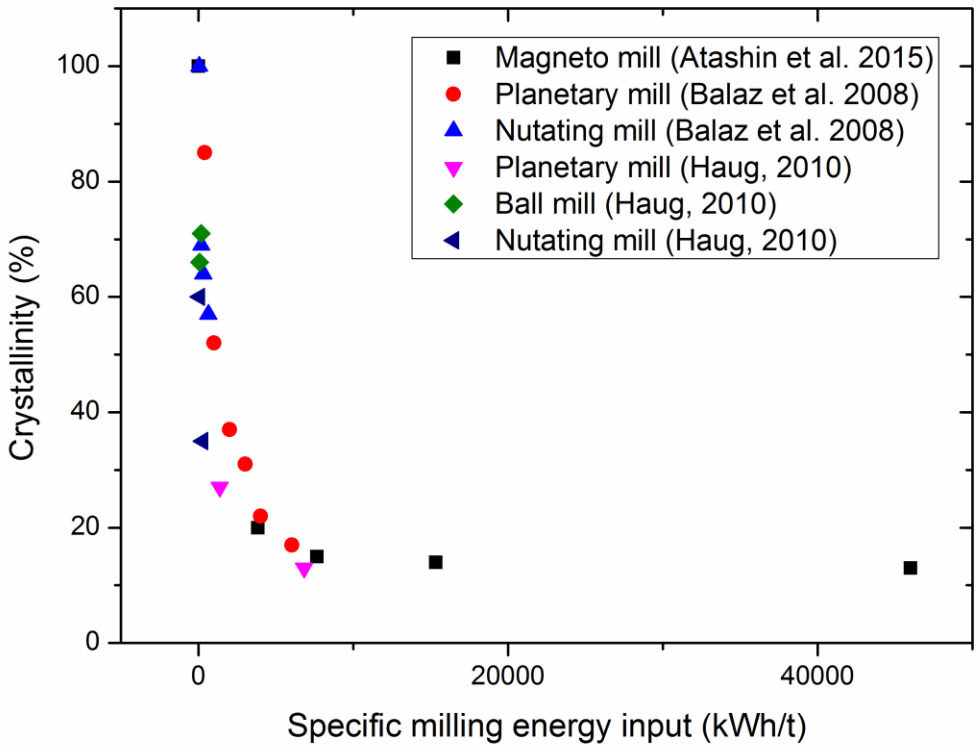

Figure 2.3 Crystallinity percentage variation as a function of specific milling energy input. (Modified from ref. (Atashin et al., 2015: pg. 560)). Reprinted with permission from (Atashin et al., 2015). Copyright 2014 Elsevier Limited.

Using line profile analysis under a proper line fitting process, the full width at half maximum (FWHM) and the integral width of samples can be used to obtain information regarding crystal size, strain and dislocation density (Pourghahramani, 2007). Diffraction peaks of olivine used to analyze their crystal structures include (131) (211) (Summers et al., 2005: pg. 142), (020) (Baláž et al., 2008: pg. 3; Haug, 2010: Part II, Paper II, pg. 18) and (120) (031) (131) (211) (112) (142) (Sandvik et al., 2011: pg. 147). Up to now, Scherrer method and Williamson-Hall method have been used to resolve the crystallite size and strain value of mechanically activated olivine (Atashin et al., 2015). A trend of decreasing in crystallite size and increasing in micro-strain with

the increase of specific milling energy has been found. However, these simple functions only give the approximate values. Also, the accuracy of the value obtained from simple functions is challenging, due to the large amount of peaks and extinct anisotropic behaviors exist in the X-ray diffraction pattern of olivine. It is necessary to find an efficiently way to precise characterize the detailed microstructure information of mechanically-activated olivine.

2.3.1.3 The effects of grinding aids on the mechanical activation on olivine

The properties of mechanically-activated olivine in dry grinding and wet grinding modes differ significantly from each other. It has been agreed among researchers that the mechanical-activated product shows the greatest increase of surface area and finest particle size in wet grinding (Baláž et al., 2008; Haug, 2010; Summers et al., 2005). The relatively smaller surface area and larger particle size is due to the formation of agglomerate, which is quite common in prolonged dry grinding. Even though the surface area is smaller, dry grinding provides the most reactive material with the highest level of disordered crystal structure (Baláž et al., 2008).Thus, water acts as a grinding aid such that it increases surface area and reduces the degree of amorphization. When environmental factors are considered, wet milling may be more practical as it reduces dust generation (Baláž et al., 2008).

Baláž et al. have tested the effects of water addition levels in wet grinding during the mechanical activation of olivine. Water contents of 5 wt.%, 20 wt.% and 50 wt.% were used. It was found that lower water contents resulted in the creation of larger specific surface areas (Baláž et al., 2008). Similar results have been obtained in other studies comparing dry grinding, wet grinding and moister (10% H_2O) grinding conditions (Haug et al., 2010: pg. 1548; Sandvik et al., 2011: pg. 418).The samples milled under moister conditions combine the effects of both wet and dry milling, with large surface areas as in the wet-milled samples, and a high degree of

amorphization as in the dry-milled samples. The milling under moister conditions involves kneading, where the small amount of water acts as a lubricant for solid state diffusion (Sandvik et al., 2011).

Rigopoulos et al. have compared the effect of 10% ethanol with 10% H_2O during the intensive ball milling of olivine. Ethanol tend to facilitate the formation of smaller, more uniform and rounded nanoparticles with larger specific surface area and pore volume compare to H_2O (Rigopoulos et al., 2015: pg. 223). O'Conner et al.(2001: pg. 6) experimented with the use of a caustic solution (1M NaOH, 1M NaCl) as a grinding aid. The results proved effective with respect to size reduction but insufficient in terms of the downstream mineral carbonation process. Although this study did not result in the finding of a profitable option for industrial use, the idea of combining a chemical pretreatment with the mechanical activation of olivine needs to be investigated further.

2.3.1.4 The effects of mill type on the mechanical activation of olivine

In order to assess the overall feasibility of the mechanical activation on olivine for implementation on an industrial scale, Baláž and co-workers conducted an investigation of different types of laboratory mills (planetary ball mill, attrition mill) and an industrial mill (nutating mill). They compared the physic-chemical changes induced by milling as a function of mechanical energy input. Milling in the planetary ball mill obtained the maximum value for the amorphization phase. Milling in the attrition mill resulted in the most surface area. Milling in the nutating mill lead to both the least surface area and the lowest degree of amorphization values, corresponding to a lower milling energy when compared to the other two mills (Baláž et al., 2008). A similar conclusion was reported by Haug, who compared different mills in terms of mill intensity (Haug, 2010). The milling intensity from high to low is as follows: planetary mill dry>planetary

mill wet>nutating mill dry>attrition mill wet>ball mill dry>ball mill wet. Milling intensity probably controls the effects on the material after the grinding limit, as the planetary mill induced the largest changes on all material characteristics. From the point of view of efficiency, the nutating mill and the attrition mill are the most promising for applications in industry (Haug, 2010). Research up to now not yet optimized the grinding conditions, such as grinding mechanism (impact/shear), ball to material ratio, media material and so on, which are all likely bring about products with divergent structures.

2.3.2 Mechanical activation on serpentine

Research studies on the mechanical activation of serpentine for direct mineral carbonation are limited. Only ARC and a recent study in Italy have conducted tests on the prolong grinding-induced mechanical activation features for mineral carbonization (Nelson, 2004; O'Connor et al., 2001; Trapasso et al., 2012), the majority of which were related to acid dissolution (Kim and Chung, 2002; Zhang et al., 1997), or simultaneous less intensive grinding with dissolved serpentine (Park and Fan, 2004).

2.3.2.1 The mechanism of mechanical activation on serpentine

Serpentine is derived from the exothermic hydration process of primary minerals, such as peridotites (including olivine) (Hurlbut and Sharp, 1998). The serpentine group $Mg_3Si_2O_5(OH)_4$ is a group of common rock-forming hydrous magnesium phyllosilicate minerals (Ciullo, 1996). Normally, minor amounts of iron, nickel, aluminum and other cations can be substituted into the Mg position (Tartaj et al., 2000). Most serpentines fall within the color ranges of white to grey, yellow to green, and brown to black. They are light (specific gravity between 2.2–2.9 g/cm^3), and soft (hardness 2.5–4) (Barthelmy, 2014). The structure of serpentine consists of two layers, one tetrahedral silica layer and one octahedral brucite layer (Dlugogorski and Balucan, 2014: pg. 354).

Fig. 2.4 shows the anisotropic structure and three different surfaces for serpentine (Bobicki et al., 2014: pg. 97). Because of the larger lateral dimension of the octahedral sheet than the tetrahedral, serpentine is forced to form in various arrangements. From among all polymorphs, lizardite, antigorite, and chrysotile are the most common serpentine minerals found in nature. Lizardite has an ideal layer topology which forms a platy morphology. Antigorite is modulated and shows a corrugated structure. Chrysotile is coiled, and is a soft and fibrous silicate mineral, and makes up the most common form of asbestos (Halder and Tisljar, 2013) .

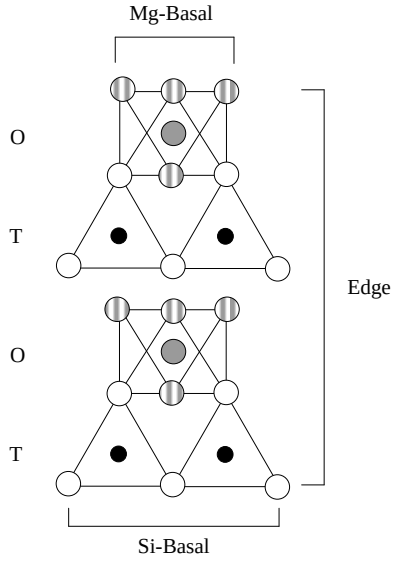

Figure 2.4 The atomic scale structure of serpentine. T represents a tetrahedral layer, O represents an octahedral layer, a white circle represents an oxygen atom, a black circle represents a silicon atom, a grey circle represents a magnesium atom, and a stripped circle represents a hydroxyl group. Reprinted with permission from (Bobicki et al., 2014: pg. 98). Copyright 2014 Elsevier Limited.

Mechanical activation provides an effect similar to that which has been produced by calcination, due to its capability of dehydroxylating serpentine minerals (Liao and Senna, 1992). The amorphization of serpentine by mechanical activation is affected mainly along the c axis of the structural unit, as can be observed through chemical (AEM, analytical electron microscopy)

and structural analysis (FTIR) (Drief and Nieto, 1999). This corresponds to the disordering around the Mg-OH octahedral structure (Kim and Chung, 2002; Zhang et al., 1997). The structural hydroxyls are transformed into adsorbed water during the dry grinding of serpentine, thus significantly accelerating the dehydroxilation reaction (Drief and Nieto, 1999). As a result of dehydroxilation, the Si/Mg molar ratio increases and reaches a value equivalent to the composition of forsterite after prolonged dry grinding (up to 240min) (Zhang et al., 1997: pg. 330). This process is best described in reaction 2.4.

$$Mg_6Si_4(OH)_8 \rightarrow 6MgO \cdot 4SiO_2 \cdot 4H_2O \rightarrow 3(Mg_2SiO_4) \cdot SiO_2 \cdot 4H_2O \quad (2.4)$$

Mechanical activation not only accelerates dehydroxylation, but also postpones the recrystallisation of activated serpentine from topotactic structures to more rigid structures (forsterite and enstatite). The reaction rate of magnesium silicate carbonation, in decreasing order are disordered serpentine, forsterite, serpentine and enstatite. Disordered serpentine which involves little or no recrystallization is preferred for the downstream reactions.

2.3.2.2 The effects of energy input on the mechanical activation of serpentine

The physical changes made to mechanically-activated serpentine are similar to those of olivine, and involve primary size reduction and secondary agglomeration formation (Gerdemann et al., 2003). However, serpentine easily becomes amorphous through dry grinding. This process can be observed through the near disappearance of XRD peaks after 120 min dry grinding. However, for diopside, magnetite; tremolite, which are harder, the XRD diffraction peaks remain even after 120 minutes of grinding (Kim et al., 2008: pg. 26). Because of this feature, the literature suggests that serpentine can be activated in a very short period of time (Sanna et al., 2013), or through the use of less intensive mills (Park and Fan, 2004).

2.3.2.3 The effects of grinding aids on the mechanical activation of serpentine

With respect to the mechanical activation of serpentine, most studies which have been conducted have used dry grinding to generate dehydration (Kim and Chung, 2002; Zhang et al., 1997). Few investigations have been carried out into the use of water in the grinding process as hydration would be expected to occur during wet grinding, and this would serve to contradict to the purpose of the mechanical activation of serpentine (Bobicki et al., 2015). Furthermore, Park and Fan (2004) found that dissolution was not enhanced through wet milling alone, while a combination of mechanical activation and chemical activation (dissolution) lead to rapid serpentine dissolution. Similar conclusions have been drawn by ARD, where after 3 hours of wet grinding in a caustic solution (1M NaOH, 1M NaCl), serpentine was found to have higher carbonation conversion and reaction rates than through thermal activation (O'Connor et al., 2001: pg. 6). As such, the wet grinding of serpentine in various acid, base and salt solutions has been studied extensively (see section 2.4.3.2).

2.3.2.4 The effects of mill type on the mechanical activation of serpentine

Various studies have examined different high intensity mills including the planetary mill (Kim and Chung, 2002; Zhang et al., 1997), the vibratory mill (Nelson, 2004), and the attrition mill (O'Connor et al., 2001; Sanna et al., 2013). Others have tested the less intensive grinding techniques using low-energy attrition-type grinding devices, such as a fluidized-bed reactor (Park and Fan, 2004), tank reactor with continuously agitating and stirring (Van Essendelft and Schobert, 2009a). It seems that less intensive grinding with acid solution is preferred for the mechanical activation of serpentine as it could get rid of the passive layers during dissolution (see section 2.4.3.2).

However, none of the current literature was found to compare the effects of mill efficiency in the area of the mechanical activation serpentine. Most current studies have been designed to optimize the grinding step with the aim of activating the solid through a maximally-activated surface area and degree of amorphization, and with a minimum level of energy consumption.

2.4 Mineral carbonation of mechanically activated magnesium silicates

Researchers have focused on two broad methods with respect to mineral carbonation: direct and indirect mineral carbonation (Fig. 2.5). Direct mineral carbonation is completed in one single reaction step. Indirect carbonation introduces one or more additional steps by extracting the reactive compound from the matrix of raw samples by chemical activation (Bobicki et al., 2012). Both direct and indirect methods have two different processes, namely a dry process and an aqueous process, which have different CO_2 sorption characteristics. In the dry process, CO_2 molecules are chemisorbed to the solid by the formation of strong chemical bonds or physisorbed by the formation of weaker inter-molecular bonds due to the interactions between CO_2 molecules and a sorbent (Kwon, 2011). In the case of aqueous sorption, CO_2 is first dissolved into the solvent, and then is reacted with olivine or serpentine (Guthrie et al., 1999).

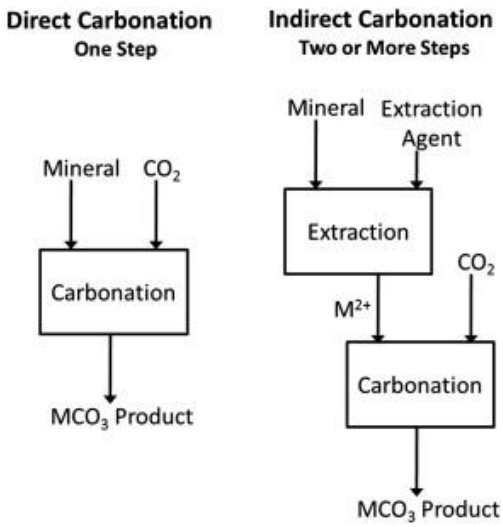

Figure 2.5 The concept of direct and indirect mineral carbonation. M refers to either calcium (Ca) or magnesium (Mg). Reprinted with permission from (Bobicki et al., 2012: pg. 305). Copyright 2012 Elsevier Limited.

The mechanical activation of olivine and serpentine through various forms of milling modifies their structure, resulting in enhanced reactivity in carbonation or dissolution. However, the resultant structural and morphological changes affect the reaction rate of different downstream reactions very differently. Mechanically-activated olivine and serpentine have been tested in the direct solid/gas process, direct aqueous process and acid leaching process (the initial step of the indirect process. Current literature on this topic focuses mainly on the case of olivine. Serpentine has been tested primarily with respect to the process of acid leaching.

2.4.1 Direct gas/solid carbonation

The most straightforward mineral carbonation process is direct gas-solid carbonation. The major advantages of this two-phase carbonation process route over three-phase processes are its simple process design and the possibility of recycling the reaction heat produced from carbonation. Los Alamos National Laboratory, Arizona State University (initially), and more recently, Åbo Akademi University in Finland, have undertaken major research attempts to study this process.

Gas pressures and the reaction temperature control the reaction rate. Extremely high temperatures and pressure were used, but the conversion rate remained very low. Because of the thermodynamic limitations of carbonation on Mg-silicate minerals, several studies suggest that the reaction rates of the gas-solid process that have been achieved so far are too slow for large scale applications (Huijgen and Comans, 2005). Instead of Ca/Mg-silicate minerals, direct dry carbonation on $(Ca/Mg)(OH)_2$ appears to be the kinetically favorable option (Zevenhoven and Fagerlund, 2009). Mechanical activation disorders the crystal lattice around Mg ions of olivine or serpentine, and stores excess energy on the particle surface and bulk, and makes CO_2 adsorption can be achieved under ambient conditions (low temperature, low temperature).

2.4.1.1 Carbonation after mechanical activation

CO_2 chemisorption on mechanically-activated olivine by attrition milling at room temperature has been tested by Fabian et al. (2010). Before CO_2 chemisorptions, mechanically-activated olivine is outgassed at 350 ºC to obtain a clean surface. The amount of CO_2 strongly chemisorbed was calculated by adsorption isotherm at up to 0.27 bar. The capacity of CO_2 adsorption on olivine sand which was mechanically-activated in an attrition mill for 120 min was found to be 3.2 mg CO_2/g of olivine (Fabian et al., 2010: pg. 617). Hydrocarbonates were the only products employed under these test conditions (Fabian et al., 2010). Another CO_2 chemisorption test at 500 ºC found that the maximum CO_2-storage capacity (9.8 mg CO_2/g of olivine) after 30 min adsorption was reached by 4 h of milling with 50 wt.% ethanol, the product of which has the highest pore volume compared to 1 h, 2 h and 8 h of milling (Rigopoulos et al., 2015: pg. 226).

Sandivik et al. (2010) found that the amount of CO_2 adsorption is sensitive to the moment samples are exposed to CO_2. Samples were exposed to pure carbon dioxide gas in the mill chamber at 5 bar and room temperature. Being exposed to CO_2 for 30 min, samples both prior to activation

and those activated after 60 min relaxation, showed values below the detection limit. An exposure to CO_2 of 30 min immediately after mechanical activation resulted in a concentration of about 2.9 mg CO_2 per gram of olivine (Sandvik et al., 2011: pg. 420). However, the simultaneous activation and exposure to CO_2 for 30 min, shows an 8 times higher conversion rate than the value exposure immediately after activation. A 41.2 mg CO_2 per gram of final product was reached after 60 min of simultaneous activation (Sandvik et al., 2011: pg. 420).

2.4.1.2 Carbonation during mechanical activation

Mechanochemical adsorption of CO_2 (intensive grinding in the presence of CO_2) on various Ca- and Mg-containing silicates was initially studied in Russia by Kalinkina et al. (Kalinkin et al., 2009; Kalinkina et al., 2001). The results indicate that the intense penetration of gas molecules in the bulk of the particle and their dissolution in a structurally disordered silicate matrix in the form of distorted CO_3^{2-} ions occurs together with the increasing amorphization of the mineral. The resulting product is comparable to silicate melt quenching, in which CO_2 is dissolved under the conditions of magma state. The authors conclude that the amount of carbon dioxide consumed as a result of grinding increases with the increasing CaO content in the chemical formula of the minerals, and this correlates with Gibbs free energy of reactions of the crystalline minerals with CO_2. As a result of stronger Mg-O bonds in comparison to Ca-O bonds, the absence of calcium in enstatite obstructs its carbonation process (Kalinkina et al., 2001).

The mechanochemical carbonation of forsterite and lizardite was first noted by Nelson (2004) at the University of Utah. After 15-20 min of mechanochemical carbonation, a considerable structural change was noted in the lizardite due to the presence of pure CO_2 (Nelson, 2004). A similar effect was also found with respect to the mechanical activation of antigorite in the presence of flue gas (contain 10% CO_2). This experiment resulted in additional amorphization when

compared with its counterpart in the presence of air (Sanna et al., 2013). However, no significant carbonation conversion of silicate minerals was noted in these studies. Only small amounts of carbon were fixed by 10 min's grinding in the presence of gaseous CO_2, including 0.5 wt% CO_2 in forsterite, 0.6 wt% CO_2 in lizardite, 1.09 wt% CO_2 in enstatite (Nelson, 2004: pg. 5).

Recently, research groups from both Norway and Slovakia have conducted studies with a primary focus on forsterite (Sandvik et al., 2011; Turianicová and Baláz, 2008). Turianicová & Baláž (2008) recognize the importance of water appearing in the mechanochemical adsorption process, and suggest that it can double the amount of CO_2 in the final product (Turianicová and Baláz, 2008). However, the carbonation mechanism changes to direct aqueous carbonation (see details in section 2.4.2.2). Sandvik et al. (2011) believe that conventional grinding in a tumbling mill within a CO_2 atmosphere may compete with high energy efficiency mills for large-scale carbon mineralization (Sandvik et al., 2011). Some results related to the mechanochemical adsorption of CO_2 on Ca/Mg silicates are listed in Table 2.1. Apparently, the degrees of carbonation of wollastonite for 30 min of mechanochemical carbonation were found to be quite different in the studies by Kalinkin et al. (Kalinkin et al., 2009) and Nelson (Nelson, 2004). The main reason for the disparity in these results involves the variety in mechanical activation conditions including milling motion and grinding intensity.

Table 2.1 **Published results for mechanochemical adsorption of CO_2 on selected Mg/Ca silicate in batch experiments**

t_M (min)	Sample	A_{CO_2} (mg/g)	Mill types	Reference
30	Diopside $CaMgSi_2O_6$	87.0	PM	(Kalinkin et al., 2009: pg. 187)
30	Wallanstonite $CaSiO_3$	123.0	PM	(Kalinkin et al., 2009: pg. 187)
10	Diopside $CaMgSi_2O_6$	49.9	PM	(Kalinkin et al., 2009: pg. 187)
10	Wallanstonite $CaSiO_3$	57.3	PM	(Kalinkin et al., 2009: pg. 187)
10	Vermiculites $(Mg,Ca)_{0.4}(Mg,Fe)_3(Si,Al)_4O_{10}(OH)_2*4.5H_2O$	17.6	PM	(Turianicová et al., 2014: pg. 90)
10	Forsterite Mg_2SiO_4	5.4	VM	(Nelson, 2004: pg. 5)
10	Lizardite $Mg_3Si_2O_5(OH)_4$	6.3	VM	(Nelson, 2004: pg. 5)
10	Estitite $MgSiO_3$	10.9	VM	(Nelson, 2004: pg. 5)
10	Wallanstonite $CaSiO_3$	14.3	VM	(Nelson, 2004: pg. 5)
30	Wallanstonite $CaSiO_3$	20.9	VM	(Nelson, 2004: pg. 5)
10	Forsterite Mg_2SiO_4	11.5	PM	(Sandvik et al., 2011: pg. 420)
30	Forsterite Mg_2SiO_4	26.0	PM	(Sandvik et al., 2011: pg. 420)
30	Forsterite Mg_2SiO_4	14.5	PM	(Turianicová and Baláz, 2008: pg. 317)
5	Forsterite Mg_2SiO_4	7.4	PM 50% H_2O	(Turianicová and Baláz, 2008: pg. 317)
30	Forsterite Mg_2SiO_4	25.2	PM 50% H_2O	(Turianicová and Baláz, 2008: pg. 317)

Note: t_M denotes the mechanical activation time (min), A_{CO_2} denotes the CO_2 adsorption capacities at 1 bar (mg CO_2/g material), PM is planetary mill, VM is vibratory mill.

The kinetics of the mechaochemical adsorption on Ca-containing silicates has recently been studied by the research group in Russia (Kalinkin, 2009). Kalinkin divided the process into two stages. The first stage consisted mainly of a cleavage mode in the first 1-2 min, and the second stage was primarily made up of a friction mode after 2 min. Two minutes is the time it takes to reach the grinding limit (see section 2.2). CO_2 chemisorbed on the surface of silicate particles as a thin carbonized layer in the first stage, while the rapid chemical interaction of mechanosorption was found to be diffusion-controlled in the second stage. The phenomenon of CO_2 diffusion into the disordered silicate matrix under mechanical shock can be described by mechanosorption

coefficients. This is positively correlated with the temperature of complete carbonate removal from the product (Kalinkin, 2009; Kalinkin et al., 2009). Due to the similarity of the processes, the kinetics of mechaochemical adsorption on Mg-containing silicates may be similar, and further study in this area is needed.

2.4.2 Direct aqueous carbonation

Although dry carbonation is clearly advantageous over aqueous carbonation due to its inherent simplicity, its slow reaction kinetics remain problematic (Huijgen and Comans, 2005; Power et al., 2013b). The step that limits the reaction rate is the removal of magnesium from the mineral lattice. The focus of research has recently turned from a gas-solid carbonation path to an aqueous path (Sipilä et al., 2008). Aqueous carbonation can be divided into direct and indirect aqueous carbonation routes. In direct aqueous carbonation, CO_2 and water react directly with solids (Gerdemann et al., 2007; O'Connor et al., 2005). Direct aqueous carbonation involves two processes: silicate dissolution and carbonates precipitation. The rate of the process as a whole is determined by the slower process.

Of the many mineral carbonation options, the direct carbonation process developed by ARC is recognized as the most optimal one (Huijgen and Comans, 2005). Its reaction occurs at a temperature of 185°C and at a partial pressure of CO_2 of 115 atm for olivine and 115°C, 150 atm for serpentine, with a carrier solution of 0.64 M $NaHCO_3$ and 1 M NaCl, with 15% solid content (O'Connor et al., 2005: pg. 14).

2.4.2.1 Carbonation after mechanical activation

According to results achieved by ARC, the effects of mechanical activation on direct mineral carbonation can be seen directly. Mechanical activation could significantly increase the level of carbonation conversion under optimum conditions over a short period of time. Using an

attrition mill, the level of carbonation conversion for 5-min and 30-min activated olivine are 6% and 82%, respectively (O'Connor et al., 2001: pg. 6). Mechanical activation can also decrease the carbonation conditions. Using 24 hours' attritted serpentine as a sequestration feedstock at room temperature and a pressure of 1 MPa even within 15 min, the conversion rates were found comparable to those obtained for non-activated mafic and ultramafic minerals at considerably higher temperatures and pressure (O'Connor et al., 2001: pg. 8). Similar results were also found in later studies (Haug, 2010; Summers et al., 2005).

Table 2.2 lists some of the published results for direct aqueous carbonation on mechanically-activated olivine with the solid content of 15 wt %. Due to the differences in carbonation conditions including temperature, CO_2 partial pressure, reaction time, and buffer solution, the results are so varied that they may not be comparable. However, despite the application of various grinding conditions, they all arrived at the similar conclusion that over a certain energy input, further intensive milling is not economical with respect to direct aqueous carbonation (Haug, 2010: pg. 65; Summers et al., 2005: pg. 144). Summers et al. (2005: pg. 144) provides maximal mechanical energy inputs as being 100 kWh/t. Haug (2010) believes that mechanical activation and carbonation conditions can be balanced through a consideration of the kinetics of direct carbonation. When the precipitation rate controls the entire direct carbonation rate, further mechanical activation is not needed, as mechanical activation only increases the mineral dissolution rate. At this point, a less energy-consumptive milling alternative, such as a conventional ball mill, can be used.

Table 2.2 **Published results for direct carbonation of mechanically-activated olivine in batch experiments (modified after (Haug, 2010: Part II, Paper III, pg. 65))**

Particle size	T (ºC)	P (bar)	Buffer solution	t_C [c] (h)	R_X [d] (%)	References
-37 µm	185	115	H_2O	24	91	(O'Connor et al., 2001: pg. 6)
-37 µm	185	115	0.5 M $NaHCO_3$, 1M NaCl	6	84	
-75 µm	185	150	0.64 M $NaHCO_3$, 1M NaCl	1	≈5.1	(Summers et al., 2005: pg. 141)
Varying[a]	185	150	0.64 M $NaHCO_3$, 1M NaCl	1	≈70-89	
Varying[b]	185	115	DI Water	2	3.6-44	(Haug, 2010: Paper III, pg. 8)
Varying[b]	185	115	DI Water	18	23-96	
Varying[b]	128	150	DI Water	0.02-0.75	1.3-7.3	

Note: a) Ground with a stirred media detritor and attrition mill, either wet or dry for 1 hour and 24 hours, b) Ground with different mills over different periods of time, c) t_C is the carbonation time, d) R_X is the carbonation sequestration reaction efficiency, which is the percent stoichiometric conversion of available cations in silicate feed to carbonates. It is calculated according to Equation 7 in (Penner et al., 2004: pg. 2).

Types of magnesium carbonates produced by mechanically-activated olivine have recently aroused the interests of researchers (Turianicová et al., 2013). As with the optimum carbonation conditions employed by ARC, magnesite can be produced with high temperature and CO_2 partial pressure (O'Connor et al., 2001). However, the presence of amorphous magnesium carbonate in the form of hydromagnesite ($(MgCO_3)_4 \cdot Mg(OH)_2 \cdot 4H_2O$) has been confirmed under direct carbonation conditions at a CO_2 pressure of 60 bar and 25°C (Turianicová et al., 2013: pg. 76). These results differ from the common understanding that the formation of nesquehonite ($MgCO_3 \cdot 3H_2O$) is favored at relatively low temperatures and CO_2 partial pressures, while hydromagnesite favors higher temperatures of over 40ºC (Case et al., 2011: pg. 85; Hänchen et al., 2008: pg. 1013). The mechanical activation of forsterite has a higher likelihood of producing a relatively stable carbonation format under ambient conditions.

2.4.2.2 Carbonation during mechanical activation

Turianicová and Baláž (2008) have recently examined the wet mechanical activation of olivine in the presence of carbon dioxide. This three phase mechanical activation results in a relatively larger specific surface area with respect to the solid, as well as a nearly twice as much CO_2 adsorption (see Table 2.1). The main reason of the effects is the presence of water, which rendered the mechanical activation process with the feature of wet milling, and altered the mineral carbonation process from gas/solid reaction to aqueous one (Turianicová and Baláž, 2008).

Werner et al. have recently developed a novel process which combines CO_2 capture from flue gas with the wet grinding of heat-treated serpentine. Use of the ball mill successfully decreases the starting time of precipitation, and reduces the temperature and time needed for nesquehonite to hydromagnesite transformation. However, under all investigated grinding conditions, including milling intensities of 600 rpm, 800 rpm,1200 rpm, 2400 rpm, and grinding temperatures of 30ºC, 50ºC, 60ºC, the extent of carbonation remained at less than 20% (Werner et al., 2013: pg. 5935). They suggest that an indirect carbonation process that separates serpentine dissolution and Mg-carbonate precipitation can better control the critical operating conditions, may improve overall carbonation efficiency (Werner et al., 2013).

2.4.3 Indirect aqueous carbonation

Indirect carbonation involves the additional step of magnesium extraction from rock/minerals followed by an acid-base reaction between metal (hydro) oxides and CO_2 (Maroto-valer et al., 2005; Wang and Maroto-valer, 2011). Although multi-steps in the indirect carbonation process results in extra energy consumption, the possible recycling of pure products may contribute to the reduction of the sequestration cost. Various strong or weak acids (Lackner et al., 1997; Park et al., 2003; Teir et al., 2007), alkali solutions (Maroto-valer et al., 2005) or ligands

(Park et al., 2003) were used to dissolve or leach Mg from minerals. Among these, H_2SO_4 is recognized as being the most effective for leaching serpentine (Maroto-valer et al., 2005).

2.4.3.1 Leaching after mechanical activation

(1) Leaching of olivine after mechanical activation

The dissolution of olivine in acid can be expressed through the following reaction 2.5:

$$(Mg, Fe)_2SiO_4 + 4H^+ \rightarrow 2(Mg^{2+}, Fe^{2+}) + H_4SiO_4^0 \quad (2.5)$$

A stoichiometric release of Mg^{2+} and Fe^{2+} in acid can be observed regardless of whether olivine is mechanically activated or not (Kleiv and Thornhill, 2006). However, Haug (2010) observed that Fe^{2+} concentrations were randomly distributed with a small amount, due to the steel contamination that induce the precipitation of Fe phase. Haug (2010: pg 1552) also found that the average Mg:Si ratios in water samples (2.2) is higher than the stoichiometric Mg:Si ratio (1.86), because that Mg^{2+} is preferred dissolved and Si-phase tend to precipitated during dissolution.

Kleiv and Tornhill (2006) have investigated the initial phase of mechanically-activated olivine dissolution in diluted nitric acid (0.01 M). They claim that the considerable increase in the dissolution reactivity is largely due to the structural disordering of olivine surfaces created by prolonged intensive milling (Kleiv and Thornhill, 2006). For example, the specific rate constant of material that has been ground for 60 min is 9 time higher than the counterpart ground for 1 min. Since the specific surface area of the former material was 1.8 times higher than that of the latter one, the structural changes effect the reactivity by a factor of nearly 5 was obtained (Kleiv and Thornhill, 2006: pg. 342).

Haug and et al. (2010) have applied a 0.01 M HCl solution under ambient conditions to investigate the dissolution behaviors of olivine which has been mechanically activated in a variety of different mill types (Haug et al., 2010; Sandvik et al., 2011). They found that when sample

products such as those that have been wet milled and moist milled are at high crystalline states, the specific surface area was the most important parameter for increasing the initial specific dissolution rates of mechanical-activated olivine. These samples showed a strong correlation between specific surface area and the amount of dissolved olivine. However, the correlation no longer fit for the minerals which were at an amorphous state. For example, the samples which had been milled dry had the lowest specific surface area, but had the largest rate of constant. In this case, the degree of amorphous/crystallinity was essential for the dissolution of olivine (Haug et al., 2010).

A geological model using PHREEQCi was built to describe the complicated dissolution processes of mechanically-activated olivine (Haug et al., 2010). Equation 2.5 considers the initial surface area, the shrinking core model, the reaction rate dependent on pH, the reduction in reaction rate (R_i) when approaching equilibrium, and also introduces two correction parameters, f_m and f_r .

$$R_i = f_r \cdot (A_0 \cdot \beta') \left(\frac{N_i}{N_0} \right)^{f_m} \cdot r \cdot \left(1 - \frac{IAP_i}{K_{f_0}} \right) \tag{2.5}$$

where, A_0 is the total surface area (m^2), β' corrects the surface area for the presence of contamination. N_0 is the initial moles of olivine. N_i is the amount of olivine still not dissolved during i^{th} interval. r is the reaction rate dependent of pH. IAP_i is the ion activity product for forsterite at the modeling step i. K_{f_0} is the equilibrium constant for forsterite. f_m is the exponent in the shrinking core model. It is an empirical value that summarizes the total decrease in the calculated leaching rate constants resulting from the mechanical activation, which includes preferential dissolution of fines, surface properties and changes in the crystal lattice due to

activation. f_m varies from 6.9 to 20. f_r is the ratio between the initially-observed rate constant of the sample and the theoretical rate constants. f_r varies from 4 to 1000.

(2) Leaching of serpentine after MA

The acid leaching properties of mechanically-activated serpentine has been studied in relatively high acid concentrations (1M HCl or 0.1-3M H_2SO_4) (Kim and Chung, 2002: pg. 161; Yoo et al., 2009: pg. 1226; Zhang et al., 1997: pg. 325). 100% extraction of Mg and Fe from 240 min dry ground serpentine was achieved within 5 min (Kim and Chung, 2002: pg. 166). The dissolution rate of Mg from the milled serpentine increased as grinding time extended, acid concentration rose, and leaching temperature elevated (Yoo et al., 2009). However, when serpentine is deeply activated mechanically, such as after 240 min dry grinding, the release of magnesium is no longer dependent on leaching time and acid concentrations at low temperatures (Zhang et al., 1997: pg. 328). As the dissolution temperature was increased to 90 ºC, little mechanical effects on the dissolution of Mg^{2+} in H_2SO_4 solution were observed (Yoo et al., 2009: pg. 1228). As grinding progressed, the Mg:Si molar ratio decreased and ultimately reached a value of almost two, which is the same as that for forsterite (Zhang et al., 1997: pg. 329).

Through fitting the experimental data into the Jander equation, Yoo et al. (2009) found that the kinetics of Mg dissolution was controlled by diffusion on the surface of serpentine particles which contain thin channels between the layers of silica. The calculated activation energies of the serpentein-H_2SO_4 dissolution system decreased from 82.0 kJ/mol to 76.7 kJ/mol after mechanical activation (Yoo et al., 2009: pg. 1229).

2.4.3.2 Leaching during mechanical activation

Leaching during MA is a result of a combination of chemical and mechanical activation. At the time of this writing, no literature has yet been found with respect to leaching forsterite during MA since no significant results have been obtained in the initial trials for this process (O'Connor et al., 2001). However, the combination of two pre-treatment methods can achieve unexpected activation effects for serpentine. The advantage of leaching during MA is to refresh the surface of serpentine particles during the dissolution process by depleting the SiO_2 layer, which is the diffusion barrier formed during silicate dissolution. Low energy attrition type internal grinding can achieve this purpose (Park and Fan, 2004).Collaboration between two pretreatment methods can increase the reaction kinetics (Park and Fan, 2004). Park and Fan (2004) have reported that internal grinding alone did not significantly dissolve serpentine. However, concurrent internal grinding in acidic solvent (EDTA) nearly doubled the kinetics of serpentine dissolution (Park and Fan, 2004). Similar results were obtained when the digestion of serpentine was conducted simultaneously with grinding in a single strong acid (H_2SO_4) (Van Essendelft and Schobert, 2009a).

A predictive kinetics model describes the behaviors of serpentine during grinding in a strong acid was built, providing a valuable approach and information for industrial equipment design (Van Essendelft and Schobert, 2009b). As the best description of the reaction condition, the kinetics model takes account of particle size distribution, surface morphology, electrical double layer, surface reaction, ash layer diffusion, material balance, solution equilibrium (Van Essendelft and Schobert, 2009a), temperature, acid concentration and grinding energy input (Van Essendelft and Schobert, 2009b). These authors found that rather than impact, attrition accounted for changing the effective diffusivity in the process.

A study conducted at McGill University in Montreal, Canada proposed an approach that involves the disintegration of the serpentine fibers (clinochrysotile) through a combination of chemical (H_2SO_4) and mechanical treatments for CO_2 sequestration and mineral processing (Uddin et al., 2012). The researchers applied this technique to process an ultramafic ore. The disintegration of fibers can reduce entanglement and pulp viscosity, thus improving selective flotation. Also, the formation of elemental sulphur and the increase of ionic strength (Mg^{2+}) in solution eliminate the need for collectors and frothers in downstream flotation. After a 1 hour grinding treatment, a 90% rejection of MgO-bearing gangue was achieved, and was responsible for the increase of Ni recovery from 45% to 80% in downstream flotation (Uddin et al., 2012).

2.4.4 Integrated activation processes

The combination of mechanical, chemical and thermal activation could reach unexpected results (McKelvy et al., 2005). There are two ways to combine the pre-treatment methods, integrated mechanical and thermal activation, and integrated mechanical and chemical activation.

2.4.4.1 Integrated mechanical and thermal activation

Serpentine dehydroxylation takes place between 550 and 800 °C. The differential thermal analysis (DTA) peak temperature of antigorite, lizardite and chrysotile are 715, 714, and 654 °C, respectively (Viti, 2010: pg. 365). The mechanical activation disrupts the structure of serpentine, and leads to the thermal decomposition at a relative low temperature than the crystallite one (Drief and Nieto, 1999). Little difference can be observed in the thermal profile between wet and dry mechanically-activated serpentine (Balucan and Dlugogorski, 2013). Due to the mechanical energy input, the hydroxyl group in the structure of serpentine becomes disordered, at the same time water is formed and adsorbed on surface of the mineral. The total removal of the adsorbed water requires additional heating (Dlugogorski and Balucan, 2014). This is the reason why the

existence of water in mechanically-activated serpentine does not appear to inhibit carbonation, since good carbonation results are obtained (O'Connor et al., 2001).

Combining mechanical activation with thermal activation, namely thermaomechancial activatioin, can achieve significant results. When grinding is conducted at 300-600°C, serpentine's mechanical activation properties are improved and can easily reach the status of products which have been thermally-treated at higher than 850 °C (Yu et al., 2011: pg. 1737). When thermomechanically activated lizardite in a stirred mill at 300 rpm, with the grinding temperature increased up to 250°C, the amount of hydroxide removal is increased, the specific surface area is decreased, and the carbonation reactivity is enhanced. However, higher grinding intensity (e.g. 500 rpm) is less effective for accelerate carbonation reactivity of lizardite, due to the particle sintering associated with thermomechanical activation at temperature less than 250°C (McKelvy et al., 2005: pg. 19).

2.4.4.2 Integrated mechanical and chemical activation

The use of the molten salt process has been abandoned in the area of mineral carbonation since 2003 because of its use of corrosive chemicals and its high energy consumption (Huijgen and Comans, 2003). However, the mechanochemical treatment of serpentine with ammonium salts has recently been the focus of some interest (Highfield et al., 2012). For Mg extraction, serpentine is dry milled with ammonium bisulfate (NH_4HSO_4). The process efficiently extracts 30% Mg^{2+} ions from serpentine as boussingaultite ($(NH_4)_2Mg(SO_4)_2 \cdot 6H_2O$) even after brief manual grinding, and extracts more than 60% Mg^{2+} ions in 2 to 4 hours of grinding. For mineral carbonation, the mechanochemical activation of various Mg-based solids ($MgSO_4$, $MgSO_4 \cdot 7H_2O$, $Mg(OH)_2$, MgO, $Mg_3Si_2O_5(OH)_4$) with ammonium bicarbonate (NH_4HCO_3) at an ambient temperature was investigated. The fraction of CO_2 sequestrated in serpentine was found to be 20% after 16 hours

of milling. The product is a stable hydromagnesite ($Mg_5(CO_3)_4(OH)_2 \cdot 4H_2O$) and is soluble in an aqueous mineral environment (Highfield et al., 2012: pg. 6547).

2.5 Potential application in an integrated mineral carbonation process

At present, mineral carbonation with pretreatment by mechanical activation is still too energy intensity to be applied in an industrial site. To reduce the cost of mineral carbonation, industrial wastes became good candidates for their use as feedstock (Bobicki et al., 2012). Mine waste materials from ultramafic-hosted deposits, such as nickel, diamond, and PEG mines, are industrial wastes that offer potential long-term solid storage buffers for CO_2. Mining activities produce large amounts of ultramafic waste materials, such as waste rock, tailings, and slag, which are mainly composed of olivine and serpentine, and have a large CO_2 sequestration capacity (Hitch et al., 2010). Mechanical activation may applicable in an integrated mineral carbonation process in such mines.

As reviewed above, olivine and serpentine response differently with respect to mechanical activation. Since olivine and serpentine always occur together in mine waste materials and both of them are available to contribute to permanent storage of CO_2, purification or separation of the mine waste materials are not necessary for the purpose of mineral carbonation. However, mechanical activation of mine waste materials is quite different from that of individual minerals. Under prolonged milling, the interaction among them may create unexpected phenomena. It would be an advantage to test mine waste material under various mechanical activation and carbonation condition.

Crystal structure characterization is essential for determining the effectiveness of mechanical activation. The crystallinity or amorphization degree, which was obtained from X-ray diffraction pattern, has been commonly applied in pure minerals. However, the values may be not

applicable when the X-ray diffraction patterns contain multiple mineral phases, especially phase transfer happened among the containing minerals. As such, searching for suitable models to resolve the microstructure parameters (i.e. crystallite size, and micro-strain) of the mechanical activated mine waste material is of great interests to characterize the structure change of mine waste materials after mechanical activation.

The economic analysis on an integrated mineral carbonation process with mechanical activation as pretreatment is vital to evaluate its feasibility. The mineral carbonation process of mechanically-activated magnesium/calcium silicate involves two separate processes, feedstock milling and downstream CO_2 carbonation. Since prolonged milling increases the reactivity of feedstock during the carbonation process, the increase of energy input in the milling process can absolutely lower the energy requirements of the carbonation process to a defined conversion. An economic analysis of the whole process must consider the specific energy consumption of both processes. However, the integrated mineral carbonation process involves more than two processes. Feasibility studies on the integrated mineral carbonation process would be more complicated. A life cycle analysis on the integrated mineral carbonation process involved all processes need to be taken into consideration.

2.6 Conclusions

This study reviews the carbonation process with mechanical activation as a pretreatment method, focusing on olivine and serpentine separately. The following findings are addressed:

(1) Because of their structural differences, the mechanical activation properties of olivine and serpentine show a great deal of diversity. The soft mineral (serpentine) becomes amorphous more readily, while hard mineral (olivine) stores its excess energy by decreasing its crystal size

and increasing lattice strain. Mechanical activation of olivine tends to disorder its Mg-O structure while mechanical activation on serpentine dehydrates its Mg-OH structure.

(2) Wet grinding in an attrition mill has been found to be most appropriate for the mechanical activation of olivine. Even though no studies have focused on a comparison of mill types for the mechanical activation of serpentine, dry intensive grinding is clearly the most favorable for serpentine dehydration.

(3) To date, none of the current methods in use for the mechanical activation of olivine and serpentine for mineral carbonation has been found to be faultless, and none have been deemed to be appropriate for application in industry. Developing a well-integrated mineral carbonation method is urgently needed to reduce process energy consumption to a practical level and environmentally appropriate level in terms of CO_2 production.

Chapter 3: Characterization of the microstructure of mechanically-activated olivine using X-ray diffraction pattern analysis[2]

3.1 Introduction

Mechanical activation by high intensity milling has been commonly used as an effective pretreatment method in various areas, such as mining, metallurgy and materials engineering. Mechanical activation is one of the three broad catalogues for grinding, the other two being coarse grinding and fine grinding (Boldyrev et al., 1996). In mineral processing, the aim of coarse and fine grinding is liberating the ore for downstream separation. Furthermore, fine grinding also used after mineral separation in order to give concentrates the right particle size distribution or a sufficiently high surface area. Whereas mechanical activation aims to enhance a reaction (Baláž, 2008). A level of mechanical activation can be achieved as the material is milled to the brittle-ductile transition range (Boldyrev et al., 1996). Beyond the integration of particles and the formation of new surfaces, mechanical activation alters the properties of a material (Tkáčová, 1989). Additional changes such as structural distortions are crucial in determining the reactivity of material. These distortions result in the storage of excess enthalpy, which lowers the activation energy of subsequent reactions (Boldyrev et al., 1996). The main advantages of mechanical activation include: a) its simplicity as a process, which can be completed over a single grinding stage; b) its attractiveness as a more environmentally friendly process, as it does not use solvents, gas, etc.; c) its ability to obtain metastable state products or nano-particles, which are hard (if not impossible) to achieve using traditional methods (Boldyrev, 2006). The only drawback to

[2] A version of this chapter has been submitted for publication. Li, J and Hitch, M., 2015. Characterization of the microstructure of mechanically-activated olivine using X-ray diffraction pattern analysis, Minerals Engineering, 86: 24-33.

mechanical activation is its intensive energy consumption. However, when integrated as part of the total milling process, the operational energy consumption can be reduced to a practical level (Haug et al., 2010).

Olivine is an industrial mineral composed of an independent SiO_4 tetrahedral linked by divalent ions in 6-fold coordination (such as Mg^{2+}, Fe^{2+}), with a theoretical formula of $(Mg, Fe)_2SiO_4$ (Kerisit et al., 2013: pg. 81). Traditionally, olivine is used for refractory material, slag conditioner, blasting sand and foundry sand. When the reactivity of olivine's surface is enhanced, it has many new applications, such as a neutralizer for sulphuric acid, a heavy metal adsorbent, a catalyst for decomposing toxic organic chemicals, a magnesium source for soil improvement in agriculture, and an additive in water treatment (Kleiv and Thornhill, 2006). Most recently, olivine, especially its magnesium end-member forsterite, is recognized as one of the most promising feedstock in CO_2 sequestration by mineral carbonation.

In recent years, mechanical activation of olivine has been a popular object of study, and specifically the importance of crystal structure changes for downstream reactions (Fabian et al., 2010; Haug, 2010; Kleiv and Thornhill, 2006; Turianicová and Baláz, 2008). Kleiv and Thornhill (2006) found that structural disordering of the olivine surface is largely responsible for the disproportionate increase in the reactivity of acid leaching. Similarly, Summers et al. (2004) found that dry grinding that caused structural damage improved reactivity by changing the diffusion rate in direct aqueous mineral carbonation. Atashin et al. (2015: pg. 560) suggested that the most desirable microstructure for CO_2 sequestration is about 55 kJ/g milling energy input.

Many studies quantified the structure changes using X-ray diffraction patterns. The crystal structure of olivine has been presented using several parameters from peak geometry, such as full width at half maximum (FHWM) (Kleiv and Thornhill, 2006; Summers et al., 2005), peak intensity

(Rigopoulos et al., 2015), and integral area of peak (Baláž et al., 2008; Haug, 2010). Haug (2010) has found that the crystallinity calculation based on peak area of the XRD pattern demonstrated the best correlation with energy consumption. The main reason for this is that the crystallinity calculation contains all the factors influencing the shape of the XRD pattern, such as crystallite size, grain size of particles and amorphization materials. However, it is better to analyze the individual structural characteristics in order to have a better understanding of how mechanical energy activates olivine. At present, little work has been done on accurate characterization of structural distortions caused by the mechanical activation of olivine, such as changes in crystallite size, micro-strain, lattice parameter, and phase transformation.

The aim of the present study is the quantitative and qualitative characterization of microstructural changes in olivine in response to dry mechanical activation, based on X-ray diffraction pattern. Various models for microstructure characterization are discussed, including the Scherrer method, Williamson-Hall method, Multiple Whole Profile fitting and Rietveld method.

3.2 Material and experimental

The olivine foundry sand (olivine) used in this study was purchased from Ward's Canada Limited, and was from the Twin Sisters ultramafic complex in northwest Washington State, USA. The chemical composition of olivine was analyzed using X-ray fluorescence (XRF) at Acme Analytical Laboratories Ltd. The major oxides of olivine powder were 50.94% MgO, 40.7% SiO_2, 8.39% Fe_2O_3, 0.68% Cr_2O_3, 0.15 % Al_2O_3, 0.09% CaO, 0.02% TiO_2, and 0.12% MnO, and loss on ignition (LOI) was 0. X-ray powder diffraction analysis (XRPD) detected approximately 97.9% pure olivine, 0.2% lizardite, 1.5% chromite, and 0.4% quartz in the foundry sand. Normalization of the analytical data produced from XRF and XRPD, revealed that the olivine sand contained approximately 93% forsterite (Mg_2SiO_4) and 7% fayalite (Fe_2SiO_4), with a formula of ($Mg_{1.86}Fe_{0.14}$)

SiO_4. The received material was crushed using a porcelain mortar and pestle to prevent contamination. The crushed olivine was screened using 140 mesh Tyler sieve (106 μm), and the materials that passed the sieve were used as the starting sample for mechanical activation. The starting sample had an 80% passing size of 91.4 μm, a specific surface area of 0.8 m^2/g, and a density of 3.3 g/cm^3.

Mechanical activation tests were carried out in a commercial Spex Mixer/Mill mod. 8000 (SPEX Industries, Inc., Edison, NJ). The vial of SPEX 8000 has a lateral, back-and-forth shaking motion. In each test, 10 g feed material was ground in a 25 mL hardened steel vial, and two 6 mm hardened steel ball under a dry air atmosphere. The vial was vibrated with an amplitude of 50 mm and a frequency of 20 Hz. Samples ground for 30, 60 and 120 min were collected, sealed into plastic tubes, and kept in a freezer for characterization tests. After each run, the milling vials and balls were washed with a brush and water and dried in an oven, with the intention of eliminating the contamination from previous milling tests. In order to prevent overheating, milling was performed at intervals of 30 min milling, and 30 min rest. The milling temperature was kept under 40°C, which was measured by a thermocouple right away after the stops.. The milling energy consumption was monitored by a Watts-up?™ Pro electrical watt meter during the grinding test. The energy consumption was calculated as the difference between the power draw of milling with an empty vial and a vial filled with sample and grinding media.

The particle size distribution and granulometric surface area of samples were measured by a particle size analyzer instrument (Mastersizer 2000, Malvern, U.K.) using the laser diffraction method in the liquid mode. Ultrasonic vibration for 5 seconds was applied to the suspension to ensure the representative samples were properly dispersed. The BET surface areas were measured by a nitrogen adsorption instrument (Autosorb-1MP, Quantachrome, USA) at –198°C. The X-ray

diffraction (XRD) patterns were collected through a Bruker D8 powder diffractormeter (Bruker AXS GmbH, Germany) using Co Ka radiation (λ =0.1789 nm) at 35 kV and 40 mA in the range 2θ=3-80°. All patterns were collected using a step size of 0.03° and a counting time 0.7s per step. For XRD analysis, the samples were reduced to an optimum grain-size (<10 μm) by milling in ethanol in a vibratory McCrone Micronising Mill for 7 min. Considering the short period of re-grinding compare to mechanical activation process, it can be assume that the microstructures of the samples were not altered (Tkáčová et al., 1993).

3.3 Microstructural characterization (background)

The key components of XRD profile contains information of microstructure of minerals. Line profile analysis methods can effectively extract the microstructure information from XRD pattern.

3.3.1 Key components of XRD profile

X-ray diffraction (XRD) is a powerful tool for characterization of material with crystal structures. Proper analysis of the XRD profile allows for qualitative and quantitative analysis of the material. The changes in the microstructure of the material structure produced by prolonged grinding conditions and high-energy ball mills can be characterized as well (Pourghahramani, 2007).

The XRD profile contains several types of key information about the crystals in a material. The key components in an XRD profile include peak position (2θ), the maximum height of the peak (I_{max}), and the width of the peak. The width of the peak is usually expressed by the full-width at half of the maximum height (FWHM) or the integral breadth (β_i).

The 2θ stands for a specific crystalline component of the mineral. The presence or disappearance of a peak at 2θ implies a mineral appearing or vanishing. According to the Bragg's

Law (Equation 3.1), the shifting in 2θ means the expansion or shrinking in the lattice diameters (Bragg, 1913: pg. 436).

$$n\lambda = 2d\sin\theta \tag{3.1}$$

Where, d is the interplanar spacing, n is known as the order of reflection (n=1, 2, 3…) Fig. 3.1a shows a typical unit cell, where a, b, c are the lattice constants that present three dimensions in the lattice, and α, β, γ are the three angles between them. For an orthorhombic lattice, the lattice angle β=90°. The volume of the unit cell (V) can be calculated by Equation 3.2.

$$V = abc \tag{3.2}$$

The plane-spacing equation for the orthorhombic forsterite crystal systems is expressed in Equation 3.3.

$$d = \frac{1}{\sqrt{\left(\frac{h}{a}\right)^2 + \left(\frac{k}{b}\right)^2 + \left(\frac{l}{c}\right)^2}} \tag{3.3}$$

Where, h, k, l are Miller indices of diffraction planes.

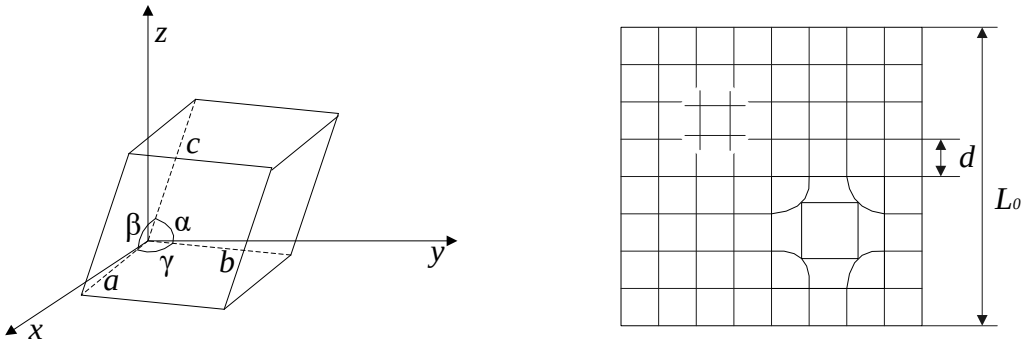

(a) (b)

Figure 3.1 (a) An unit cell definition using parallelepiped (modified after (Waseda et al., 2011: pg. 23)); (b) Schematic representation of lattice strain in a square cross section of a crystallite (modified after (Pourghahramani, 2007: pg. 15)).

I_{max} usually corresponds to the abundance of a phase and can be used for quantitative analysis of mixtures. The typical methods for quantitative analysis include reference intensity ratio method (Chung, 1974), internal standard method (Alexander and Klug, 1948) and Rietveld method (Rietveld, 1969). Where there is no phase transfer, the reduction in I_{max} means that amorphization has shortened the long ranged order of the lattice (Ohlberg and Strickler, 1962).

Since the peak shape of an ideal crystal has a negligible width, the measured FWHM or β_i contains the information of instrumental effects, crystallite size and lattice strain. As proposed by the National Institute of Standards and Technology of USA, the instrumental broadening effects can be removed through an X-ray diffraction pattern of a standard sample powder LaB_6, which was obtained in the same way as the other samples. Crystallite size (D) is the size of diffracting domains, which is different from the size of a particle aggregating one or more crystals. Each crystallite may be build up of single or several coherently reflecting domains. Fig. 3.1b shows a crystallite with an edge length diameter L_0, which consists of columns vertical to the latttice planes. Crystallite size broadening is usually due to extended imperfections, including dislocation arrays, stacking faults, and twins. Strain (ε) is defined as $\varepsilon = \Delta d / d$, where, d is lattice spacing of an unstrained sample, and Δd is the change in d at a strained status (Fig. 3.1b). Strain broadening is caused by defects, such as dislocations, vacancies, interstitials, and substitutional defects. To accurately extract the microstructure characteristics, the contribution of each factor towards peak broadening needs to be separated. The typical methods for resolving crystallite size and microstrain include the Scherrer method, Williamson-Hall method, Warren-Averbach method, and Rietveld method (Pourghahramani, 2007).

3.3.2 Line profile fitting method

Line profile fitting on the X-ray diffraction profile is the primary step for the extraction of microstructure information. The measured X-ray diffraction profile was fitted using PANalytical X'Per HighScore Plus v3.0e (Speakman, 2014). First, the background of the obtained profiles was determined. The $K_{\alpha 2}$ component was removed by assuming the intensity of $K_{\alpha 2}$ is half of that of $K_{\alpha 1}$. In order to reduce the bias in calculation, smoothing of the XRD patterns was excluded during the fitting. Each diffraction peak was empirically fitted by the Pseudo-Voigt line shape function, which is a linear combination of Cauchy and Gaussian function. The weighted profile residual (R_{wp}) is used to determine the fitting quality. R_{wp} is the residual difference between measured and fitted pattern with a weighting function emphasizing on high intensity data points. The selected difflections of each sample were refined until the R_{wp} was less than 10, which implies a good fit with the measured data.

Fig. 3.2 is an example of XRD data after fitting. Then the instrumental broadening is corrected and the overlap peaks are separated carefully. Eight of the most intensive reflection peaks of forsterite (020), (012), (130), (131), (112), (122), (140), (222) were separated and selected for the microstructure analysis. The key components of the XRD profile were extracted from each adjusted line profile for the Scherrer and Williamson-Hall analysis. The fitted profiles of the eight reflection peaks, which were corrected for background, K_{a2} component, instrumental broadening, and overlapping peaks, were saved carefully for Multiple Whole Profile fitting method (MWP) analysis.

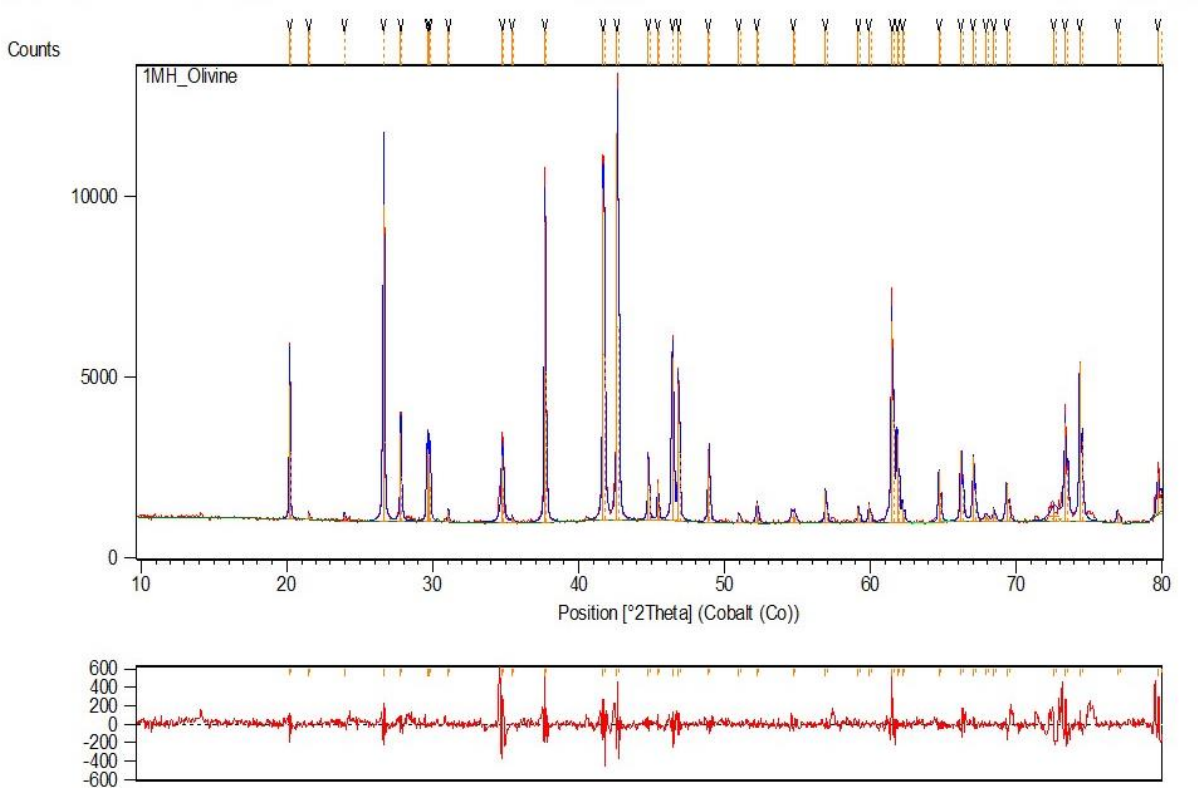

Figure 3.2 XRD profile for pristine olivine fitted by the Pseudo-Voigt function.

3.3.2.1 Scherrer Method

The Scherrer method assumes that the line broadening is entirely due to the effect of crystallite size. This method is suitable to estimate the crystallite size less than 100 nm. The Scherrer method calculates the volume weighted crystallite size (D_V) as follows (Scherrer, 1918: pg. 99).

$$D_V = \frac{K\lambda}{\beta_f}\cos\theta \tag{3.4}$$

Where, K is a unit cell geometry-dependent constant, K= 0.89 was in use for the integral breadth in the case of spherical crystals with cubic symmetry (Langford and Wilson, 1978); λ

corresponds to the wavelength of the X-ray radiation used; β_f is the integral width of a representative peak of the sample after correction for the instrumental broadening.

When only considering the strain effect for the line broadening, the strain (ε) can be calculated as follows (Stokes and Wilson, 1944: pg.178):

$$\varepsilon = \frac{\beta}{4}\cos\theta = \frac{\beta}{4\tan\theta} \tag{3.5}$$

3.3.2.2 Williamson-Hall method

Williamson and Hall proposed a simple method for resolving both size-induced broadening and strain-induced broadening based on their order dependence. The approximate results are capable of giving a qualitative indication of sample microstructure. The Williamson-Hall plots can be applied to a Gaussian profile (Equation 3.6) (Williamson and Hall, 1953: pg. 24).

$$B^2 = \frac{1}{D_V{}^2} + 4\varepsilon^2 d^{*2} \tag{3.6}$$

Where, $B = \frac{\beta_f \cos\theta}{\lambda}$, and $d^* = \frac{2\sin\theta}{\lambda}$. A plot of B^2 against $4d^{*2}$ gives a straight line. From the intercept and slope of the line, D_V and ε can be calculated.

3.3.2.3 Multiple Whole Profile fitting method

Multiple whole profile (MWP) fitting method is a set of complex analytical functions, which could give finer details of sample microstructure (Ribárik et al., 2001). In the MWP fitting method, the normalized Fourier transforms of the prepared 8 peaks are fitted by the theoretical Fourier transforms. The modified Warren-Averbach Fourier method (Equation 3.7) (Ungár and Borbely, 1996: pg. 3174) was used for the analysis of the microstructure of the mineral.

$$\ln A_L \cong \ln A_L^S - \rho\frac{\pi b_v{}^2}{2} L^2 \ln\left(\frac{R_e^*}{L}\right)(g^2\overline{C}) \tag{3.7}$$

Where, L is the Fourier length, A_L is the cosine Fourier coefficients of the peak profile. A_L^S relates to the crystal size. The second part of the equation relates to the strain. ρ is the average dislocation density, b_v is the Burgers vector of dislocation, g is the diffraction vector, $\overline{C}$ is the average dislocation contrast factor, and R_e^* is the effective outer cut-off radius of dislocation.

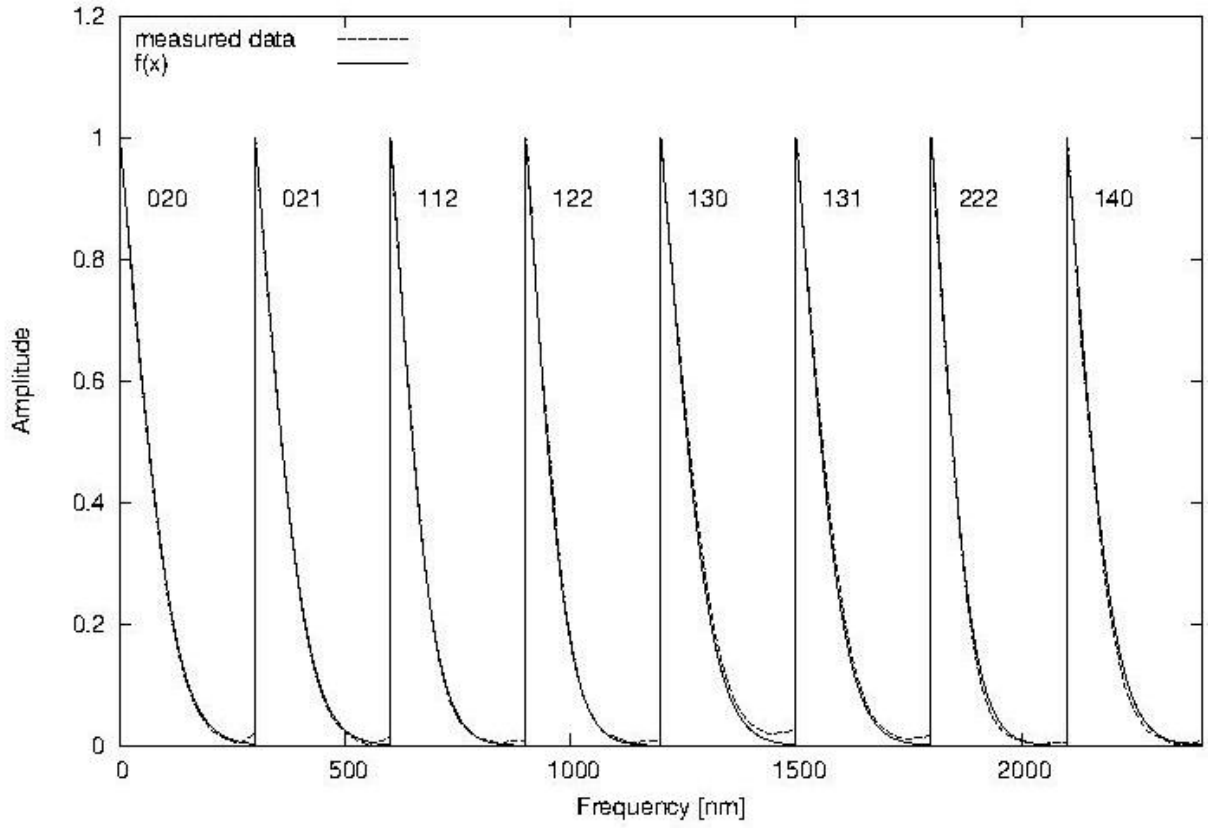

Figure 3.3 Fourier transforms for the selected peaks in the XRD pattern of pristine olivine as a function of frequency.

The *Evaluate* program was used for the WMP fitting of the olivine profile (Ribárik et al., 2001). Since the olivine was an orthorhombic crystal that is more complicated than hexagonal, the cubic crystal system was selected and spherical size function was in use during fitting. The

value of the input parameters includes lattice constants (a=0.47700 nm, b=1.021200 nm, c=0.59840 nm) came from the mineralogy database. b_v equals ½[001] (0.299 nm) for forsterite calculated in Adjaoud et al. (2012: pg. 757), and $<\overline{C}>\cong 0.4$ for the olivine suggested in Couvy et al. (2004: pg. 880). Fourier transforms method was selected for the fitting. All the other parameters related to sampling of Fourier transform of the measured data, initial values of fitting parameters and point of stopping were set as default. The details of the other parameters selection were as described in Ribárik et al. (2001). Fig. 3.3 shows the result of the MWP fitting on the selected 8 peaks in pristine olivine.

Assuming the crystallite size follows a log normal size distribution function, the MWP method calculates the median (m) and the variance (σ) (Ribárik et al., 2001). Then the average volume weighted crystallite diameter D_V can be obtained (Equation 3.8) (Ribárik et al., 2001: pg. 671):

$$D_V = \frac{3m\exp[(7/4)(2^{1/2}\sigma)^2]}{4} \tag{3.8}$$

The MWP method also provides two dislocation structure parameters, ρ and M^*. M^* is the arrangement of dislocations used for measuring the dipole character of dislocations, $M^* = R_e^*\rho^{1/2}$ (Ribárik et al., 2001: pg. 674). A small or large M value indicates a strong or weak dipole character, respectively. With the obtained values, the mean square strain $<\varepsilon_L^2>$ can be calculated accordingly (Equation 3.9) (Ribárik et al., 2001: pg. 670).

$$<\varepsilon_L^2> = (\frac{b_v}{2\pi})^2 \pi\rho C f(\frac{L}{R_e^*}) \tag{3.9}$$

where, C is the contrast factor of the dislocations and f is the strain function.

3.3.3 Full pattern fitting and Rietveld method

Rietveld method estimates the value of crystallite size and strain from the width of refined profile, based on full pattern fitting method (Balzar et al., 2004). This method gradually becomes popular for the characterization of sample microstructure. The full pattern fitting method fits the measured XRD pattern to the crystallographic structure models by least-square calculation. Through refining several adjustable parameters, the residual value of the figure-of-merit function R_{fom} between calculated and measured data can be set to a minimum. R_{fom} is defined by Equation 3.10 (Rietveld, 1969: pg. 69).

$$R_{\text{fom}} = \sum_i w_i [y_i(\text{obs}) - y_i(\text{calc})]^2 \tag{3.10}$$

Where, w_i is the coefficient and equals $1/y_i(\text{obs})$, $y_i(\text{calc})$ denotes the calculated intensity and $y_i(\text{obs})$ is the measured intensity at the i^{th} step. The values of R_{fom} obtained in the present experiments were less than 10, which were considered as a good fit.

Rietveld refinements were done with refinement software DIFFRAC plus Topas Version 4.2 (Bruker AXS GmbH, Karlsruhe, Germany) (Bruker Axs GmbH, 2009) using the fundamental parameter approach (FPA) to estimate the instrumental influence (Cheary and Coelho, 1992). Table 3.1 lists the sources of crystal structure data for Rietveld refinement. The first-order Chebyshev polynomials was used to model the diffraction backgrounds curve, and an additional 1/x term was adopted to assist in the fitting of the background at low angles. The refinement step refines the parameters including zero error, cell parameters, preferred orientation, and Pseudo-Voigt crystallite size and strain of forsterite. Fig. 3.4 shows the result of the Rietveld refinement on the XRD pattern of pristine olivine.

Table 3.1 Sources of crystal structure data used in this study.

Mineral	Source
Forsterite	(Yu, 1997)
Chromite	(Lenaz et al., 2009)
Lizardite-1T	(Mellini and Viti, 1994)
Quartz	(Glinnemann et al., 1992)

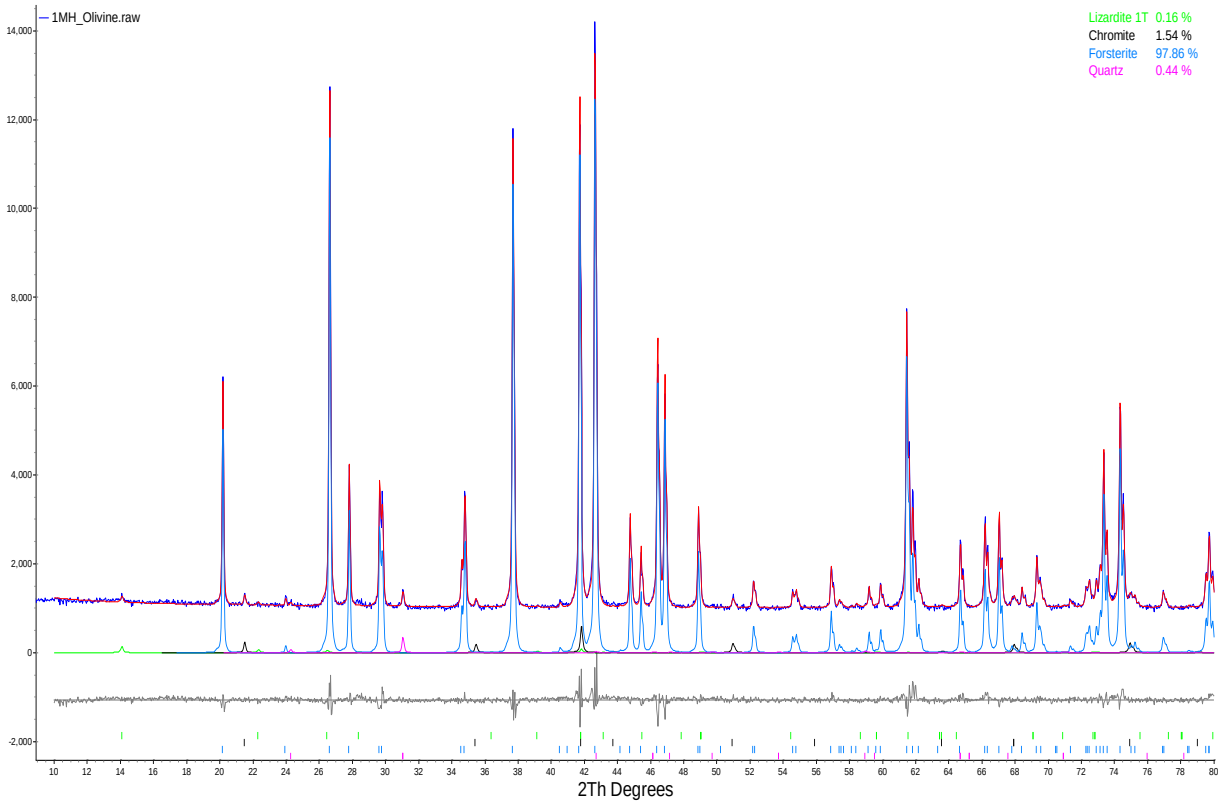

Figure 3.4 Rietveld analysis for X-ray powder diffraction of pristine olivine. The measured data (dark blue continuous solid line), simulated patterns (red continuous solid line is), and the difference between them (continuous gray line under diffraction pattern). The weight percentage of each mineral phase was shown on the top right.

In the Rietveld method, integral breadth β obtained from the Pseudo-Voigt function is used to present the broadened sample. Cauchy components of β (β_C) and Gaussian components of β (β_G) can be expressed by Equations 3.11 and 3.12:

$$\beta_C = \beta_{SC} + \beta_{DC} \tag{3.11}$$

$$\beta_G^{\,2} = \beta_{SG}^{\,2} + \beta_{DG}^{\,2} \tag{3.12}$$

Where β_{SC} and β_{SG} are Cauchy and Gaussian components of size-integral breadth, respectively, and β_{DC} and β_{DG} are the corresponding strain-integral breadth. Once the total-size-integral breadth(β_S) and total-strain-integral breadth (β_D) are resolved, the volume-weighted crystallite size (D_V) and maximum lattice strain (ε) can be calculated by Equation 3.13 and 3.14 (Balzar et al., 2004: pg. 917):

$$D_V = \lambda / \beta_S \cos\theta \tag{3.13}$$

$$\varepsilon = \beta_D / 4\tan\theta \tag{3.14}$$

All calculated data are the average value from 3 tests with standard deviation.

3.4 Results and discussion

3.4.1 Particle size and surface area

Table 3.2 lists the changes in characterized particle size (d_{10}, d_{50}, d_{90}), granulometric surface area (S_G), BET surface area (S_{BET}) and BET size (d_{BET}) with mechanical activation time (t_M) and specific milling energy input (W_N). d_{BET} is the equivalent diameter of particle with spherical shape, which is calculated according to Equation 3.15.

$$d_{BET} = \frac{6}{\rho' S_{BET}} \tag{3.15}$$

Where, ρ' is the density of material (g/cm^3).

Table 3.2 The characterization of particle size and surface area

Grinding variables		Laser diffraction method				BET method	
t_M (min)	W_N (kJ/g)	d_{10} (μm)	d_{50} (μm)	d_{90} (μm)	S_G (m^2/g)	S_{BET} (m^2/g)	d_{BET} (μm)
0	0	3.4±0.1	44.5±0.6	110.3±1.6	0.04	0.8±0.1	2.3
30	9	1.1±0.0	8.4±0.1	36.8±3.1	0.21	2.70±0.5	0.67
60	18	0.8±0.1	5.3±0.0	41.1±0.0	0.27	3.94±1.1	0.46
120	36	0.7±0.0	6.7±0.6	94.4±3.8	0.16	4.38±0.7	0.42

As seen in Table 3.2, there are two stages of particle size change in the process. At the early stage of grinding, d_{50} sharply decreased from 44.5 μm to 10 μm within 30 min's milling and reached ultrafine grinding range. Afterwards, d_{50} decreased slowly or slightly increased with progress in milling. The results indicate that the breakage rate is great initially and continuously decreases as W_N increases. The changes in d_{50} are in agreement with previous observation (Atashin et al., 2015), where the minimum particle size of olivine is found at $W_N \approx 13.8$ kJ/g.

During the whole process, the S_{BET} of olivine keeps increasing from 0.8 m^2/g (unground sample) to 4.38 m^2/g after 120 min's milling, though the increasing rate becomes slow as the milling time goes up. This does not align with Atashin et al. (2015: pg. 557), who found that after 13.8 kJ/g milling energy input, the S_{BET} decreased. The variation in milling instrument is the main cause for the difference. That vibration motion can produce larger S_{BET} than planetary and tumbling motion was also found in Pourghahramani (2007).

Table 3.2 also shows that S_{BET} is 12.8-27.4 times larger than S_G. The S_G increased initially and then decrease slightly with t_M increase, which differs from the changing trend of S_{BET}. The dramatic variation in S_G and S_{BET} is the typical phenomenon of particle agglomeration. The

agglomeration of olivine particles during extended dry grinding was addressed in two recent studies (Atashin et al., 2015; Haug, 2010).

When t_M increases, the changes in d_{90} are similar to that in d_{50}. The two values illustrate the extent of particle aggregation, but do not represent the actual size of particles after mechanical activation as it relates to the rate of downstream reaction. However, d_{10} was found to continuously decrease as t_M increases, which is the same change as in d_{BET}. d_{10} would be a better value than d_{50} and d_{90} to present the particle size of a mechanically activated sample. A similar conclusion is addressed by Haug (2010). For a given t_M, the d_{BET} is smaller than d_{10}, which indicates the presence of pore agglomerates in primary and mechanically-activated olivine.

3.4.2 X-ray diffraction analysis

Fig. 3.5 shows the X-ray diffraction pattern of starting and ground olivine. No significant phase transfer was found during milling. With an increasing t_M, a continuous broadening of the diffraction peaks and decreasing in intensity were observed. The changes indicate that the structure of olivine was disordered due to mechanical activation. In order to quantitatively present the changes in peak profile, the geometry of (020) diffraction peak during grinding were listed in Table 3.3.

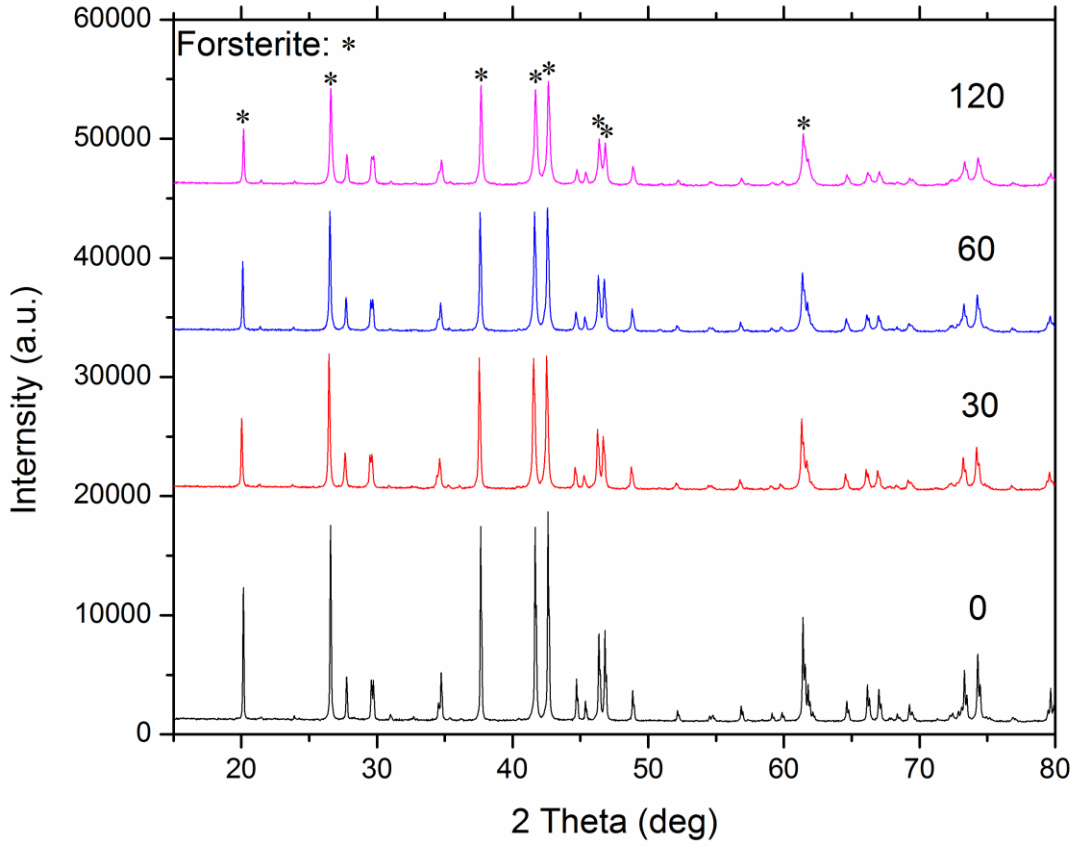

Figure 3.5 XRD patterns of the pristine and mechanically-activated olivine for various milling time. (*) lables the eight most intensive peaks of forsterite which were chosen for Scherrer method, Willamson-Hall method and MWP analysis

Table 3.3 The key components of forsterite (020) diffraction peak

t_M (min)	2θ	I_{max}/I_B	FWHM	β
0	20.134	6.71	0.076	0.063
30	20.011	3.19	0.102	0.084
60	20.086	3.38	0.091	0.090
120	20.150	2.65	0.101	0.112

Note: I_B is the intensity of background, $\beta = A_{XRD}/I_{max}$, where A_{XRD} is the area of selected XRD peak.

According to the geometry of (020) diffraction peak, the amorphization degree (A) is calculated by Equation 3.16 (Ohlberg and Strickler, 1962: pg. 170).

$$A = 1 - \frac{B_0 I_X}{B_X I_0} \times 100\% \tag{3.16}$$

Where I_0 is the integral intensity of a diffraction peak for a non-activated mineral, B_0 is the background of the diffraction peak for a non-activated mineral, and I_X and B_X are the same values for the mechanically activated mineral. The equation is under the assumption that the non-activated mineral is of 100% crystallinity.

Fig. 3.6 shows that the A of olivine increases with t_M and reaches 40% with 120 min's grinding. Rapid loss of the long-range ordering in olivine was found at the early stage of milling and the speed of loss become steadily afterwards. The results agree with the mechanical activation of hematite (Pourghahramani, 2007) and gibbsite (Alex et al., 2014).

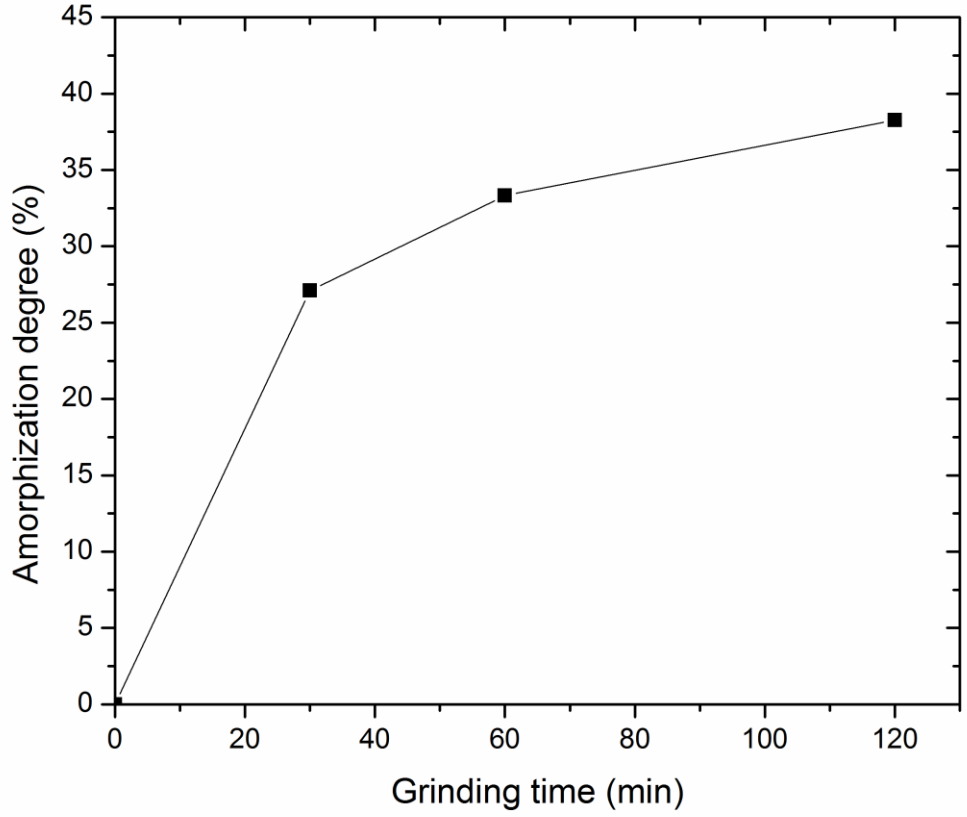

Figure 3.6 The relationship between amorphization degree of olivine and grinding time

3.4.3 Microstructure characterization

3.4.3.1 Williamson-Hall plot

Fig. 3.7 shows the Williamson-Hall curves of the pristine and mechanically-activated olivine. According to Equation 3.5, the Williamson-Hall curves were obtained by the linear regression method using 8 of the most intensive diffraction peaks. The values of residual squared for the four Williamson-Hall curves are between 46.4% and 60.0%. In the Williamson-Hall plots, none of the regression line points are found on the straight line. This indicates the slight deviations

in crystallite size in various directions due to the orthorhombic crystal structure of forsterite. The obtained results are in line with those found by Couvy et al. (2004: pg. 884). The values of B^2 are non-monotonous, which indicates the existence of strong strain anisotropy. The increase in the value of the intercept and slope of the Williamson-Hall curves with $t_{M,}$ indicates that mechanical activation decreases D_V and increases ε, respectively. The values of D_V and ε that calculated from the regression shown in Fig. 3.7 were presented in Table 3.6.

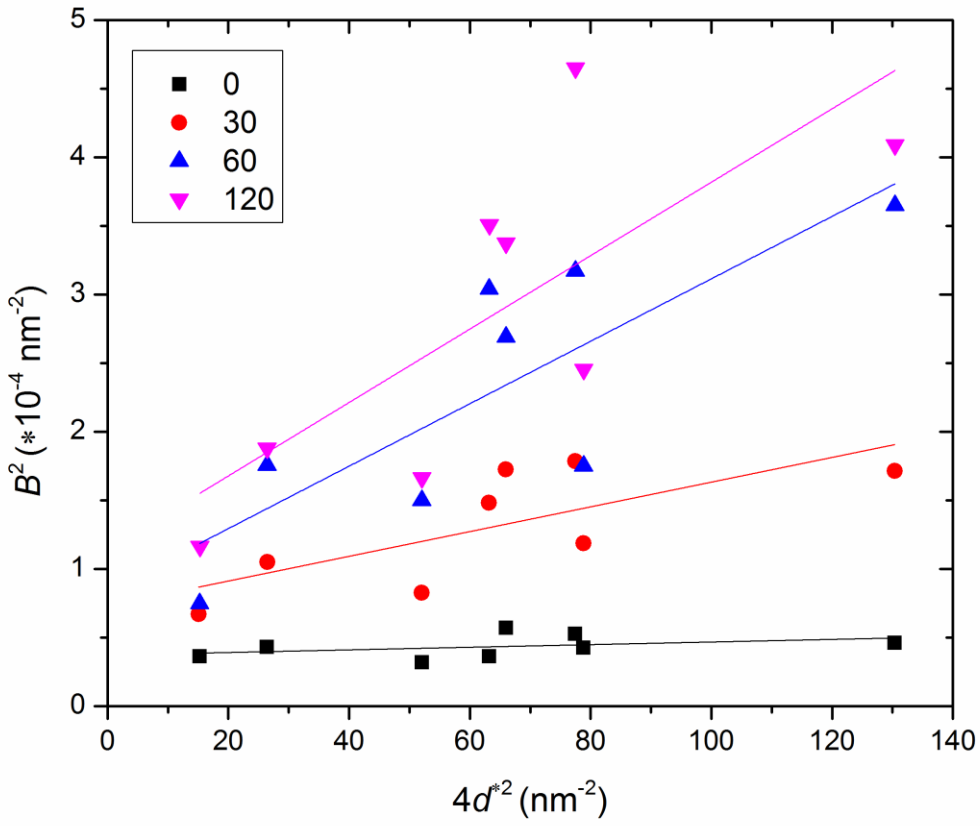

Figure 3.7 Williamson-Hall plots of pristine and mechanically-activated olivine samples.

3.4.3.2 Crystallite size distribution and strain structure

To obtain more details about the crystallite size distribution and microstrain structure, the MWP method, using Fourier transforms, was applied to analyze the XRD pattern of pristine and mechanically-activated olivine. Table 3.4 lists the median (m) and the variation（σ）of the crystallite size distribution function, the average dislocation density (ρ) and the arrangement of dislocation (M^*). As the mechanical activation time increases, m decreases, ρ and M^* continuously increase, and σ is nearly unchanged. ρ increased from 0.6×10^{12} m^{-2} before mechanical activation up to 1.2×10^{13} m^{-2} after 120 min's mechanical activation. The value after mechanical activation is comparable to olivine after pressing at 5 GPa, 1100°C for 8 hours, and deformed at 11 GPa and 1400°C Couvy et al. (2004: pg. 884). The obtained results indicate that intensive grinding can activate the olivine to a level that can be reached using extremely high temperature and pressure. All the values of M^* are smaller than 1, meaning the strain fields of mechanically-activated olivine have narrow dislocation dipoles and a strong screening among them.

Table 3.4 Selected key parameters obtained by MWP method fitted using the Fourier transforms.

t_M (min)	m (nm)	σ	ρ ($\times10^{12}$ m^{-2})	M^*
0	134.50	0.33	0.60	0.023
30	102.81	0.37	4.07	0.099
60	91.78	0.40	5.84	0.128
120	90.67	0.35	12.00	0.115

3.4.3.3 Lattice parameters

The changes in the lattice parameters were evaluated using the Rietveld refinement method. Table 3.5 shows that the forsterite in the pristine olivine yields the value of lattice parameters (a=0.47609 nm, b=1.02199 nm, c=0.59911 nm and V=0.291503 nm), which were slight variations from the values provided in the mineralogy database (a=0.47700 nm, b=1.021200 nm, c=0.59840 nm and V=0.290690 nm). The length of a, b, c, and the value of V decrease initially (30 min), and then increase at longer t_M. The obtained results are not in line with the results for mechanical activation of hematite in a vibratory mill (Pourghahramani, 2007), where an expansion of lattice volume of hematite was found after extensive milling. It reveals that the changes in the lattice parameters not only depend on the types of mineral crystals.

Table 3.5 The changes in lattice parameter of forsterite with different mechanical activation time

t_M (min)	a (nm)	b (nm)	c (nm)	V (nm^3)
0	1.02199	0.59911	0.47609	0.29150
30	1.02183	0.59902	0.47599	0.29135
60	1.02186	0.59903	0.47602	0.29139
120	1.02210	0.59912	0.47612	0.29156

3.4.3.4 Crystallite size and strain

In order to determine a better model for solving crystallite size and strain for mechanically-activated olivine, we compared the average value obtained from the Scherrer equation, Williamson-Hall method, MWP method using the eight most intensive reflections, and Rietveld method by taking all diffractions into account. Table 3.6 lists the calculated results of crystallite size and strain by these various methods. All methods gave the same trend of changes in microstructure, which was a decrease in crystallite size and an increase in strain as the t_M grows. The obtained results are in agreement with previous investigations (Atashin et al., 2015). Based

on the result of this study, the calculated strain follows the order, from large to small, of the Scherrer method, Williamson-Hall method, Rietveld method, and MWP method. The calculated crystallite size using the Williamson-Hall method is similar to that for the MWP method, which are larger than the results obtained from the Rietveld method and Scherrer method.

The variation in the quantitative results of crystallite size and strain is mainly due to the differences in the underlying assumptions of the individual methods. The Scherrer method assumes that line broadening is due to only size effect or only strain effect, which is not the case of mechanically-activated samples. The other three methods separate the broadening into the two components of crystallite size and strain, but differently. The Williamson-Hall method plot and Rietveld method express the maximum lattice strain. The results show that the Willamson-Hall method dedicated less broaden portion to crystallite size than strain, compared to the Rietveld method. The MWP method calculates the root mean square strain (RMSS), assuming the limited random distribution of limitless long parallel screw dislocations. Due to the difference definition of parameter, the maximum strain and RMSS are not comparable. Balzar (1999) found that the ratio of maximum strain to the RMSS can be in the range of 0.5 to 5. The maximum strain calculated using the Rietveld method and RMSS calculated by the MWP method is in agreement with Balzar (1999). Since the olivine dislocation (relates to the RMSS) calculated by the MWP method has been proved to be accurate by TEM technology (Couvy et al., 2004), the Rietveld method can be claimed to be the best way to calculate the maximum strain.

As observed in the Williamson-Hall plot, the crystallite size in various reflection directions shows slight difference because of the anisotropy in the XRD. The selection of diffraction peaks for the analysis will accordingly affect the analytical results. The results displayed in Table 3.6 indicate that the microstructure analysis based on the eight most intensive diffraction peaks may

result in a larger crystallite size than in the Rietveld method, which averages the value of all diffractions in the whole profile. The Rietveld method takes into consideration the correction of perfect orientation, which is not possible in other methods. The crystallite size calculated by the Rietveld method is therefore more accurate than the other methods considered here.

Table 3.6 Comparision of the crystallite size and strain obtained from different calculation method

	Scherrer method		Willamson-Hall method		Rietveld method		MWP	
t_M (min)	D_V (nm)	ε ($\times 10^{-3}$)	D_V (nm)	ε ($\times 10^{-3}$)	D_V (nm)	ε ($\times 10^{-3}$)	D_V (nm)	$<\varepsilon_L^2>^{1/2}$ ($\times 10^{-3}$)
0	137.05	0.84	163.96	0.31	133.91	0.28	148.62	0.08
30	77.42	1.47	116.96	0.95	84.95	0.45	123.49	0.14
60	63.98	1.95	109.24	1.51	71.27	0.53	119.13	0.15
120	56.82	2.15	93.66	1.64	51.77	0.73	104.89	0.28

Except for accurate analysis of the crystallite size and strain values, the Rietveld method can accurately split the overlap peaks from material containing various minerals, especially when each mineral contains several diffraction peaks, such as olivine containing mine waste. The only drawback is that due to its limited capability for analysis, the Rietveld method cannot provide the information of crystallite size distribution and strain structure. However, the Fourier transform method could combine with the Rietveld method to overcome these disadvantages.

3.5 Conclusion

This study analyzes the changes in olivine due to mechanical activation with special focus on the characterization of microstructure. Microstructure parameters were obtained from several commonly used models based on the XRD pattern. The following findings were observed:

(1) The surface area and the degree of amorphization for particles increases as the specific milling energy input increases, with rapid change evident in the early stages of milling.

(2) With deep mechanical activation, the crystallite size continuously decreases, strain increases, and lattices are initially compressed, then expanded.

(3) The dislocation density of olivine obtained by mechanical activation is comparable to the sample treated at extremely high temperature and pressure.

(4) The strain value calculated by the models, from large to small, follow the order of the Scherrer method, Williamson-Hall method, Rietveld method, and MWP method.

(5) The Rietveld refinement method for characterizing the microstructure of olivine is in good agreement with the MWP approach, and is the most promising method for characterizing the microstructure of olivine containing mine waste materials.

Chapter 4: Ultra-fine grinding and mechanical activation of mine waste rock using a high-speed stirred mill for mineral carbonation [3]

4.1 Introduction

Carbon capture and sequestration (CCS) is widely recognized as the quickest and most efficient way to solve the problem of climate change caused by CO_2 emissions (IPCC, 2013). CO_2 sequestration by mineral carbonation is the only known process that can permanently store anthropogenic CO_2 (Power et al., 2013b). Mineral carbonation mimics the natural weathering of Ca/Mg silicates and involves three steps: CO_2 dissolution into rainwater, dissolution of Ca/Mg silicates, and precipitation of Ca/Mg carbonates and silica. Olivine and serpentine are the most abundant minerals suitable for mineral carbonation. The mineral carbonation reaction on both minerals is simply described in reactions 4.1 and 4.2. These thermodynamically favorable processes are extremely slow, naturally occurring over millennia.

$$Mg_2SiO_4 + 2CO_2 \rightarrow 2MgCO_3 + SiO_2 \quad (4.1)$$

$$Mg_3Si_2O_5(OH)_4 + 3CO_2 \rightarrow 3MgCO_3 + 2SiO_2 + 2H_2O \quad (4.2)$$

CO_2 sequestration by mineral carbonation was first proposed in 1990; since then, the researchers have sought ways to accelerate the process with less energy consumption (Power et al., 2013b). Despite these efforts, the process has yet to be economically developed. The use of inexpensive feedstock, the development of a less energy-intensive pre-activation method, and the

[3] A version of this chapter has been published. Li, J and Hitch, M., 2015. Ultra-fine grinding and mechanical activation of mine waste using high speed stirred mill for mineral carbonation. International Journal of Minerals, Metallurgy, and Material. 22(10): 1005-1016.

elimination of the use of chemicals could reduce the costs of mineral carbonation (Bobicki et al., 2015).

Mine waste rocks (especially tailings) from ultramafic-hosted ore deposits, including nickel, copper, chromium, and platinum-group element deposits, are favored mineral carbonation processes (Hitch et al., 2010). Ultramafic-hosted mines could benefit from the mineral carbonation of their waste material, with the final products adding value through secondary revenue (Hitch and Dipple, 2012). The economical mineral-free tailings are fine-sized grains that are rich in magnesium silicates. Using mine waste rock as a potential substrate for mineral carbonation reduces the need for a primary energy-consumptive grinding stage (Wilson, 2009). As the base metal resources become increasingly fine-grained, beneficiation and refractory processes are needed to grind them to increasingly finer sizes, even to the ultra-fine range (90 wt.% particles below 10 μm) (He et al., 2004, pg. 95). In this case, the operational energy consumption of mechanical activation as a pre-treatment method for mineral carbonation could be reduced to a more practical level when mechanical activation is integrated as a part of the total milling process (Haug, 2010).

Mechanical activation uses mechanical energy to change the physical, chemical, and structural behaviors of materials, thereby enhancing the downstream reactions (Baláž, 2008). Compared with the conventional comminution, the effects of mechanical activation are not limited to a decrease in the particles size and an increase in the surface area. Mechanical activation also stores excess energy as long-lived defects through the introduction of imperfections into the crystal lattice, which is essential for the materials to overcome the activation energy in downstream reactions (Pourghahramani, 2007). The necessary level of mechanical activation can be achieved

by prolonged grinding in a high-intensity mill, such as a planetary mill, attrition mill, or vibratory mill (Baláž, 2008).

Mechanical activation has the ecologically clean attributes (i.e., no chemicals added) and offers a high activation extent that is similar to that of calcination, which makes this process preferable to thermal and chemical activation (Power et al., 2013b). The mechanical activation of olivine (Baláž et al., 2008; Haug, 2010; O'Connor et al., 2005; Sandvik et al., 2011; Summers et al., 2005) and serpentine (Bobicki et al., 2015; Drief and Nieto, 1999; Kim et al., 2008) has been studied in detail. These studies have all demonstrated an acceleration of the carbonation process or other downstream acid leaching processes. Because of the difference in physical features, chemical composition, and crystal structure of olivine and serpentine, the mechanisms for mechanical activation on each mineral also differ. For example, the serpentine easily becomes amorphous through dry grinding. This transformation has been observed through the partial disappearance of X-ray diffraction (XRD) peaks of serpentine after a 120-min dry grinding, whereas the XRD peaks of forsterite remain even after 240 min of grinding (Kim et al., 2008: pg. 26). Mine waste rocks are always mixtures containing both primary ultramafic minerals (olivine) and weathered minerals (serpentine). Because both minerals are favorable for mineral carbonation, studying the mechanical activation of such mixtures is important for saving energy during the separation process.

Previous studies have primarily focused on the individual minerals, and the interactions between both minerals during mechanical activation and downstream carbonation have yet to be investigated. Thus far, batch-mode grinding has been adopted in most cases of mechanical activation. Continuous grinding has the potential to enhance the energy efficiency and enlarge the

production quantity (Sandvik et al., 2011), which could push the mechanical activation into widespread application.

In this study, the changes in slurry rheological properties, particle size, surface area, and crystallinity of mine waste rock and pure olivine were investigated during fine grinding and mechanical treatment under wet conditions. An IsaMill operated in continues mode was chosen for the purpose of mechanical activation because this type of stirred-ball mill has been successfully used for ultrafine grinding. Because of its quick response to CO_2 sequestration, a direct aqueous mineral carbonation process was used to test the extent of mechanical activation. The aim was to study the interaction between serpentine and olivine during the process of mechanical activation under wet conditions for mineral carbonation.

4.2 Materials and experiments

4.2.1 Materials

The mine waste rock or whole ore (TAW) used in this study was provided by Hard Creek Nickel from a 06-110 drill core from their Turnagain deposit in northern British Columbia, Canada. The olivine foundry sand (NWO) was provided by OCL Industrial Materials, Ltd., and originated from Norway. The elemental composition of the as-received materials is given in Table 4.1. X-ray powder diffraction analysis indicated the mineral proportions of TAW were 64.7% forsterite, 29.6% lizardite, 4.2% magnetite, 0.3% quartz, and 2.5% brucite. NWO was determined to contain 95.7% forsterite, 1.3% enstatite, 0.5% lizardite, 0.3% talc, 1.5% magnetite, 0.3% quartz, and 0.4% brucite. Forsterite is the magnesium end member of the olivine group, and lizardite is a polymorph of the serpentine-group of minerals. NWO is similar to the mineral used in various mechanical activation works in Norway (Baláž et al., 2008; Haug, 2010). Both the received materials were ground by a laboratory bond ball mill and screened using 140 mesh Tyler sieve

(106 μm). The undersized materials were used as the feed for the IsaMill. Because of the low grade of nickel in the Turnagain project, the composition of mine waste rock and whole ore should be similar, allowing TAW to be considered as mine waste rock.

Table 4.1 X-ray fluorescence analysis results for NWO and mine TAW

Component	NWO (wt%)	TAW (wt%)	Component	NWO (ppm)	TAW (ppm)
SiO_2	40.7	38.7	Cu	12	3
Al_2O_3	0.15	0.15	Zn	18	43
Fe_2O_3	8.39	10.39	Ni	2986	2263
CaO	0.09	0.3	Co	120	124
MgO	50.94	45.51	Mn	852	1267
MnO	0.12	0.16	Sr	n/d	2
TiO_2	0.02	0.03	V	n/d	25
Cr_2O_3	0.677	0.671	La	n/d	2
LOI	n/d	4.09	Sn	n/d	2
TOT/C	n/d	0.05	Nb	n/d	n/d
TOT/S	0.06	0.03	Sc	2	5

Note: n/d stands for the value below the detection limit, LOI the loss on ignition which presents the volatile content such as water, TOT/C the total carbon tested using Leco method, and TOT/S the total S tested using Leco method.

4.2.2 Grinding tests

The laboratory grinding tests were conducted using a 4-L IsaMill (Netzsch, Germany). The IsaMill is a horizontal stirred ball mill with an effective volume of 2.48 L. The agitator shaft for the mill has seven polyurethylene discs, each with a diameter of 0.106 m. 80% of the mill chamber volume is filled with Keramax MT1 ceramic beads with a diameter of 2 mm. Pulp, with a solids content of 30% by weight, was prepared by mixing 5 kg of samples and 11.7 kg of water. For each test, the slurry was fed into the mill, ground, collected, sampled, and then re-fed into the mill. This cycle was repeated up to nine times, during which the chamber temperature reached 40°C. The flow rate was controlled at 2–3 L/min. The agitator speed was maintained at 1500 r/min for the

tests. The applied parameters and procedures were the general ones provided by Xstrata for the development of the signature plot, which was used to design a full-scale IsaMill (Glencore Technology, 2016). The sampled slurry from each cycle was dried in an oven at 100°C overnight and subsequently deagglomerated. Samples from the feed, pass 1, pass 4, and pass 9 were selected for the carbonation and characterization tests.

4.2.3 Carbonation tests

For the carbonation tests, 7.5 g of dried samples were mixed with 50 mL of background solutions containing 1 mol/L NaCl and 0.64 mol/L $NaHCO_3$; the resulting mixtures were transferred to a 100 mL autoclave (Parr Instruments, Moline, IL, USA). The background solution helped to achieve the optimum extent of carbonation by increasing the concentration of HCO_3^- in the aqueous solution and maintaining a constant pH value between 7 and 8 (O'Connor et al., 2005: pg. 11). The slurry samples were carbonated at 185°C and 6 MPa CO_2, with a stirring speed of 1500 r/min over a period of 1 h. The carbonation conditions were chosen according to the optimum conditions for the direct aqueous mineral carbonation of olivine (O'Connor et al., 2005: pg. 14), the only difference being that the CO_2 pressure in this work was approximately two-fifths of the optimum pressure (15 MPa) because of the limitations of the experimental setup. Also, it was expected that the mechanical activation could enable the use of milder carbonation conditions, resulting in lower carbonation costs.

4.2.4 Materials characterization

The elemental compositions of the as-received materials were analyzed by Acme Analytical Laboratories, Ltd. (Vancouver) using X-ray fluorescence (XRF) spectroscopy and inductively coupled plasma mass spectrometry (ICP-MS) techniques. The rheological properties of settling suspensions were measured using an elongated concentric cylinder fixture developed by Klein et

al.(1995). The particle size distribution (PSD) was measured with a laser diffraction particle size analyzer (Mastersizer 2000, Malvern, U.K.). The specific surface areas and porosities were measured by a nitrogen gas adsorption/desorption instrument (Autosorb-1MP, Quantachrome) at −198°C. The particle shape and morphology were observed using a Helios NanoLab 650 focused ion beam scanning electron microscope (FEI, Eindhoven, The Netherlands) equipped with a secondary electron detector; the microscope was operated at 50 pA and 1 kV. X-ray diffraction data for microstructure analysis and quantitative analysis were collected using a Bruker D8 Focus Bragg–Brentano diffractometer (Bruker AXS GmbH, Germany) equipped with a Co Kα radiation source; the samples were scanned at a step size of 0.03° over the 2θ range from 3° to 80°. X-ray powder diffraction (XRPD) data were refined with the Rietveld program Topas 4.2 to determine the amounts of carbon minerals present before and after mineral carbonation.

All calculated data are the average value from 3 tests with standard deviation.

4.3 Results and discussion

The energy consumption, throughput, and size reduction for fine and ultra-fine grinding processes are complicated, involving a large number of process parameters. As one example, 44 such parameters have been identified for a stirred ball mill (Jankovic, 2003: pg. 338). The most important of these parameters are the process state and mill configuration variables. Process state variables include PSD, shape of feed, solid density, slurry density, slurry flow rate, and slurry rheology. Mill configuration variables include impellor design, mill speed, media size, media load, and media density (Jankovic, 2003). Coarse grinding is rather well understood, and using an energy based approach, one can satisfactorily describe the correlation between the average particle size and intensity or duration of milling. For example, Rittinger's Law describes the energy cost as being proportional to the new surface area produced in size reduction. This is reasonably accurate

in the fine grinding range (10-1000μm). Kick's Law assumes the required work to be proportional to particle volume reduction. This applies fairly well in the crushing range (> 1 cm). The third law of comminution, Bond's Law states that the work input is proportional to the work presented by the product minus that represented by the feed. This is reasonably accurate in the range of conventional rod-mill and ball-mill grinding (Wills and Napier-Munn, 2006: pg. 110). All these theories of comminution assume that the materials are brittle, and these ideas are too simple to apply to ultra-fine grinding. Analysis of the relationship between energy consumption and ultrafine grinding will aid in the evaluation and optimization of all of the primary operating parameters of a mill in a well-planned and executed laboratory or pilot test.

4.3.1 Energy consumption

The net specific energy consumption (W_N) is usually used to compare the energy efficiency for modifying the properties of materials under various milling conditions (Haug, 2010). In a stirred mill, energy is transmitted from the agitator to the grinding media and the slurry, and is subsequently transferred to the particles through impact, compression, and abrasion loading. W_N represents the energy transferred to the charge and can be calculated through Equations 4.1–4.3. The residence time (t_M) in the IsaMill is calculated according to Equation 4.4.

$$P_N = P_0 - P_{NL} \tag{4.1}$$

$$W_N = \frac{P_N}{M} \tag{4.2}$$

$$M = Q \cdot C_s \cdot \rho_s \tag{4.3}$$

$$t_M = \frac{V_M}{Q} \tag{4.4}$$

Where, P_0 is the operational power (kW), P_{NL} is the average power draw when running the mill empty with no water or media (kW), P_{NL} of the IsaMill used in this study is 0.8 kW in the. P_0 and P_{NL} can be read from the agitator panel, M is the mass of sample milled per hour (t/h), Q is the flow rate of sample feed in the mill chamber (m^3/h), C_s is the solid content by weight (%), ρ_s is the slurry density (t/m^3), t_M is the mechanical activation time and V_M is the net mill volume (2.4 L). Table 4.2 summarizes the power-related parameters of each milling cycle. The flow rate is constant in NWO and in the initial cycles of NWO. After cycle 8, an observed decrease in the flow rate of TAW results in a longer residence time in subsequent cycles.

Table 4.2 Power parameters during grinding of TAW and NWO in an IsaMill

Pass No	TAW					NWO				
	P_0 (kW)	P_N (kW)	W_N (kWh·t^{-1})	Cum. W_N (kWh·t^{-1})	t_M (s)	P_0 (kW)	P_N (kW)	W_N (kWh·t^{-1})	Cum. W_N (kWh·t^{-1})	t_M (s)
1	3.6	2.8	45.4	45.4	50	4.8	4.0	66.9	66.9	52
2	3.5	2.7	45.3	90.7	102	4.8	4.0	66.2	133.1	103
3	3.6	2.8	47.1	137.8	154	4.2	3.4	53.6	186.7	151
4	2.9	2.1	35.0	172.9	205	3.8	3.0	49.6	236.3	202
5	2.8	2.0	32.0	204.9	254	3.6	2.8	44.5	280.8	251
6	2.7	1.9	30.9	235.8	304	3.5	2.7	44.2	325.0	302
7	2.7	1.9	31.1	266.9	354	3.3	2.5	39.7	364.7	350
8	2.5	1.7	35.6	302.5	418	3.3	2.5	41.9	406.6	402
9	2.5	1.7	35.5	338.0	482	3.3	2.5	40.9	447.5	453

Note: Cum. W_N represents to the cumulative net specific energy consumption which can be used as specific energy input at corresponding t_M .

4.3.2 Slurry rheological properties

The rheological data of grinding slurries were modeled using the Bingham flow curve equation (He et al., 2004: pg. 99), as shown in Equation 4.5.

$$\tau = \tau_y + \eta\gamma \tag{4.5}$$

where τ is the shear stress (Pa), τ_y the Bingham yield stress (Pa), η the Bingham viscosity (Pa·s), and γ the shear rate (s^{-1}).

Fig. 4.1 shows the change in yield stress of slurry during IsaMill grinding. With the energy input, the yield stress increases because of the generation of fine particles, which is in agreement with the observed rheological properties of stirred mill slurries (Yue and Klein, 2004). The increase rate of yield stress during grinding of TAW is much higher than that during grinding of NWO. This difference is a consequence of the presence of anisotropic and non-spherical-shaped serpentine minerals in TAW. The serpentine suspension, especially chrysotile with fibrous shape, exhibits the high yield stress and viscosity (Ndlovu et al., 2011). High viscosity and yield stress reduce the grinding efficiency and adversely affect comminution (Yue and Klein, 2004). The increase in the yield stress of slurry can explain the significant decrease in the flow rate of TAW for the eighth cycle.

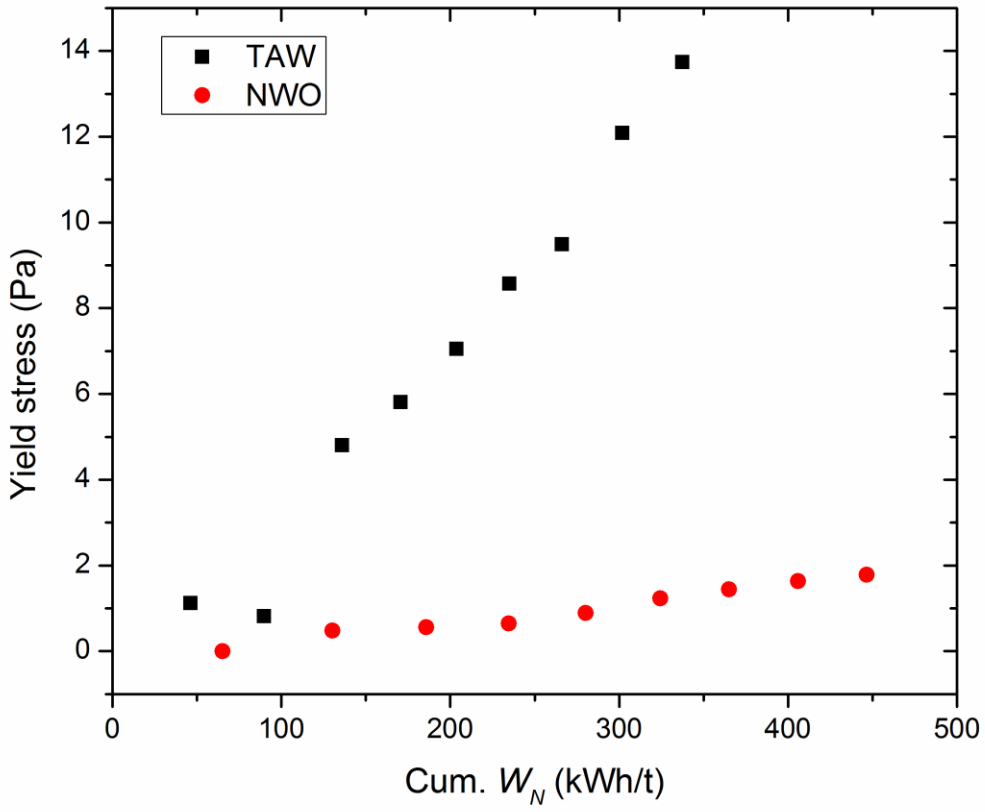

Figure 4.1 Yield stress of slurries with specific energy input.

4.3.3 Mechanical activation effects

Mechanical activation effects are usually observed to occur in response to changes in particle size, surface area, and degree of amorphization. All these attributes of the materials are characterized for the sake of comparison with previously published results. The particle size distribution and the microstructure change were analyzed in detail in Appendix A. Table 4.3 lists the mean particle size (P_{50}), the specific surface area (S_{BET}), the average degree of amorphization

on fosterite (A_{Fo}), and the degree of amorphization on lizardite (100) phase ($A_{Li(100)}$) of the feed materials and the products from passes 1, 4, and 9.

Table 4.3 Physical and structural parameters of the selected samples during milling in an IsaMill.

Pass No.	TAW				NWO			
	P_{50} (μm)	S_{BET} (m^2/g)	$A_{Li(100)}$ (%)	A_{Fo} (%)	P_{50} (μm)	S_{BET} (m^2/g)	$A_{Li(100)}$ (%)	A_{Fo} (%)
Feed	35.4	3.1	0	0	74.1	0.7	0	0
1	7.2	7.2	–35	1.4	10.8	2.1	26.6	20.8
4	2.6	12.6	–32	0	3.4	8.6	25.7	24.0
9	1.6	17.8	–2	8.7	1.9	15.5	50.0	34.5

4.3.3.1 Particle size

The specific milling energy input vs. 80% passing size (P_{80}) is drawn in a log-log plot, which is commonly used for designing a full-scale stirred mill from lab-sized tests (Glencore Technology, 2016). Fig. 4.2 shows the signature plot of an IsaMill for TAW and NWO. The decrease in P_{80} follows an exponential function with the specific energy input for both materials, as shown in Equations 4.6-4.7. The continuous decrease in P_{80} with this specific milling energy input is consistent with the results reported in a previous study of the mechanical activation of olivine under wet conditions (Haug, 2010: pg. 46).

$$\text{NWO: } W_N = 1332(P_{80})^{-0.93} \tag{4.6}$$

$$\text{TAW: } W_N = 1002(P_{80})^{-1.028} \tag{4.7}$$

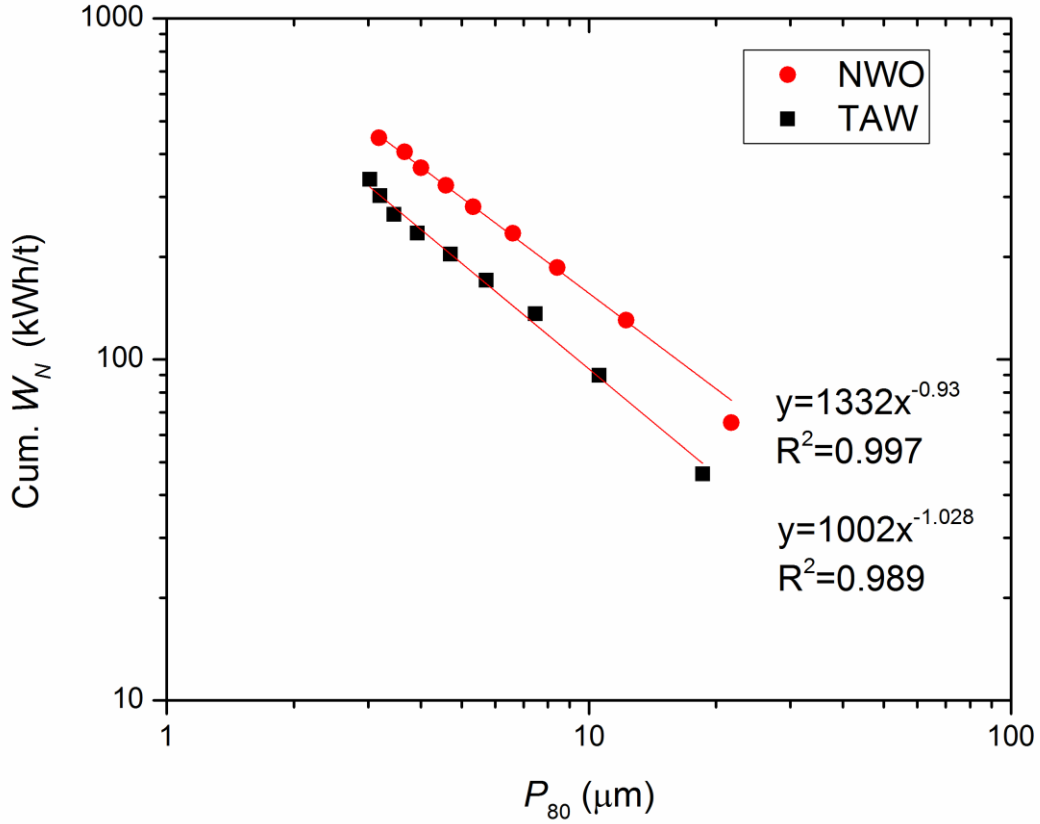

Figure 4.2 Signature plot for the IsaMill.

The particle size of TAW is smaller than that of NWO in all grinding cycles. The mean particle sizes (P_{50}) recorded in Table 4.3 show the same trend. Because the feed particle size of TAW is smaller than that of NWO, merely comparing the actual particle size is insufficient for explaining the changes. Specific breakage energy, which describes the amount of energy required to reduce a particle size by one micron (Roufail, 2011), was used to analyze the mill breakage efficiency. Under the assumption that the P_{80} was reduced from 100 to 2 μm, the average specific

breakage energies calculated from Equations 4.6 and 4.7 were 6.94 and 4.92 kWh/tμm, respectively. These results indicated that TAW was easier to break down to a fine size.

As shown in Fig. 4.2, the actual specific breakage energy is slightly higher than the calculated value in mechanically activated TAW when the particle size is less than 3 μm. However, this is not the case in the mechanically activated NWO, possibly because of the increasing yield stress in the slurry during grinding of TAW, as discussed in section 4.3.2. This phenomenon can also be explained by the material properties related to the grinding limit. The grinding limit is an important parameter in a fine grinding approach, wherein the particle size no longer changes (Roufail, 2011). Deep stages of mechanical activation can be substituted if the grinding limit reaches the brittle-plastic transition (Boldyrev et al., 1996). Soft materials break quicker and reach their grinding limit faster than harder materials (Roufail, 2011). The Mohs hardness of serpentine is 2.5–4 (Barthelmy, 2014) and that of olivine is 6.5–7 (Barthelmy, 2014; Halder and Tisljar, 2013: pg. 59). The high specific breakage energy in TAW indicates that the lizardite may reach its grinding limit at the seventh pass. This observation agrees with the results of breakage mechanism studies on silica and galena mixtures ground in an IsaMill (Roufail, 2011). Because the weight ratio of forsterite and lizardite in the mixture is 2.3:1, the forsterite breakage mechanism effect is dominant in TAW. Forsterite does not appear to reach the grinding limit because the actual and calculated specific breakage energies agree with each other until pass 9 in the case of NWO.

4.3.3.2 Specific surface area and morphology

The results in Table 4.3 show that the specific surface areas increase linearly with increasing energy input during IsaMill grinding. The same trend has been observed in other studies related to mechanical activation by wet grinding in atrritors (Baláž et al., 2008; Haug, 2010). The specific surface area of milled TAW is greater than that of NWO, irrespective of specific energy input, as

shown in Table 4.3. This difference is mainly due to the finer particles in TAW compared to those in NWO.

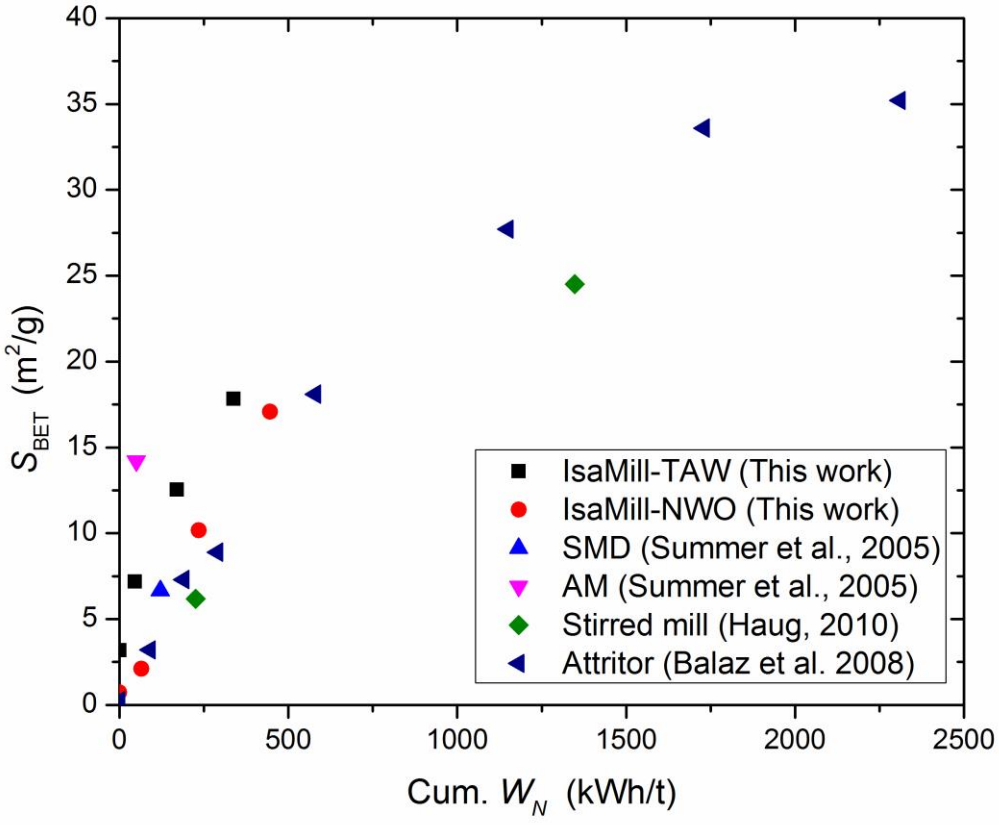

Figure 4.3 Specific surface areas as a function of specific energy input.

Fig. 4.3 shows the results of a comparison of our experimental data with that from the literature. The IsaMill exhibits greater efficiency in generating new surfaces compared to the attritor used by Baláž et al. (2008) and the stirred mill used by Haug (2010); its efficiency is similar to that of the stirred media detraitor (SMD), but less efficient than the attritor mill (AM) used by Summer et al. (2005). Because the energy consumption for AM is calculated using the Society for

Mining, Metallurgy, and Exploration (SME) work index formula (Summers et al., 2005), the results may contain errors. The IsaMill exhibits greater efficiency than the conventional ball mill and other stirred mills with respect to size reduction in the fine range, and is consistent with previously reported results (Jankovic, 2003). An energy input greater than 500 kWh/t is outside the scope of this work because it is only considered energy input levels relevant in industrial applications.

Fig. 4.4 shows the scanning electron microscopy (SEM) micrographs of both products from pass 9, where some sharp particles approximately 1 μm in diameter are still present in both samples. The presence of these particles indicates that forsterite is highly resistant to milling. A similar result has been reported in a study on olivine morphology after wet milling in an attritor (Summers et al., 2005). Both the NWO and TAW samples contain aggregates with nanoparticles. The nanoparticles in NWO are spherically shaped with smooth surfaces, as shown in Fig. 4.4(a), whereas those in TAW are noodle-shaped with rough surfaces in Fig. 4.4(b). The circular particles with a smooth surface (forsterite) indicate that the breakage mechanism is transgranular, whereas that of the counterpart (serpentine) is intergranular. These results agreed with those of Roufail (2011), who observed that hard materials suffered the abrasion breakage across the grains, whereas soft materials endured the fracture breakage mostly along the grain boundaries at high agitating speeds in an IsaMill. The SEM micrograph in Fig. 4.4(a) confirms that the lizardite particles with rough surfaces contribute to the small particle size and large surface area in TAW.

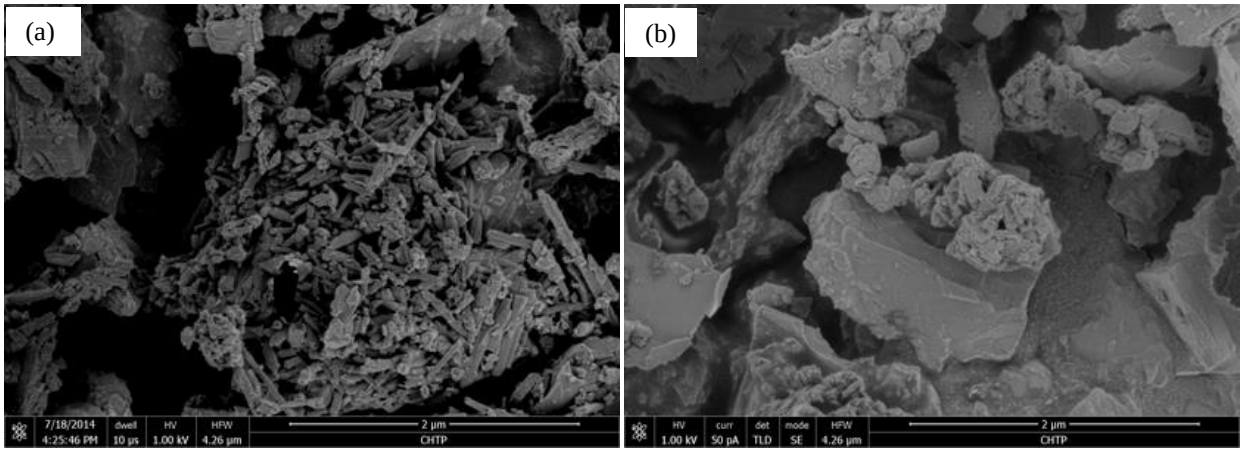

Figure 4.4 SEM micrographs of the products from pass 9: (a) TAW; (b) NWO. Scale bars in are 1 μm.

4.3.3.3 Changes in crystallinity and amorphization degree

XRD patterns are sensitive to the changes in the crystallinity of samples after mechanical activation. Fig. 4.5(b) shows the XRD peaks of forsterite in NWO become less intense and wider and the background level increases with increasing grinding energy input. A similar loss of crystallinity has also been detected in mechanically activated olivine in other stirred mills (Baláž et al., 2008; Haug, 2010). Contrary to expectations, TAW does not follow this pattern. Fig. 4.5(a) shows that the forsterite peaks of TAW are nearly unchanged and the lizardite (001) peak becomes even more intense than that in the feed in the first four cycles. Both minerals exhibit XRD peaks, even after being ground for 9 cycles, which indicates a large amount of crystallized forsterite and lizardite remained in the milled products.

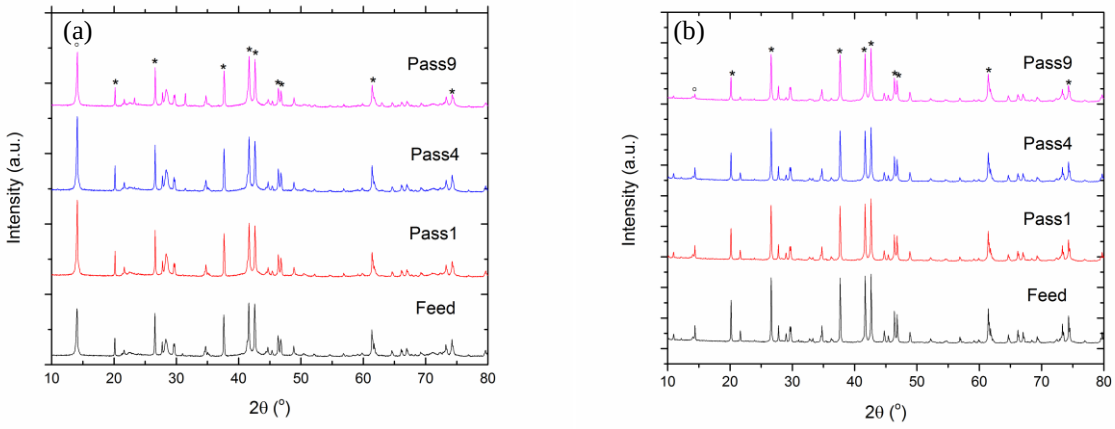

Figure 4.5 XRD patterns of (a) TAW and (b) NWO.

Equations 4.8 and 4.9 are used to calculate the crystallinity (C_{XRD}) and the degree of amorphization (A) of mechanically activated samples according to the XRD diffraction data (Ohlberg and Strickler, 1962: pg. 170). The results are shown in Table 4.3.

$$C_{XRD} = \frac{B_0 I_x}{B_x I_0} \times 100\% \tag{4.8}$$

$$A = 1 - C_{XRD} \tag{4.9}$$

Where I_0 and I_x are the integral intensity of diffraction peak for the non-activated mineral and the mechanically activated mineral, respectively, B_0 and B_x the background of diffraction peak for the non-activated mineral and the mechanically activated mineral, respectively. These equations assume that the non-activated mineral is 100% crystalline. C_{XRD} and A are bulk properties that include the effects of fine particle size, crystallite size, strain, and deformation of the crystal lattice.

Table 4.3 lists the changes in the A values of forsterite (A_{Fo}) and lizardite ($A_{Li(001)}$) with specific energy input. A_{Fo} is the average value calculated on the basis of the (020), (021), (031),

(131), (112), (221), (140), (222), and (260) forsterite diffraction peaks, which correspond to the peak positions (2θ) of approximately 20.1°, 26.6°, 37.7°, 41.7°, 42.6°, 46.4°, 46.9°, 61.5°, and 74.3°, respectively. $A_{Li(001)}$ is obtained from the lizardite (001) phase because mechanical activation is mainly affected along the *c*-axis of the lizardite structural unit (Drief and Nieto, 1999). The value of A_{Fo} initially increases quickly to 20.8% at pass 1 and then increases slowly to 34.5% at pass 9 in the case of mechanically activated NWO. However, the value of A_{Fo} remains nearly unchanged up to pass 4 and increases to 8.7% at pass 9 in the case of mechanically activated TAW. The value of $A_{Li(001)}$ changes similarly to that of A_{Fo} in mechanically activated NWO because only a trace of lizardite (0.5%) is present in this material. In contrast, $A_{Li(001)}$ decreases to −35% in the first cycle in mechanically activated TAW and then increases with increasing specific energy input. The negative values of $A_{Li(001)}$ in the case of TAW indicate that the lizardite that appears in the ground products is more crystalline than that in the feed. Lizardite phase formation can be promoted in two ways: either through the conversion via the chemical reaction of forsterite with water or through the recrystallization from an amorphous phase. The latter approach is more likely in a lab setting because the XRD pattern of pure olivine does not show a distinct increase in the intensity of lizardite diffraction peaks. Lizardite has a planar disorder structure and is considered to be an amorphous phase in XRD analyses (Wilson, 2009). The conversion mechanism between the amorphous phase and the lizardite structure through wet milling is not the focus of this study.

In mineral carbonation, mechanical activation of lizardite in wet milling conditions did not promote the desired reaction and was therefore not recommended (Bobicki et al., 2015). Studies related to the activation of serpentine minerals were focused primarily on the removal of –OH bonds, either through dry milling or through a thermal treatment (Gualtieri et al., 2012). However, the influence of lizardite on the wet milling process should not be neglected. As seen in Table 4.3,

when it is abundant in forsterite, lizardite appears to act as a dispersant to prevent or postpone the disorder in forsterite phases through wet milling.

The authors of several studies have used the diffraction peaks of forsterite (020) to calculate and represent C_{XRD} (Baláž et al., 2008: pg. 3; Haug, 2010: Part II, Paper II, pg. 18). C_{XRD} was calculated in the same manner for purposes of comparison in this study. As shown in Fig. 4.6, the decrease in the value of C_{XRD} in the first cycle of IsaMill grinding is similar to that reported in the literature. Afterwards, the efficiency of C_{XRD} in the IsaMill is considerably less than that reported for other stirred mill tests. This difference may be attributable to the milling mode. The IsaMill is operated in continuous mode, whereas other stirred mill tests for mechanical activation are conducted in batch mode. Continuous-mode grinding can prevent overheating because the material passes through the grinding chamber quickly. At the same time, continuous-mode grinding reduces the chance of accumulating long-lived defects in samples and limits the deep imperfections in the sample.

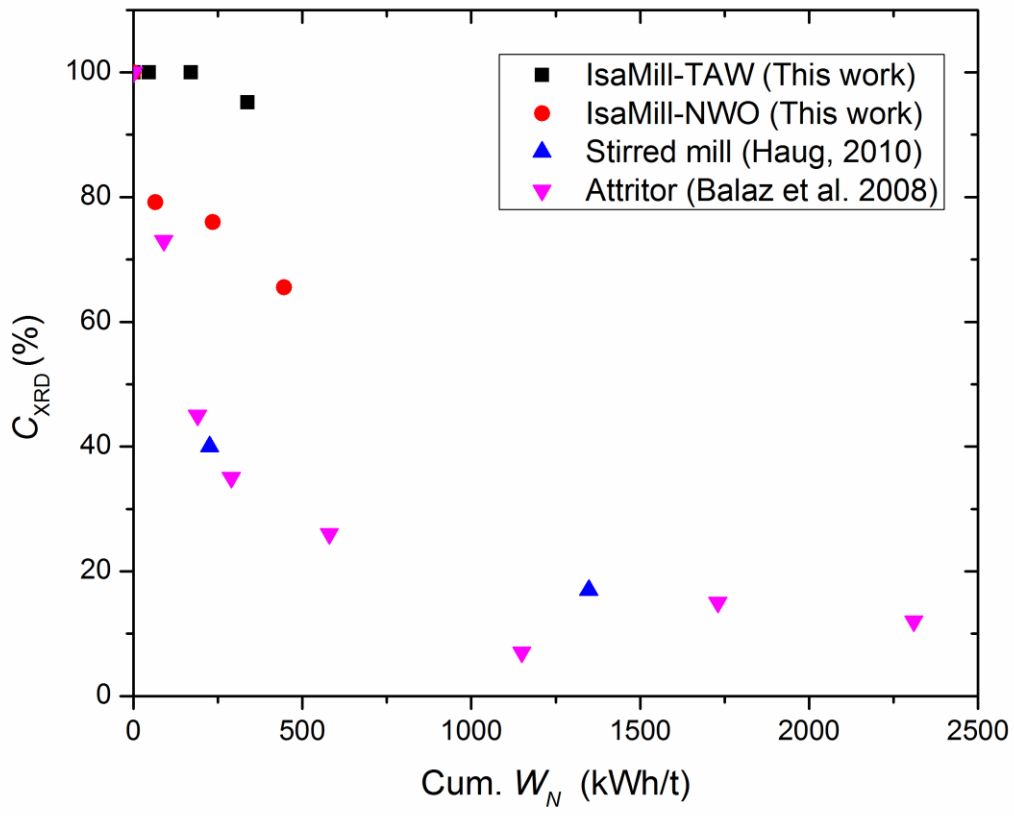

Figure 4.6 Crystallinity as a function of specific energy input.

4.3.4 Effect of milling energy on mineral carbonation

Quantitative analysis of mine waste rock by Rietveld refinement was undertaken by (Wilson et al., 2006) and was adopted in this study to quantify the carbonated products from mine waste materials. In this method, lizardite was considered as an amorphous phase by fitting the structureless pattern to the planar disorder in lizardite. This method may overestimate the lizardite and underestimate other phases because of the surface roughness of all of the minerals. However,

the phases with more than 5% abundance in mine waste rock can be estimated accurately with low absolute errors (Wilson et al., 2006: pg. 1334).

The extent of carbonation is expressed by the CO_2 sequestration reaction efficiency (R_X), which is the percentage stoichiometric conversion of Mg^{2+}, Ca^{2+}, and Fe^{2+} cations in the silicate feed to carbonate (Penner et al., 2004: pg. 2), as shown in Equation 4.10.

$$R_X = \frac{x_{CO_2}}{\varepsilon_A (1 - x_{CO_2})} \tag{4.10}$$

Where x_{CO_2} is the weight percent of CO_2 in the carbonated products, which is calculated by QXRD method, and ε_A is the percent weight added if all available cations are converted into carbonates.

As shown in Fig. 4.7, R_X increases with the mechanical activation energy input. The R_X value of TAW is greater than that of NWO when the energy input is less than 350 kWh/t, indicating that the mechanical activation of mine waste rock that contains serpentine results in better carbonation efficiency than that achieved with pure olivine mineral. Similarly beneficial effects were observed in a study of the in-situ CO_2 mineral sequestration in partially serpentine peridotites (Hövelmann et al., 2011).

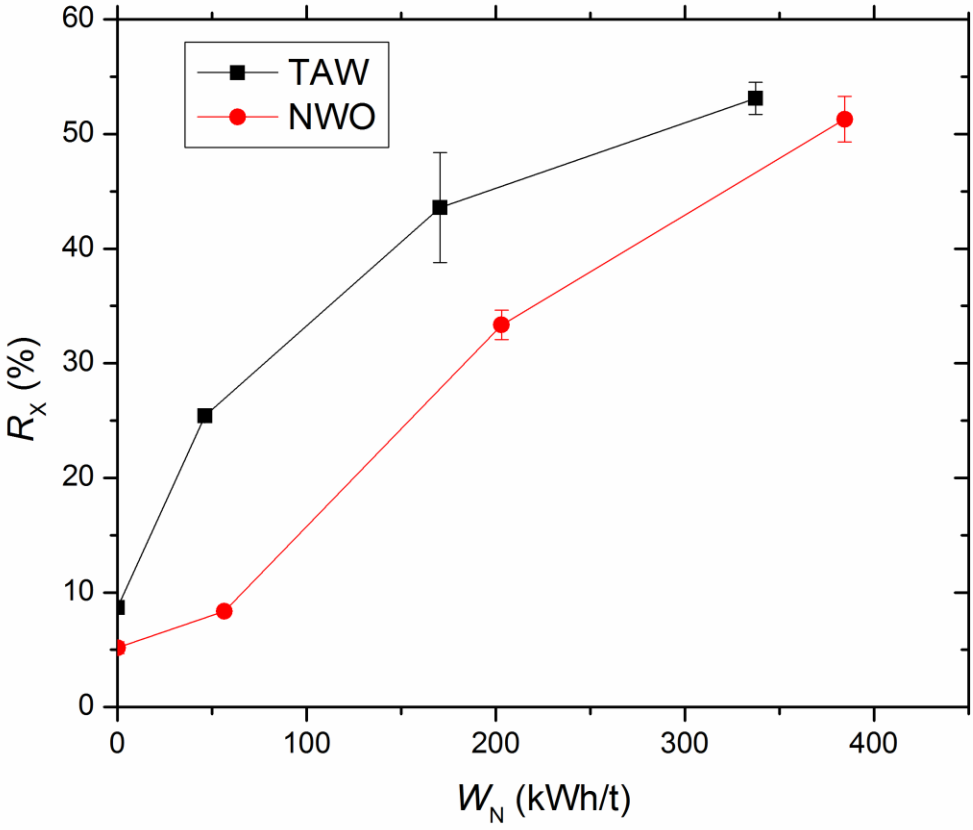

Figure 4.7 Relationship between R_X and cumulative W_N. The experimental condition: 15 wt% solid content in solution containing 1M NaCl, 0.64 M $NaHCO_3$, at 185°C, 6 MPa CO_2 partial pressure, for 1 hour.

Fig. 4.8(a) shows that R_X increase with the increase in BET surface area. The obtained results is in agreement with previous study of mechanical activation for direct aqueous carbonation (Gerdemann et al., 2007). When carbonation potential is plotted with S_{BET} (as show in Fig. 4.8(a)), a linear correlation is observed in mechanical activation up to 9 cycles for NWO, in the initial phase of mechanical activation up to cycle 4 for TAW. Materials after 9 cycles of grinding exhibit a large S_{BET} value; however, the R_X is not as high as expected according to the extrapolation line obtained from previous cycles for TAW. At this time, the rate of carbonation process is controlled

by $MgCO_3$ precipitation instead of by magnesium silicate dissolution. In the case of a precipitation-controlled reaction, further mechanical activation is not necessary. The optimum condition for mechanical activation of TAW would be between cycle 4 and cycle 9.

Fig. 4.8(b) shows that R_X increases with the decreases in crystallinity of forsterite in NWO, while R_X increases even there is no change in crystallinity of forsterite in TAW. The results imply that crystallinity is not the best fit for the observed differences in R_X when TAW is mechanically activated in IsaMill. The observation is in line with mechanical activation of olivine in an attritor (Haug, 2010), the variation in specific area was found to be the most important value for downstream dissolution when the crystallinity is high.

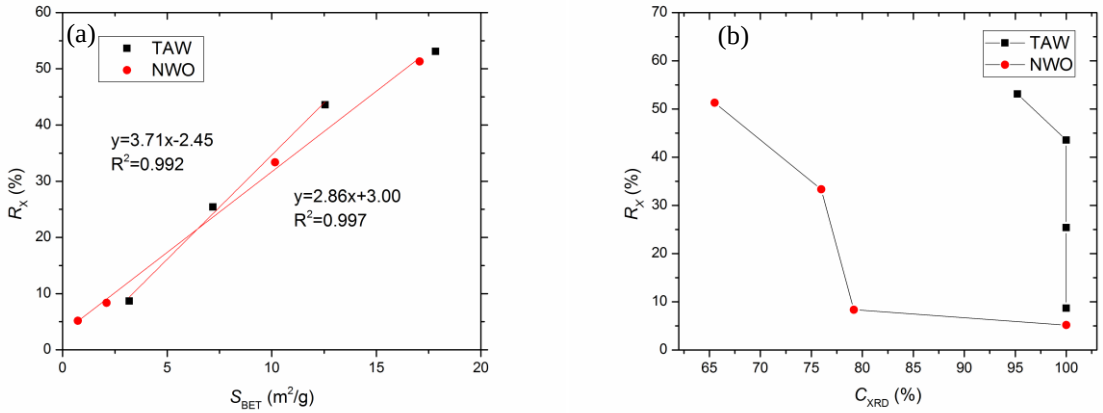

Figure 4.8 Relationship between R_X and (a) S_{BET}, (b) C_{XRD}. The experimental condition: 15 wt% solid content in solution containing 1M NaCl, 0.64 M $NaHCO_3$, at 185°C, 6 MPa CO_2 partial pressure, for 1 hour.

Fig. 4.9 shows the contents of forsterite, lizardite, and magnesite by mass in feed and carbonated products. In the figure, Feed-C1, PASS1-C1, PASS4-C1, PASS9-C1 represent the 1-hour carbonation product of feed, samples from pass 1, 4 and 9, respectively. Magnesite is the result of forsterite being carbonated under laboratory conditions. The content of lizardite remains

the same. These results were in agreement with the results of the studies of direct aqueous mineral carbonation on mechanically activated serpentine ore, where the value of R_X did not exhibit a distinct increase even after being attrited for 1 h (Bobicki et al., 2015). Therefore, a high content of forsterite in the raw material was required for choosing wet mechanical activation as a pretreatment method for mineral carbonation. Actually, under the high-carbonate alkalinity, olivine simultaneously produced magnesite and lizardite (Lafay et al., 2014). The most likely explanation for the higher R_X in mechanically activated TAW was that lizardite impurities acted as the catalyzers in the whole process. Lizardite promoted the surface area exposure for Mg^{2+} depletion in the solution. Simultaneously, lizardite precipitated with magnesite and maintained an equal quantity. Mechanically activated TAW benefited from a large surface area under low specific energy input.

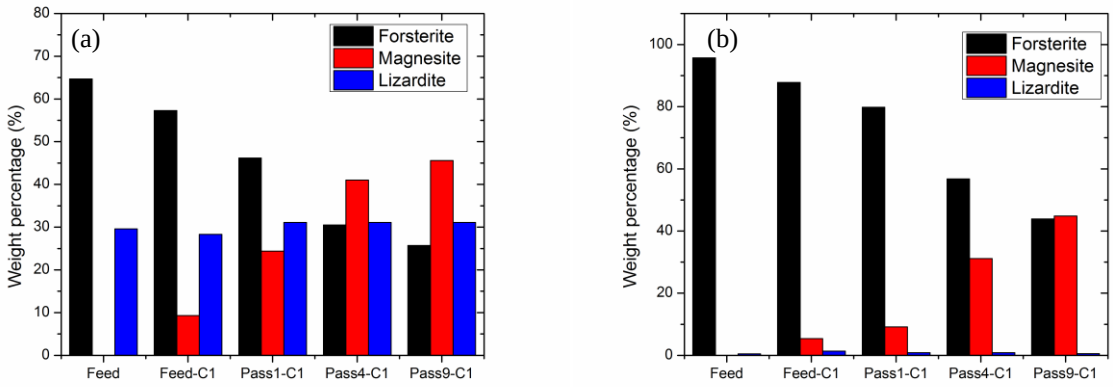

Figure 4.9 Mineralogy changes in (a) 06-11 and (b) NWO after carbonation for 1 h.

The expected R_X per S_{BET} in TAW is lower than that of NWO, due to the different amounts of contained forsterite. However, only initial samples follow this trend (Table 4.8(a)).

After mechanical activation, R_X per S_{BET} in TAW is higher than that in NWO. The lizardite content seems promote TAW to reach to a higher level of activation during intensive wet grinding. S_{BET} is not the only value that influence R_X. Since the crystallinity has an less impact on R_X, other micro-structural values, such as lattice parameters, crystallite size, and micro-strain, may play important roles to control R_X. These values were evaluated in Appendix A.3. The results show that the changes in crystallite size of samples is similar to crystallinity. Only slightly changes are observed in the lattice parameters of forsterite in both samples. However, the volume of fosterite in TAW is higher than that in NWO. The most likely explanation is that serpentinization process enlarges the lattice volume of forsterite, which made TAW (partially-serpentinized olivine) sensitive to wet grinding and resulted in a large value of R_X per S_{BET} in mechanically activated TAW than in mechanically activated NWO.

4.3.5 Comparison of the obtained results with reference data

Table 4.4 lists some reference results related to the direct aqueous carbonation of olivine and serpentine. The extent of carbonation for feed material in this work (R_X = 8.7% for TAW and R_X = 5.2% for NWO) is comparable to that reported in the literature for untreated olivine. The extent of carbonation of mechanically activated material after 8 min (R_X = 53.1% for TAW and R_X = 51.2% for NWO) is comparable to that reported in the literature for olivine (−38 μm) under carbonation at a CO_2 pressure four times greater than that used here. Thus, the extent of mechanical activation and the carbonation conditions can be balanced to achieve an economically optimal process. The carbonation conversion achieved in this work is not as high as that reported by Summer et al. (2005); however, the relative increases in R_X are similar (84.3%/39.6% = 2.13 for

grinding in AM in (Summers et al., 2005: pg. 141), and 53.1%/25.7% = 2.07 in our work). Greater carbonation conversion is achieved in the present investigation than in the investigation by Haug (2010), which demonstrates the importance of the carrier solution for direct aqueous mineral carbonation. Methods to enhance the rate of magnesium carbonate precipitation are essential for the whole process because mechanical activation can only accelerate the process by enhancing the silicate dissolution rate.

Table 4.4 Reference data for direct carbonation of mechanically activated olivine and serpentine in batch experiments

	MA	t_M (min)	R_X (%)	Carbonation condition	Ref.
Olivine	—	—	49.5	185°C, 25 MPa, 1 h, –38 µm, in 1 mol/L NaCl and 0.64 mol/L $NaHCO_3$	(Gerdemann et al., 2007: pg. 4589)
Olivine	—	—	39.6	185°C, 15 MPa, 1 h, –38 µm, in 1 mol/L NaCl and 0.64 mol/L $NaHCO_3$	(Gerdemann et al., 2007: pg. 4590)
Olivine	—	—	25.7	185°C, 6 MPa, 1 h, –38 µm, in 1 mol/L NaCl and 0.64 mol/L $NaHCO_3$	(Gerdemann et al., 2007: pg. 4590)
Olivine	—	—	5.1	185°C, 15 MPa, 1 h, –75 µm, in 1 mol/L NaCl and 0.64 mol/L $NaHCO_3$	(Summers et al., 2005: pg. 141)
Olivine	SMD	25	69.9	185°C, 15 MPa, 1 h, in 1 mol/L NaCl and 0.64 mol/L $NaHCO_3$	(Summers et al., 2005: pg. 141)
Olivine	AM	60	84.3	185°C, 15 MPa, 1 h, in 1 mol/L NaCl and 0.64 mol/L $NaHCO_3$	(Summers et al., 2005: pg. 141)
Olivine	Attritor	60	19.0	185°C, 11.5 MPa, 2 h, in water	(Haug, 2010: Part II, Paper III, pg. 9)
Olivine	Attritor	60	87.0	185°C, 11.5 MPa, 18 h, in water	(Haug, 2010: Part II, Paper III, pg. 9)

	MA	t_M (min)	R_X (%)	Carbonation condition	Ref.
Serpentine	—	—	2.5	185°C, 15 MPa, 1 h, –38 μm, in 1 mol/L NaCl and 0.64 mol/L $NaHCO_3$	(Gerdemann et al., 2007: pg. 4589)
Pipe ore[a]	Attritor	15–60	7–9	155°C, 12.4 MPa, 1 h, in 1 mol/L NaCl and 0.64 mol/L $NaHCO_3$	(Bobicki et al., 2015: pg. 47)
OK ore[a]	Attritor	15–60	9–12	155°C, 12.4 MPa, 1 h, in 1 mol/L NaCl and 0.64 mol/L $NaHCO_3$	(Bobicki et al., 2015: pg. 47)

Note: [a] corresponds to the serpentine hosted nickel ore.

Compared to the batch-mode attritors, the IsaMill operated in continuous mode is equally efficient in producing new specific surfaces and demonstrates equal initial efficiency in reducing crystallinity. However, the overall efficiency of crystallinity reduction in the continuous mode is lower than that in the batch mode because the continuous mode permits energy relaxation during each cycle to prevent overheating. Since the structure change is not as important as specific surface area in wet mechanical activation for enhancing the carbonation conversion, IsaMill operated in continuous mode, can compete with batch-mode attritors for the use of mechanical activation. The IsaMill used in this study could increase a large specific surface area in much shorter time than batch-mode attritors used in previous studies, making it a more appropriate tool for the mechanical activation of mine waste. Further research and development of an overall economic analysis of a mineral processing plant that integrates the mineral carbonation process with mechanical activation as a pretreatment method will help to explain the feasibility of process in detail.

4.4 Conclusions

(1) When olivine and serpentine are ground concurrently, the yield stress of slurry increases dramatically and the breakage efficiency of mill decreases.

(2) The serpentine content in the mine waste rock facilitates an increase in the specific surface area, but prevents the crystallinity from being reduced during wet mechanical activation.

(3) Compared to pure olivine, mine waste rock stores more excessive energy during grinding in the form of generating new surface area, which leads to the greater carbonation conversion in a defined specific milling energy input.

(4) Forsterite is the main mineral being activated and carbonated, and lizardite catalyzes the whole process. The proposed process can be effectively applied when forsterite is the major phase in the mine waste rock.

(5) The attritor in continuous mode can activate olivine or mine waste rock within a short residence time and with a large production quantity; it is therefore viable for the industrial practice of mineral carbonation.

Chapter 5: Ultra-fine grinding and mechanical activation of mine waste using a planetary mill for mineral carbonation [4]

5.1 Introduction

Global climate systems have been observed to be warming since the 1950's, with increased temperatures being detected in the atmosphere and the oceans, snow and ice levels diminishing, and sea levels being raised. The dominant cause of climate change has been attributed to the cumulative emissions of global anthropogenic greenhouse gases, particularly carbon dioxide (CO_2) (IPCC, 2014). CO_2 capture and sequestration (CCS) has been proposed as a solution for mitigating climate change through reducing CO_2 emissions. Of all the CCS methods, mineral carbonation (MC) provides an alternative strategy to geological sequestration, and is considered to be a preferred option with respect to the storage of CO_2 for small and medium-sized industrial emitters (< 2.5 Mt CO_2) (Sanna et al., 2014: pg. 8051). MC mimics a natural weathering process, whereby magnesium or calcium silicates spontaneously react with CO_2 to form stable carbonates. The reaction of mineral carbonation on olivine and serpentine is described in reactions 5.1 and 5.2, respectively. Due to the thermodynamically favorable processes, MC can guarantee the permanent and environmentally-friendly storage of CO_2.

$$Mg_2SiO_4 + 2CO_2 \rightarrow 2MgCO_3 + SiO_2 \quad (5.1)$$

$$Mg_3Si_2O_5(OH)_4 + 3CO_2 \rightarrow 3MgCO_3 + 2SiO_2 + 2H_2O \quad (5.2)$$

Since the process of MC was first proposed in 1990 (Seifritz, 1990), researchers have focused on finding ways to accelerate the process, including through the selection of process routes

[4] A version of this chapter has been published. Li, J and Hitch, M., 2017. Ultra-fine grinding and mechanical activation of mine waste using a planetary mill for mineral carbonation, International Journal of Mineral Processing, (158): 18-26.

and conditions, and the pre-treatment of feedstock at low levels of energy consumption (Power et al., 2013b). However, MC is currently not yet economically viable for large scale deployment. Magnesium silicates, olivine and serpentine are the most abundant feedstocks available for mineral carbonation (Lackner et al., 1999). Olivine is composed of a mixture of the magnesium-rich forsterite (Mg_2SiO_4) and the iron-rich fayalite (Fe_2SiO_4). Olivine has an orthorhomibic structure with an independent SiO_4 tetrahedra linked by divalent ions in 6-fold coordination (Klein et al., 1993). Serpentine ($Mg_3Si_2O_5(OH)_4$) consists of a group of common rock-forming hydrous magnesium phyllosilicate minerals. In all its polymorphs, lizardite, antigorite, and chysotile are the most common serpentine minerals found in nature. The structure of serpentine consists of an overlapping sheet of SiO_4 tetrahedra and a sheet of Mg octahedral (brucite-like) in which the -OH base is bonded (Klein et al., 1993). Both olivine and serpentine make up the dominant contents of mine waste rock and tailings in ultramafic deposits, such as nickel mines, diamond mines, PGE mines and former asbestos mines (Hitch et al., 2010). Turning ultramafic waste rocks or tailings into valuable CO_2 feedstock can benefit a deposit both environmentally and economically (Hitch and Dipple, 2012). With respect to the process of integrated mineral carbonation, the pre-treatment method of mechanical activation (MA) might become practical because the energy consumption of the operation is reduced when MA is integrated as part of the milling procedure in mineral processing (Haug, 2010).

MA uses mechanical force to accelerate a downstream process. Studies on the use of MA on ultramafic rocks are constantly expanding. They have focused on comparing individual mineral (i.e. olivine or serpentine) (Kim et al., 2008; Rigopoulos et al., 2015) responses to the grinding energy input (Atashin et al., 2016, 2015), milling instruments (i.e. planetary mills, vibration mills, attrition mills, or tumbling mills) (Baláž et al., 2008; Haug, 2010), milling atmosphere (i.e. N_2,

CO_2 or air) (Turianicová et al., 2013), milling solutions (i.e. water, alcohol or acid) (Rigopoulos et al., 2015; Sandvik et al., 2011), and milling temperatures (Trapasso et al., 2012). These studies agree that MA induces changes in the surface properties and crystal structures of minerals, and that it thus enhances their rates of dissolution (Kleiv and Thornhill, 2006), -OH dehydration (Hrsak et al., 2008), carbonation (Summers et al., 2005), CO_2 adsorption (Fabian et al., 2010), and solid state reactions (Atashin et al., 2016). However, the concurrent grinding of olivine and serpentine was rarely studied. The authors have investigated fine grinding and mechanical activation of mine waste materials in a wet condition (Chapter 4), the interactions between two minerals were confirmed through various characterization methods. Nevertheless, the mechanical activation of mine waste materials in dry condition has not yet been studied.

The aim of the present paper is to investigate the physical, structural and chemical properties of mine waste rock (that contains both olivine and serpentine), and which has been subjected to mechanical activation under dry conditions. MA was induced using a planetary mill since this is a type of high-intensity mill that is commonly used for MA. A direct aqueous mineral carbonation process was used to test the effects of the MA due to it being the most competitive route for industrial application. Different types of characterization techniques were used to recognize mechanically-induced changes in mine waste rock.

5.2 Materials and experiments

5.2.1 Materials

The olivine foundry sand (TSO) was obtained from the Twin Sisters Deposit in northwest Washington State, USA. TSO samples were used as a control. The mine waste rock or whole ore (TAW) was provided by Hard Creek Nickel Corp. from their Turnagain deposit in northern British Columbia, Canada. All received materials were ground by a laboratory bond ball mill, and

screened using 140 mesh Tyler sieve (106 µm). The undersized materials were used as the starting sample for the planetary milling and the chemical and mineralogical compositions tests.

Table 5.1 shows the content of major elements of samples, expressed as wt% oxide, which were analyzed using X-ray fluoresces (XRF) at Acme Analytical Laboratories Ltd. Canada. The mineral compositions of the samples received were tested using X-ray powder diffraction (XRPD) analysis in the Earth and Ocean Science Department at the University of British Columbia. XRPD detected 97.9% forsterite, 0.2% lizardite, 1.5% chromite, and 0.4% quartz in olivine. Mine waste contains 64.7% forsterite, 29.6% lizardite, 4.2% magnetite, 0.3% quartz and 2.5% brucite.

Table 5.1 XRF results for the TSO and TAW (wt%)

Component	SiO_2	Al_2O_3	Fe_2O_3	CaO	MgO	MnO	TiO_2	Cr_2O_3	LOI	TOT/C
TSO	40.7	0.15	8.39	0.09	50.94	0.12	0.02	0.677	-0.3	<0.02
TAW	38.7	0.15	10.39	0.3	45.51	0.16	0.03	0.671	4.09	0.05

5.2.2 Grinding test

The laboratory grinding tests were conducted using a planetary ball mill (Micro Mill Pulverisette 7, Fitsch GmbH, Germany). The two bowls of the Pulverisette 7 have a planet-like movement, where the bowls rotate around a central axis and also simultaneously around their own axis in opposite directions with the same rotational speed (Abdellahi and Bahmanpour, 2015). The rational speed of the mill was kept constant at 500 rpm.In each test, 10 g of feed material was ground with seven 15 mm zirconium oxide balls in a 45mL zirconium oxide mill bowl (95% ZrO_2, density 5.7 g/cm^3) under a dry atmospheric condition. The ball to solid weight ratio was fixed to 7:1. The samples were ground for 0 min., 30 min, 60 min, and 120 min, and were then selected, carbonated and characterized. Every 15-min of grinding was followed by a 15-min rest interval to

prevent the overheating of the material and of the milling ball. The milling temperature was maintained below 30 °C, as monitored by a thermocouple. The energy consumption is monitored by a Watts-up?^{TM} Pro electrical watt meter (Think Tank Energy Products Inc., Vermont, USA) at a 0.2s interval.

5.2.3 Carbonation test

The carbonation condition is chosen according to the optimum conditions for the direct aqueous mineral carbonation of olivine (O'Connor et al., 2005) except for the working pressure which was reduced from 15 MPa to 6 MPa due to limitations of the experimental set-up, in which gas was supplied directly from a gas cylinder without the aid of a booster pump. 7.5 g of samples were mixed with 50 mL solutions containing 1 mol/L NaCl and 0.64 mol/L $NaHCO_3$, and transferred to a 100 mL Hastelloy-4566C Parr bench-top stirred autoclave (Parr Instruments, Moline, IL, USA).The maximum working temperature and pressure of the autoclave are 500°C and 20.7 MPa, respectively. Through increasing the concentration of HCO_3^- in the aqueous solution and maintaining a constant pH of between 7 and 8, the solution can be used to help achieve the optimum extent of carbonation. The sample slurry was carbonated at 185°C and 6 MPa CO_2, with a stirring speed of 1,500 rpm for 1 hour.

5.2.4 Material characterization

Particle size distribution (PSD) was measured with a laser diffraction particle size analyzer (Mastersizer Hydro 2000s, Malvern, U.K.). The proper dispersion of the representative sample that was suspended in water was ensured through the use of an ultrasonic vibration for 5 seconds. The Mastersizer-S software applies the Mie scattering model by assuming that the morphology of particles is spherical. It can accurately predict the particle size of a material in the range of 0.02

μm to 2,000 μm. The refractive index used for the particle size analysis on TSO is 1.77 (Haynes, 2014: pg. 4-142), and TAW is 1.70 (Haynes, 2014: pg. 4-143).

The specific surface area was measured using a nitrogen gas adsorption/desorption instrument (Autosorb-1MP, Quantachrome, Boynton Beach, USA) at –198°C. The specific surface areas were calculated based on 11 points using the Brunauer–Emmett–Teller (BET) method. Particle shape and morphology were observed using a Helios NanoLab 650 Focused Ion Beam Scanning Electron Microscope (FEI, Eindhoven, the Netherlands) with a secondary electron detector of 50 pA at 1 kV. To prevent the effects of charging, the surfaces of the tested samples were coated with 8 nm of iridiumin a Leica sputter coater.

X-ray diffraction data for microstructure analysis and quantitative analysis were collected using a step size of 0.03° and a count time 0.7 s/step on a Bruker D8 Focus Bragg-Brentano diffractometer (Bruker AXS GmbH, Germany) over the two theta range of 3° to 80° with each scan taking 30.3 min. A long fine-focus Co X-ray tube (λ= 1.79021) was operated at 35 kV and 40 mA, and a Fe monochromator foil was employed. Samples were mounted in a back-loading Al cavity holder (Raudsepp and Pani, 2003). A pattern of standard sample LaB_6 (SRM 660a) was collected using the same procedure, and was used to obtain the instrumentally broadened profile, as suggested by the US National Institute of Standards and Technology (NIST). The X-ray diffractogram was analyzed with reference to the International Centre for Diffraction Database PDF-4 and Search-Match software DIFFRACT^{plus} EVA (Bruker AXS GmbH, Germany). X-ray powder diffraction data for the sample were refined using the Rietveld program Topas 4.2 (Bruker AXS GmbH, Germany). The sample was reduced to an optimum grain-size range of <10 μm by grinding in ethanol in a vibratory McCrone Micronising Mill for 7 min. Considering the short period of re-grinding, it can be assume that the microstructures of the samples were not altered

(Tkáčová et al., 1993). The Rietveld refinement procedures for quantitative analysis on TAW are the same as those found in Wilson et al.'s (2006) study, where they considered serpentine to be in an amorphous phase and fitted the structureless pattern to the lizardite with planar disorder. The microstructure characterization based on Rietveld method follow with respect to Chapter 3.

All calculated data are the average value from 3 tests with standard deviation.

5.3 Results

5.3.1 Energy consumption

The net specific energy consumption W_N (kWh/t), which is the energy transferred to the powder, is calculated according to Equations 5.1 and 5.2.

$$P_N = P_0 - P_{NL} \tag{5.1}$$

$$W_N = \frac{P_N}{m} \times t_{\mathrm{M}} \tag{5.2}$$

Where P_N is the specific power (kW), P_0 is the operational power (kW), and P_{NL} is the power draw (kW) when running the mill empty with no material or media. P_0 and P_{NL} are monitored by the electrical watt meter. *m* is the mass of sample milled (t). t_{M} is the MA time (hour). As no changes have occurred in the milling parameters, the net specific energy consumption for a specific duration remains the same. The materials that were mechanically-activated for 30 min, 60 min, and 120 min, correspond to the net specific energy consumption of 900 kWh/t, 1,800 kWh/t and 3,600 kWh/t, respectively. Grinding time and specific milling energy input are considered to have the same influence on the effects of mechanical activation.

5.3.2 Comminution behaviours

The changes in particle size and surface area are commonly observed during comminution. Mechanical activation also induces these communtion behaviours.

5.3.2.1 Changes in particle size

Fig. 5.1 shows the frequency plot of the particle size distributions of TSO and TAW milled for different periods of time in a planetary mill. Fig. 5.1(a) presents that the monomodal size distribution of the initial TSO transforms to a broad bimodal one on milling, with two distinct maxima occurring at ~2.5-5.0 μm and ~11-25 μm. A large number of fine particles of <2 μm, are generated as grinding time increases. In contrast, TAW keeps its monomodal size distribution until it has been milled for 60 min, with a maxima occurring at ~11-31 μm (Fig. 5.1(b)). The amount of fine particles of <2 μm remains nearly unchanged, but the particle size distribution appears to become broader with an increase in milling time. Particles larger than 100 μm appear after 120 min of MA on TAW, as seen in Fig. 5.1(b).

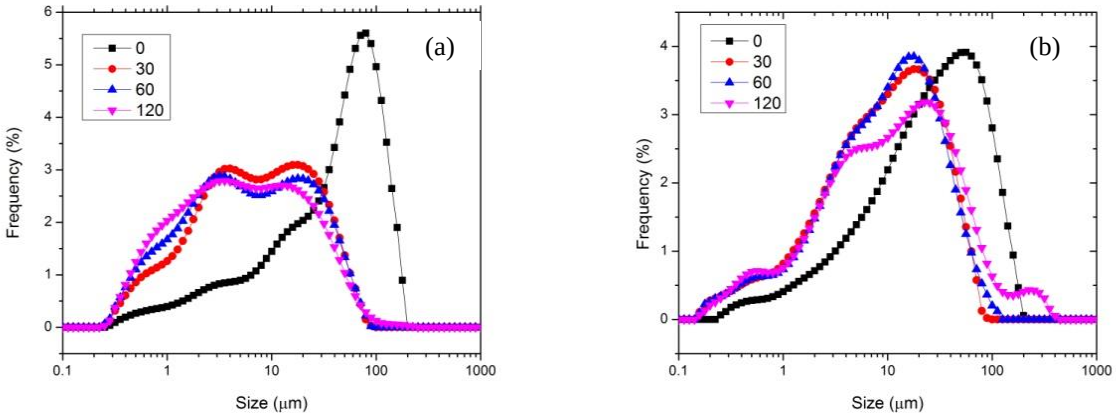

Figure 5.1 Particle size distributions (frequency plot) of samples milled for different time interval in a planetary mill. (a) TSO, (b) TAW

Table 5.2 lists the characteristic diameters (i.e. d_{10}, d_{50} and d_{90}) of samples with t_M and W_N. The characteristic diameters were extracted from their respective cumulative curves. d_{10}, d_{50} and d90 of TSO sharply decreased from 3.5 μm, 44.5 μm and 110.3 μm to 1.0 μm, 6.5 μm and 32.1 μm, respectively after 30 min of milling. It can further be noted that all the characteristic diameters continue to decrease, but not significantly, thereafter.

As seen in Table 5.2, d_{50} of TAW decreased steeply to the minimum of 9.2 μm after 30 min of grinding, which is nearly 1.5 times that of 30 min ground TSO. The d_{10} and d_{90} of TAW also sharply decreased. A gradual increase was observed with further milling. For example, d_{50} gradually increased to about 10.5 μm after 120 min of milling. The increase in particle size was more pronounced for d90 than for the other characteristic diameters. Fig. 5.1(b) shows that the position of the mode at ~30 μm shifts towards a larger particle size as milling progresses. All evidences suggest the aggregation of particles. It indicates that serpentine content aggravates the agglomeration of particles during MA.

Table 5.2 Variation of characteristic diameters (d_{10}, d_{50} and d_{90}) with milling time

t_M	W_N	TSO (μm)			TAW (μm)		
(min)	(kWh/t)	d_{10}	d_{50}	d_{90}	d_{10}	d_{50}	d_{90}
0	0	3.4±0.1	44.5±0.6	110.3±1.6	3.0±0.1	25.6±0.0	89.1±0.4
30	900	1.0±0.0	6.5±0.1	32.1±0.9	1.2±0.0	9.2±0.0	35.2±0.4
60	1800	0.8±0.0	5.6±0.1	31.5±0.5	1.3±0.0	10.0±0.7	38.2±3.9
120	3600	0.8±0.0	5.1±0.3	29.6±1.1	1.2±0.0	10.5±0.4	53.0±2.4

5.3.2.2 Changes in surface properties

Fig. 5.2 shows that overall, the BET surface area increased from 0.8 m^2/g in the initial TSO to 2.4, 2.6, 2.7 m^2/g in mechanically-activated TSO for 30, 60 and 120 min, respectively. The rate

of growth in BET surface area of TSO was found to be quite slow during milling. As seen in Fig. 5.2, the BET surface area increased from 3.1 m^2/g in the initial TAW to 9.9, 12.4, 14.3 m^2/g in mechanically-activated TAW for 30, 60 and 120 min, respectively. The substantial initial growth rate in BET surface area of TAW slowed down over the period of 30 to 120 min milling time. The BET surface area in mechanically-activated TAW is 4.2-5.2 times higher than in mechanically-activated TSO over the same period of milling time.

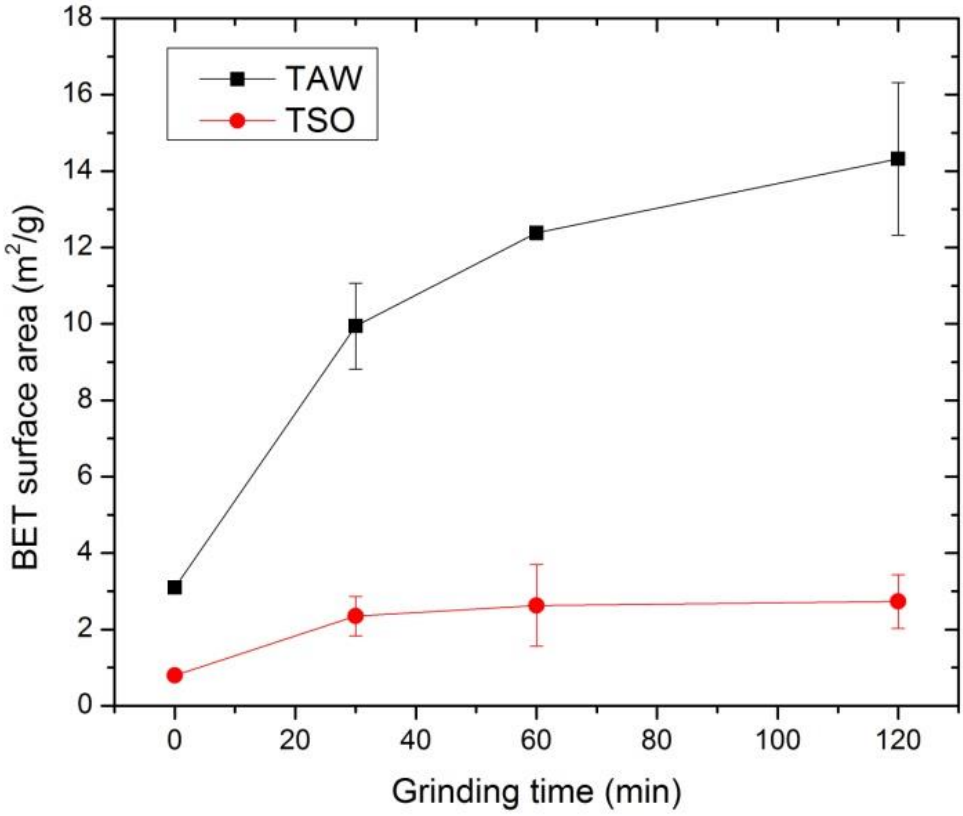

Figure 5.2 The variation of BET surface area with grinding time

Fig. 5.3 shows the SEM micrographs for the 120 min mechanically-activated TSO and TAW. As observed in the micrographs, the particles agglomerate (Fig. 5.3(a)(c)) and become fused (Fig. 5.3(b)(d)). Sharply angled particles with 10 μm diameters remained in existence in TSO after 120 min of milling (Fig. 5.3(a)). The maintenance of the particle shapes and sizes of olivine, even under intensive milling conditions, confirms the resistant nature of olivine during MA treatment. In Fig. 5.3(c), we note that large particles no longer exist in the 120 min mechanically-activated TAW. The micrographs indicate that the substances inherent within TAW (i.e. serpentine) assisted in breaking forsterite into fine particles during MA.

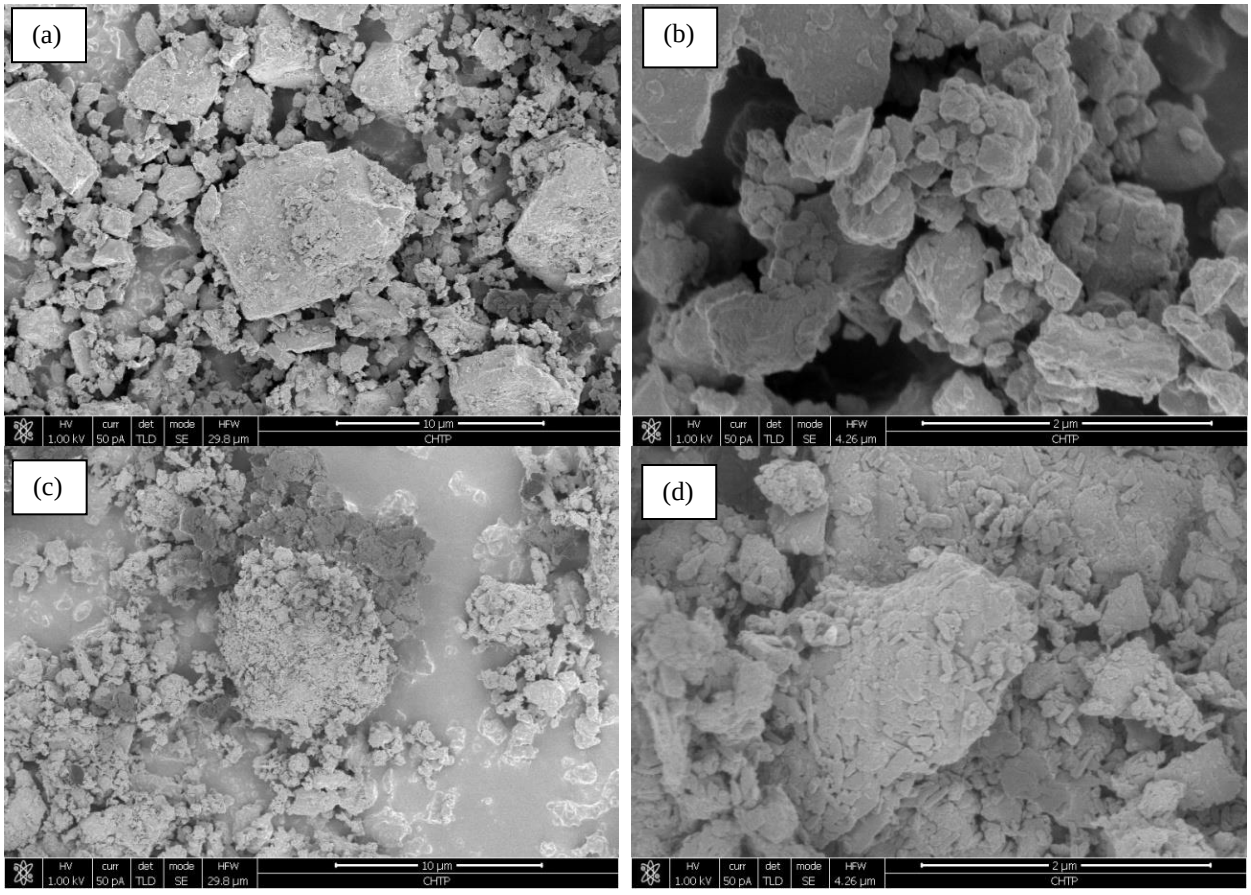

Figure 5.3 Morphology of samples after 120 min milling in planetary mill. (a) (b) TSO and (c) (d) TAW. Scale bars in (a) (c) are 10 μm. Scale bars in (b) (d) are 2 μm.

5.3.3 Crystal structure changes

The distinct difference in ultrafine grinding or mechanical activation from coarse grinding is disordering in crystal structure of material during grinding. The crystal structure information such as crystallinity or amorphization degree, lattice parameter, crystallite size and micro-strain can be extracted from their X-ray diffraction patterns (see Chapter 3).

5.3.3.1 XRD pattern characterization

In X-ray diffraction patterns, the peak positions (2θ) present mineral phases. The shifting of 2θ indicates an expansion or compaction in the dimensions of lattice. The intensity of peaks (I) clearly signifies the abundance of the minerals in the material. The crystallinity can be described by the ratio of I_{max} to the correspondence intensity of background (I_B). Under conditions without phase transfer, a weakening in the intensity of peaks relates to the generation of amorphous phase. The breadth of the peak always expressed using full widths at half maximum (FWHM) or integral breadth (β). The broadening of peaks indicates the changes in microstructure such as a reduction in the crystallite size or increases in microstrain (Pourghahramani, 2007).

The XRD patterns the initial TSO, as well as those of the TSO ground in the planetary mill are provided in Fig. 5.4(a). All of the peaks were in accordance with the standard XRD pattern of forsterite $(Mg_{1.86}Fe_{0.14})SiO_4$ (ICSD No. 39794). The ratio between Mg and Fe is calculated from XRF and XRD data of the TSO as received. Only forsterite reflections are represented in the initial and mechanically-activated TSO, indicating that no phase transitions took place during the MA of TSO.

Fig. 5.4(b) illustrates the XRD patterns of the initial and mechanically-activated TAW. It indicates that the major peaks were congruent with the standard XRD pattern of forsterite $(Mg_{1.849}Fe_{0.151})(SiO_4)$ (ICSD No. 69474) (Yu, 1997: pg. 179) and lizardite $Mg_3(Si_2O_5)(OH)_4$

(ICSD No. 75933) (Mellini and Viti, 1994: pg. 1194). No new phases appeared after the MA of TWA. However, the phase transfer between forsterite and lizardite may occur during MA.

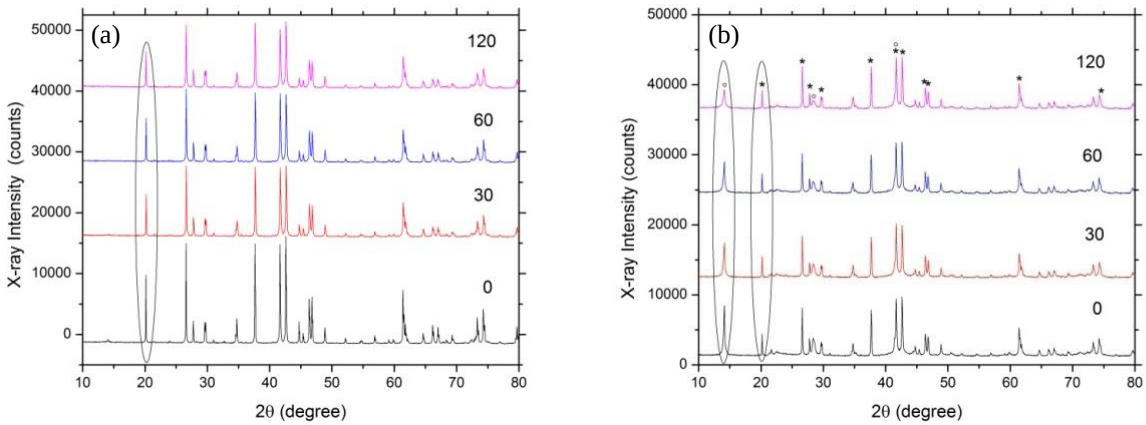

Figure 5.4 XRD patterns of the initial sample and mechanically activated samples for different milling times. (a) TSO; (b) TAW. (*) is forsterite peaks, (o) is the lizardite peak.

Table 5.3 lists the geometry of forsterite (020) and lizardite (001) peaks in pristine and mechanically-activated TSO and TAW. All peaks demonstrate a shift in 2θ, a reduction in I_{max}/I_B and a broadening in FWHM as grinding time increased. All these changes indicate that the crystal structures of forsterite and lizardite become amorphous due to the mechanical activation.

Table 5.3 The variation in shape parameters of XRD selected peaks with milling time.

Material	t_M (min)	Forsterite (020)			Lizardite (001)		
		2θ	I_{max}/I_B	FWHM	2θ	I_{max}/I_B	FWHM
TSO	0	20.134	6.71	0.076	-	-	-
	30	20.173	4.07	0.090	-	-	-
	60	20.168	4.40	0.086	-	-	-
	120	20.149	3.44	0.094	-	-	-
TAW	0	20.050	2.00	0.086	13.972	3.35	0.212
	30	20.181	1.80	0.096	14.095	2.38	0.242
	60	20.166	1.63	0.100	14.083	1.99	0.262
	120	20.180	1.46	0.107	14.084	1.16	0.334

5.3.3.2 Changes in microstructure

The Rietveld method was applied to study the lattice parameters and microstructural changes of TSO and TAW during MA based on the full pattern fitting methods using the Pseudo-Voigt approach. Rietveld method fits the measured XRD pattern with respect to the crystallographic structure models through least-square calculation. Pseudo-Voigt approach is a weight liner combination of Lorentzian and Gaussian functions, which can satisfactorily model the broadened peaks and resolve the crystallite size and microstrain components of the presented mineral. The volume-weighted crystallite size (D_V) and maximum lattice strain (ε) can be calculated using Equations 5.3 and 5.4 (Balzar et al., 2004: pg. 917):

$$D_V = \lambda / \beta_S \cos\theta \tag{5.3}$$

$$\varepsilon = \beta_D / 4\tan\theta \tag{5.4}$$

Where λ is the wavelength, β_S is the total-size-integral breadth, and β_D is the total-strain-integral breadth.

The lattice parameters are calculated based on Bragg's Law Equation 5.5, and the plane-spacing equation for the orthorhombic forsterite and hexagonal lizardite crystal systems are expressed in Equations 5.6 and 5.7, respectively.

$$n\lambda = 2d_{hkl}\sin\theta \tag{5.5}$$

$$d_{hkl} = \frac{1}{\sqrt{\left(\frac{h}{a}\right)^2 + \left(\frac{k}{b}\right)^2 + \left(\frac{l}{c}\right)^2}} \tag{5.6}$$

$$d_{hkl} = \frac{1}{\sqrt{\frac{4}{3}\left(\frac{h^2 + hk + k^2}{a}\right)^2 + \left(\frac{l}{c}\right)^2}} \tag{5.7}$$

Where, d_{hkl} is the interplanar spacing, n is known as the order of reflection (n=1, 2, 3…) and (h, k, l) are Miller indices of diffraction planes, and a, b, c are lattice constants (nm).

Tables 5.4 and 5.5 summarize the results for microstructure analysis using the Rietveld method. The forsterite in the initial TSO yields the value of lattice parameters (a=0.47609 nm, b=1.02199 nm, c=0.59911 nm and V=0.29150 nm), displaying very slight variations from the values provided in the mineralogy database (a=0.47700 nm, b=1.021200 nm, c=0.59840 nm and V=0.29069 nm). So do the lattice parameter of forsterite and lizardite in initial TAW (Table 5.5). The lattice parameters of forsterite in TSO initially increased slightly with grinding up to 60 min, and then decreased with longer grinding time. In contrast, the lattice parameters of forsterite in TAW fluctuate around the initial values after grinding. All the lattice parameters of forsterite in TAW are larger than those in TSO, regardless of milling time. The unit cell of c in the lizardite lattice expanded slightly, while the values of a and V in the lizardite lattice decreased slightly with increasing grinding time.

Table 5.4 and 5.5 show a decrease in the D_V, and an increase in the ε of forsterite and lizardite in both TSO and TAW with the grinding time increasing. The D_V of forsterite decreased from 135.0 nm to 74.4 nm after 120 min of MA on TSO, while the value only decreased from 91.4 to 86.9 nm after 120 min of MA on TAW. The D_V of forsterite in initial TAW is smaller than that in initial TSO. The extent of changes for forsterite in mechanically-activated TAW is not as distinct as it is for mechanically-activated TSO. Lizardite has a smaller D_V and a larger ε than forsterite in both the initial and the mechanically-activated TAW.

In contrast to TSO, except for microstructural changes, the phase transfer from lizardite to forsterite is observed in TAW by the Rietveld method (Table 5.5). The weight ratio of forsterite to

lizardite in the initial TAW and the 120 min mechanically-activated TAW are 2.19 and 3.13, respectively.

Table 5.4 Changes in the microstructure of TSO with grinding time

t_M (min)	Lattice parameter				D_V (nm)	ε ($\times 10^3$)
	a (nm)	b (nm)	c (nm)	V (nm^3)		
0	0.47609	1.02199	0.59911	0.29150	135.0	0.28
30	0.47612	1.02211	0.59918	0.29158	83.3	0.46
60	0.47613	1.02212	0.59919	0.29161	85.3	0.45
120	0.47607	1.02210	0.59915	0.29154	74.4	0.51
Ref.	0.47570	1.02120	0.59840	0.29069	-	-

Table 5.5 Changes in the microstructure of TAW with grinding time

t_M (min)	Phase	Lattice parameter				D_V (nm)	ε ($\times 10^3$)	Weight percentage (%)
		a (nm)	b (nm)	c (nm)	V (nm^3)			
0	Fo	0.47635	1.02283	0.59951	0.29210	91.4	0.42	64.7
	Li	0.53282		0.73056	0.17962	28.4	1.34	29.6
30	Fo	0.47631	1.02280	0.59946	0.29204	87.1	0.44	67.1
	Li	0.53266		0.73050	0.17950	23.4	1.62	27.7
60	Fo	0.47641	1.02299	0.59948	0.29221	84.6	0.45	67.5
	Li	0.53250		0.73059	0.17941	22.1	1.72	27.4
120	Fo	0.47630	1.02290	0.59952	0.29209	86.7	0.44	72.2
	Li	0.53177		0.73072	0.17895	18.5	2.05	23.1
Ref.	Fo	0.47620	1.02210	0.59910	0.29160	-	-	-
	Li	0.53330		0.73240	0.18039	-	-	-

Note: Fo donates the forsterite phase, Li donates the lizardite phase.

5.3.4 Changes in carbonation conversion

The carbonation conversion is expressed by the CO_2 sequestration reaction efficiency (R_X), which is the percentage stoichiometric conversion of Mg^{2+}, Ca^{2+} and Fe^{2+}cations in silicate feed to carbonate (Equation 5.8) (Penner et al., 2004: pg. 2).

$$R_X = \frac{x_{CO_2}}{\varepsilon_A (1 - x_{CO_2})} \tag{5.8}$$

Where x_{CO_2} is the weight percent of CO_2 in solid products, and ε_A is the percent weight added if all the available cations convert to carbonates.

Fig. 5.5 indicates that the R_X obtained from one hour of carbonation enhanced with the increasing of grinding time. The R_X increased from 6.1% for the initial TSO to a maximum of 24.9% for 60 min mechanically-activated TSO, and stabilized at 22.5% for 120 min mechanically-activated TSO. The R_X increased following a linear fashion from 8.7% to 31.7% in the initial TAW and 120 min mechanically-activated TAW, respectively. Thus, it appears that TAW containing serpentine results in better carbonation efficiency than does the TSO. The changes in R_X of the two samples exhibited a similar trend up to 60 min mechanical activation, while various afterwards.

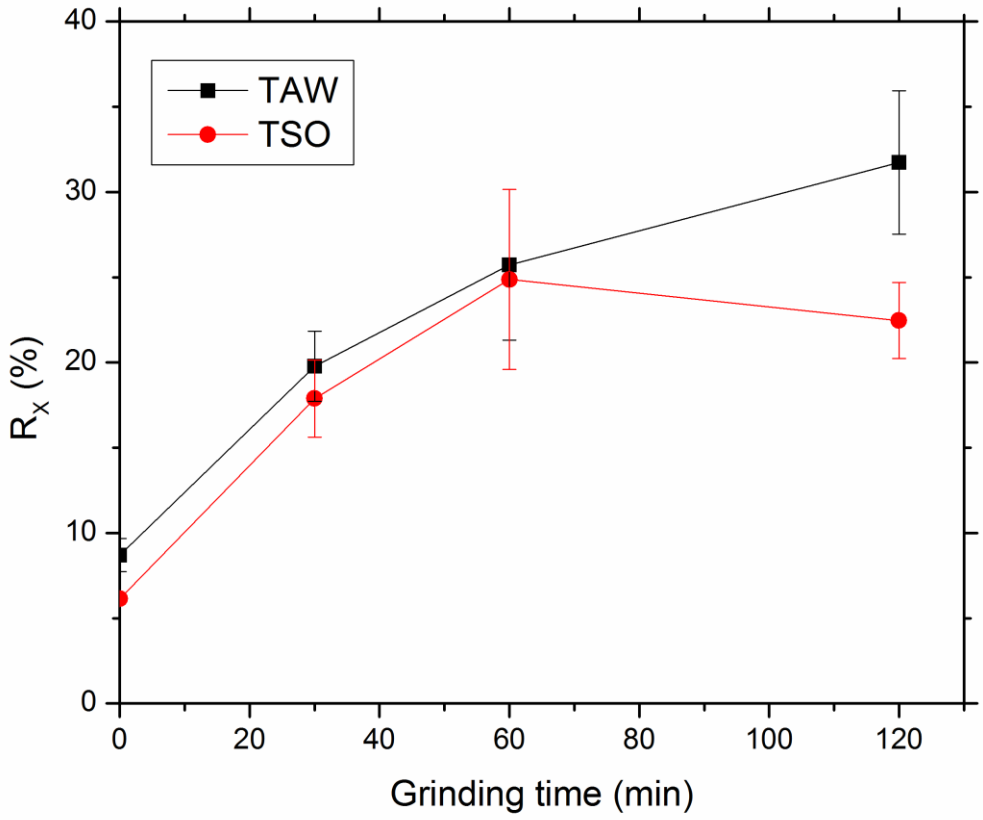

Figure 5.5 CO_2 sequestration reaction efficiency of mechanically-activated materials with grinding time, the experimental condition: 15 wt% solid content in solution containing 1M NaCl, 0.64 M $NaHCO_3$, at 185°C, 6 MPa CO_2 partial pressure, for 1 hour

Table 5.6 lists the weight percentages of forsterite and lizardite in the initial and mechanically-activated samples, and in their carbonated products. The abundance of forsterite in TSO remains unchanged after MA. After carbonation, the ratio of lost weight in forsterite increased from 6.8% to 21.6% after 120 min of MA on TSO. As shown in Tables 5.5 and 5.6, in mechanically-activated TAW, the weight percentage of forsterite increased, while that of lizardite decreased with increased grinding time. Nearly 21.5% of the original lizardite content converted to forsterite after 120 min of milling. After 1 hour of carbonation, the ratio of lost weight in

forsterite increased from 6.4% in untreated TAW to 34.4% in 120 min mechanically-activated TAW. The ratio of lost weight in lizardite stayed constant at 14.39±3.3% for up to 120 min of MA on TAW. It is possible that CO_2 sequestration using TAW resulted mainly from the carbonation of forsterite under laboratory conditions. As such, the enhanced R_X would be due to the mechanically-activated forsterite content in TAW.

Table 5.6 The weight percentage of forsterite and lizardite in TSO and TAW.

t_M (min)	TSO Forstertie (wt%)		TAW Forsterite (wt%)		TAW Lizardite (wt%)	
	MA	MC	MA	MC	MA	MC
0	97.0	90.4	64.7	58.0	29.6	27.7
30	97.0	80.6	67.1	52.6	27.7	25.0
60	97.0	74.2	67.5	51.9	27.4	24.0
120	97.0	76.0	72.2	47.2	23.1	22.8

Note: MA means t_M min mechanically-activated sample. MC means carbonated products of correspondence mechanically-activated sample.

5.4 Discussion

5.4.1 The effect of mechanical activation on TSO

As seen in Fig. 5.1(a), the presented multimodal size distribution of TSO indicates that impact that is responsible for the transgranular cleavage, and abrasion that create intergranular breakage, simultaneously play significant roles in the planetary milling process. The micrographs of 120 min mechanically-activated TSO (Fig. 5.3(a)(b)) provide strong support for the coexistence of large (>10 μm) particles with smooth surfaces, as well as small (<2.5 nm) particles with coarse surfaces. Similar findings were observed during the MA of gibbsite using a planetary mill (Alex et al., 2014).

During the process of MA on TSO, the particle size decreased and reached the grinding limit after 30 min of grinding since no significant decrease in particle diameters is observed thereafter (Table 5.2). Afterwards, although the particle sizes had not changed, the specific surface area continued to increase (Fig. 5.2), and the microstructure became disordered (Table 5.4). The disorder of microstructure is expressed by an alteration of the lattice parameters, decreasing in crystallite size and increasing in microstrain. The characteristic values are comparable to those of previous study of milling energy on particle size variation for ground olivine (Atashin et al., 2015). The specific energy input at 120 min of milling under our lab conditions is 3,600 kWh/t, which is approximately the optimal value (3,833.3 kWh/t) achievable for minimum particle sizes. The values for crystallite size and microstrain calculated through the Rietveld method in our study are found to be similar to those calculated by (Atashin et al., 2015) using the Willamson-Hall method with the same specific milling energy inputs. This indicates that the results of the Rietveld refinement method have a high level of accuracy with respect to microstructure characterization.

During the mechanical activation of TSO, the slow increase in the BET surface area after having reached the grinding limit maybe the result of the variation in characterization techniques. Laser diffraction could not detect particles smaller than 2 μm. A large number of fine particles, even nano-sized particles, are generated during MA. Fine or ultrafine particles contribute to the growth of specific surface area. Changes may also result from the aggregation of fine particles. Agglomeration is identified as large particles in laser diffraction techniques. While, differs from large particles, agglomeration contains a lot of pores, that are accessible for nitrogen gas used during the BET analysis (Haug, 2010). The latter explanation was confirmed by the SEM micrograph (Fig. 5.3b). The typical aggregation of fine particles after dry milling is in line with those found in previous investigations (Haug, 2010; Summers et al., 2005).

5.4.2 The effect of mechanical activation on TAW

Some commonalities exist between how TAW and TSO respond to MA. These include that particle size is initially greatly reduced, both reach their grinding limit at, or before 30 min milling, and they both increase in BET surface area, decrease in crystallite size, and increase in micro-strain after up to 120 min of MA. However, some distinct differences exist between the mechanically-activated TSO and TAW.

To begin, the particle size at the grinding limit in TAW is larger than that found in TSO (Table 5.3). As well, further grinding leads to an increase in the particle size of TAW after it has reached the grinding limit. Instead of showing a multimodal size distribution, mechanically-activated TAW shows a unimodal particle size distribution with the maximum frequency at large size region (>10 μm) (Fig. 5.1b). Some agglomerates that are larger than 10 μm appear in the SEM micrograph of 120 min ground TWA (Fig. 5.3c and d). These results indicate that the extent of fine particle aggregation is more intense in mechanically-activated TAW than in TSO. This is mainly the result of the link between the grinding limit and the type of materials in use. The Moh's hardness for serpentine is 2.5-4 (Barthelmy, 2014: pg. 1) and olivine is 6.5–7 (Barthelmy, 2014; Halder and Tisljar, 2013: pg. 59). The presence of serpentine content results in an easier aggregation for TAW than TSO. This is congruent with the findings of a previous study by Roufail (2011) on the fine grinding of ores with various levels of hardness using a horizontal stirred ball mill. This study found that soft materials break down faster, reach their grinding limit faster, and start to aggregate earlier than do hard ones.

The BET surface area of TAW is much higher than that of TSO (Fig. 5.2). Since soft serpentine disintegrates more easily than does hard olivine, to some extent, fine serpentine particles contribute to extra surface area. However, the main reason for the greatly enhanced surface area is

that the serpentine content assists olivine disintegration. This is clearly confirmed in the SEM micrograph (Fig. 5.3d). Quantitative analysis from XRD data confirms the existence of partial phase transitions from serpentine to olivine during the MA of TAW (Tables 5.3 and 5.5). This result is in line with Zhang et al.'s findings that the molar ratio of dry mechanically-activated serpentine is equivalent to that of forsterite composition (Zhang et al., 1997). This phase transfer involves the dehydration process of serpentine. Zulumyan et al.(2011) have suggested that the structural OH was transformed to adsorbed water during serpentine dehydration induced by MA. With the water generated from serpentine dehydration, the whole system is transformed from a process of dry grinding to one of kneading. The small amounts of water can provide a lubricant for solid-state diffusion and lead to a dramatic increase in specific surface area during the MA of TAW. Similar kneading behaviors were observed in mechanically-activated olivine with a small amount of water (5 wt%) added in. This resulted in the generation of a product with a specific surface area that was as large as that achieved through wet milling, and with the high extent of structure disorder as that achieved through dry milling (Baláž et al., 2008).

Given the same specific energy input, the variation in the microstructure in the forsterite of TAW is smaller than that of TSO (Tables 5.4 and 5.5). The presence of serpentine content is the main reason for this. XRD patterns show that the crystal structure of soft lizardite becomes disordered more easily than does the crystal structure of hard forsterite. This is in line with previous observations that the XRD peaks of serpentine disappear, while those of hard minerals still remain after 120 min of high energy milling of serpentine with hard mineral impurities (Kim et al., 2008). Most of the milling energy stores in the form of new surface generation, phase conversion, and lizardite crystal structure deformation during the MA of TAW. Therefore, only few of the milling energy stores as forsterite crystal structure disordering.

5.4.3 The contribution of mechanical activation to mineral carbonation

MA on both TSO and TAW increased their R_X in direct aqueous mineral carbonation (Fig. 5.5). Table 5.7 lists some of the results published on the direct aqueous carbonation of olivine and serpentine. The R_X for the feed material of TSO (6.1%) was comparable to that published in the literature for untreated olivine. The R_X for the feed material of TAW (8.7 %) was higher than that of TSO. It seems that the large specific surface area and the poorly ordered structure of TAW, are responsible for its high reactivity in relation to the presence of serpentine. Similar beneficial effects were found in a study on in-situ CO_2 mineral sequestration in partially serpentine peridotites (Hövelmann et al., 2011).

Table 5.7 Published results for direct carbonation of mechanically-activated olivine and serpentine in batch experiments

	MA	W_N	t_M (min)	R_X (%)	Carbonation condition	References
Olivine	-	83	-	39.6	185°C 15 MPa, 1 h, -38 µm ,in 1 M NaCl and 0.64 M $NaHCO_3$	(Gerdemann et al., 2007: pg. 4589)
Olivine	-	83	-	25.7	185°C 6 MPa, 1 h, -38 µm ,in 1 M NaCl and 0.64 M $NaHCO_3$	(Gerdemann et al., 2007: pg. 4589)
Olivine	-	13	-	5.1	185°C 15 MPa, 1 h, -75 µm,in 1 M NaCl and 0.64 M $NaHCO_3$	(Summers et al., 2005: pg. 141)
Olivine	AM	729	60	75.7	185°C 15 MPa, 1 h, in 1 M NaCl and 0.64 M $NaHCO_3$	(Summers et al., 2005: pg. 141)
Olivine	AM	15100	1440	88.8	185°C 15 MPa, 1 h, in 1 M NaCl and 0.64 M $NaHCO_3$	(Summers et al., 2005: pg. 141)
Olivine	PM	896	10	27	185°C 11.5 MPa, 2 h, in water	(Haug, 2010: Part II, Paper III, pg. 9)

	MA	W_N	t_M (min)	R_X (%)	Carbonation condition	References
Olivine	PM	4431	60	32	185°C 11.5 MPa, 2 h, in water	(Haug, 2010: Part II, Paper III, pg. 9)
Lizardite	-	83	-	2.5	185°C 15 MPa, 1 h, -38 µm, in 1 M NaCl and 0.64 M $NaHCO_3$	(Gerdemann et al., 2007: pg. 4589)
Pipe ore[a]	Attritor	-	15-60	7-9	155°C 12.4 MPa, 1 h, in 1 M NaCl and 0.64 M $NaHCO_3$	(Bobicki et al., 2015: pg. 47)
OK ore[a]	Attritor	-	15-60	9-12	155°C 12.4 MPa, 1 h, in 1 M NaCl and 0.64 M $NaHCO_3$	(Bobicki et al., 2015: pg. 47)

Note: [a] Serpentine hosted nickel ore

The R_X for 120 min mechanically-activated TSO (22.5%) was comparable to that published in the literature for olivine (-38µm) under the same carbonation conditions. The R_X for 120min mechanically-activated TAW (31.7%) was comparable to that published in the literature for olivine (-38µm) under high CO_2 partial pressure (15 bar). The concurrent dry grinding of serpentine and olivine can achieve better carbonation results than can mechanically-activated olivine alone. This is mainly due to the behavior of serpentine content during MA, which greatly enhances the formation of new surface. However, serpentine content is not largely carbonated. This is congruent with the results of previous studies regarding the direct aqueous mineral carbonation on mechanically-activated serpentine ore, as R_X did not show a distinct increase even after being attrited for an hour (Bobicki et al., 2015; O'Connor et al., 2005).

The ball milling decreases the crystallite size of forsterite in TSO for up to 120 min (Table 5.4). However, the R_X of TSO after MA for 120 min is lower than that for 60 min (Fig. 5.5). The crystal defects caused by MA are likely not to favor the production of carbonates. Similar findings can be found in a study by Rigopoulos et al. (2015). Direct aqueous carbonation may also benefit

from the mechanically-activated TAW with respect to the mitigated disorder in forsterite structure due to the presence of serpentine content (Table 5.5). Changes in the trend of lattice parameters of forsterite are well correlated with R_X. The expansion in lattice volume of forsterite corresponds to a high R_X. Therefore, the lattice parameters of forsterite are probably critical parameters with respect to the mineral carbonation of mechanically-activated materials.

The MA of TAW has a better carbonation conversion than does that of TSO with the same specific milling energy input (Fig. 5.5). In the proposed process, forsterite is the primary mineral being carbonated (Table 5.6). Thus, forsterite has to be the major mineral in mine waste material, when choosing MA as the pretreatment method for mine waste carbonation.

The overall mechanical activation efficiency in enhancing mineral carbonation using planetary mill operate in dry condition couldn't compete with that of IsaMill operate in wet condition, which is presented in chapter 4. The BET surface area of mechanically-activated TAW is 12.4 m^2/g after grinding in planetary mill for 60 min, and the value is 12.6 m^2/g after grinding in IsaMill for 4.3 min; and their R_X are 25.7% and 43.6%, respectively. Although the BET surface areas of mechanically-activated TAW are similar, their R_X are quite different. This difference is mainly due to the variation in milling patterns and conditions, which activate the other features of minerals (i.e. crystal structures, chemical phases) in different ways. The detailed comparison of these mechanical activation effects on mine waste in various milling conditions is necessary to find out the most effective way to activate mine waste materials.

To this date, the process of mineral carbonation using mechanical activation as pre-treatment has not yet been optimized. Further research evaluating the performance of scalable grinding mills is essential in order to continue to develop the technology to the point that its implementation could

be viable on an industrial scale. Also, an economic analysis of the integrated mineral carbonation process of a mineral processing plant would be valuable since it could provide insight into how the energy consumption of the process could be reduced.

5.5 Conclusions

This study examines the characteristics of initial and mechanically-activated mine waste and their performance in direct aqueous mineral carbonation. It provides a promising process for the use of mine waste material for CO_2 sequestration. Some key findings are as follows:

(1) Much as in the MA of TSO, the MA of TAW results in particle size reduction and aggregation, an increase in surface area, and a disordering of the crystal structure with increased grinding time.

(2) Serpentine content promotes particle aggregation and assists with an increase in the specific surface area, but mitigates the disorder in the crystal structure of forsterite during the MA of TAW. A small amount of serpentine also converts to olivine during intensive dry grinding.

(3) Compared to TSO, TAW has a higher carbonation with respect to a defined specific energy input.

(4) Forsterite is the primary mineral that is being activated and carbonated. Unreactive lizardite serves only to assist forsterite in reaching a higher level of MA during high-energy dry grinding.

Chapter 6: Structural and chemical changes in mine waste mechanically-activated in various milling environments [5]

6.1 Introduction

The enhanced ex-situ carbonation of mine waste rock or tailings from the processing of ultramafic ores, such as nickel mine waste, is currently recognized as a promising way of mitigating anthropogenic CO_2 (Hitch and Dipple, 2012). The ex-situ carbonation of ultramafic rocks can be achieved using either a direct or indirect method in a gas-solid or aqueous phase (Sanna et al., 2014). In a direct carbonation process, both the dissolution of magnesium silicate and CO_2 and the precipitation of magnesium carbonate occur in a single reaction step; the indirect carbonation process differs from the direct process in that it introduces an additional step wherein the reactive compound is extracted from the matrix before carbonation. A pre-treatment method is often applied prior to both carbonation process in order to enhance the rate of reaction, with the appropriate method being determined depending on the primary mineral in the feedstock: thermal and chemical activation is most effective when serpentine is the majority mineral (Bobicki, 2014), while mechanical activation is preferable when olivine is the majority mineral in the feedstock (Chapters 4-5).

Mechanical activation, which uses mechanical energy such as intensive grinding to enhance a reaction (Baláž, 2008), is one of the most effective pre-treatment methods for sequestering CO_2 via mineral carbonation (Power et al., 2013b). From a thermodynamic

[5] A version of this chapter has been published. Li, J and Hitch, M., 2017. Structural and chemical changes in mine waste mechanically-activated in various milling environments. 308: 13-19.

perspective, mechanical activation stores excess energy in the minerals in the form of long-lived defects, such as the formation of new surface area, new crystallite phases, amorphous materials, and lattice distortion (Pourghahramani, 2007). This excess energy lowers the activation energy of the downstream reaction (Tkáčová et al., 1993).

Research into enhancing mineral carbonation through the use of mechanical activation is constantly leading to new advances in this technique (Kim et al., 2008; Li and Hitch, 2016a; Rigopoulos et al., 2015). Numerous investigations have focused on how various grinding conditions, such as grinding modes (Haug, 2010; Sandvik et al., 2011), grinding solutions (Rigopoulos et al., 2016, 2015), grinding atmosphere (Kalinkina et al., 2001; Turianicová et al., 2013), and grinding instruments (Baláž et al., 2008; Haug, 2010), effect on the structural changes of mechanically-activated ultramafic rocks. Sandivik et al. (2011) has compared the mechanical activation effects of olivine under various grinding modes, include wet, moisture (10 wt% H_2O), dry modes. They found that grinding under wet conditions typically produces finer particle sizes and larger surface areas than dry grinding at the same energy input. While prolonged dry grinding tends to create aggregates and agglomerates with large particle sizes and a high degree of change to the crystal structure. However, intensive grinding under moisture mode generates surface areas as large as wet grinding and disorders the crystal structure as high as dry grinding (Sandvik et al., 2011). Haug (2010) has studied the structure changes of olivine in different mills using milling intensity as the important parameter for comparison. For example stirred mill and nutation mill are best compared at medium intensity for industrial applications (Haug, 2010). However, most previous studies have focused on the changes in specific surface area and the degree of amorphization (Baláž et al., 2008; Fabian et al., 2010; Haug, 2010; Kleiv and Thornhill, 2016; Rigopoulos et al., 2016; Sandvik et al., 2011), there has been little investigation into the changes

in lattice micro-structure (e.g. crystallite size and micro-strain) (Atashin et al., 2015) and chemical transformation (Li and Hitch, 2016b) induced by mechanical activation. The structure amorphization of minerals that do not undergo chemical transformation during mechanical activation (i.e. pure olivine) can simply be quantified using the peak area of the X-ray diffraction pattern. For ultramafic mine waste, which is partially serpentinized and weathered, the milling system would be very complicated; thus, a study on the long-lived defects of new phase formation and lattice distortion could provide a more robust understand of how mechanical energy activates the mine waste.

This study investigates the mechanical activation of mine waste under various milling conditions by using different characterization methods to examine the long-lived defects (surface, micro-structure, and chemical changes) that occur as a result of milling. Ideally, the results of this analysis will indicate which conditions are optimal for mechanically activating mine waste for use in mineral carbonation.

6.2 Materials and experiments

The experiments proceeded according to the following steps: mechanical activation, autoclave carbonation, and physical and chemical characterization (Fig. 6.1). Firstly, the material is sampled for characterization before being mechanically activated in a high-energy mill for different periods of time. Once the designated time interval had expired, the material was then re-sampled for characterization. The physical changes in materials were characterized by testing the particle size distribution (PSD) and BET surface area , and its structural and chemical information was obtained by using X-ray diffraction (XRD) and Fourier Transform Infrared (FTIR) spectroscopy. The initial and mechanically-activated samples were then carbonated using a direct aqueous process, and, once this step had been completed, the carbonation conversion of the

materials after mechanical activation was obtained via quantitative analysis of the carbonated products using their XRD patterns.

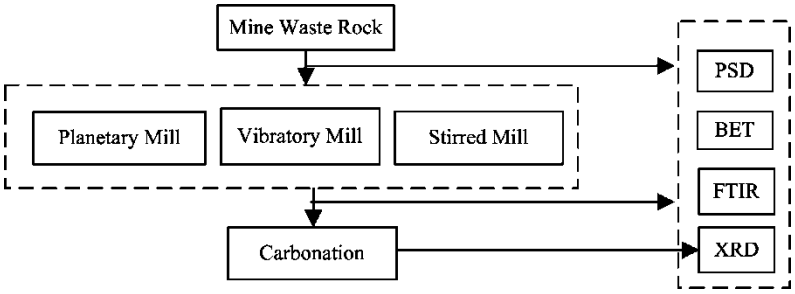

Figure 6.1 Procedures of the experiments

6.2.1 Materials preparation

The mine waste material (TAW) was provided by Hard Creek Nickel's (HCN) Turnagain project in Northern British Columbia, Canada. The received material was ground using a laboratory bond ball mill and screened with a 140 mesh Tyler sieve (160 μm). The undersized materials were used as the initial material for mechanical activation. The initial material had an 80% passing size of 73 μm, a specific surface area of 3.1 m^2/g, and a density of 3.1 g/m^3. X-ray powder diffraction (XRPD) analysis revealed that the starting material was composed of approximately 64.7% Forsterite (Mg_2SiO_4) and 29.6% Lizardite ($Mg_3Si_2O_5(OH)_4$), with trace amounts of magnetite, quartz, and brucite also being present. Table 6.1 shows the oxide values of samples analyzed using X-ray fluorescence (XRF), the loss on ignition (LOI), and the total C (TOT/C) tested using theLeco method at Acme Analytical Laboratories Ltd., Canada.

Table 6.1 XRF results for mine waste (wt%)

Component	SiO_2	Al_2O_3	Fe_2O_3	CaO	MgO	MnO	TiO_2	Cr_2O_3	LOI	TOT/C
TAW	38.7	0.15	10.39	0.3	45.51	0.16	0.03	0.671	4.09	0.05

6.2.2 Mechanical activation

In order the test the behaviour of mine waste materials under various milling conditions, three types of high-energy mill were used for the mechanical activation:

(1) Planetary mill (PM): The selected planetary mill was a Pulverisette 7 (Fitsch GmbH, Germany) containing seven, 15 mm zirconium oxide balls in a 45 ml zirconium oxide mixing bowl. The mill was loaded with 10g of feed material, and the ball-to-solid weight ratio was 7:1. The rotational speed of the mill was kept constant at 500 rpm under dry atmospheric conditions and at ambient temperature.

(2) Vibratory mill (VM): The selected vibratory mill was an SPEX 8000 (SPEX Industries, Inc., Edison, NJ) that was loaded with a hardened 25 mL steel vial containing10 g of feed material and two 6 mm hardened steel balls. The vial was vibrated at an amplitude of 50mm and a frequency of 20 Hz under dry atmospheric conditions and ambient temperature.

(3) Stirred mill (SM): The stirred mill chosen for the experiments was a horizontal stirred ball mill LME-4 (Netzsch, Germany) which had a 2.48 L effective milling chamber that was loaded with 2 L of 2 mm Keramax MT1 ceramic beads. Pulp with 30 wt.% solids content was prepared by mixing 5 kg of sample with 11.7 kg water before being fed into the charged chamber. The milling products were collected, sampled, and then re-fed into the mill, andthis cycle was repeated up to nine times until the slurry temperature reached 40°C. The sampled slurry was dried in an oven at 100°C for 12 hours and subsequently deagglomerated. During the tests, the pulp flow rate was controlled at 2.3 l/min, and the mill agitator speed was maintained at 1500 rpm.

Table 6.2 lists the samples collected from each mill and the milling variables. For the characterization and carbonation tests, the samples were collected, sealed in plastic tubes, and stored in a freezer at 0 °C. The milling energy consumption recorded in Table 6.2 indicates the net

energy consumed of each sample, which was calculated as the difference between the power draw of milling with an empty vial and milling with a vial filled with sample and grinding media. The calculation of specific milling energy input (W_N) for the stirred mill is the same as used in Chapter 4, and the calculations for the planetary mill and the vibratory mill are the same as in Chapter 5. Mill intensity (I_M) is equal to the specific energy input divided by time.

Table 6.2 Milling variables of collected samples.

Sample name	Mill type	t_M (min)	H_2O (wt. %)	W_N (kWh/t)	I_M (kW/t)
PM30	Planetary mill	30	0	900	1800
PM60	Planetary mill	60	0	1800	1800
PM120	Planetary mill	120	0	3600	1800
VM30	Vibratory mill	30	0	2500	5000
VM60	Vibratory mill	60	0	5000	5000
VM120	Vibratory mill	120	0	10000	5000
SMP1	Stirred mill	0.9	70	66.9	3000
SMP4	Stirred mill	3.4	70	236.3	3053
SMP9	Stirred mill	7.6	70	447.5	2668
FEED	-	0	-	0	0

Note: t_M is the mechanical activation time

6.2.3 Carbonation test

For carbonation testing, 7.5g solid sample and 50 mL of background solution (1 mol/L NaCl and 0.64 mol/L$NaHCO_3$) were load into a 100 ml Hastelloy-4566C Parr bench-top stirred reactor (Parr Instruments, Moline, IL, USA). The slurry samples were carbonated at a temperature of 185 °C and 6 MPa CO_2 for one hour with a stirrer speed of 1500 rpm. This carbonation condition was selected based on the optimum condition for olivine in a direct aqueous carbonation process

(O'Connor et al., 2005). A pressure of 6 MPa (rather than 15 MPa) was used because it could be reached directly from a gas cylinder, thereby eliminating the need for a booster pump. Once the reaction had been achieved, the slurry samples were cooled and removed from the autoclave and left to settle overnight. After removing the supernatant, the residue slurry was dried in an oven at 60 °C and deagglomerated for quantitative analysis.

6.2.4 Characterization methods

The particle size of the samples was measured using a laser diffraction particle size analyzer (Mastersizer 2000, Malvern, U.K.). In order to disperse the representative samples prior to the tests, the samples were added to the distilled water and treated for 5 seconds using ultrasonic vibration.

The specific surface area of each samples was characterized by its N_2 adsorption isotherm at -198 °C on the Autosorb-1 (Quantachrome instruments, USA), and this data was obtained using the Brunauer–Emmett–Teller (BET) method.

X-ray diffraction (XRD) measurements were carried out using a Bruker D8 Focus Bragg-Brentano diffractometer (Bruker AXS GmbH, Germany) equipped with Co-Kα radiation source, working in 2θ geometry with a recorded range from 3 to 80° with a step size of 0.03°. There corded XRD data were refined with the Rietveld program, Topas 4.2.The Rietveld refinement procedures for quantitative analysis followed those of Wilson et al. (2006), and the procedures for microstructure characterization were the same as Chapter 3 and used Equations 6.1–6.2:

$$D_V = \lambda / \beta_S \cos\theta \tag{6.1}$$

$$\varepsilon = \beta_D / \tan\theta \tag{6.2}$$

where, D_V is the crystalline size, ε is the micro-strain, λ is the wavelength, β_S is the total-size-integral breadth, and β_D is the total-strain-integral breadth.

Diffuse Reflectance Fourier Transform Infrared (DRIFT) spectra were measured using Perkin Elmer Spectrum 100 Fourier Transform Infrared (FTIR) spectrometers (PerkinElmer Inc., MA, USA). Samples were diluted in KBr at 1% concentration, and the spectra were acquired via 25 scans of the 4000-400 cm^{-1} region at 1 cm^{-1} resolution.

All calculated data are the average value from 3 tests with standard deviation.

6.3 Results and discussion

6.3.1 Characterization of milled products

Mechanical activation of TAW was performed in the 3 types of high intensity mills. Table 3 lists the specific milling energy input W_N, medium particle size P_{50}, BET surface area S_{BET}, crystallite size D_V, micro-strain ε, and carbonation conversion R_X of selected samples. As shown in Table 6.3, a decrease in P_{50}, an enlargement of S_{BET}, a decrease in D_V, an increase in ε, and an enhancement of R_X were observed with the progress of milling in all three mills. However, there are some differences among these values for the different grinding methods.

Table 6.3 The variation of medium particle size (P_{50}), BET surface area (S_{BET}), crystallite size (D_V), micro-strain (ε), and carbonation conversion (R_X) with specific milling energy input (W_N).

Sample name	W_N (kWh/t)	P_{50} (μm)	S_{BET} (m^2/g)	Forsterite		Lizardite		R_X (%)
				D_V (nm)	ε ($\times 10^3$)	D_V (nm)	ε ($\times 10^3$)	
PM30	900	12.3	9.9	87.1	0.44	23.4	1.62	19.8
PM60	1800	14.4	13.1	84.6	0.45	22.1	1.72	25.7
PM120	3600	14.4	14.4	86.7	0.44	18.5	2.05	31.7
VM30	2500	12.8	7.7	93.1	0.41	23.7	1.6	19.4
VM60	5000	15.4	11.1	72.0	0.53	20.2	1.88	22.2
VM120	10000	22.8	11.0	72.6	0.52	17.4	2.19	25.7
SMP1	45.4	8.7	7.2	92.8	0.41	29.4	1.29	25.4
SMP4	172.9	3.8	12.6	86.2	0.44	30.3	1.25	43.6
SMP9	338.0	2.4	17.8	79.1	0.50	27.6	1.38	53.1
FEED	-	31.8	3.1	96.8	0.39	28.6	1.38	8.7

Note: The data for SM and PM came from chapter 4 and 5 respectively.

6.3.1.1 Changes in particle size and surface area

In the case of dry grinding, prolonged grinding in both the planetary and vibratory mills provided a rapid initial decrease in P_{50}; however, that number began to increase as milling progressed. This increase was accompanied by the rapid initial increase in S_{BET} which continued to change slightly as the milling went on. These results agree with previous studies on the mechanical activation of various minerals under dry conditions that attributed particle enlargement (aggregation and/or agglomeration) to prolonged milling (Baláž et al., 2008). Grinding the samples in the stirred mill provided a continuous and rapid decrease in P_{50} and an increase in S_{BET}. A comparison of the mills based on W_N revealed that the stirred mill brings about the smallest P_{50} and the largest S_{BET} due to the presence of water, which prevents the formation of aggregates and

agglomerates. A similar difference has also been detected in the mechanical activation of olivine in both wet and dry conditions (Haug, 2010).

The value of S_{BET} produced by the mechanical activation of mine waste in the planetary mill (S_{BET} =13.1 m^2/g, W_N = 3,600 kWh/t) was much higher than that of pure olivine in the magneto mill in (Atashin et al., 2015) (S_{BET} =8.7m^2/g, W_N = 3,834 kWh/t). The magneto mill has been recognized as being the most efficient mill for generating new surface area through the mechanical activation of olivine in dry conditions (Atashin et al., 2015). The existence of serpentine assists the formation of new surface area during the mechanical activation of mine waste in a dry condition. This result has been documented in Chapters 4-5 that compares the mechanical activation effects of mine waste and those of pure olivine under the same intensive grinding. Although the milling intensity of the vibratory mill is higher than the planetary mill (Table 6.2), the value of S_{BET} produced by the vibratory mill is lower than that of the planetary mill (Table 6.3). This result is incongruent with observations related to the mechanical activation of various pure minerals, such as olivine (Atashin et al., 2015), orhematite (Pourghahramani, 2007). Therefore, a lower milling intensity may be preferable for generating new surface area in mine waste during mechanical activation.

6.3.1.2 Changes in micro-structure

In the case of dry grinding, prolonged grinding in both the planetary mill and the vibratory mill produced a rapid initial decrease in the D_V of forsterite and continued to change slightly as milling progressed. Changes in the micro-structure of forsterite appear to have a mechanical activation limit, which is similar to a behavior observed in the mechanical activation of olivine in the Magneto mill (Atashin et al., 2015). The comparison of planetary and vibratory milling showed

that mine waste that was mechanically activated in the planetary mill reached this limit earlier than it did in the vibratory mill; for instance, forstertite's D_V value at the mechanical activation limit in the planetary mill is higher than it is in the vibratory mill. The experimental results suggest that there is a direct relationship between grinding intensity and the extent of disorder in forsterite's microstructure at the mechanical activation limit: the higher the grinding intensity, the higher the extent of disorder in the microstructure of forsterite at the mechanical activation limit.

When mine waste was mechanically activated in the stirred mill, the D_V of forsterite continuously decreased as milling progressed. Although the mechanical activation limit of forsterite's microstructure may not be reached until the stirred mill's energy input reaches 446.5 kWh/t, a comparison of the three mills revealed that, given the same amount of W_N, the stirred mill produced the smallest D_V for forsterite.

The D_V of lizardite continuously decreased as milling progressed in dry conditions, which indicated that the mechanical activation limit of lizardite's microstructure had yet to be reached. Given the same mechanical activation time, the D_V of mechanically-activated lizardite in the planetary mill was comparable to its D_V in the vibratory mill. These results suggest that changes in lizardite's microstructure are time-dependent rather than W_N-dependent or milling-intensity-dependent. In this case, the planetary mill was more effective than the vibratory millat producing micro-structural changes in lizardite. Furthermore, the mechanical activation of mine waste in the stirred mill did not show any evidence of a decrease in D_V or an increase in ε in lizardite. The results of the tests suggested that water may act as a depressor that inhibits disorder in the microstructure of lizardite in the stirred mill.

Fig. 6.2 shows different combinations mine waste characteristics — for example, 10% passing size (d_{10}), BET surface area (S_{BET}), and crystallite size of forsterite ($D_{V\text{-}Fo}$) — after various mechanical pretreatments. Although these characteristics exhibit linear correlations after mechanical activation in the stirred mill, they do not exhibit a correlation after mechanical activation in the planetary mill and the vibratory mill. This variation in correlation can be mainly attributed to the existence of agglomerate. A similar result was obtained in (Haug, 2010), which documented how agglomerate possesses a large particle size, a large specific surface area, and a low crystallite size. The non-correlated relationships indicate that d_{10} and S_{BET} cannot replace D_V or ε in evaluating the micro-structure values during intensive dry grinding.

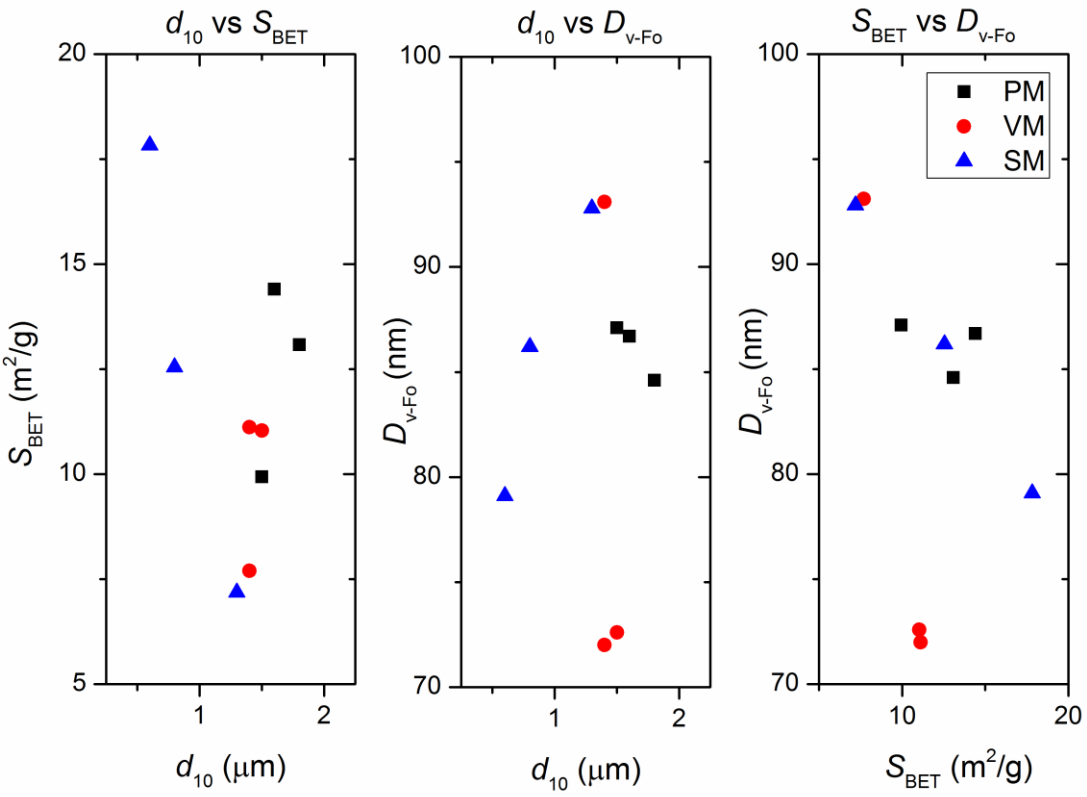

Figure 6.2 Correlation between the 10% passing particle size (d_{10}), BET size (S_{BET}), crystallite size of forsterite ($D_{V\text{-}Fo}$) in planetary mill (PM), vibratory mill (VM), and stirred mill (SM).

6.3.1.3 Changes in carbonation conversion

The carbonation of mechanically-activated mine waste was used to test how mechanical energy activates the materials in a downstream reaction. The CO_2 sequestration reaction efficiency (R_X) is the stoichiometric conversion of divalent cations (i.e. Mg^{2+}, Ca^{2+} and Fe^{2+}) in silicate to carbonate. This relationship is shown in Equation 6.3 (Penner et al., 2004),

$$R_X = \frac{x_{CO_2}}{\varepsilon_A (1 - x_{CO_2})} \tag{6.3}$$

where x_{CO_2} is the weight percentage of CO_2 in solid products and ε_A is the percentage of weight added if all of the divalent cations are converted to carbonates.

Fig. 6.3 depicts the connection between carbonation conversion and specific milling energy input, which is of special interest in interpreting the effect of mechanical activation on mine waste. It is well-established that longer grinding times in a mill lead to more carbon dioxide being stored in the mine waste. According to Fig. 6.3, for a given specific milling energy input, the activated mine waste in the stirred mill had the highest carbonation conversion rate while the vibratory mill had the lowest. The difference in carbon uptake between the mills is due to variations in milling efficiency during the conversion of mechanical energy into excess energy that is stored in the mine waste materials. These results are in line with the results obtained for hematite (Pourghahramani, 2007). The R_X can be related to W_N as described in Equations 6.4-6.6:

Stirred mill: $$R_X = 13.77 \ln W_N - 27.19 \tag{6.4}$$

Planetary mill: $$R_X = 8.58 \ln W_N - 38.64 \tag{6.5}$$

Vibratory mill: $$R_X = 4.54 \ln W_N - 16.27 \tag{6.6}$$

The correlation efficient of the experimental data and the fitted data exceeded 0.99, which suggests an excellent model.

According to Table 6.3, although PM120 (S_{BET} =14.4 m^2/g , $D_{V\text{-}Fo}$ =86.7 nm , R_X =31.7%) and SMP4 (S_{BET} =12.6 m^2/g , $D_{V\text{-}Fo}$ =86.2 nm , R_X =43.6%) are of the similar value of S_{BET} and $D_{V\text{-}Fo}$, their R_X are quite different. In order to gain more information about the effect of mechanical activation on mine waste, more detailed examinations were conducted using quantitative X-ray diffraction and FTIR spectroscopy.

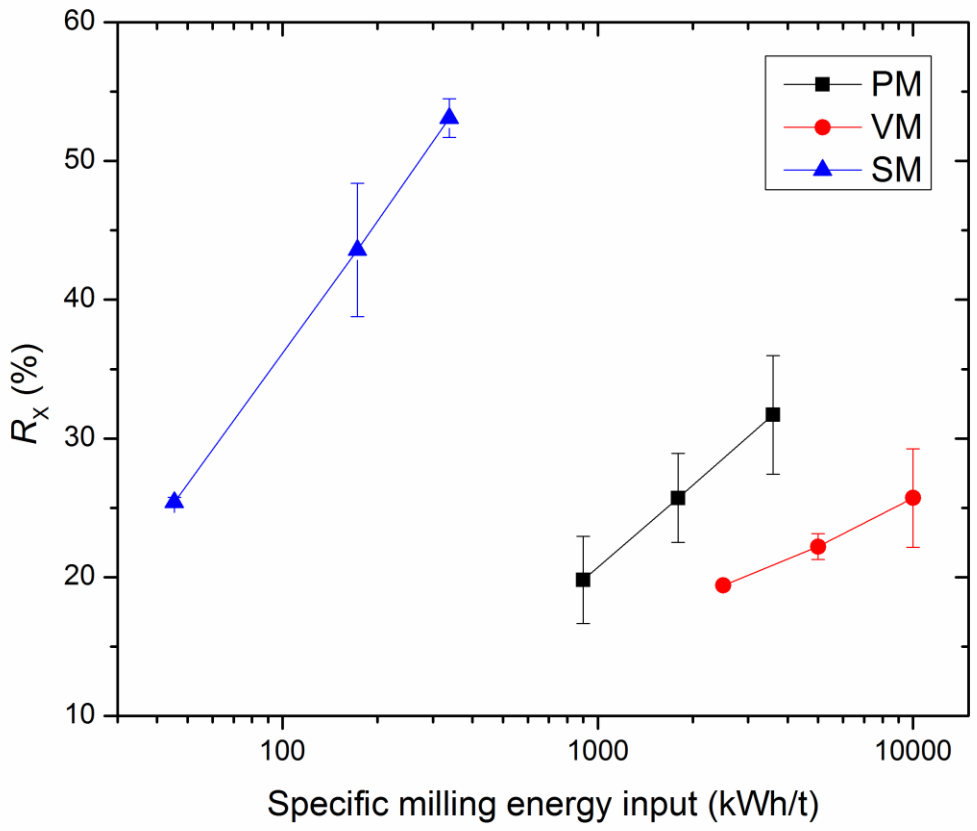

Figure 6.3 Carbonation conversion as a function of specific milling energy input. The experimental condition: 15 wt% solid content in a solution containing 1M NaCl, 0.64 M $NaHCO_3$ at 185°C, and 6 MPa CO_2 partial pressure. Data with error bars are the average value from 3 tests with standard deviation.

6.3.2 Quantitative X-ray diffraction

Quantitative X-ray diffraction was used to analyze the chemical transformation induced by mechanical activation. Fig. 6.4 shows the weight percentage of forsterite and lizardite in selected samples in relation to specific milling energy inputs. The continuous loss in lizardite content and the increase in forsterite content during planetary milling and vibratory milling were observed. There are two possible explanations for these phenomena. The most likely explanation is that olivine (moh's hardness 6.5 – 7) is more resistant to becoming amorphous than serpentine (moh's hardness 2.5-3) during mechanical activation in dry conditions, and this resistance results in a higher percentage of forsterite in the remaining crystalline material. A similar observation was noted by (Kim et al., 2008), who found that soft minerals tended to become amorphous more easily than hard minerals. The second explanation is that a small portion of lizardite is dehydroxlated and forms forsterite-like materials; this mitigates forsterite amorphization or even promotes forsteritere crystallization during dry mechanical activation. Since many prior studies have confirmed the dehydration of serpentine during dry grinding (Zhang et al., 1997), and this study has observed that the crystallite size of forsterite remains nearly unchanged or slightly increases during extensive dry mechanical activation, this explanation could possibly explain the continuous loss of lizardite content and the increase in forsterite content during planetary milling. The weight percentage of both forsterite and lizardite remain constant after wet grinding, which indicates that no phase transfer occurred between forsterite and lizardite during stirred milling. This observation is consistent with those in previous experiments wherein no serpentine content was observed when mechanical activation was used on olivine in wet conditions Chapter 4.

Fig. 6.4 also shows the weight percentage of forsterite and lizardite in the carbonated product of selected samples. After 1 hour of carbonation, 10.4% of the forsterite from the initial

sample was lost, and 34.6, 35.1, and 60.0% of the forsterite was lost in PM120, VM120, and SMP9, respectively. The weight percentage loss of lizardite in all selected samples ranged from -4.0 to 1.9%.The negative value refers to the formation of lizardite during carbonation in VM60. Spontaneous serpentization and carbonation during the direct aqueous carbonation process was also observed in (Lafay et al., 2014). The loss of forsterite is much greater than the loss of lizardite regardless of the type of mill chosen for mechanical activation, which indicates that forsterite is the main mineral being activated and carbonated in the direct aqueous carbonation process. Further studies that examine other potentially effective methods of carbonating both forsterite and lizardite are necessary in order to test the efficiency of mechanical activation on mine waste.

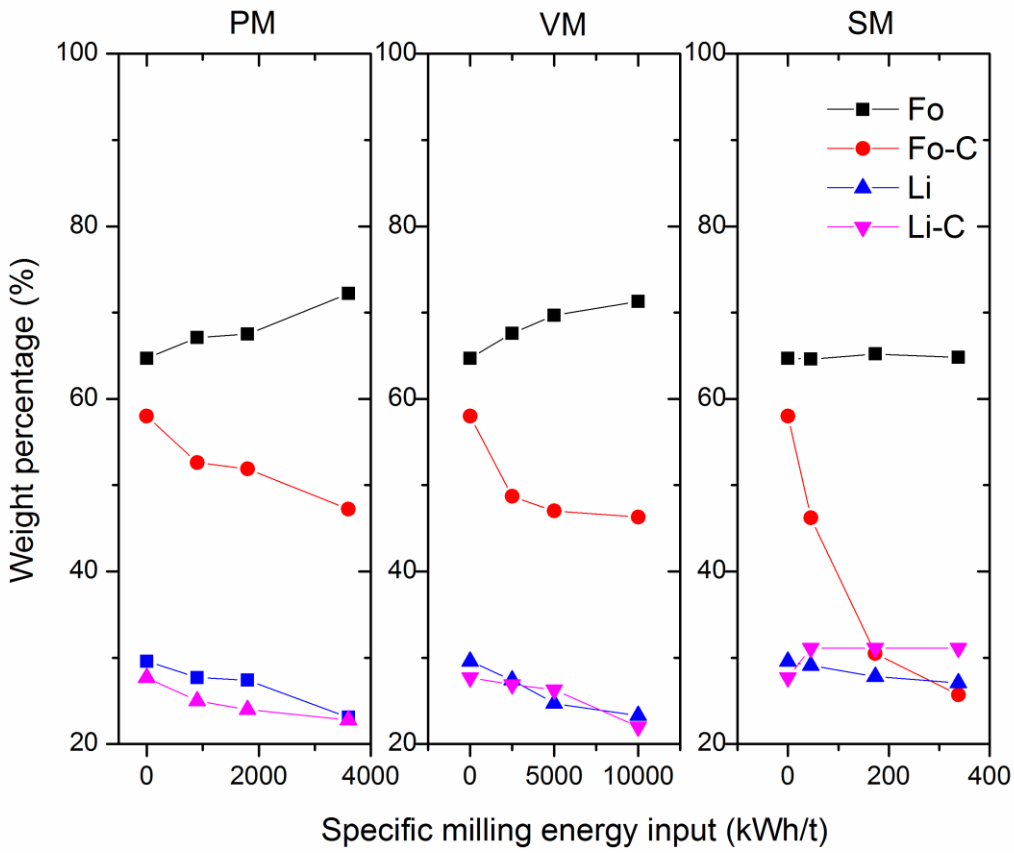

Figure 6.4 The weight percentage of forsterite (Fo) and lizardite (Li) in initial and mechanically-activated TAW in the planetary mill (PM), vibratory mill (VM) and stirred mill (SM), and their weight percentage in the carbonated products (C) of correspondence mechanically-activated materials.

It should also be noted that the amorphous content has also been considered as lizardite in other quantitative analyses of mine waste using the X-ray diffraction method (Wilson et al., 2006b). Consequently, the weight percentage of lizardite in mechanically-activated mine waste may be overestimated, as mechanical activation disorders the crystal structure of minerals and produces amorphous content.

6.3.3 FTIR spectroscopy

FTIR spectroscopy was used to obtain additional information about the crystal structure of the samples after mechanical activation. The absorption bands in the FTIR spectra of a crystallite solid are generally assigned to the vibration of ions in the crystal lattice (Nakamoto, 2009). Fig. 6.5 shows the FTIR spectra of the initial mine waste powder (FEED) and the milled powders from three mills (PM120, VM120, and SMP9) in the 4000-400 cm^{-1} range. An FTIR spectrum of a forsterite sample (fo-std) was obtained in the same way as the other samples (Fig. 6.5). The bands indicative of the characteristic peaks of forsterite appear at 1007, 986, 960, 873, and 838 cm^{-1} (SiO_4 stretching); 616, 527, and 507 cm^{-1} (SiO_4 bending); and 475 cm^{-1} for modes of octahedral MgO_6 (Barzegar Bafrooei et al., 2014). The bands related to the characteristic peak of lizardite appear at 3652 and 3688cm^{-1} (inner OH stretching) (Trittschack et al., 2012); 951 cm^{-1} (basal Si-O stretching); 1080 cm^{-1} (apical Si-O stretching); 565cm^{-1} (Si-O bending); 609 cm^{-1} (inner MgO-H bending); and 439 cm^{-1} (Mg-OH bending) (Mellini et al., 2002).

The observed bands in the FTIR spectrum for the initial powder correspond to a mixture of forsterite and lizardite. As the FTIR spectra shows in Fig. 6.5, the positions of the bands remain nearly unchanged after mechanical activation, but become more intense and well-resolved. This result can be explained by Rayleigh's equation, which shows that light scattering is related to the particle diameter (Baláž et al., 2008). The most distinct changes in FTIR spectra intensity are

evident in the sample that had been ground in the stirred mill, as nearly all of the identical peaks of forsterite and lizardite can be found in the FTIR spectra of SMP9. For example, the FTIR peaks at 986 and 960 cm^{-1} appear separatelyin SMP9, while they overlap as one peak in the other samples. The smallest changes in FTIR spectra can be found in VM120, which indicates that the particle diameter of VM120 is larger than in PM120 and SMP9. This observation is consistent with the particle-size measurements obtained via the laser-diffraction method.

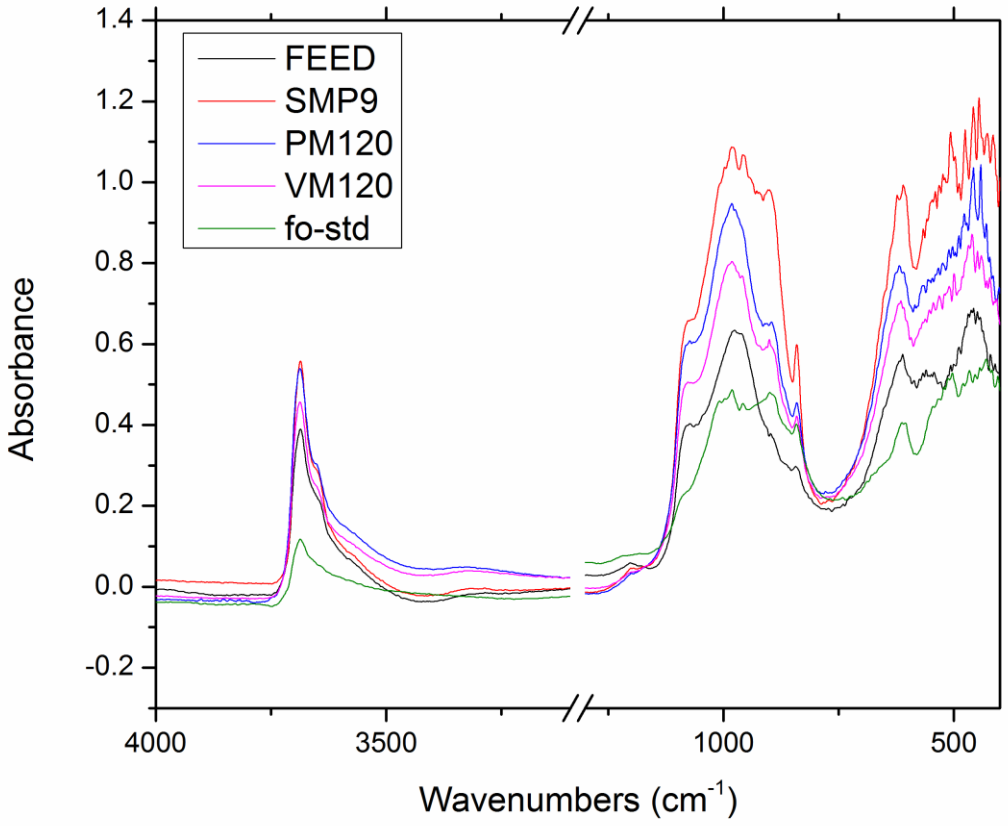

Figure 6.5 The FTIR spectra of the selected samples. The spectrum of unreacted forsterite (fo-std) is shown for reference.

The changes in the bands representing fosterite were greater than that representing lizardite in all the three mechanically-activated samples. The FTIR spectrum of SMP9 is similar to that of the forsterite standard. This indicates that forsterite undergoes size reduction to a greater extent than lizardite during mechanical activation, as the lizardite in the FEED is already fine enough to show the distinct peaks in the FTIR spectra of FEED. The changes in the bands representing fosterite in SMP9 is more distinct than PM120 and VM120, which indicate that forsterite particle in SMP9 is smaller than that in other materials and contribute a large ratio of the surface area in SMP9. Since forsterite is the main mineral being carbonated, the surface area contributed by forsterite (not S_{BET}) in the mechanically activated mine waste is an important value that controls the carbonation conversion. This could explain why the similar value of S_{BET} and $D_{V\text{-Fo}}$, result in different value of R_{X} in the mine waste materials grould in different mills (Table 6.3).

The stretching vibration band of hydroxyl groups becomes wider after dry milling in both the planetary and vibratory mills, while it remains nearly unchanged after wet grinding in the stirred mill. This indicates the disorder in or the loss of the –OH band in lizaridite after dry milling, which closely agrees with the structure and phase transfer measurements obtained during XRD analysis. Furthermore, as the grinding time was increased in all three mills, the intensity of the overlapping band in the 1100-800 cm^{-1} domain was also increased without shifting the peak's position. One possible explanation for this may be the presence of minor deformations in the SiO_4 tetrahedral. In the 400-800 cm^{-1} range, a dramatic difference between the initial material and the material after it had been milled was observed (Fig. 6.5). However, it is hard to accurately interpret the spectra in this region due to the overlapping of the vibrational modes of different bonds; in this region, it is possible to find frequencies that are characteristic of the bending vibration band of Si-

O, Mg-OH, and even of Mg-O_6. We speculate that the bands at around 450 cm^{-1} were intensely increased, broadened, and shifted to higher wavenumbers due to distortion of the Mg-O_6 octahedral or the Mg-OH octahedral as a result of mechanical activation. This speculation is supported by prior observations that note conditions wherein the MgO_6 octahedral becomes distorted while the SiO_4 tetrahedral remains unaffected when forsterite is compressed (Wang et al., 1993). Further investigation using techniques such as TGA and Mössbauer spectroscopy is required to confirm the structural and chemical changes of mine waste induced by mechanical activation.

6.4 Conclusions

This chapter investigates potential ways of enhancing mineral carbonation through the mechanical activation of ultramfic mine waste under various milling conditions. Much like pure minerals, the mechanical activation of mine waste under dry conditions tends to form agglomerate, while grinding in wet conditions tends to generate the smallest particle size and largest specific surface area. However, some particular differences were observed; these are summarized as follows:

(1) When mine waste is ground in wet conditions, the microstructure of forsterite becomes increasingly disordered while the microstructure of lizardite is not activated as the specific milling energy input increased.

(2) There is a mechanical activation limit with respect to the crystallite size of forsterite during the mechanical activation of mine waste in dry conditions. The higher the grinding intensity, the more disordered the forsterite crystal structure can become.

(3) Lizardite is dehydrated during intensive dry grinding and becomes crystallized during wet milling.

(4) The stirred mill proved to be the most effective for enhancing the reactivity of mine waste in the direct aqueous carbonation process, followed by the planetary mill and the vibratory mill, respectively.

(5) The surface area of forsterite in the mine waste, other than the surface area of the mine waste, is the important value that controls the carbonation rate of mine waste.

Chapter 7: Economic analysis on the application of mechanical activation in an integrated mineral carbonation process [6]

7.1 Introduction

Anthropogenic greenhouse gas (GHG) emissions since the pre-industrial era has widespread impacts on the natural systems (Valentin, 1993; Zadrazil and Puniya, 1994) and leads to climate change (IPCC, 2014). Carbon dioxide (CO_2) is a type of GHG (Chen et al., 2013). CO_2 emissions constitute about 70% of total GHG emissions annually, which is much larger than other GHG variations, such as methane (CH_4) and nitrous oxide (N_2O) (IPCC, 2014). Substantial and sustained reduction in CO_2 emissions is urgently required.

Mineral carbonation (MC) is part of natural silicate weathering process which occurs on a geological time scale (Bordenave et al., 2013; Favero-Longo et al., 2006; Herrera et al., 2004). During this process, CO_2 is dissolved in rain water and reacts with magnesium or calcium bearing rocks to form carbonate rocks. As a result of the formation of stable carbonates, MC has been recognized as an effective way to permanently store CO_2. Over the past two decades, CO_2 sequestration by MC has evolved as an option and is being pursued globally with hopes for its large-scale implementation. The conversion or MC processes have been accelerated using various carbonation routes and conditions, as well as pre-treatment methods for different feedstock (Power et al., 2013b). Until recently, only a few MC technologies have achieved the commercial stage. The high cost of MC (50-300 \$/t CO_2) limits their application (Sanna et al., 2014: pg. 8049). The methods reduce the cost of carbonation include using mine waste materials as feedstock (Bobicki

[6] A version of this chapter has been published. Li, J and Hitch, M., 2016. Economic analysis on the application of mechanical activation in an integrated mineral carbonation processes. International Biodeterioration & Biodegradation. In press. DOI: 10.1016/j.ibiod.2016.08.026.

et al., 2012; Bodor et al., 2013), sequestering CO_2 from flue gas directly (Pasquier et al., 2014a), producing valuable carbon products (Hemmati et al., 2014), or integrating MC into a suitable industry plant, such as ultramafic rock hosted mining deposit (Hindle, 2011).

Integrating MC into the metal mining industry has been addressed be an energy efficient way and sustainable growth method towards reducing its contribution to CO_2 emissions (Ballantyne, 2010). The suitable mining plants are usually open pit mines whose deposits are hosted by ultramafic or mafic rocks, such as nickel, diamond, chromite, and platinum group elements (PGE) mines (Hitch et al., 2010). Mining activities in these mines generate a great quantity of waste materials (i.e. waste rock, and tailings), that are mainly composed of Mg- and Ca- bearing silicates (i.e. olivine, serpentine) with huge CO_2 sequestration capacity (Hitch et al., 2010). In general, an active mine includes mining, ore processing, rock transportation, and waste materials disposal. Adding MC facilities after ore processing can utilise the fine-sized tailings as feedstock for CO_2. The CO_2 would be transported from its source after CO_2 capture and compression (Jacobs, 2014). Sharing the same infrastructure as the mine adds value to the metal products and decreases e the cost of MC (Lackner et al., 2008). At the same time, by applying MC, the mine can potentially lower the mine cut-off grade and render marginal projects economically feasible and environmentally attractive (Hitch and Dipple, 2012). In a case study of Turnagain Nickel Deposit located in northern BC, Canada, the theoretical carbonation potential was estimated to be 81.9 Mt CO_2 over a 29-year mine life (Hitch et al., 2010: pg. 73). The integrated mineral carbonation process yielded a $131.5 million of NPV at an discount rate of 8%, with a operating cost of 83$/t CO_2 (Hitch and Dipple, 2012: pg. 272). However, the parameters of these studies were assumed on the basis of literature data, which may not applicable to the mine waste materials

with complex mineralogy. An accurate estimation can be obtained through developing experimental tests on the specific mine wastes, and using advanced MC techniques.

Metallic minerals that are hosed in ultramafic rocks are commonly disseminated and need to be liberated prior to processing. In order to liberate fine-grained complex ores, grinding below 15 μm is required (Gao et al., 2002). Instead of conventional ball mills, high intensity mills are required to optimize milling efficiency relative to energy consumption. The application of high intensity mills for regrinding in mineral processing makes mechanical activation as a pre-treatment method suitable for an integrated mineral carbonation process. Fig. 7.1 shows the concept of an integrated mineral carbonation process in a nickel deposit with mechanical activation as pre-treatment.

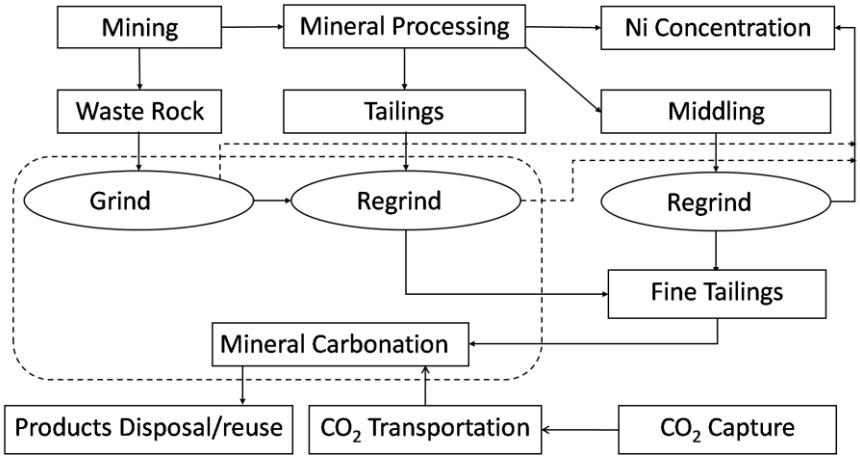

Figure 7.1 The concept of an integrated mineral carbonation process with mechanical activation as pre-treatment method.

Mechanical activation means using mechanical energy (i.e. intensive grinding) to enhance a reaction (Baláž, 2008). Research on the use of mechanical activation on magnesium silicates is constantly being advanced under various milling conditions (Baláž et al., 2008; Haug, 2010). Initially, the studies of mechanical activation have focused on pure minerals, such as olivine

(Atashin et al., 2015; Kleiv and Thornhill, 2016), serpentine (Trapasso et al., 2012; Zulumyan et al., 2011). Most recently, the ultramafic rocks with a mixture of several magnesium silicates has rouse the attention (Li and Hitch, 2016a, 2016b; Rigopoulos et al., 2016). All these studies recognized that, mechanical activation produces a large surface area and introduces imperfections to the crystal structure in the mineral. However, economic analysis and optimization as a result of mechanical activation as pretreatment, in the integrated mineral carbonation process, remains to be undertaken.

The aim of this study is to determine the feasibility of an integrated mineral carbonation process with mechanical activation as a pretreatment method. A case study was developed for the Turnagain Nickel Deposit, and the analysis was based on the economic model developed by Hitch and Dipple (2012). An IsaMill was chosen for mechanical activation, because this type of mill has been successfully applied for ultrafine grinding in mineral processing. A direct aqueous carbonation process was used to test the efficiency of mechanical activation, because it provides the most successful carbonation conversion in the literature to date.

7.2 Materials and experiments

For the experimental component, mine waste material was mechanically activated using a high-speed horizontal stirred ball mill operate in continuous mode and grinding in wet condition. Afterwards, the initial and mechanically-activated mine waste materials were carbonated in an autoclave using direct aqueous method. Characterization methods include laser diffraction, gas adsorption, and X-ray diffraction, helped to understand the changes in particle size, BET surface area, microstructure and mineralogy due to the mechanical activation. X-ray diffraction method was also used to quantify the carbonated product to obtain the carbonation conversion results.

7.2.1 Materials

The mine waste material (TAW) studied in this research comes from drill core 06110 at the Turmagain project, Hard Creek Nickel (HCN), Canada. X-ray powder diffraction (XRPD) analysis revealed the material to be composed of approximate 64.7% Forsterite (Mg_2SiO_4), 29.6% Lizardite ($Mg_3Si_2O_5(OH)_4$). Small amount of accessory minerals like magnetite, quartz and brucite were also found in the sample. As analyzed by X-ray fluorescence, the main oxides of the material were 46.64% MgO, 38.70% SiO_2, 10.39% Fe_2O_3, 0.671% Cr_2O_3, 0.30% CaO, 0.16% MnO, 0.15 % Al_2O_3, and 0.03% TiO_2. The loss on ignition (LOI) up to 1000 °C was 4.09%. The total carbon content tested using Leco method was 0.05%. The top particle size of the material was 106 μm, and its specific surface area was 3.19 m^2/g. The bond index of TAW is 3.1.

7.2.2 Mechanical activation

The mechanical activation was conducted using a 4-litre IsaMill (Netzsch, Germany), which is a high speed horizontal stirred mill. 80% of the net mill volume (2.48 L) was loaded with Keramax MT1 ceramic beads (d = 2 mm). The mill is operated in a continuous mode at 1,500 rpm for 9 cycles. For each cycle, slurry (30 wt.% solid content) was fed to the mill at the flow rate of 2 to 3 L/min, and the milled product was collected and sampled. The collected slurry was then re-fed to the mill to start the next cycle. The sampled slurry was dried in an oven at 100ºC for 12 hours. The dried samples from the feed, cycle 1, cycle 4 and cycle 9 were selected for the carbonation and characterization tests. The mechanical activation instrument, procedure, and energy consumption are the same as Chapter 4.

7.2.3 Carbonation test

Experimental mineral carbonation was performed in a 100 ml Hastelloy-4566C Parr bench-top stirred reactor. In each test, 7.5 g solid samples were added in a carbonation medium consisting

of 50 mL of 1 mol/L NaCl and 0.64 mol/L $NaHCO_3$. The carbonation condition was maintained at a temperature (T) of 185 °C, and CO_2 partial pressure (P_{CO_2}) of 60 atm., with a stirrer speed at 1500 rpm. The conditions were selected according to (Gerdemann et al., 2007). After being carbonated for 1, 2 or 6 hours, the slurry was collected and allowed to settle down overnight. The solids were filtered and dried in an oven at 100ºC for 12 hours. Representative samples were then taken for quantitative analysis. The carbonation instrument and procedure are the same as Jacobs (2014).

7.2.4 Characterization methods

The particle size of the samples was measured with a laser diffraction particle size analyzer (Mastersizer 2000, Malvern, U.K.). The specific surface area was measured by a nitrogen gas adsorption/desorption instrument (Autosorb-1MP, Quantachrome) at -196 °C using Brunauer–Emmett–Teller (BET) theory. The microstructure and quantitative analysis were based on X-ray diffraction (XRD) patterns, which were observed through a Bruker D8 Focus Bragg-Brentano diffractometer (Bruker AXS GmbH, Germany), using Co-Kα radiation with a step size of 0.03° and a recorded range from 3° to 80. The recorded XRD data were refined with the Rietveld program Topas 4.2. The Rietveld refinement procedures for quantitative analysis on mine waste rock are the same as Wilson et al. (2006), and for the microstructure characterization followed that of Chapter 3. The volume-weighted crystallite size (D_V) and strain (ε) can be obtained by Equations 7.1–7.2 (Balzar et al., 2004: pg. 917):

$$D_V = \lambda / \beta_S \cos\theta \tag{7.1}$$

$$\varepsilon = \beta_D / 4\tan\theta \tag{7.2}$$

Where, λ is the wavelength, and equals 0.1789 nm for Co Ka radiation, θ is the scattering angle, β_S is the total-size-integral breadth, and β_D is the total-strain-integral breadth.

7.3 Results and discussion

The results obtained from experiments were presented and discussed as follows. The effects of mechanical activation on the physical and structural changes in mine waste material, and the effect of mechanical activation on carbonation conversion were discussed in detail. These results were the basis for the economic analysis.

7.3.1 Mechanical activation effects

Table 7.1 lists the dependency of the specific surface area S_{BET}, crystallite size D_V, microstrain ε on specific milling energy input W_N and mechanical activation time t_{M}. The continuous increase in S_{BET}, decrease in D_V of forsterite, and increase in ε of forsterite was found with the progress of milling. However, the slightly increase in D_V of lizardite, and decrease in ε of lizardite as milling going on, indicates that the lizardite may become more crystallized. Table 7.1 also lists weight percentage of forsterite and lizardite in the initial and mechanically-activated samples. The initial and mechanically-activated samples contain 64.8±0.3% forsterite and 28.4±1.1% lizardite. Due to the detection limit of quantitative analysis by XRD being around 5% (Wilson et al., 2006: pg. 1334), the mineral phases are assumed to be unchanged during milling. A detailed study of mechanical activation on mine waste in wet conditions can be found in Chapter 4.

Table 7.1 Variation of BET surface area (S_{BET}), crystallite size (D_V), microstrain (ε), weight percentage (wt%), with mechanical activation time (t_M) and specific milling energy (W_N).

t_M (s)	W_N (kWh/t)	S_{BET} (m^2/g)	Forsterite			Lizardite		
			D_V (nm)	ε ($\times 10^3$)	wt% (%)	D_V (nm)	ε ($\times 10^3$)	wt% (%)
0	0	3.1	96.8	0.39	64.7	28.6	1.38	29.6
50	45.4	7.2	92.8	0.41	64.6	29.4	1.29	29.1
205	172.9	12.6	86.2	0.44	65.2	30.3	1.25	27.8
480	338.0	17.8	79.1	0.50	64.8	27.6	1.38	27.1

Note: W_N is the energy transferred to the powder, correspondence to the value of Cum. W_N, in Table 4.2. S_{BET} is from Table 4.3. D_V, ε and wt% come from Table A.5.

7.3.2 Mineral carbonation

The extent of carbonation is expressed by the CO_2 sequestration reaction efficiency (R_X), which is the percentage stoichiometric conversion of Mg^{2+}, Ca^{2+} and Fe^{2+} cations in silicate feed to carbonate (Equation 7.3) (Penner et al., 2004: pg. 2):

$$R_X = \frac{x_{CO_2}}{\varepsilon_A (1 - x_{CO_2})} \tag{7.3}$$

Where, ε_A is the percent weight added if all available cations are converted into carbonates, x_{CO_2} is the weight percent of CO_2 in the solid products. ε_A and x_{CO_2} were obtained through quantitative analysis on the materials before and after carbonation, respectively.

Fig. 7.2 shows the dependence of R_X on the carbonation time t_C and milling energy W_N. The R_X was initially (in the first 1 hour) found to increase quickly, but then the rate of increase slowed down as t_C increased. Mechanical activation promotes the R_X at a defined t_C up to 6 hours. After carbonation for one hour, the R_X for mechanically-activated TAW with W_N =338.0 kWh/t is 5.8 times higher than that of the initial TAW. A maximum R_X of 67.3% was reached when the

sample was ground with 172.9 kWh/t specific milling energy input and carbonated for 6 hours. It should be noted that the R_X of the sample ground with 172.9 kWh/t specific milling energy input is slightly higher than the R_X of the sample ground with 338.0 kWh/t specific milling energy input after carbonation for 6 hours. The phenomena were not in agreement with a previous study by (O'Connor et al., 2005), who found that olivine shows a continuous increase in R_X with W_N, while serpentine shows a virtually unchanged R_X with W_N. The extremely fine serpentine particles may prevent the R_X in some extent with a long time of direct aqueous carbonation. The kinetics analysis on the carbonation of mechanically activated mine waste was in Appendix B.

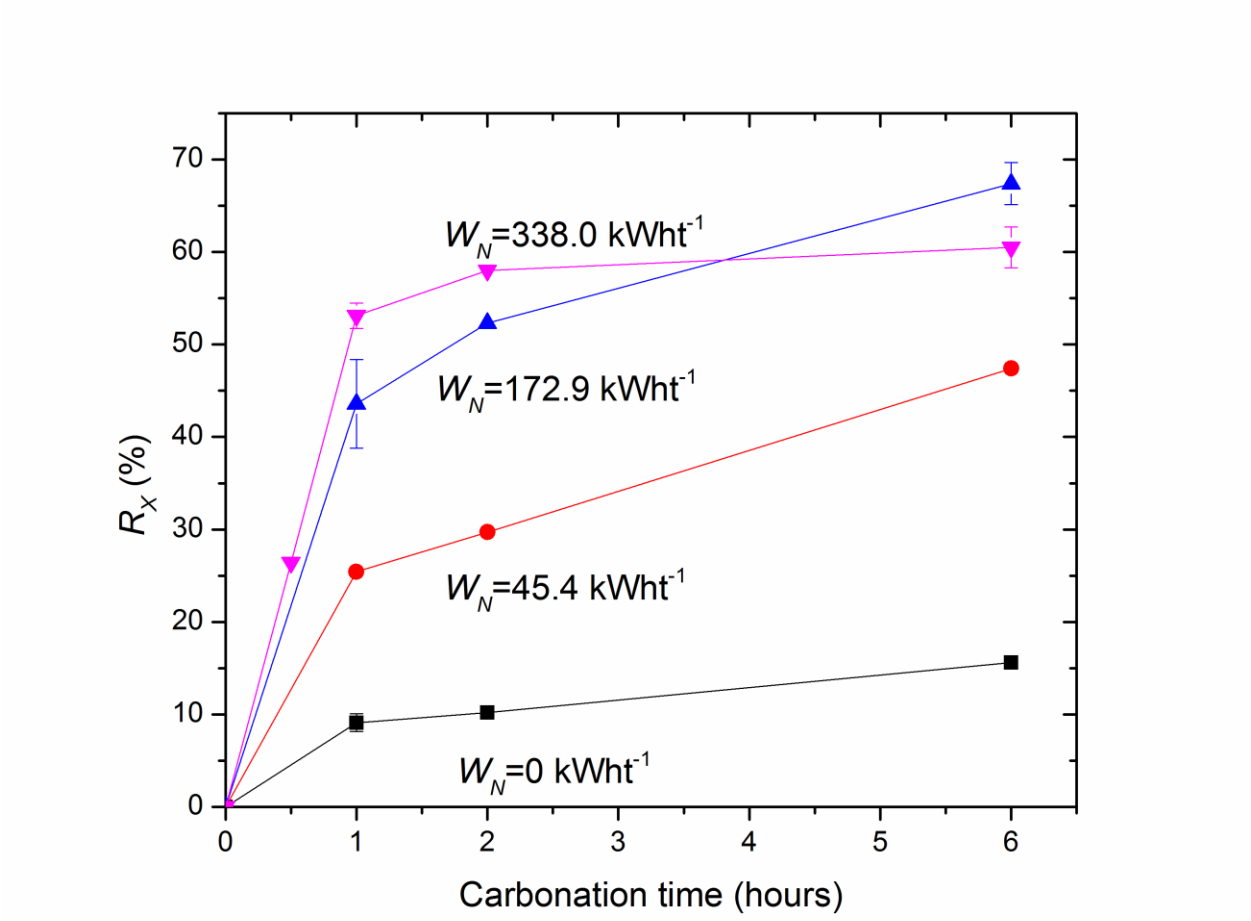

Figure 7.2 The relationship between CO_2 sequestration reaction efficiency and carbonation time. The experimental condition: 15 wt% solid content in solution containing 1M NaCl, 0.64 M $NaHCO_3$, at 185 °C, 6 MPa CO_2 partial pressure. Data with error bars are the average value from 3 tests with standard deviation.

7.4 Economic analysis

Based on the experimental results, the economic analysis on the integrated mineral carbonation process considers the energy requirements, cost modeling, and carbon balance. The feasibility of the proposed integrated mineral carbonation process was assessed, through comparing of the obtained results with literature.

7.4.1 Energy requirements of mechanical activation and mineral carbonation

One of the extinct features of IsaMill technology is its accurately one-to-one direct scale up from testwork in a 4-liter laboratory mill. Fig. 7.3 is a log-log plot of W_N versus 80% passing size (P_{80}), which is a signature plot commonly used for designing a full-scale stirred mill from lab-size tests (Glencore Technology, 2016). Fig. 7.3 show the continuous decrease in particle size with specific milling energy input. The relationship between W_N versus P_{80} from the signature plot can be expressed as Equation 7.4.

$$W_N = 1002(P_{80})^{-1.028} \tag{7.4}$$

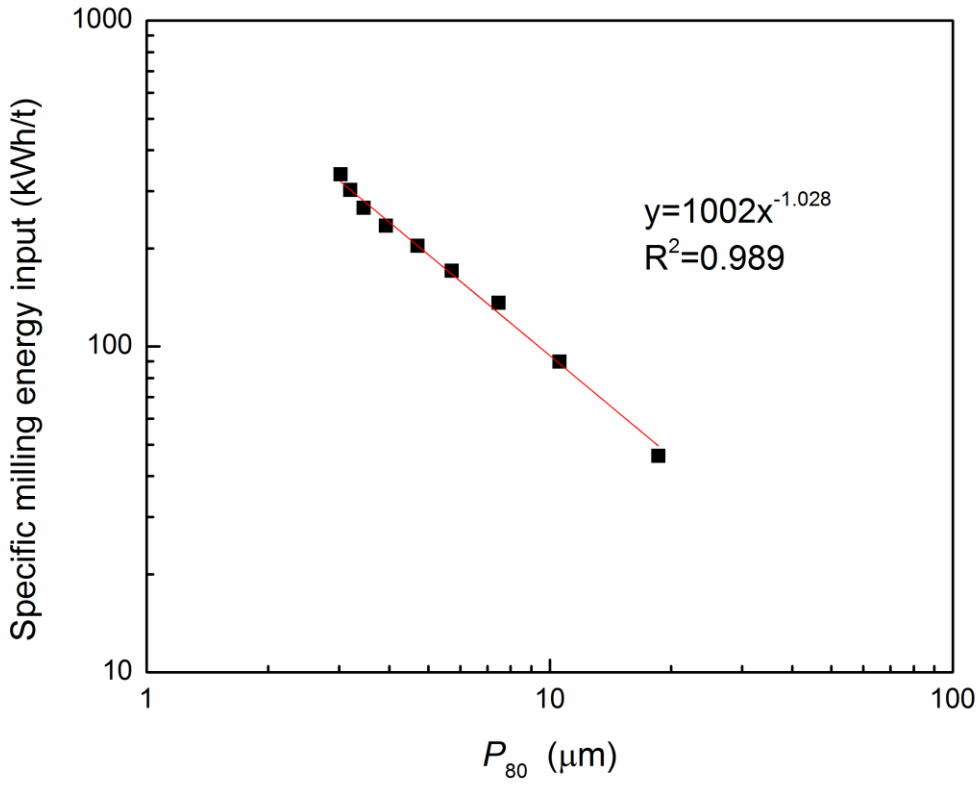

Figure 7.3 The signature plot of TAW in IsaMill.

Energy consumption from mechanical activation (E_M) is calculated according to Equation 7.5 (Haug, 2010: Part II, Paper IV, pg. 14).

$$E_M = W_{O(L)} = \frac{W_N}{\text{Energetic efficiency large mill}/100\%} \quad (7.5)$$

$W_{O(L)}$ presents an estimation for the total scale energy consumption if these mills were used in an industrial process. The IsaMill, which is a type of attritor, was assumed to have energetic efficiencies of approximately 70% (Haug, 2010: Part II, Paper IV, pg. 15). Thus, E_M of 50, 205, and 480 seconds' grinding are 95.6, 337.6 and 639.3 kWh/t, respectively.

Energy consumption for mineral carbonation (E_C) is calculated according to the feasibility study by the National Energy Technology Laboratory (NETL) (Lyons et al., 2003). The CO_2 sequestration cost is \$18 per tonne solid for one hour of carbonation at T=185 ºC P_{CO_2} =150 atm, 30% solid content, with a carrier solution of 0.64M $NaHCO_3$, 1M NaCl (O'Connor et al., 2005: pg. 11). According to the P_{CO_2} sensitivity analysis in NETL, the cost was reduced to 14 \$/t solid at P_{CO_2} =60 atm. Since the CO_2 sequestration cost is 23 \$/t solid for two hours of carbonation at P_{CO_2} =150 atm, the processing cost for sequestration in one hour is 5 \$/t solid. Assuming the reduction ratio of the processing cost is the same as that of the total CO_2 sequestration cost when lowering the P_{CO_2} , the operation cost of CO_2 sequestration is around 3.86 \$/t solid in this study. In the NETL study, the electricity price of 0.054 \$/kWh was used (O'Connor et al., 2005: pg. 16). The E_C in this study is estimated at 71.5, 143.0, and 428.9 kWh/t of carbonation for 1, 2, and 6 hours, respectively.

Fig. 7.4 compares E_M with E_C, where E_C is the operating energy consumption per tonne of TAW obtaining a 60% of R_X. The sum of E_M and E_C illustrates the total operating energy consumption per tonne of TAW carbonation associated with mechanical activation and direct aqueous carbonation. As shown in Fig. 7.4, the minimum total operation energy requirement of mechanical activation and carbonation was found at around TAW milled for 130 seconds and carbonation for 3.6 hours. The total operating energy consumption is around 470 kWh/t with E_M E_M =210 kWh/t and E_C =260 kWh/t ore.

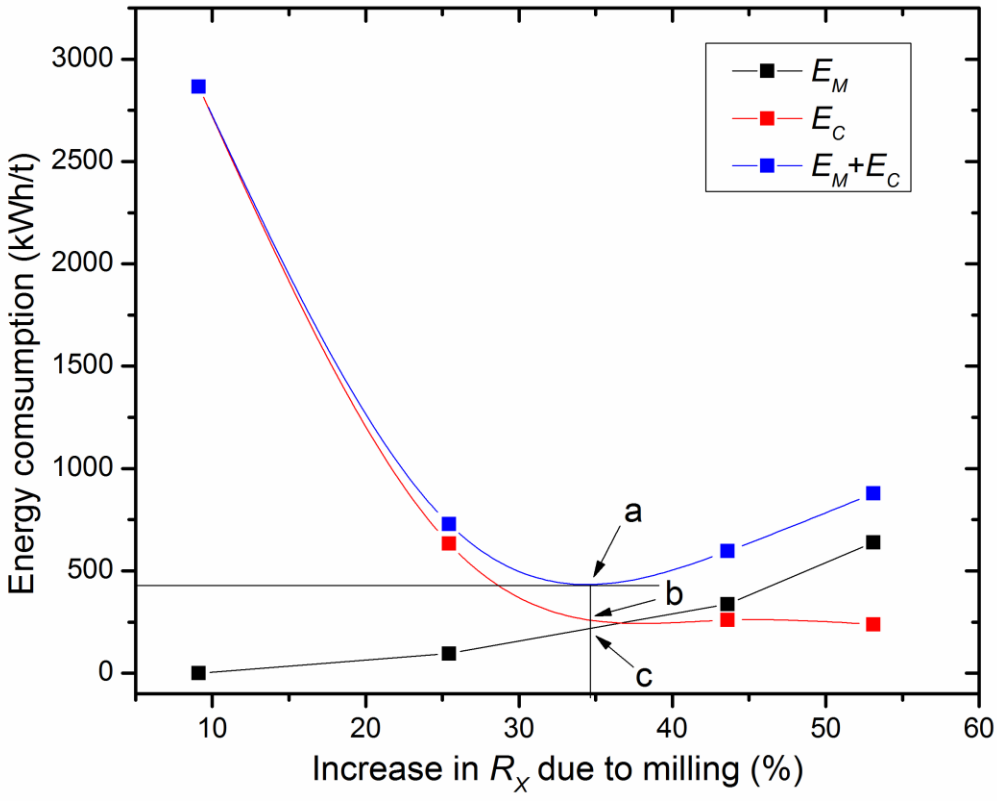

Figure 7.4 Comparison of milling energy and carbonation energy. Point a is the minimum $E_M + E_C$, point b is E_C at minimum $E_M + E_C$, point c is E_M at minimum $E_M + E_C$.

7.4.2 Cost modeling

The life cycle of a mineral carbonation process includes feedstock mining, feedstock processing, CO_2 capture, feedstock or CO_2 transportation, CO_2 sequestration and product disposal or reuse. Integrate mineral carbonation process into a mine could eliminate or minimize the cost of mining, waste disposal and feedstock process. The cost model estimates the operation cost of a mineral carbonation process added to a mine site. The evaluation was made on the basis of the amount of residues available at the nickel mine.

Table 7.2 lists the main parameters of the cost model of mineral carbonation plant at the Turnagain project, located in northern British Columbia. The source of the CO_2 is assumed from an oil and gas exploration and development 250 km away from the Turnagain deposit. CO_2 is assumed to be captured using membrane separation, the energy requirement of which is 70-75 kWh/t CO_2 captured (Khoo and Tan, 2006: pg. 213). CO_2 compression power is estimated at 100 kWh/t CO_2 captured (Nduagu et al., 2012: pg. 118). The CO_2 transportation by pipeline cost 0.02 $/km per t of CO_2 (Hitch and Dipple, 2012: pg. 272). The mechanical activation cost and CO_2 sequestration cost is on the basis of the experimental results presented in section 7.3. The current price for electricity is 0.055 $/kWh in British Columbia for large power consumption (Hydro-Québec, 2014). The optimum condition with 60% CO_2 sequestration efficiency will have a processing cost of 11.6 $/t feed (37.7 $/t CO_2) and a sequestration cost of 14.3 $/t feed (46.5 $/t CO_2).

Table 7.2 Parameters related to the cost model of the integrated mineral carbonation process (revised after Hitch and Dipple, (2012: pg. 272))

Input parameter	Unit	Base case value	References
Throughput	tpd	84,600	(AMC Consultants, 2011: pg. i)
Strip ratio	-	0.4	(AMC Consultants, 2011: pg. x)
Olivine in waste	%	64.7	This study
Wt.% MgO	Wt.%	46.64	This study
Processing cost (Ball mill to P80 =75 μm)	$/t feed	0.91	This study
Processing cost (Mechanical activation)	$/t feed	11.6	This study
Sequestration efficiency	%	60.0	This study
Sequestration operating cost	$/t feed	14.3	(O'Connor et al., 2005: pg. 16)
CO_2 capture cost (include compression cost)	$/t CO_2	9.6	(Khoo and Tan, 2006: pg. 213; Nduagu et al., 2012: pg. 118)
CO_2 transportation distance	km	250	(Hitch and Dipple, 2012: pg. 272)
CO_2 transportation cost	$/km CO_2	0.02	(Hitch and Dipple, 2012: pg. 272)
Total operation cost (Using tailings)	$/t CO_2	104	This study
Total operation cost (Using mine waste rock)	$/t CO_2	106	This study

Assuming both tailings and waste rock are available for mineral carbonation and their mineralogy are the same as the sample in use in this study, mine tailings have an 80% passing size (P80) of 75μm and are ready for direct mechanical activation in an IsaMill. However, mine waste has a large particle size around 0.1 m. The cost for size reduction to 75 μm will have to be added to the whole process. The average bond index of mine waste is 19.8 kWh/t (AMC Consultants, 2011: pg. 43). Based on the classic Bond theory (Wills and Napier-Munn, 2006), the energy consumption for size reduction from 0.1 m to 75 μm is 22.2 kWh/t. The large-scale energetic efficiency for ball mills is 90% (Musa and Morrison, 2009: pg. 596). Therefore, using waste rocks requires adding an additional 0.91 $/t ore to the processing cost for crushing and grinding to the

required feed size. In total, the operation cost is 106 \$/t CO_2 using mine waste rock and 104 \$/t CO_2 using tailings. Fig. 7.5 shows the anticipated break down of the complete cost of mineral carbonation using tailings as feedstock. The cost of processing and CO_2 sequestration take up 82.0% of the total cost.

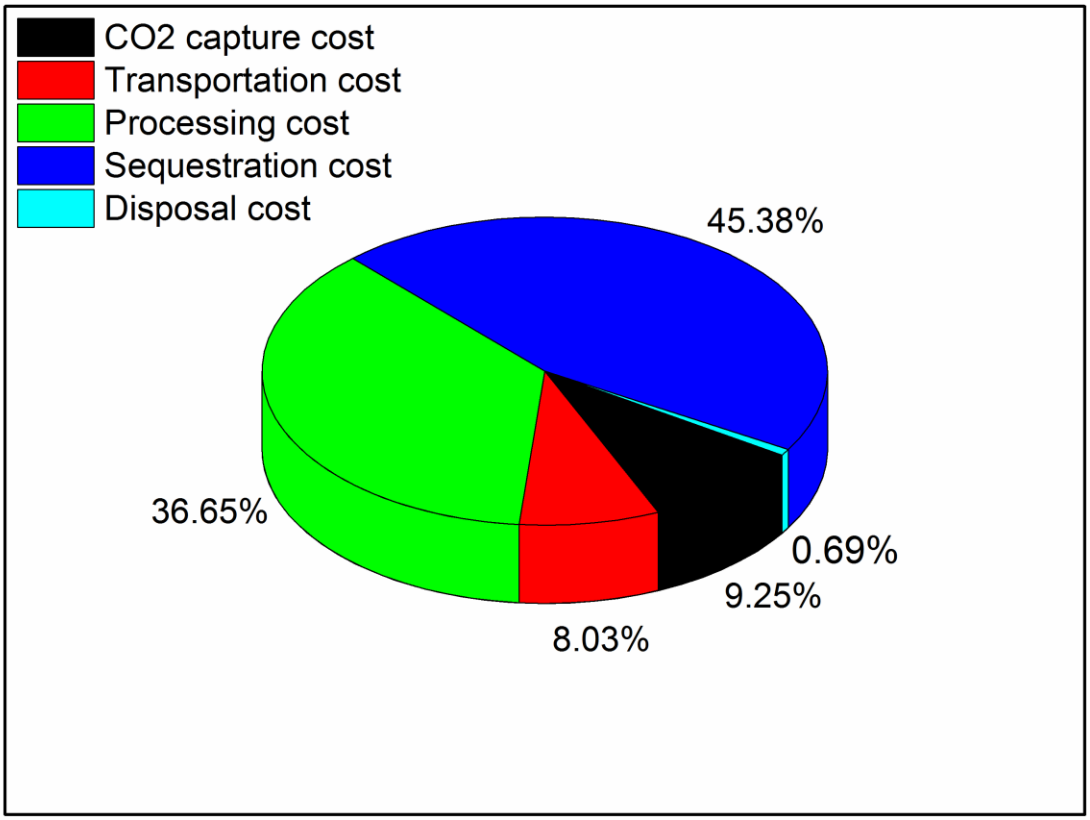

Figure 7.5 Breakdown of major cost of mineral carbonation at Turnagain.

It is important to note that all the assumptions used in the cost model have a large degree of uncertenty. The obtained carbonation cost is based on at the minmum energy requirement for mechanical activation and mineral carbonation at R_X =60%, and the most promising techniques up

to now for other steps. The calculated carbonation cost would be the minimum cost for the proposed integrated mineral carbonation process at current technology level. However, with the rapid development of technologies, the cost will be reduced in the further. Assuming a 20% error exists in the estimated operating cost. The operation cost (83-125 \$/t CO_2) is in the range of the previous estimation (28-238 \$/t CO_2) (Hitch and Dipple, 2012: pg. 272).

7.4.3 Carbon balance

The Turnagain project is proposed to be an open pit mine with throughput of an average 43,400 tonnes per day (tpd) during the first five years and an average 84,600 tpd thereafter over a 28-year mine life (AMC Consultants, 2011: pg. vi). Since the average grade of the ore is 0.21% Ni, the generation of tailings is assumed to be the same as the throughput. The strip ratio of the project is 0.4 (AMC Consultants, 2011: pg. x). The project will generate 762.9 Mt tailings and 317.9 Mt of waste rock over the life-of-mine (AMC Consultants, 2011: pg. 94). Around 35% of mine waste rock will be used for tailings dam construction (AMC Consultants, 2011: pg. 96). Assuming all tailings and the rest of the mine waste rock are available for mineral carbonation. With 60% sequestration efficiency, 1 t of mine waste could storage 0.24 t of CO_2. the carbonation sequestering capacity of tailings and waste rock are 187.9 Mt CO_2 and 50.9 Mt CO_2, respectively. The total CO_2 sequestration potential (238.8 Mt CO_2) is much higher than the estimated 64.0 Mt CO_2 given by Jacobs (2014: pg. 194). The main reason is that the CO_2 sequestration reaction efficiency is enhance from 19.9% (Jacobs, 2014: pg. 191)to 60% (this work) through the feedstock pretreatment by mechanical activation. However, this work assumes that all the mine waste materials have a consistent mineralogy (containing 64.7% olivine) (Table 7.2), which may overestimate the overall CO_2 sequestration capacity. Further experimental would focus on testing

on more samples with different ratio of olivine and serpentine, which could improve the estimation on the overall CO_2 sequestration capacity.

In the process of mineral carbonation, CO_2 emissions due to energy consumption directly contribute to the process and have to be considered when determining process feasibility. Equations. 7.6 and 7.7 define the calculation of CO_2 avoided (Hindle, 2011: pg. 13) and the CO_2 avoidance ratio (η_{CO_2}), respectively (Huijgen et al., 2006: pg. 9184).

$$CO_{2,\text{ avoided}} = CO_{2,\text{ sequestrated}} - CO_{2,\text{ emitted}} \tag{7.6}$$

$$\eta_{CO_2} = \frac{CO_{2,\text{ avoided}}}{CO_{2,\text{ sequestrated}}} = 1 - \frac{E_{\text{power}}\varepsilon_{\text{power}} + E_{\text{heat}}\varepsilon_{\text{heat}}}{CO_{2,\text{ sequestrated}}} \tag{7.7}$$

Where E_{power} is the amount of power used in the carbonation process (kWh), $\varepsilon_{\text{power}}$ is the amount of CO_2 produced when generating the necessary amount of power (kg CO_2/kWh). E_{heat} is the amount of heat used in the carbonation process (kWh), $\varepsilon_{\text{heat}}$ is the amount of CO_2 produced when generating the necessary amount of heat (kg CO_2/kWh). The value of $\varepsilon_{\text{power}}$ is 4 g of CO_2/kWh in British Columbia (BC Hydro, 2016: pg. 1), due to hydroelectric power supply for the Turnagain project (AMC Consultants, 2011: pg. vii). Table 7.3 shows the result after deriving CO_2 avoidance, with the assumption that all the energy came from power and no heat was recycled. Little difference was found before considering the CO_2 emissions.

Table 7.3 Energy consumption for the integrated mineral carbonation process using mechanical activation, with derived CO_2 avoided.

Feed stock	t_M (s)	t_C (hr)	E_{power} (kWh/t $CO_{2,Seq.}$)	$CO_{2,\ avoided}$ (Mt CO_2)	η_{CO_2}	Carbonation cost ($/t $CO_{2,avoided}$)
Waste rock	130	3.6	2275	186.2	0.991	107
Tailings	130	3.6	2220	50.4	0.991	105

7.4.4 Comparison of the obtained results with published data

In this study, the optimum condition to achieve equivalent 74% mean stoichiometric forsterite to magnesite is E_M =210 kWh/t ore mechanical activation, in 3.6 hour carbonation at 185 °C and 6 MPa, which is E_C =260 kWh/t ore. The optimum E_M is comparable to the NETL study (220 kWh/t ore), which were 70 kWh/t ore for P80 size reduction from 75 μm to 38μm, and 150 kWh/t ore for further mechanical activation (O'Connor et al., 2005: pg. 7). However, in the NETL study, about 81% carbonation of olivine in two hours at 185 °C and 15 MPa (O'Connor et al., 2005: pg. 2), the operating cost of which is $10 per tonne ore (O'Connor et al., 2005: pg. 16), corresponds 185.2 kWh/t ore. It seems our study requires additional operating cost for mineral carbonation and reaches a lower R_X than the NETL study. One reason is that the autoclave in use in this study is less efficient than that in NETL study. Jacobs (2014: pg. 88)found that the R_X obtained using the autoclave in this study is about 8% lower than that in NETL study, when the same olivine sample was carbonated at 185 °C and 6 MPa for 1 hour. Even though the operating cost for mineral carbonation from this study is higher than that found in the NETL study, when considering the capital cost, the overall cost can be balanced. The capital cost can be reduced through the lowered requirement for the instrument and the removed requirement for a booster pump (Jacobs, 2014).

Currently, 90% of electricity production in British Columbia relies on renewable, low- or no-carbon emission energy, such as the hydroelectric generation system. For such systems, the CO_2 avoidance ratio can be assumed as 1. However, most of the world's electricity supply is predominantly based on combustion processes using fossil fuels. The value for a natural gas fired system is 0.36 kg CO_2 per kWh, and for a pulverized coal fired power plant the value is 0.80 kg CO_2 per kWh (Rubin et al., 2004: pg. 4), which are significantly larger than the case in this study (2 g CO_2 per kWh). The concern over CO_2 emission arises for these processes, and the avoidance ratio has to be put into consideration, which is about 72% of sequestered CO_2 as suggested by O'Connor et al. (2005: pg. 2).

Mechanical activation of mine waste is energy intensive. 3 \$/t $CO_{2,avoided}$ can be saved when using tailings instead of mine waste. However, the 105 \$/t $CO_{2,avoided}$ is still high for application. There are some potential modifications to reduce the overall cost of the process. If using Ni-pyrometallurgical slag, which is already mechanically activated for mineral carbonation, 38.0 \$/t CO_2 can be saved. The drawback is that the Ni-pyrometallurgical slag has a limited abundance. Using flue gas directly for the carbonation avoids the requirement for a separate CO_2 capture process. Thus, 9.6 \$/t CO_2 of capture cost can be saved. While the transportation cost may increase due to the low concentration of CO_2 in flue gas, this can be balanced with reduced CO_2 capture cost. Using the carbonated product as sellable material can add values to the overall process. However, the impurity of carbonated product from a direct aqueous carbonation process limits its application. Further study could focus on choosing or developing a less expensive carbonation process that suitable for mechanically activated mine waste materials.

7.5 Conclusions

This chapter investigates the feasibility of mechanical activation of waste rock and tailings for mineral carbonation, which offers a novel way to mitigate CO_2 emissions on a mine site. There are several key findings in this study:

(1) Mechanical activation of mine waste material in a high speed stirred mill decreases the particle size, increases the surface area, changes the surface morphology, reduces the crystalinity and crystallite size of forsterite, and thus increases the CO_2 sequestration reaction efficiency in direct aqueous carbonation.

(2) The crystallinity and crystallite size of serpentine become increased during wet mechanical activation. After 6 hours carbonation, the extremely fine serpentine content in mechanically-activated mine waste material for 447.5 kWh/t of specific milling energy input prevents the direct aqueous carbonation of forsterite to some extent.

(3) To achieve 60% CO_2 sequestration efficiency, the optimum condition was found at 210 kWh/t of specific milling energy input and 260 kWh/t of energy cost in direct aqueous carbonation of mine waste at 6 MPa and 185 °C.

(4) The processing cost for the integrated carbonation process using optimum condition was found at 105 \$/t $CO_{2,avoided}$ using mine waste rock and 107 \$/t $CO_{2,avoided}$ using tailings.

(5) The Turnagain nickel project can be a medium-sized mineral carbonation plant with a total 238.8 Mt of CO_2 sequestration capacity using their mine waste rock and tailings generated due to the mining process.

Chapter 8: Conclusion and recommendation

8.1 Concluding remarks

CO_2 sequestration via mineral carbonation can permanently store CO_2 and mitigate climate change. However, the cost and reaction rate of mineral carbonation must be balanced if it is to be viable for industrial applications. This thesis has been devoted to reducing carbonation costs by using mine waste rock as a feedstock and by enhancing the reaction rate using mechanical activation as a pre-treatment method. In order to reach this objective, updated studies of mechanical activation on magnesium silicate for the purpose of mineral carbonation were reviewed (Chapter 2). This review revealed that prior studies of the mechanical activation of magnesium silicate had only focus on pure minerals. Consequently, this research examined and demonstrated three viable approaches to evaluating mechanical activation on mining waste rock for mineral carbonation. Firstly, the microstructure of olivine containing materials was accurately characterized using line profile analysis on the X-ray diffraction patterns (Chapter 3). In addition, the physical, structural and chemical changes of mechanically-activated mine waste materials were characterized, and the mechanisms of concurrently grinding olivine and serpentine in wet (Chapter 4) and dry (Chapter 5) conditions were analyzed and compared (Chapter 6). Furthermore, the feasibility of mechanical activation as pretreatment method was studied in an integrated mineral carbonation process (Chapter 7).

8.1.1 Microstructure characterization

The X-ray diffraction patterns were found to be present in response to the microstructure of olivine. Various models, including the Scherrer method, Williamson-Hall method, Multiple Whole Profile fitting method, and Rietveld method, proved useful in providing an inclusive understanding of the microstructure changes of olivine during mechanical activation.

Overall, the olivine's XRD reflection peaks were reduced in intensity, broadened, and shifted positions as specific milling energy input were increased. These changes reflect an increase in the degree of amorphization, a decrease in the crystallite size and an increase in the micro-stains, and a change in the lattice dimension, respectively. The strain value calculated by the models, from large to small, follows the order of the Scherrer method, Williamson-Hall method, Rietveld method, and MWP method, respectively. The Rietveld method, which is based on whole pattern fitting, proved to be the most suitable method for accurately characterizing the microstructure of olivine and mine waste materials containing olivine.

8.1.2 Mechanical activation

Pure olivine was ground under the same milling conditions as mechanically-activated mine waste material and was used as a control to assist in understanding the mechanism of mine waste material during mechanical activation. Planetary, vibratory, and stirred mills were used for mechanical activation. Direct aqueous carbonation experiments of milled samples as the main chemical parameter clearly indicated how milling conditions affect the process. Laser diffraction, BET surface area, SEM micrograph, XRD pattern, and FTIR spectroscopy were the main analytical methods used to describe the mechanically-activated samples.

There are some common trends of mechanical activation on olivine and mine waste material. The intensive dry grinding of materials led to the agglomeration of particles, which resulted in an increase in the particle size of the materials after their grinding limits had been reached. The minimum particle sizes of olivine and mine waste material were found at around 5000 kWh/t (18 kJ/g) and 900 kWh/t (3.24 kJ/g), respectively. However, the particle size continued to decrease during wet grinding. After 338.0-447.5 kWh/t of wet milling, the mean particle size reduced to less than 2 μm. This is likely due to the fact that water acts as dispersant that prevents

agglomeration. The specific surface area of the material increased with specific milling energy input regardless of whether mechanical activation was conducted in wet or dry conditions. After 3600 kWh/t of dry milling, the specific surface area of olivine and mine waste material was enhanced from 0.8 and 3.1 m^2/g to 2.7 and 14.3 m^2/g, respectively; after 338.0-447.5 kWh/t of wet milling, the surface areas increased from 0.7 and 3.1 m^2/g to 15.5 and 17.8 m^2/g, respectively. The specific surface area increased more quickly during wet grinding than it did during dry grinding. An increase in the degree of amorphization, the reduction of crystallite size, and the accumulation in forsterite micro-strain were also observed at specific milling energy inputs. After 3600 kWh/t of dry milling, the crystallite sizes of forsterite of olivine and mine waste decreased from 135 and 91.4 nm to 74.4 and 86.7, respectively; after 338.0-447.5 kWh/t of wet milling, they were reduced from 109.3 and 91.3 nm to 66.0 and 79.1 nm, respectively. The microstructure changes in wet grinding are comparable to those observed during dry grinding. Stirred milling in wet conditions produced the largest specific surface area, and vibratory milling in dry conditions generated the most disordered materials.

However, due to the existence of serpentine content in the mine waste material, there are several differences between the mechanical activation of mine waste material and the mechanical activation of olivine. The Moh's hardness of serpentine is lower than that of olivine. The serpentine content, which makes the mine waste materials softer than pure olivine, directly affects the grindability of mine waste materials. Compared to pure olivine, mine waste is easier to break down to a fine size during wet milling and tend to aggregate more easily in intensive dry milling. The shape of serpentine minerals is anisotropic and non-spherical, which leads to an increased rate-of-yield stress during wet milling that is times higher than that of olivine. The serpentine contents were dehydrated during intensive dry grinding, forming adsorbed water and forsterite-like material.

The small amount of water acts as lubricant during the dry mechanical activation of mine waste material and results in a surface area that is 4.2-5.2 times larger than that of mechanically-activated olivine with the same specific milling energy input. The forserite-like material prevents disorder in the crystal structure of forsterite during dry mechanical activation of the mine waste. The crystallite size of forserite in the initial mine waste is smaller than that in the initial olivine sample, while the efficiency of disordering the forsterite structure in mine waste is lower than it is in under mechanical activation. A mechanical activation limit for the reduction in the crystallite size of forsterite was found during the dry grinding of mine waste material: the higher the milling intensity, the smaller the forsterite's crystallite size will be at the mechanical activation limit.

8.1.3 Mineral carbonation

Mechanical activation promotes the CO_2 sequestration conversion. The carbonation conversion rates after subjecting the initial olivine and mine waste to one hour of direct aqueous carbonation were 5.2-6.1% and 8.7%, respectively. However, after 3600 kWh/t of dry milling in the planetary mill, the values increased to 22.5% and 31.5%, respectively; similarly, after 338.0-447.5 kWh/t of wet milling in the stirred mill the values increased to 53.1% and 51.3%, respectively. A higher of CO_2 sequestration conversion rate was obtained through mechanical activation in wet conditions than in dry conditions given the same specific milling energy input. The stirred mill proved to be the most efficient instrument for enhancing the carbonation rate via mechanical activation in a direct aqueous condition, followed by the planetary mill and the vibratory mill.

Regardless of whether grinding took place in dry or wet conditions, the CO_2 sequestration conversion of mechanically-activated mine waste material was higher than mechanically-activated pure olivine given the same specific milling energy input. For the purposes of mineral carbonation,

the mechanical activation of mine waste material is preferable to simply grinding pure olivine. Forsterite makes up the majority of the content being activated and carbonated under selected carbonation conditions with lizardite acting as catalyzer during the whole process. Thus, forsterite has to be the major mineral in mine waste material when choosing mechanical activation as the pretreatment method for direct aqueous carbonation.

8.1.4 Economic analysis

The Turnagain nickel project, which is a nickel mining operation in British Columbia, was used as a case study to test the concept of an integrated mineral carbonation process that uses mechanical activation as pre-treatment method. The feasibility study on the process was based on a life cycle analysis that considered mining, processing, CO_2 sequestration, CO_2 capture, CO_2 transportation, and product disposal. The CO_2 sequestration data came from mechanical activation of mine waste material in a high-speed stirred mill and carbonation in a direct aqueous process. The optimum condition for 60% CO_2 sequestration efficiency was found at a mechanical activation for 210 kWh/t ore and carbonation for 260 kWh/t ore. At the optimum condition, the operating cost of the overall process using tailings and waste rock as CO_2 feedstock was 104.6 \$/t $CO_{2,avoided}$ and 107.3 \$/t $CO_{2,avoided}$, respectively. During the 28-year life of the mine, the proposed integrated mineral carbonation plant using tailings and waste rock and as CO_2 feedstock can potentially sequester 187.9 Mt CO_2 and 50.9 Mt CO_2, respectively. The Turnagain nickel project can be considered a medium-sized mineral carbonation plant.

8.2 Major contribution

8.2.1 Theoretical contribution

This work represents the first time that the activation of olivine's individual microstructure characteristics (e.g. amorphization degree, lattice parameter, crystallite size, micro-strain) by

mechanical energy has been documented. The Rietveld method, which is based on full pattern fitting, proved to be suitable for characterizing the microstructure of olivine and olivine-containing materials.

This work first investigated the use of mechanical activation on mine waste materials made up of olivine and serpentine. The interactions between the minerals were studied using various characterization methods. Due to the presence of serpentine in the mine waste, enhanced surface area formation and reduced forsterite structure disordering were observed during mechanical activation. This observation is highly significant, as partially serpentinized-olivine is the most common form of ultramafic rock throughout the world.

Mechanical activation is a fast and effective way to improve the carbonation conversion of mine waste. The increase in surface area, disorder in forsterite structure, and dehydration of serpentine leads to enhanced CO_2 uptake. Mechanically-activated mine waste has a higher carbonation conversion rate than pure olivine given the same specific milling energy input and the same milling conditions. This work denotes the first time that the mechanical activation of mine waste has been reported to enhance mineral carbonation.

8.2.2 Applied contribution

This work stands as an exclusive approach to CO_2 sequestration via mineral carbonation. Pre-treatment by mechanical activation has been developed to enhance the carbon sequestration capacity of mine waste, and its application can potentially liberate fine-size ore particles and therefore recover more metals. As a result, mechanical activation can potentially turn a marginal mining project into an economically favorable one. In other words, pre-treatment of ultramafic mine waste material via mechanical activation makes the integrated mineral carbonation process in an ultramafic mining operation both environmentally and economically feasible.

A pilot scale stirred mill operated in a continuous mode was first used for the mechanical activation of magnesium silicate for mineral carbonation. The experimental data could be upscaled in a full size mill, which could then be directly applied in a mineral processing plant.

The cost model of the integrated mineral carbonation process in a nickel mine was improved using mechanical activation as pretreatment method and the advanced CO_2 capture technology.

8.3 Suggestions and recommendations

Investigations into the mechanical activation of mine waste for mineral carbonation are only in their infancy. More work that explores micro-structure is recommended; in addition, it would be useful to further examine grinding variables in order to fully understand what kinds of defects are formed in the crystals of magnesium silicates co-ground under different mechanical actions, and the influence that these defects exert on reactivity in various types of carbonation processes. This study can be expanded upon in three key respects: experimental studies, analytical methods, and application consideration.

8.3.1 Experimental studies

Further experiments and research on mechanical activation are recommended. In particular, it would be useful to extend the experiments in this study to other types of mine waste—for example, olivine with a different degree of serpentization, or peridotites (i.e. forsterite, and enstatite) with different types of weathering (i.e. serpentization, carbonation)—to investigate possible structural and chemical changes in the minerals and the effects on their reactivity caused by mechanical activation. Continued research into the mechanical activation of these naturally occurring rocks is of importance for the large scale application of mineral carbonation.

Systematic investigations on the effects of grinding variables—such as process-state variables (e.g. particle size and distribution shape of feed, solid density, slurry density, slurry flow rate and slurry rheology), and mill configuration variables (e.g. impellor design, mill speed or frequency, media size, media load, and media density)—are necessary in order to optimize the mills. In order to compare the efficiency of different mills, more work should be done to improve the experimental designs and based on a proper definition of milling intensity.

Further investigation should focus on optimizing the carbonation of mechanical-activated feedstock. For direct aqueous carbonation, it would be useful to examine how temperature, pressure, and inorganic or organic additives affect the carbonation of mechanically-activated feedstock. Other methods of mineral carbonation have also been suggested for testing the effect of mechanical activation of mine waste materials, such as the indirect aqueous carbonation process developed at the Åbo Akademi University (ÅAU) in Finland, which is suitable for serpentine carbonation and can compete economically with the direct aqueous carbonation process adopted in this work.

8.3.2 Analytical methods

The Rietveld method is recommended for microstructure characterization when different phases exist or a mineral contains several diffraction peaks. However, the combination of the Fourier transform method and the Rietveld method appears promising for investigating each mineral's detailed microstructure information (e.g. the crystallite size distribution and strain structure) and should therefore be investigated further.

Additional work should also be conducted on the microstructure characters versus the reaction kinetics in order to generate a correlation that can be used for a quick preliminary prediction of the carbonation sequestration potential of mine waste materials. Geochemical

modeling is recommended for the interpretation of the experiments and the perdition of the extent of reaction.

8.3.3 Application considerations

To apply the proposed technique in a mineral processing plant, a complete, detailed analysis of the froth flotation of mechanically-activated ultramafic nickel ores should be performed. Doing so would allow for enhanced ore recovery due to the potential liberation of fine pentlandite particles and the dehydration of serpentine, which is a problematic mineral in flotation.

The utilization of the carbonated products is important and should be investigated further. The proposed process yields fine products, which are mixtures containing magnesium silicate, magnesium carbonate, amorphous silica, and iron oxides. If the carbonated products can be turned into valuable materials such as construction material and aggregates, the project would be able to be applied on a commercial scale due to the cost reduction in waste disposal and the value generated from by-products.

The cost model of the integrated mineral carbonation process is improved with experimental data and shows a promising CO_2 avoidance value. The discount cash flow approach and sensitivity analysis are recommended methods for further investigation. Life cycle assessment on the environmental aspect of the project is also suggested to aid in decision making.

Bibliography

Abdellahi, M., Bahmanpour, M., 2015. Rapid synthesis of nanopowders in high energy ball milling; Optimization of milling parameters. Ceram. Int. 41, 1631–1639.

Adjaoud, O., Marquardt, K., Jahn, S., 2012. Atomic structures and energies of grain boundaries in Mg_2SiO_4 forsterite from atomistic modeling. Phys. Chem. Miner. 39, 749–760.

Alex, T.C., Kumar, R., Roy, S.K., Mehrotra, S.P., 2014. Mechanically induced reactivity of gibbsite: Part 1. Planetary milling. Powder Technol. 264, 105–113.

Alexander, L., Klug, H.P., 1948. Basic aspects of X-ray absorption in quantitative diffraction analysis of powder mixtures. Anal. Chem. 20, 886–889.

AMC Consultants, 2011. Turnagain Project Hard Creek Nickel Corporation Preliminary Economic Assessment. Vancouver, BC.

Assima, G.P., Larachi, F., Beaudoin, G., Molson, J., 2013. Dynamics of carbon dioxide uptake in chrysotile mining residues – Effect of mineralogy and liquid saturation. Int. J. Greenh. Gas Control 12, 124–135.

Assima, G.P., Larachi, F., Molson, J., Beaudoin, G., 2014. Comparative study of five Québec ultramafic mining residues for use in direct ambient carbon dioxide mineral sequestration. Chem. Eng. J. 245, 56–64.

Atashin, S., Wen, J.Z., Varin, R.A., 2015. Investigation of milling energy input on structural variations of processed olivine powders for CO_2 sequestration. J. Alloys Compd. 618, 555–561.

Atashin, S., Wen, J.Z., Varin, R.A., 2016. Optimizing milling energy for enhancement of solid-state magnesium sulfate ($MgSO_4$) thermal extraction for permanent CO_2 storage. RSC Adv. 6, 68860–68869.

Avvakumov, E., Senna, M., Kosova, N., 2001. Soft mechnochemical synthesis, A basics for new chemical technologies. Kluwer Academic Publishers, New York, Boston, Dordrecht, London, Moscow.

Azapagic, A., Cue, R.M., 2015. Carbon capture, storage and utilisation technologies: A critical analysis and comparison of their life cycle environmental impacts. J. CO_2 Util. 9, 82–102.

Azdarpour, A., Asadullah, M., Mohammadian, E., Hamidi, H., Junin, R., Karaei, M.A., 2015. A review on carbon dioxide mineral carbonation through pH-swing process. Chem. Eng. J. 279, 615–630.

Baláz, P., 2003. Mechanical activation in hydrometallurgy. Int. J. Miner. Process. 72, 341–354.

Baláž, P., 2008. Mechanochemistry in nanoscience and minerals engineering. Springer, Verlag Berlin Heidelberg.

Baláž, P., Turianicová, E., Fabián, M., Kleiv, R.A., Briancin, J., Obut, A., 2008. Structural changes in olivine $(Mg, Fe)_2SiO_4$ mechanically activated in high-energy mills. Int. J. Miner. Process. 88, 1–6.

Ballantyne, S.M., 2010. Greenhouse Gas Emissions in mining operations: Challenges and opportunities in British Columbia, Canada. Univerisity of British Columbia.

Balucan, R.D., Dlugogorski, B.Z., 2013. Thermal activation of antigorite for mineralization of CO_2. Environ. Sci. Technol. 47, 182–190.

Balzar, D., 1999. Voigt-function model in diffraction line-broadening analysis, in: Snyder, R.L., Bunge, H.J., Fiala, J. (Eds.), Microstructure Analysis from Diffraction. Oxford university, New York, pp. 94–126.

Balzar, D., Audebrand, N., Daymond, M.R., Fitch, A., Hewat, A., Langford, J.I., Le Bail, A., Louër, D., Masson, O., McCowan, C.N., Popa, N.C., Stephens, P.W., Toby, B.H., 2004. Size-strain line-broadening analysis of the ceria round-robin sample. J. Appl. Crystallogr. 37, 911–924.

Barthelmy, D., 2014. Mieralogy Database. http://webmineral.com/

Barzegar Bafrooei, H., Ebadzadeh, T., Majidian, H., 2014. Microwave synthesis and sintering of forsterite nanopowder produced by high energy ball milling. Ceram. Int. 40, 2869–2876.

BC Hydro, 2016. Greenhouse Gas Intensities.

Bobicki, E.R., 2014. Pre-treatment of ultramafic nickel ores for improved mineral carbon sequestration. University of Alberta.

Bobicki, E.R., Liu, Q., Xu, Z., 2014. Microwave heating of ultramafic nickel ores and mineralogical effects. Miner. Eng. 58, 22–25.

Bobicki, E.R., Liu, Q., Xu, Z., 2015. Mineral carbon storage in pre-treated ultramafic ores. Miner. Eng. 70, 43–54.

Bobicki, E.R., Liu, Q., Xu, Z., Zeng, H., 2012. Carbon capture and storage using alkaline industrial wastes. Prog. Energy Combust. Sci. 38, 302–320.

Bodénan, F., Bourgeois, F., Petiot, C., Augé, T., Bonfils, B., Julcour-Lebigue, C., Guyot, F., Boukary, A., Tremosa, J., Lassin, A., Gaucher, E.C., Chiquet, P., 2014. Ex situ mineral carbonation for CO_2 mitigation: Evaluation of mining waste resources, aqueous carbonation processability and life cycle assessment (Carmex project). Miner. Eng. 59, 52–63.

Bodor, M., Santos, R.M., Gerven, T., Vlad, M., 2013. Recent developments and perspectives on the treatment of industrial wastes by mineral carbonation - a review. Cent. Eur. J. Eng. 3, 566–584.

Boldyrev, V. V., 2006. Mechanochemistry and mechanical activation of solids. Russ. Chem. Rev. 75, 177–189.

Boldyrev, V.V., Pavlov, S.V., Goldberg, E.L., 1996. Interrelation between fine grinding and mechanical activation. Int. J. Miner. Process. 44-45, 181–185.

Boot-Handford, M.E., Abanades, J.C., Anthony, E.J., Blunt, M.J., Brandani, S., Mac Dowell, N., Fernandez, J.R., Ferrari, M.-C.M.-C., Gross, R., Hallett, J.P., Haszeldine, R.S., Heptonstall, P., Lyngfelt, A., Makuch, Z., Mangano, E., Porter, R.T.J., Pourkashanian, M., Rochelle, G.T., Shah, N., Yao, J.G., Fennell, P.S., Fernández, J.R., Ferrari, M.-C.M.-C., Gross, R., Hallett, J.P., Haszeldine, R.S., Heptonstall, P., Lyngfelt, A., Makuch, Z., Mangano, E., Porter, R.T.J.,

Pourkashanian, M., Rochelle, G.T., Shah, N., Yao, J.G., Fennell, P.S., 2014. Carbon capture and storage update. Energy Environ. Sci. 7, 130–189.

Bordenave, S., Chatterjee, I., Voordouw, G., 2013. Microbial community structure and microbial activities related to CO_2 storage capacities of a saalt cavern. Int. Biodeterior. Biodegradation 81, 82–87.Bragg, W.L., 1913. The diffraction of short electromagnetic waves by crystals. Proceeding R. Soc. London A 88, 428–438.

Bragg, W.L., 1913. The diffraction of short electromagnetic waves by crystals. Proceeding R. Soc. London A 88, 428–438.

Bruker Axs GmbH, 2009. Topas 4.2 Tutorial. Karlsruhe, Germany.

Bruno, M., Massaro, F.R., Prencipe, M., Demichelis, R., Pierre, M.D. La, Nestola, F., Caluso, V.V., Geoscienze, D., Gradenigo, V., 2014. Ab Initio calculations of the main crystal surfaces of forsterite (Mg_2SiO_4): a preliminary study to understand the nature of geochemical processes at the olivine interface. J. Phys. Chem. C 118, 2498–2506.

Case, D.H., Wang, F., Giammar, D.E., 2011. Precipitation of magnesium carbonates as a function of temperature, solution composition, and presence of a silicate mineral substrate. Environ. Eng. Sci. 28, 881–889.

Cheary, R.W., Coelho, A., 1992. A fundamental parameters approach to X-ray line-profile fitting. J. Appl. Crystallogr. 25, 109–121.

Chen, Q., Ma, J., Liu, J., Zhao, C., Liu, W., 2013. Characteristics of greenhouse gas emission in the Yellow River Delta wetland. Int. Biodeterior. Biodegradation 85, 646–651.

Chung, F.H., 1974. Quantitative interpretation of X-ray diffraction patterns of mixtures. II. Adiabatic principle of X-ray diffraction analysis of mixtures. J. Appl. Crystallogr. 7, 526–531.

Ciullo, P.A., 1996. Silicate structures, in: Industrial Minerals and Their Uses -A Handbook and Formulary. William Andrew Publishing/Noyes, Westwood, New Jesey, pp. 1–16.

Couvy, H., Frost, D.J., Heidelbach, F., Nyilas, K., Ungár, T., Mackwell, S., Cordier, P., 2004. Shear deformation experiments of forsterite at 11 GPa - 1400°C in the multianvil apparatus. Eur. J. Mineral. 16, 877–889.

Cowie, J., 2013. Climate Change: Biological and Human Aspects. Cmbridge University Press.

Declercq, J., Bosc, O., Oelkers, E.H., 2013. Do organic ligands affect forsterite dissolution rates? Appl. Geochem. 39, 69–77.

Dlugogorski, B.Z., Balucan, R.D., 2014. Dehydroxylation of serpentine minerals: Implications for mineral carbonation. Renew. Sustain. Energy Rev. 31, 353–367.

Doucet, F.J., 2011. Scoping study on CO_2 mineralization technologies. Pretoria.

Drief, A., Nieto, F., 1999. The effect of dry grinding on antigorite from mulhacen, Spain. Clays Clay Miner. 47, 417–424.

Fabian, M., Shopska, M., Paneva, D., Kadinov, G., Kostova, N., Turianicová, E., Briančin, J., Mitov, I., Kleiv, R.A., Baláž, P., 2010. The influence of attrition milling on carbon dioxide sequestration on magnesium–iron silicate. Miner. Eng. 23, 616–620.

Fagerlund, J., Highfield, J., Zevenhoven, R., 2012. Kinetics studies on wet and dry gas–solid carbonation of MgO and $Mg(OH)_2$ for CO_2 sequestration. RSC Adv. 2, 10380.

Favero-Longo, S.E., Castelli, D., Salvadori, O., Belluso, E., Piervittori, R., 2006. Pedogenetic action of the lichens Lecidea atrobrunnea, Rhizocarpon geographicum gr. and Sporastatia testudinea on serpentinized ultramafic rocks in an alpine environment. Int. Biodeterior. Biodegradation 56, 17–27.

Gadikota, G., Fricker, K., Jang, S.-H., Park, A.-H.A., 2015. Carbonation of silicate minerals and industrial wastes and their potential use as sustainable construction materials, in: Advances in CO_2 Capture, Sequestration, and Conversion. Washington DC, pp. 295–322.

Gao, M., Young, M., Allum, P., 2002. IsaMill fine grinding technology and its industrial applicaiton at Mount Isa mine, in: 34th Annual Meeting of The Canadian Mineral Processors. pp. 1–18.

Geerlings, H., Zevenhoven, R., 2013. CO_2 mineralization-bridge between storage and utilization of CO_2. Annu. Rev. Chem. Biomol. Eng. 4, 103–17.

Gerdemann, S.J., O'Connor, W.K., Dahlin, D.C., Penner, L.R., Rush, H., 2007. Ex situ aqueous mineral carbonation. Environ. Sci. Technol. 41, 2587–93.

Ghacham, A. B., Cecchi, E., Pasquier, L.-C., Blais, J.-F., Mercier, G., 2015. CO_2 sequestration using waste concrete and anorthosite tailings by direct mineral carbonation in gas-solid-liquid and gas-solid routes. J. Environ. Manage. 163, 70–77.

Giannoulakis, S., Volkart, K., Bauer, C., 2014. Life cycle and cost assessment of mineral carbonation for carbon capture and storage in European power generation. Int. J. Greenh. Gas Control 21, 140–157.

Glencore Technology, 2016. IsaMillTM Breakign the boundaries. http://www.isamill.com/EN/IsaMillsAdvantages/Pages/AccurateScaleUp.aspx

Glinnemann, J., King Jr., H.E., Schulz, H., Hahn, T., La Placa, S.J., Dacol, F., 1992. Crystal structures of the low-temperature quartz-type phases of silica and germanium dioxide at elevated pressure. Z. Krist. 198, 177–212.

Global CCS Institution, 2016. Large Scale CCS Projects. http://www.globalccsinstitute.com/projects/large-scale-ccs-projects (accessed 10.4.16).

GMD, 2016. Trends in atomospheric carbon dioxide. http://www.esrl.noaa.gov/gmd/ccgg/trends/data.html (accessed 9.18.16).

Goff, F., Guthrie, G.D., Lipin, B., Fite, M., Chipera, S., Counce, D., Kluk, E., Ziock, H., 2000. Evalustion of ultramafic deposites in eastern United States and Puerto Rico as sources of mgnesium of carbon dioxide sequestration. LA-13694-MS. Los Alamos National Laboratory. Los Alamos, New Mexico.

Goldich, S.S., 1938. A Study in Rock-Weathering. J. Geol. 46, 17–58.

Gualtieri, A.F., Giacobbe, C., Viti, C., 2012. The dehydroxylation of serpentine group minerals. Am. Mineral. 97, 666–680.

Gualtieri, M.L., Romagnoli, M., Miselli, P., Cannio, M., Gualtieri, A.F., 2012. Full quantitative phase analysis of hydrated lime using the Rietveld method. Cem. Concr. Res. 42, 1273–1279.

Guthrie, G.D., Carey, J.W., Bergfeld, D., Byler, D., Chipera, S., Ziock, H., Lackner, K.S., 1999. Geochemical aspects of the carbonation of magnesium silicates in an aqueious medium. Los Alamos, New Mexico.

Halder, S.K., Tisljar, J., 2013. Basic Mineralogy, in: Introduction to Mineralogy and Petrology. Elsevier Science, Saint Louis, pp. 39–79.

Hänchen, M., 2007. CO_2 storage by aqueous mineral carbonation: olivine dissolution and precipitation of Mg-carbonates. ETH ZURICH.

Hänchen, M., Prigiobbe, V., Baciocchi, R., Mazzotti, M., 2008. Precipitation in the Mg-carbonate system - effects of temperature and CO_2 pressure. Chem. Eng. Sci. 63, 1012–1028.

Harrison, A.L., 2014. Mechanisms of carbon mineralization form the pore to field scale: implications for CO_2 sequestration. The University of British Columbia.

Harrison, A.L., Power, I.M., Dipple, G.M., 2013. Accelerated carbonation of brucite in mine tailings for carbon sequestration. Environ. Sci. Technol. 47, 126–34.

Haug, T.A., 2010. Dissolution and carbonation of mechanically activated olivine. Norwegian University of Science and Technology.

Haug, T.A., Kleiv, R.A., Munz, I.A., 2010. Investigating dissolution of mechanically activated olivine for carbonation purposes. Appl. Geochem. 25, 1547–1563.

Haynes, W.M., 2014. CRC handbook of chemistry and physics, 95th ed. Apple Academic Press Inc.

He, M., Wang, Y., Forssberg, E., 2004. Slurry rheology in wet ultrafine grinding of industrial minerals: a review. Powder Technol. 147, 94–112.

Hemmati, A., Shayegan, J., Sharratt, P., Yeo, T.Y., Bu, J., 2014. Solid products characterization in a multi-step mineralization process. Chem. Eng. J. 252, 210–219.

Herrera, L.K., Arroyave, C., Guiamet, P., Saravia, S.G. de, Videla, H., 2004. Biodeterioration of peridotite and other constructional materials in a building of the Colombian cultural heritage. Int. Biodeterior. Biodegradation 54, 135–141.

Herzog, H., 2016. Lessons Learned from CCS Demonstration and Large Pilot Projects. Cambridge, MA, USA.

Highfield, J., Lim, H., Fagerlund, J., Zevenhoven, R., 2012. Mechanochemical processing of serpentine with ammonium salts under ambient conditions for CO_2 mineralization. RSC Adv. 2, 6542–6548.

Hindle, S.R., 2011. Feasibility and sensitivity analysis of integrating mining and mineral carbonation: A case study of the Turnagain Nickel Project. University of British Columbia.

Hitch, M., Ballantyne, S.M., Hindle, S.R., 2010. Revaluing mine waste rock for carbon capture and storage. Int. J. Mining, Reclam. Environ. 24, 64–79.

Hitch, M., Dipple, G.M., 2012. Economic feasibility and sensitivity analysis of integrating industrial-scale mineral carbonation into mining operations. Miner. Eng. 39, 268–275.

Hövelmann, J., Austrheim, H., Beinlich, A., Munz, I.A., 2011. Experimental study of the carbonation of partially serpentinized and weathered peridotites. Geochim. Cosmochim. Acta

75, 6760–6779.

Hrsak, D., Sucik, G., Lazic, L., 2008. The thermophysical properties of serpentinite. Metalurgija 47, 29–31.

Huijgen, W.J.J., Ruijg, G.J., Comans, R.N.J., Witkamp, G.-J., Equipment, P., 2006. Energy consumption and net CO_2 sequestration of aqueous mineral carbonation. Ind. Eng. Chem. Res. 45, 9184–9194.

Huijgen, W.J.J., Comans, R.N.J., 2003. Carbon dioxide sequestration by mineral carbonation. Report No. ECN-C--03-016. Energy research Centre of the Netherlands. Petten, the Netherlands.

Huijgen, W.J.J., Comans, R.N.J., 2005. Carbon dioxide sequestration by mineral carbonation, Literature review update 2003-2004. Report No. 2005/11 ECN-C--05-022. Energy research Centre of the Netherlands. Petten, the Netherlands.

Hurlbut, C.S., Sharp, W.E., 1998. Dana's minerals and how to study them, 4th ed. John Wiley & Sons, New York.

Hydro-Québec, 2014. Comparison of electricity prices in major north American cities: Rates effective April 1, 2014. Montreal,Canada.

IEA, 2013. CO_2 emissions from fuel combustion—highights. Paris, France.

IPCC, 2005. IPCC special report on carbon dioxide capture and storage. Cambridge University Press, Cambridge, United Kingdom/New York, NY, USA.

IPCC, 2013. Climate change 2013: The physical science basis. Cambridge University Press, Cambridge, United Kingdom/New York, NY, USA.

IPCC, 2014. Climate change 2014: Synthesis report. Contribution of working groups I, II and III to the fifth assessment report of the Intergovernmental Panel on Climate Change. IPCC, Geneva, Switzerland.

Jacobs, A.D., 2014. Quantifying the mineral carbonation potential of mine waste mineral: a new parmeter for geospatial estimation. University of British Columbia.

Jacobs, A.D., Hitch, M., 2011. Experimental mineral carbonation: approaches to accelerate CO_2 sequestration in mine waste materials. Int. J. Mining, Reclam. Environ. 25, 321–331.

Jankovic, A., 2003. Variables affecting the fine grinding of minerals using stirred mills. Miner. Eng. 16, 337–345.

Jones, D.G., Beaubien, S.E., Blackford, J.C., Foekema, E.M., Lions, J., De Vittor, C., West, J.M., Widdicombe, S., Hauton, C., Queirós, A.M., 2015. Developments since 2005 in understanding potential environmental impacts of CO_2 leakage from geological storage. Int. J. Greenh. Gas Control 40, 350–377.

Kalinkin, A.M., 2009. Kinetics of carbon disoxide mechanosorption by Ca-containing silicates, CO_2 release on heating of mechanically activated samples. J. Therm. Anal. 95, 105–110.

Kalinkin, A.M., Kalinkina, E. V., Zalkind, O.A., 2009. Mechanosorption of carbon dioxide by Ca- and Mg-containing silicates and alumosilicates. Sorption of CO_2 and structure-related chemical changes. Colloid J. 71, 185–192.

Kalinkina, E. V., Kalinkin, A.M., Forsling, W., Makarov, V.N., 2001. Sorption of atmospheric carbon dioxide and structural changes of Ca and Mg silicate minerals during grinding I. Diopside. Int. J. Miner. Process. 61, 273–288.

Keeling, R., 2015. Scripps Institution of Oceanography. www.scrippsco2.ucsd.edu/

Kenarsari, S.D., Yang, D., Jiang, G., Zhang, S., Wang, J., Russell, A.G., Wei, Q., Fan, M., 2013. Review of recent advances in carbon dioxide separation and capture. RSC Adv. 3, 22739–22773.

Kerisit, S., Bylaska, E.J., Felmy, A.R., 2013. Water and carbon dioxide adsorption at olivine surfaces. Chem. Geol. 359, 81–89.

Khoo, H.H., Sharratt, P.N., Bu, J., Yeo, T.Y., Borgna, A., Highfield, J.G., Björklöf, T.G., Zevenhoven, R., 2011. Carbon capture and mineralization in singapore: Preliminary environmental impacts and costs via LCA. Ind. Eng. Chem. Res. 50, 11350–11357.

Khoo, H.H., Tan, R.B.H., 2006. Life cycle evaluation of CO_2 recovery and mineral sequestration alternatives. Environ. Prog. 25, 208–217.

Killops, S.D., Killops, V.., 2005. Introduction to organic geochemistry, 2nd ed. Blackwell Publishing.

Kim, D., Chung, H., 2002. Effect of grinding on the structure and chemical extraction of metals from serpentine. Part. Sci. Technol. 20, 159–168.

Kim, D.J., Sohn, J.S., Ahn, J.G., Chung, H.S., 2008. Extraction of metals from mechanically milled serpentine. Geosystem Eng. 11, 25–28.

Kirchofer, A., Becker, A., Brandt, A., Wilcox, J., 2013. CO_2 mitigation potential of mineral carbonation with industrial alkalinity sources in the United States. Environ. Sci. Technol. 47, 7548–7554.

Klein, B., Laskowski, J.S., Partridge, S.J., 1995. A new viscometer for rheological measurements on settling suspensions. J. Rheol. (N. Y. N. Y). 39, 827–840.

Klein, C., Hurlbut, C.S., Dana, J.D., 1993. Manual of Mineralogy. John Wiley & Sons, New York.

Kleiv, R.A., Thornhill, M., 2006. Mechanical activation of olivine. Miner. Eng. 19, 340–347.

Kleiv, R.A., Thornhill, M., 2016. The effect of mechanical activation in the production of olivine surface area. Miner. Eng. 89, 19–23.

Kruse, N.A., Strosnider, W.H.J., 2015. Carbon dioxide dynamics and sequestration in mine water and waste. Mine Water Env. 34, 3–9.

Kwon, S., 2011. Mineralization for CO_2 sequstration using olivine sorbent in the presence of water vapor.

Lackner, K.S., 2003. A Guide to CO_2 Sequestration. Science. 300, 1677–1678.

Lackner, K.S., Butt, D.P., Wendt, C.H., 1997. Magnesite dispoal of carbon dioxide, in: 22nd International Technical Conference on Coal Utilization and Fuel System. Clearwater, FL, ON.

Lackner, K.S., Butt, D.P., Wendt, C.H., Ziock, H., 1999. Mineral carbonates as carbon dioxide sinks. Los Alamos National Laboratory.Los Alamos, New Mexico.

Lackner, K.S., Duby, P.F., Yegulalp, T., Krevor, S.C., Graves, C., 2008. Integrating steel production with mineral carbon sequestration. Report No. DE-FC36-97ID13554. American Iron and Steel Institute, Technology Roadmap Program Office. Pittsburgh, PA.

Lackner, K.S., Brennan, S., Matter, J.M., Park, A.-H.A., Wright, A., van der Zwaan, B., 2012. The urgency of the development of CO_2 capture from ambient air. Proc. Natl. Acad. Sci. 109, 13156–13162.

Lafay, R., Montes-Hernandez, G., Janots, E., Chiriac, R., Findling, N., Toche, F., 2014. Simultaneous precipitation of magnesite and lizardite from hydrothermal alteration of olivine under high-carbonate alkalinity. Chem. Geol. 368, 63–75.

Langford, J., Wilson, A., 1978. Scherrer after sixty years: A survey and some new results in the determination of crystallite size. J. Appl. Cryst. 11, 102–113.

Larachi, F., Daldoul, I., Beaudoin, G., 2010. Fixation of CO_2 by chrysotile in low-pressure dry and moist carbonation : Ex-situ and in-situ characterizations. Geochim. Cosmochim. Acta 74, 3051–3075.

Larachi, F., Gravel, J.-P., Grandjean, B.P.A., Beaudoin, G., 2012. Role of steam, hydrogen and pretreatment in chrysotile gas–solid carbonation: Opportunities for pre-combustion CO2 capture. Int. J. Greenh. Gas Control 6, 69–76.

Lenaz, D., Logvinova, A.M., Princivalle, F., Sobolev, N. V., 2009. Structural parameters of chromite included in diamond and kimberlites from Siberia: A new tool for discriminating ultramafic source. Am. Mineral. 94, 1067–1070.

Leung, D.Y.C., Caramanna, G., Maroto-Valer, M.M., 2014. An overview of current status of carbon dioxide capture and storage technologies. Renew. Sustain. Energy Rev. 39, 426–443.

Li, J., Hitch, M., 2016a. Carbon dioxide adsorption isotherm study on mine waste for integrated CO_2 capture and sequestration processes. Powder Technol. 291, 408–413.

Li, J., Hitch, M., 2016b. Mechanical activation of ultramafic mine waste rock in dry condition for enhanced mineral carbonation. Miner. Eng. 95, 1–4.

Liao, J., Senna, M., 1992. Thermal behavior of mechanically amorphized talc. Thermochim. Acta 197, 295–306.

Lyons, J.L., Berkshire, L.H., White, C.W., 2003. Mineral carbonation feasibility study, Draft report. National Energy Technology Laboratory, US DOE. Albany, OR.

MacDowell, N., Florin, N., Buchard, A., Hallett, J., Galindo, A., Jackson, G., Adjiman, C.S., Williams, C.K., Shah, N., Fennell, P., 2010. An overview of CO_2 capture technologies. Energy Environ. Sci. 3, 1645.

Markewitz, P., Kuckshinrichs, W., Leitner, W., Linssen, J., Zapp, P., Bongartz, R., Schreiber, A., Müller, T.E., 2012. Worldwide innovations in the development of carbon capture technologies and the utilization of CO_2. Energy Environ. Sci. 5, 7281.

Maroto-valer, M.M., Fauth, D.J., Kuchta, M.E., Zhang, Y., Andre, J.M., 2005. Activation of

magnesium rich minerals as carbonation feedstock materials for CO_2 sequestration. Fuel Process. Technol. 86, 1627–1645.

Matter, J.M., Stute, M., Snæbjörnsdottir, S.Ó., Oelkers, E.H., Gislason, S.R., Aradottir, E.S., Sigfusson, B., Gunnarsson, I., Sigurdardottir, H., Gunnlaugsson, E., Axelsson, G., Alfredsson, H.A., Wolff-Boenisch, D., Mesfin, K., de la Reguera Taya, D.F., Hall, J., Dideriksen, K., Broecker, W.S., 2016. Rapid carbon mineralization for permanent diposal of anthropogenic carbon dioxide emissions. Science. 352, 1312–1314.

McCutcheon, J., Dipple, G.M., Wilson, S.A., Southam, G., 2015. Production of magnesium-rich solutions by acid leaching of chrysotile: A precursor to field-scale deployment of microbially enabled carbonate mineral precipitation. Chem. Geol. 413, 119–131.

McCutcheon, J., Power, I.M., Harrison, A.L., Dipple, G.M., Southam, G., 2014. A Greenhouse-Scale photosynthetic microbial bioreactor for carbon sequestration in magnesium carbonate minerals. Environ. Sci. Technol. 48, 9142–9151.

MacDowell, N., Florin, N., Buchard, A., Hallett, J., Galindo, A., Jackson, G., Adjiman, C.S., Williams, C.K., Shah, N., Fennell, P., 2010. An overview of CO_2 capture technologies. Energy Environ. Sci. Environ. Sci. 3, 1645.

Markewitz, P., Kuckshinrichs, W., Leitner, W., Linssen, J., Zapp, P., Bongartz, R., Schreiber, A., Müller, T.E., 2012. Worldwide innovations in the development of carbon capture technologies and the utilization of CO_2. Energy Environ. Sci. 5, 7281.

McKelvy, M.J., Diefenbacher, J., Nunez, R., Carpenter, R.W., Chizmeshya, A.V.G., 2005. Simultaneous mechanical and heat activation: a new route to enhance serpentine carbonation reactivity and lower CO_2 mineral sequestration process cost. Report No. DE-FG26-02NT41546. Arizona State University. Tempe, AZ.

Mellini, M., Fuchs, Y., Viti, C., Lemaire, C., Linarès, J., 2002. Insights into the antigorite structure from Mössbauer and FTIR spectroscopies. Eur. J. Mineral. 14, 97–104.

Mellini, M., Viti, C., 1994. Crystal structure of lizardite-l from Elba, Italy. Am. Mineral. 79, 1–5.

Meyer, N.A., Vögeli, J.U., Becker, M., Broadhurst, J.L., Reid, D.L., Franzidis, J.P., 2014. Mineral carbonation of PGM mine tailings for CO_2 storage in South Africa: A case study. Miner. Eng. 59, 45–51.

Musa, F., Morrison, R., 2009. A more sustainable approach to assessing comminution efficiency. Miner. Eng. 22, 593–601.

Nakamoto, K., 2009. Infrared and Raman Spectra of Inorganic and Coordination Compounds. Part A: Therory and Applications in Inorganic Chemistry, 6th ed. John Wiley & Sons, Inc., Hoboken, NJ, USA.

Ndlovu, B.N., Forbes, E., Becker, M., Deglon, D.A., Franzidis, J.P., Laskowski, J.S., 2011. The effects of chrysotile mineralogical properties on the rheology of chrysotile suspensions. Miner. Eng. 24, 1004–1009.

Nduagu, E., Bergerson, J., Zevenhoven, R., 2012. Life cycle assessment of CO_2 sequestration in magnesium silicate rock – A comparative study. Energy Convers. Manag. 55, 116–126.

Nelson, M.G., 2004. Carbon dioxide sequestration by mechanochemical carbonation of mineral Silicates. Report No. DE-FG26-99NT41547. University of Utah. Salt Lake City, Utah.

O'Connor, W., Dahlin, D., Nilsen, D., 2001. Research status on the sequestration of carbon dioxide by direct aqueous mineral carbonation, in: 18th Annual International Pittsburgh Coal Conference. Newcastle, NSW, Austrilia, pp. 1–12.

O'Connor, W.K., Dahlin, D.C., Rush, G.E., Gerdemann, S.J., Penner, L.R., 2004. Energy and economical evaluation of ex situ aqueous mineral carbonation, in: Proceedings of the 7th International Conference on Greenhouse Gas Control Technologies. Vancouver, BC, pp. 1–4.

O'Connor, W.K., Dahlin, D.C., Rush, G.E., Gerdemann, S.J., Penner, L.R., Nilsen, D.N., 2005. Aqueous mineral carbonation: Mineral availability, pretreatment, reaction parametrics, and process studies. Report No. DOE/ARC-TR-04-002. National Energy Technology Laboratory, US DOE. Albany, OR.

Ohlberg, S.M., Strickler, D.W., 1962. Determination of percent crystallinity of partly devitrigied glass by X-ray diffraction. J. Am. Ceram. Soc. 45, 170–171.

Olajire, A.A., 2013. A review of mineral carbonation technology in sequestration of CO_2. J. Pet. Sci. Eng. 109, 364–392.

Pan, S.-Y., Adhikari, R., Chen, Y.-H., Li, P., Chiang, P.-C., 2016. Integrated and innovative steel slag utilization for iron reclamation, green material production and CO_2 fixation via accelerated carbonation. J. Clean. Prod. doi:10.1016/j.jclepro.2016.07.112.

Pan, S.-Y., Chiang, A., Chang, E.-E., Lin, Y.-P., Kim, H., Chiang, P.-C., 2015. An innovative approach to integrated carbon mineralization and waste utilization: A review. Aerosol Air Qual. Res. 15, 1072–1091.

Park, A.A., Fan, L., 2004. CO_2 mineral sequestration: Physically activated dissolution of serpentine and pH swing process. Chem. Eng. Sci. 59, 5241–5247.

Park, A.A., Jadhav, R., Fan, L., 2003. CO_2 mineral sequestration: Chemically enhanced aqueous carbonation of serpentine. Can. J. Chem. Eng. 81, 885–890.

Papirer, E., Roland, R., 1981. Grinding of chrysotile in hydrocarbons, alcohol and water. Clays Clay Miner. 29, 161–170.

Park, A.A., Fan, L., 2004. CO_2 mineral sequestration: Physically activated dissolution of serpentine and pH swing process. Chem. Eng. Sci. 59, 5241–5247.

Park, A.A., Jadhav, R., Fan, L., 2003. CO_2 mineral sequestration: Chemically enhanced aqueous carbonation of serpentine. Can. J. Chem. Eng. 81, 885–890.

Pasquier, L.-C., Mercier, G., Blais, J.-F., Cecchi, E., Kentish, S., 2014a. Reaction mechanism for the aqueous-phase mineral carbonation of heat-activated serpentine at low temperatures and pressures in flue gas conditions. Environ. Sci. Technol. 48, 5163–5170.

Pasquier, L.-C., Mercier, G., Blais, J.-F., Cecchi, E., Kentish, S., 2014b. Parameters optimization for direct flue gas CO2 capture and sequestration by aqueous mineral carbonation using

activated serpentinite based mining residue. Appl. Geochem. 50, 66–73.

Penner, L., O'Connor, W.K., Dahlin, D.C., Gerdemann, S., Rush, G.E., 2004. Mineral carbonation: Energy costs of pretreatment options and insights gained from flow loop reaction studies, in: 3rd Annual Conference on Carbon Capture & Sequestration. Exchange Monitor Publications & Forums, Washington, DC, Alexandria, VA, pp. 1–18.

Plescia, P., Gizzi, D., Benedetti, S., Camilucci, L., Fanizza, C., De Simone, P., Paglietti, F., 2003. Mechanochemical treatment to recycling asbestos-containing waste. Waste Manag. 23, 209–18.

Picot, J.C., Cassard, D., Maldan, F., Greffié, C., Bodénan, F., 2011. Worldwide potential for ex-situ mineral carbonation. Energy Procedia 4, 2971–2977.

Pourghahramani, P., 2007. Mechanical activation of hematite using different grinding methods with special focus on structural changes and reactivity. Luleå University of Technology.

Power, I.M., Harrison, A.L., Dipple, G.M., 2016. Accelerating mineral carbonation using carbonic anhydrase. Environ. Sci. Technol. 50, 2610–2618.

Power, I.M., Dipple, G.M., Southam, G., 2010. Bioleaching of ultramafic tailings by acidithiobacillus spp. for CO_2 sequestration. Environ. Sci. Technol. 44, 456–62.

Power, I.M., Harrison, A.L., Dipple, G.M., Southam, G., 2013a. Carbon sequestration via carbonic anhydrase facilitated magnesium carbonate precipitation. Int. J. Greenh. Gas Control 16, 145–155.

Power, I.M., Harrison, A.L., Dipple, G.M., Wilson, S.A., Kelemen, P.B., Hitch, M., Southam, G., 2013b. Carbon mineralization: From natural analogues to engineered systems. Rev. Mineral. Geochem. 77, 305–360.

Power, I.M., Wilson, S. A, Small, D.P., Dipple, G.M., Wan, W., Southam, G., 2011. Microbially mediated mineral carbonation: roles of phototrophy and heterotrophy. Environ. Sci. Technol. 45, 9061–8.

Ray, P.K., 2015. Hi-Tech Horticulture and Climate Change: Principle and Applications, in: Choudhary, M.. L.., Patel, V.. B.., Siddiqui, M.W., Mahdi, S.. S. (Eds.), Climate Dynamics in Horticultural Science. Apple Academic Press, pp. 1–22.

Raudsepp, M., Pani, E., 2003. Application of Rietveld analysis to environmental mineralogy, in: Jambor, J.L., Blowes, D.W., Ritchie, A.I.M. (Eds.), Environmental Mineralogy of Mine Wastes, Mineralogical Association of Canada Short Course. Mineralogical Association of Canada, Ottawa, Canada, pp. 165–180.

Ribárik, G., Ungár, T., Gubicza, J., 2001. MWP-fit : a program for multiple whole-profile fitting of diffraction peak profiles by ab initio theoretical functions. Appl. Crystallogr. 34, 669–676.

Rietveld, H.M., 1969. A profile refinement method for nuclear and magnetic structures. J. Appl. Cryst. 2, 65–71.

Rigopoulos, I., Petallidou, K.C., Vasiliades, M.A., Delimitis, A., Ioannou, I., Efstathiou, A.M., Kyratsi, T., 2015. Carbon dioxide storage in olivine basalts: Effect of ball milling process. Powder Technol. 273, 220–229.

Rigopoulos, I., Vasiliades, M.A., Ioannou, I., Efstathiou, A.M., Godelitsas, A., Kyratsi, T., 2016. Enhancing the rate of ex situ mineral carbonation in dunites via ball milling. Adv. Powder Technol. 27, 360–371.

Romanov, V., Soong, Y., Carney, C., Rush, G.E., Nielsen, B., O'Connor, W., 2015. Mineralization of Carbon Dioxide: A Literature Review. ChemBioEng Rev. 2, 231–256.

Romão, I.S.S., 2015. Production of magnesium carbonates from serpentinites for CO_2 mineral sequestration - optimisation towards industrial application. Åbo Akademi University.

Roufail, R.A., 2011. The effect of stirred mill operation on particles breakage mechanism and their morphologyical features. University of British Columbia.

Rubin, E.S., Rao, A.B., Chen, C., 2004. Comparative assessments of fossil fuel power plants with CO_2 capture and storage, in: Proceedings of the 7th International Greenhouse Gas Technology Conference. Vancouver, BC, Canada, pp. 285–293.

Rubin, E.S., Davison, J.E., Herzog, H.J., 2015. The cost of CO_2 capture and storage. Int. J. Greenh. Gas Control 40, 378–400.

Sandvik, K.L., Kleiv, R.A., Haug, T.A., 2011. Mechanically activated minerals as a sink for CO_2. Adv. Powder Technol. 22, 416–421.

Sanna, A., Uibu, M., Caramanna, G., Kuusik, R., Maroto-Valer, M.M., 2014. A review of mineral carbonation technologies to sequester CO_2. Chem. Soc. Rev. 43, 8049–8080.

Sanna, A., Wang, X., Lacinska, A., Styles, M., Paulson, T., Maroto-valer, M.M., 2013. Enhancing Mg extraction from lizardite-rich serpentine for CO_2 mineral sequestration. Miner. Eng. 49, 135–144.

Sarvaramini, A., Assima, G.P., Beaudoin, G., Larachi, F., 2014. Biomass torrefaction and CO_2 capture using mining wastes – A new approach for reducing greenhouse gas emissions of co-firing plants. Fuel 115, 749–757.

Scherrer, P., 1918. Bestimmung der Grösse und der inneren Struktur von Kolloidteilchen mittels Röntgenstrahlen. Nachr. Ges. Wiss. Göttingen 26, 98–100.

Seifritz, W., 1990. CO_2 disposal by means of silicates. Nature 345, 486.

Sipilä, J., Teir, S., Zevenhoven, R., 2008. Carbon dioxide sequestration by mineral carbonation Literature review update 2005 – 2007, Environmental Protection. Report VT 2008-1. Åbo Akademi University. Turku, Finland.

Speakman, S.A., 2014. XRD training presentations. www.prism.mit.edu/xray/

Stokes, A.R., Wilson, A.J.C., 1944. The diffraction of X-rays by distorted crystal aggregates. I. Proc. Phys. Soc. Lond. 56, 174.

Styles, M.T., Sanna, A., Lacinska, A.M., Naden, J., Maroto-Valer, M., 2012. The variation in composition of ultramfic rocks and the effect on their suitability for carbon dioxide sequestration by mineralization following acid leaching. Greenh. Gases Sci. Technol. 2, 408–418.

Summers, C.A., Dahlin, D.C., Rush, G.E., O'Connor, W.K., Gerdemann, S.J., 2005. Grinding methods to enhance the reactivity of olivine. Miner. Metall. Process. 22, 140–144.

Tans, P., 2015. NOAA/ESRL. www.esrl.noaa.gov/gmd/ccgg/trends/

Tartaj, P., Cerpa, A., Garc, M.T., García-González, M., Serna, C., 2000. Surface instability of serpentine in aqueous suspensions. J. Colloid Interface Sci. 231, 176–181.

Teir, S., Eloneva, S., Fogelholm, C., Zevenhoven, R., 2009. Fixation of carbon dioxide by producing hydromagnesite from serpentinite. Appl. Energy 86, 214–218.

Teir, S., Revitzer, H., Eloneva, S., Fogelholm, C., Zevenhoven, R., 2007. Dissolution of natural serpentinite in mineral and organic acids. Int. J. Miner. Process. 83, 36 – 46.

Tkáčová, K., 1989. Mechanical activation of minerals. Elsevier Science Publishers, Amsterdam.

Tkáčová, K., Baláž, P., 1988. Structural and temperature sensitivity of leaching of chalcopyrite with iron (III) sulphate. Hydrometallurgy 21, 103–112.

Tkáčová, K., Heegn, H., Števulová, N., 1993. Energy transfer and conversion during comminution and mechanical activation. Int. J. Miner. Process. 40, 17–31.

Trapasso, F., Croci, D., Plescia, P., Tempesta, E., 2012. Asbestos waste carbonation: A new asbestos treatment with CO_2 recovery, in: 3rd International Conference on Industrial and Hazardous Waste Management. International Waste Working Group, Chania, Greece, pp. 1–8.

Trittschack, R., Grobety, B., Koch-Muller, M., 2012. In situ high-temperature Raman and FTIR spectroscopy of the phase transformation of lizardite. Am. Mineral. 97, 1965–1976.

Turianicová, E., Baláz, P., 2008. A possible way to storage carbon dioxide on mechanically activated olivine $(Mg, Fe)_2SiO_4$, in: VI International Conference on Mechanochemistry and Mechanical Alloying. Jamshedpur, India., pp. 316–319.

Turianicová, E., Baláž, P., Tuček, Ľ., Zorkovská, A., Zeleňák, V., Németh, Z., Šatka, A., Kováč, J., 2013. A comparison of the reactivity of activated and non-activated olivine with CO_2. Int. J. Miner. Process. 123, 73–77.

Turianicová, E., Obut, A., Tuček, Ľ., Zorkovská, A., Girgin, İ., Baláž, P., Németh, Z., Matik, M., Kupka, D., 2014. Interaction of natural and thermally processed vermiculites with gaseous carbon dioxide during mechanical activation. Appl. Clay Sci. 88-89, 86–91.

Uddin, S., Rao, S.R., Mirnezami, M., Finch, J.A., 2012. Processing an ultramafic ore using fiber disintegration by acid attack. Int. J. Miner. Process. 102-103, 38–44.

Ungár, T., Borbely, A., 1996. The effect of dislocation contrast on x-ray line broadening : A new approach to line profile analysis. Am. Phys. Lett. 69, 3173–3175.

U.S. Energy Information Administration, 2016. International Energy Outlook 2016.

UNFCCC, 1992. United Nations Framework Convention on Climate Change.

UNFCCC, 1998. Kyoto Protocol To the United Nations Framework Convention on Climate Change.

UNFCCC, 2012. Doha Amendment to the Kyoto Protocol.

UNFCCC, 2015. Paris Agreement.

Valentin, N., 1993. Comparative analysis of insect control by nitrogen, argon and carbon dioxide

in museum, archive and herbarium collections. Int. Biodeterior. Biodegradation 32, 263–278.

Van Essendelft, D.T., Schobert, H.H., 2009a. Kinetics of the acid digestion of serpentine with concurrent grinding. 1. Initial investigations. Ind. Eng. Chem. Res. 48, 2556–2565.

Van Essendelft, D.T., Schobert, H.H., 2009b. Kinetics of the acid digestion of serpentine with concurrent grinding. 2. Detailed investigation and model development. Ind. Eng. Chem. Res. 48, 9892–9901.

Veetil, S.P., Mercier, G., Blais, J.-F., Cecchi, E., Kentish, S., 2014. CO_2 sequestration by direct dry gas-solid contact of serpentinite mining residues : A solution for industrial CO2 emission. Int. J. Environ. Pollut. Remediat. 2, 52–59.

Veetil, S.P., Mercier, G., Blais, J.-F., Cecchi, E., Kentish, S., 2015a. Magnetic separation of serpentinite mining residue as a precursor to mineral carbonation. Int. J. Miner. Process. 140, 19–25.

Veetil, S.P., Pasquier, L.-C., Blais, J.-F., Cecchi, E., Kentish, S., Mercier, G., 2015b. Direct gas-solid carbonation of serpentinite residues in the absence and presence of water vapor: a feasibility study for carbon dioxide sequestration. Environ. Sci. Pollut. Res. 22, 13486–13495.

Viti, C., 2010. Serpentine minerals discrimination by thermal analysis. Am. Mineral. 95, 631–638.

Vitillo, J.G., 2015. Magnesium-based systems for carbon dioxide capture, storage and recycling: from leaves to synthetic nanostructured materials. RSC Adv. 5, 36192–36239.

Vogeli, J., Reid, D.L., Becker, M., Broadhurst, J., Franzidis, J.P., 2011. Investigation of the potential for mineral carbonation of PGM tailings in South Africa. Miner. Eng. 24, 1348–1356.

Wang, S.Y., Sharma, S.K., Cooney, T.F., 1993. Micro-Raman and infrared spectral study of forsterite under high pressure. Am. Mineral. 78, 469–476.

Wang, X., Maroto-valer, M.M., 2011. Dissolution of serpentine using recyclable ammonium salts for CO_2 mineral carbonation. Fuel 90, 1229–1237.

Wang, J., Huang, L., Yang, R., Zhang, Z., Wu, J., Gao, Y., Wang, Q., O'Hare, D., Zhong, Z., 2014. Recent advances in solid sorbents for CO_2 capture and new development trends. Energy Environ. Sci. 7, 3478–3518.

Waseda, Y., Mastubara, E., Shinoda, K., 2011. X-Ray diffraction Crystallography: Introduction, examples and solved problems. Springer, Springer Heidelberg Dordrecht London New York.

Wei, Y., Yan, J., Lu, S., Li, X., 2009. Mechanochemical decomposition of pentachloriopheno by ball milling. J. Environ. Sci. 21, 1761–1768.

Werner, M., Hariharan, S.B., Bortolan, A. V., Zingaretti, D., Baciocchi, R., Mazzotti, M., 2013. Carbonation of activated serpentine for direct flue gas mineralization. Energy Procedia 37, 5929–5937.

Williamson, G.K., Hall, W.H., 1953. X-ray line broadening from field aluminum and wolfram. Acta Met. 1, 22–31.

Wills, B.A., Napier-Munn, T., 2006. Mineral Processing Technology : An Introduction to the

Practical Aspects of Ore Treatment and Mineral Recovery. Elsvier Science & Technology Books, Butterworth-Heinemann, p. 444.

Wilson, S.A., 2005. Carbon sequestration in chrysotile mine tailings. University of British Columbia.

Wilson, S.A., 2009. Mineral traps for greenhouse gases in mine tailings: a protocol for verifying and quantifying CO_2 sequestration in ultramafic mines. University of British Columbia.

Wilson, S.A., Raudsepp, M., Dipple, G.M., 2006. Verifying and quantifying carbon fixation in minerals from serpentine-rich mine tailings using the Rietveld method with X-ray powder diffraction data. Am. Mineral. 91, 1331–1341.

Yoo, K., Kim, B., Kim, M., Lee, J., Jeong, J., 2009. Dissolution of magnesium from serpentine mineral in sulfuric acid solution. Mater. Trans. 50, 1225–1230.

Yu, H.L., Xu, Y., Shi, P.J., Wang, H.M., Zhang, W., Xu, B.S., 2011. Effect of thermal activation on the tribological behaviours of serpentine ultrafine powders as an additive in liquid paraffin. Tribol. Int. 44, 1736–1741.

Yu, S.C., 1997. Effects of pressure on the crystal structure of olivine in harzburgite xenolith of basalt. Proc. Natl. Sci. Counc. Repub. China 21, 173–179.

Yue, J., Klein, B., 2004. Influence of rheology on the performance of horizontal stirred mills. Miner. Eng. 17, 1169–1177.

Yuen, Y.T., Sharratt, P.N., Jie, B., 2016. Carbon dioxide mineralization process design and evaluation: concepts, case studies, and considerations. Environ. Sci. Pollut. Res. 1–22.

Zadrazil, F., Puniya, A.K., 1994. Influence of carbon dioxide on lignin degradation and digestibility of lignocellulosics treated with Pleurotus sajor-caju. Int. Biodeterior. Biodegradation 237-244.

Zarandi, A.E., Larachi, F., Beaudoin, G., Plante, B., Sciortino, M., 2016. Multivariate study of the dynamics of CO_2 reaction with brucite-rich ultramafic mine tailings. Int. J. Greenh. Gas Control 52, 110–119.

Zevenhoven, R., Fagerlund, J., 2009. CO_2 fixation by mineral matter; the potential of different mineralization routes. IOP Conf. Ser. Earth Environ. Sci. 6, 1–2.

Zevenhoven, R., Fagerlund, J., Songok, J.K., 2011. CO_2 mineral sequestration: developments toward large-scale application. Greenhous Gases Sci. Technol. 1, 48–57.

Zhang, Q., Sugiyama, K., Saito, F., 1997. Enhancement of acid extraction of magnesium and silicon from serpentine by mechanochemical treatment. Hydrometallurgy 45, 323–331.

Zulumyan, N.H., Papakhchyan, L.R., Isahakyan, A.R., Beglaryan, H.A., Terzyan, A.M., 2011. Study of mechanical impact on the crystal lattice of serpentines. Geochemistry Int. 49, 937–941.

Appendices

Appendix A: Appendix to Chapter 4

A.1 Particle size distribution

Fig. A.1 shows the frequency plot of the particle size distributions of TAW and NWO collected form feed, passes 1, 4, and 9. Both figures present the monomodal size distribution of all samples. The particle size distribution become sharper and the manxima moved from 100 μm to 2 μm with grinding time increases. The changes in particle size distribution of TAW (Fig. A.1(a)) are similar to that of NWO (Fig. A.1(b)). The result of particle size distribution is not agree with mechanical activation on gibbsite using a stirred mill in wet condition (Alex et al., 2014), which produce two maxima after 60 min of milling. The milling design for the mechanical activation is the key reason for the difference. The IsaMill^{TM} is famous for producing a sharp PSD, which allows the materials perform better in downstream separation or leaching (Pease, 2007).

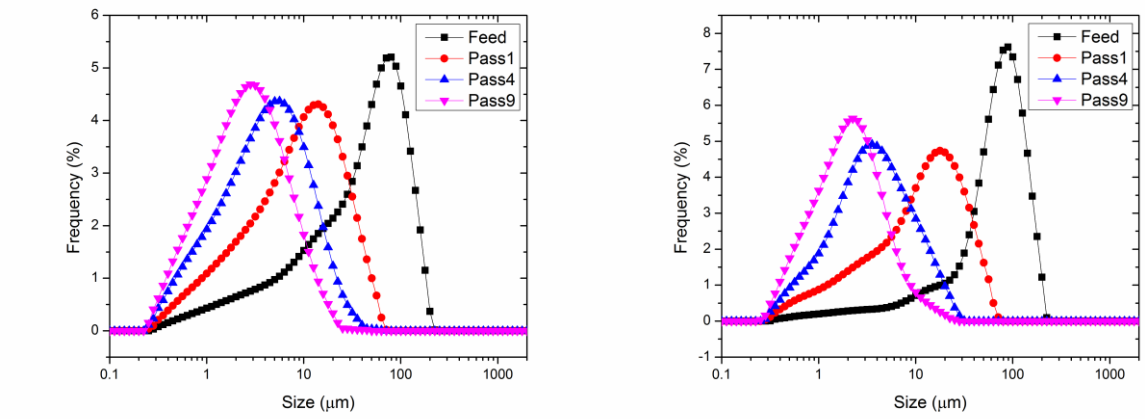

Figure A.1 Particle size distributions (frequency plot) of samples milled for different cycles in the high speed stirred mill. (a) TAW, (b) NWO.

Table A.1 lists the characteristic diameters (i.e. d_{10}, d_{50} and d_{90}) of samples with t_M and W_N. The characteristic diameters were extracted from their respective cumulative curves. d_{10}, d_{50} and d_{90} of NWO decreased from 3.4 μm, 44.5 μm and 110.3 μm to 0.7 μm, 1.9 μm and 5.4 μm, respectively after 0.8 min of milling. d_{10}, d_{50} and d_{90} of TAW decreased from 3.0 μm, 25.6 μm and 89.1 μm to 0.5 μm, 1.8 μm and 5.7 μm, respectively after 7.6 min of milling. All the characteristic diameters continue to decrease, and reach to a similar fine size after 9 cycles grinding. The particle size of TAW is smaller than that of NWO in all grinding cycles.

Table A.1 Variation of characteristic diameters (d_{10}, d_{50} and d_{90}) with milling time

t_M (min)	TSO (μm)			TAW (μm)		
	d_{10}	d_{50}	d_{90}	d_{10}	d_{50}	d_{90}
0	3.4±0.1	44.5±0.6	110.3±1.6	3.0±0.1	25.6±0.0	89.1±0.4
0.8/0.9	1.4±0.1	10.2±0.9	30.3±2.1	1.1±0.0	7.9±0.0	26.7±0.7
3.4/3.4	0.9±0.0	3.4±0.0	11.0±0.1	0.7±0.0	3.0±0.2	11.4±1.8
8/7.6	0.7±0.0	1.9±0.0	5.4±0.0	0.5±0.0	1.8±0.0	5.7±0.3

A.2 XRD pattern characterization

Table A.2 lists the geometry of forsterite (020) and lizardite (001) peaks in the XRD pattern (Fig 4.5), including the peak positions (2θ), the relative intensity (I_{max}/I_B) described by the ratio of maximum height of peaks (I_{max}) to the correspondence intensity of background (I_B), and the breadth of the peak always expressed using full widths at half maximum (FWHM). Table A.2 shows that the forsterite (020) peak in NWO and TAW become less intense and wider and the background level increases with increasing grinding energy input. A similar changes in the peak of XRD patterns has also been detected in mechanically activated olivine in other stirred mills (Baláž et al., 2008; Haug, 2010). Contrary to expectations, the lizardite (001) peak does not follow

this pattern. The lizardite (001) peak in both NWO and TAW becomes more intense than that in the feed in the first cycles. Afterwards, it reduces back to the initial level (TAW), or less intense than the initial level (NWO).

Table A.2 The variation in shape parameters of XRD selected peaks with milling time

Materials	t_M	Forsterite (020)			Lizardite (001)		
	(min)	2θ	I_{max}/I_B	FWHM	2θ	I_{max}/I_B	FWHM
NWO	0	20.134	6.71	0.076	14.022	0.36	0.33
	0.8	20.142	3.57	0.088	14.072	0.45	0.373
	3.4	20.151	3.09	0.095	14.072	0.30	0.336
	8.0	20.143	2.34	0.106	14.084	0.26	0.386
TAW	0	20.050	2.00	0.086	13.972	3.35	0.212
	0.9	20.154	1.94	0.096	14.074	4.97	0.195
	3.4	20.143	1.87	0.095	14.072	4.81	0.197
	7.6	20.160	1.45	0.099	14.082	3.47	0.207

A.3 Changes in microstructure

To gain a better understanding of how mechanical energy activates mine waste, the characterization of microstructure, including crystallite size (D_V) and maximum lattice strain (ε), lattice constants (*a, b, c*) and lattice volume (*V*), were calculated based on Rietveld method (Chapter 3). The sources of crystal structure used for Rietveld method are listed in Table A.4.

Table A.3 Sources of crystal structure data in use

Materials	Minerals	Source
TAW, NWO	Forsterite	(Yu, 1997)
TAW, NWO	Lizardite-1T	(Mellini and Viti, 1994)
TAW, NWO	Magnetite	(Tsukimura et al., 1997)
TAW, NWO	Quartz	(Glinnemann et al., 1992)
TAW, NWO	Brucite	(Nagai et al., 2000)
NWO	Enstatite	(Carlson et al., 1988)
NWO	Talc	(Gruner, 1939)

Tables A.5 and A.6 lists the microstructure values of initial and mechanically-activated samples. The lattice parameters of forsterite in NWO are nearly unchanged during mechanical activation. On the contrary, the *V* of forsterite and lizardite in TAW initially decreased up to the first cycle of grinding and then increased slightly. All the lattice parameters of forsterite in TAW are larger than those in NWO, regardless of milling cycles. It seems that the lizardite content enlarges the lattice parameters of forsterite in the mine waste material and made these values sensitive to intensive wet grinding.

The continuous decrease in D_V of forsterite and increase in ε of forsterite were observed in both NWO and 06110 with grinding progress. The reduction in the D_V of forsterite in TAW after 9 cycles of grinding is less than that in NWO. The D_V of lizardite initial increases up to 3.4 min and then decrease back to the value before mechanical activation. The changes in D_V is in line with the changes in C_{XRD} of materials mechanically activated in wet condition. The weight percentage of forsterite and lizardite in TAW are nearly unchanged. The observation indicates that D_V could represent C_{XRD} when there is no phase transfer between minerals. In the case of existence of phase transfer, D_V would be a better value than C_{XRD} to characterize the crystal structure changes of each mineral during mechanical activation.

Table A.4 Changes in the microstructure of NWO with grinding time

Pass No.	Lattice parameter				D_V (nm)	ε ($\times 10^3$)
	a (nm)	*b* (nm)	*c* (nm)	*V* (nm^3)		
Feed	0.47607	1.02185	0.59906	0.29142	109.3	0.35
1	0.47607	1.02180	0.59904	0.29140	92.9	0.41
4	0.47608	1.02183	0.59904	0.29141	80.9	0.47
9	0.47605	1.02185	0.59903	0.29140	66.0	0.58

Table A.5 Changes in the microstructure of TAW with grinding time

Pass No.	Phase	Lattice parameter				D_V (nm)	ε ($\times 10^3$)	Weight percentage (%)
		a (nm)	*b* (nm)	*c* (nm)	*V* (nm^3)			
Feed	Fo	0.47635	1.02283	0.59951	0.29210	91.4	0.42	64.7
	Li	0.53282		0.73056	0.17962	28.4	1.34	29.6
1	Fo	0.47629	1.02270	0.59944	0.29199	92.8	0.41	64.6
	Li	0.53284		0.73023	0.17955	29.4	1.29	29.1
4	Fo	0.47631	1.02267	0.59938	0.29196	86.2	0.44	65.2
	Li	0.53316		0.72997	0.17971	30.3	1.25	27.8
9	Fo	0.47637	1.02270	0.59939	0.29201	79.1	0.50	64.8
	Li	0.53380		0.73029	0.18021	27.6	1.38	27.1

Note: Fo denotes the forsterite phase, Li denotes the lizardite phase.

Appendix B: Appendix to Chapter 7, Kinetics analysis of the carbonation on mechanically activated mine waste

B.1 Linear equations

Assuming the increase in carbonation conversion (R_X) with carbonation time (t_C) follows a linear relationship (Eq. B.1) in the duration of 0-1, 1-2, 2-6 hours.

$$R_X = k_1 t_C + R_1 \tag{B.1}$$

where, coefficients k_1 and R_1 are the slop, and intercept, respectively.

Fig B.2 shows the fitting results of carbonation conversion vs carbonation time according to Equation B.1 and Table B.1 lists the fitting parameters. For SMP4 and SMP9, carbonation follows different linear equations in the three-time range, include 0 to 1 hour, 1 to 2 hours, and 2 to 6 hours. However, the carbonation of FEED and SMP1 after 1 hour, follows one linear equation. Assuming carbonation for long hours, the relationship between carbonation conversion vs carbonation time follows the same liner equation as the carbonation range of 2 to 6 hours. According to the linear equations, the carbonation time to achieve a defined carbonation conversion can be calculated. Table B.2 list the result of calculated carbonation time. The carbonation time for FEED to reach to a carbonation conversion more than 40% is more than 23.98 hours. Mechanical activation in IsaMill for only 1 cycle, could reduce the time to 4.33 hours. Mechanical activation greatly reduces the carbonation time of mine waste and is important for apply as pretreatment method.

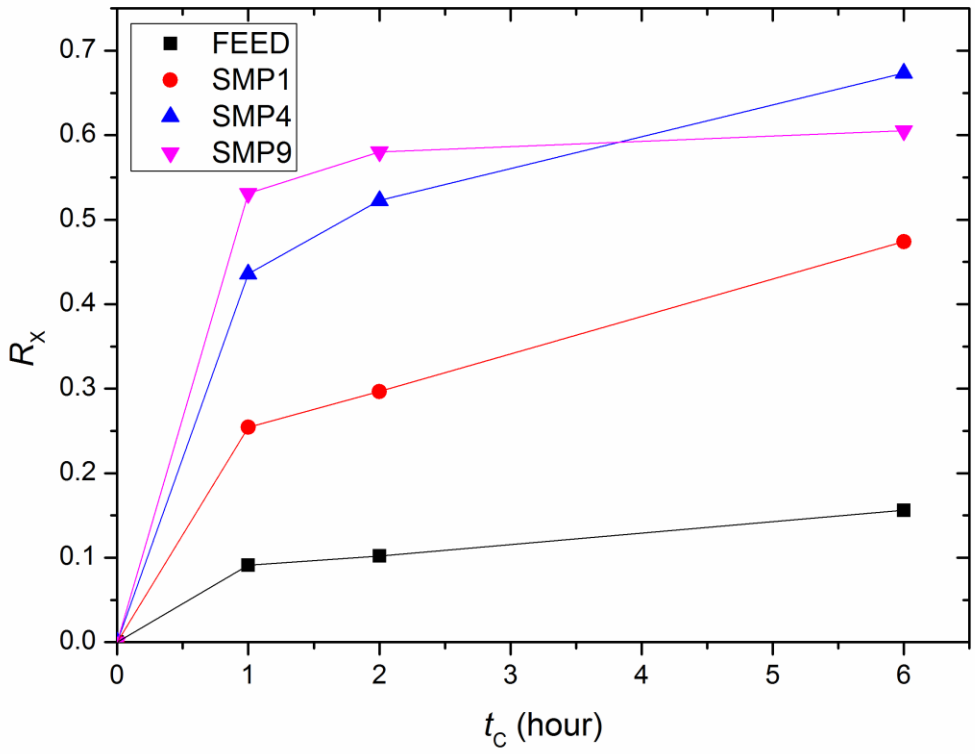

Figure B.1 Fitting the changes of the carbonation conversion with carbonation time using linear equations

Table B.1 The fitted parameter value using linear equations

	t_C =0-1		t_C =1-2		t_C=2-6	
	k_1	R_1	k_1	R_1	k_1	R_1
FEED	0.09	0.00	0.01	0.08	0.01	0.07
SMP1	0.25	0.00	0.04	0.21	0.04	0.21
SMP4	0.44	0.00	0.09	0.35	0.04	0.45
SMP9	0.53	0.00	0.05	0.48	0.01	0.57

Table B.2 The carbonation time needed to reach the sitting carbonation conversion

	R_X =0.40	R_X =0.45	R_X =0.50	R_X =0.55	R_X =0.60
FEED	23.98	27.67	31.36	35.04	38.73
SMP1	4.33	5.46	6.58	7.71	8.84
SMP4	0.92	1.16	1.74	2.72	4.05
SMP9	0.75	0.85	1.00	1.39	5.16

B.2 Pseudo second order kinetics equations

The carbonation of ultramafic rocks always follows the pseudo second order kinetics, which is described in Equation B.2.

$$\frac{dR_X}{dt_C} = k_2(R_2 - R_X)^2 \quad \text{(B.2)}$$

Where, k_2 and R_2 are coefficients for the second order kinetics equation. A plot of t_C/R_X against t_C gives a straight line (Equation B.3).

$$\frac{t_C}{R_X} = \frac{1}{k_2 R_2^2} + \frac{1}{R_2} t_C \quad \text{(B.3)}$$

From the intercept $(1/k_2R_2^2)$ and slope $(1/R_2)$ of the line, k_2 and R_2 can be calculated.

Fig B.3 shows the fitting result of carbonation conversion vs carbonation time based on Equation B.2 and Table B.3 lists the fitting parameters. The correlation coefficient R^2 indicate the pseudo second order kinetics model fit is acceptable. The longer mechanical activation time, the better their carbonation results fit the pseudo second order kinetics model. According to the obtained pseudo second order kinetics equations, the carbonation time to achieve a setting carbonation conversion were calculated. Table B.4 list the results of calculated carbonation time. The minus value in FEED and SMP1 means the defined carbonation conversion would never be reached under the applied carbonation conversion. Compare the data in Table B.2 and Table B.4, the carbonation time is shorter using pseudo second order kinetics model than using liner model. The actual carbonation time to reach 55% carbonation conversion for SMP4 is longer than 2 hours. Thus, liner equations may be more accurate than the pseudo second order kinetics models for fitting the experimental data.

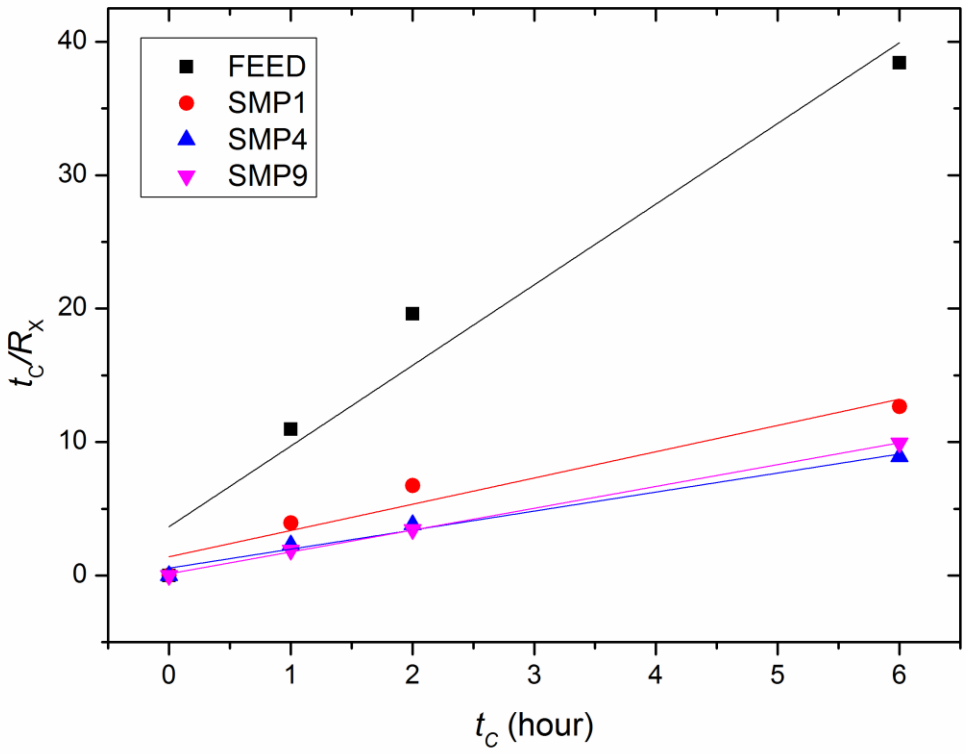

Figure B.2 Fitting the changes of the carbonation conversion with carbonation time using linear equations

Table B.3 The fitted parameter value using pseudo second order kinetics model

	$1/R_2$	$1/k_2R_2^2$	R_2	k_2	R^2
FEED	6.05	3.65	0.17	10.01	0.979
SMP1	1.97	1.40	0.51	2.77	0.973
SMP4	1.43	0.55	0.70	3.70	0.992
SMP9	1.64	0.13	0.61	20.91	0.999

Table B.4 The carbonation time needed to reach the defined carbonation conversion

	R_X =0.40	R_X =0.45	R_X =0.50	R_X =0.55	R_X =0.60
FEED	-1.03	-0.96	-0.90	-0.86	-0.83
SMP1	2.64	5.53	45.19	-9.29	-4.63
SMP4	0.51	0.69	0.95	1.40	2.27
SMP9	0.15	0.22	0.35	0.70	4.17

Appendix C: Appendix to Chapter 7, Improved cost modeling from Sarah's thesis

Highlighted Boxes Require User Input

MINING

	Unit	Value
Mine life	yrs	29
Operating days per year	days	365
Daily production rate (throughput)	tpd	84,600
Tailings production rate	tpd	82,908
Tailings ratio (throughput:tailings)	-	0.98
CO_2 ratio (tailings:CO_2)	-	0.035
CO_2 production rate	tpd	2,902

* Mining costs borne by Ni-mining operations and therefore not included

PROCESSING

Composition- mine waste material (TAW)

	assay (wt %)	output (tpd)
SiO_2	38.70%	32,085
Al_2O_3	0.15%	124
Fe_2O_3	10.39%	8,614
CaO	0.30%	249
MgO	45.51%	37,731
MnO	0.16%	133
Cr_2O_3	0.67%	556
TiO2	0.03%	25
LOI	4.09%	3,391
TOT/C	0.05%	41
TOT/S	0.04%	33
Total	100.00%	82,908

*Processing Costs***

	unit	value
Required grind size	µ	4.6
Unit processing cost at required grind size	$/t	11.34
IsaMill-new technique for grinding	kwh/t	210
Daily processing cost	$/day	940176.72

Annual processing cost	$/yr	343,164,503
Unit cost of processing	$/t feed	11.34
	$/t CO_2	38.03

SEQUESTRATION

Input

	unit	value
Waste feed	tpd	82,908
Ratio feed:CO2 for complete conversion	-	3.35
MgO available	tpd	37,731
Sequestration efficiency	%	0.6
CO2 from direct source	tpd	2,902
CO2 required for complete reaction w/ available MgO	tpd	41200

*Output****

	unit	value
MgCO3	tpd	47,359
Waste (SiO2)	tpd	16,874
Total for disposal	tpd	64,233
Daily amount of CO2 sequestered	tpd	24720
Annual amount of CO2 sequestered	tpy	9022788
CO2 avoidance ratio	-	0.991
Annual CO2 avoided	tpy	8941583

*** Output assumed to follow the generalized equation for olivine reaction

*Operating Costs*****

	unit	value
Unit carbonation cost	$/t	14.04
Autoclave carbonation	kwh/t	260
Daily operating cost	$/day	1164028
Annual operating cost	$/yr	424870337
Unit operating cost of sequestration	$/t feed	14.04
	$/t CO_2	47.09

**** Cost estimates from O'Connor using extrapolate estimation

CO2 CAPTURE		
CO2 separation and capture from flue gas	$/t CO_2	9.6
TRANSPORTATION		
	unit	value
Waste rock from pit to processing facility	km	-
CO_2 from direct source	km	-
CO_2 from external source	km	250
Unit feed transportation cost per km	$/t km	0.02
Unit CO_2 transportation cost per km	$/t km	0.02
Total feed transportation cost	$/yr	-
Total CO_2 transportation cost	$/yr	75189898
Total transportation cost	$/yr	75189898
Unit cost of transportation	$/t feed	2.48
	$/t CO_2	8.33
DISPOSAL		
	unit	value
Distance from sequestration facility to dump	km	-
Total output for disposal ($MgCO_3$ + waste)	tpd	14,186
Unit disposal cost per km	$/t km	0.02
Total disposal cost	$/yr	1985013
Unit cost of disposal	$/t feed	0.22
	$/t CO_2	0.72
TOTAL		
	unit	value
Processing cost	$/t CO_2	38.03
Sequestration cost	$/t CO_2	47.09
CO_2 capture cost	$/t CO_2	9.6
Transportation cost	$/t CO_2	8.33
Disposal cost	$/t CO_2	0.7194
Total operating cost	$/t CO_2	103.77